

SIMULATION OF
AIR-BLAST-INDUCED GROUND MOTIONS
(PHASE II)

by

Harry E. Auld
Capt USAF

Gerald P. D'Arcy
Capt USAF

Gerald G. Leigh
Capt USAF

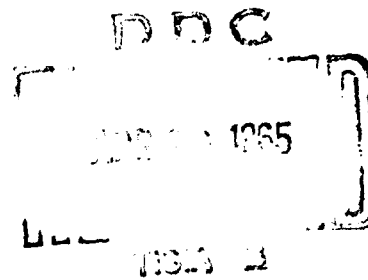
TECHNICAL REPORT NO. AFWL-TR-65-26, Volume I



Research and Technology Division
AIR FORCE WEAPONS LABORATORY
Air Force Systems Command
Kirtland Air Force Base
New Mexico

| | | |
|------------|---------|-----|
| COPY 2 | OF 3 | dar |
| HARD COPY | \$ 6.00 | |
| MICROFICHE | \$ 1.25 | |

228p
April 1965



Best Available Copy

ARCHIVE COPY

Research and Technology Division
AIR FORCE WEAPONS LABORATORY
Air Force Systems Command
Kirtland Air Force Base
New Mexico

When U. S. Government drawings, specifications, or other data are used for any purpose other than a definitely related Government procurement operation, the Government thereby incurs no responsibility nor any obligation whatsoever, and the fact that the Government may have formulated, furnished, or in any way supplied the said drawings, specifications, or other data, is not to be regarded by implication or otherwise, as in any manner licensing the holder or any other person or corporation, or conveying any rights or permission to manufacture, use, or sell any patented invention that may in any way be related thereto.

This report is made available for study with the understanding that proprietary interests in and relating thereto will not be impaired. In case of apparent conflict or any other questions between the Government's rights and those of others, notify the Judge Advocate, Air Force Systems Command, Andrews Air Force Base, Washington, D. C. 20331.

DDC release to OTS is authorized.

SIMULATION OF
AIR-BLAST-INDUCED GROUND MOTIONS
(Phase II)

by

Harry E. Auld
Capt USAF

Gerald P. D'Arcy
Capt USAF

Gerald G. Leigh
Capt USAF

April 1965

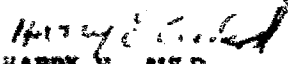
FOREWORD

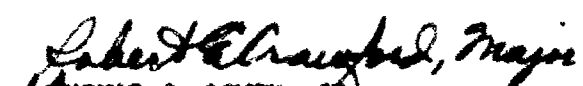
This report presents the results obtained from an in-house experimental and theoretical study on the simulation of air-blast-induced ground motions. The work was conducted under Project 5710, subtask 13.166, Program Element 7.60.06.01.5, and was funded by the Defense Atomic Support Agency. This work was conducted from 1 July 1964 to 1 February 1965. The report was submitted on 12 March 1965.

This report consists of two volumes. Volume I contains Part 1, Simulation Technique; Part 2, Air Free Field; and Part 3, Earth Free Field. Volume II contains Part 4, Underground Structure Response (Secret-NoForN); and Part 5, Hardened Communications Response (Secret-NoForN).

The assistance of the following personnel and organizations is gratefully acknowledged: the Laboratory Services Section, Civil Engineering Branch, Air Force Weapons Laboratory, assisted by personnel from the Air Force Shock Tube Facility, procured, installed, and recorded all of the free-field instrumentation. Capt Thomas E. O'Brien, Civil Engineering Branch, Air Force Weapons Laboratory, was responsible for the drilling of instrumentation holes and all of the soils testing. Lt Drayne D. Piepenburg, Civil Engineering Branch, Air Force Weapons Laboratory, was responsible for the fabrication of primacord racks and was assisted by personnel from the Explosive Ordnance Disposal Section, Deputy for Material, Air Force Special Weapons Center. Mr. Fred Peterson, Civil Engineering Branch, Air Force Weapons Laboratory, was the resident engineer for the construction on this project. Photographic coverage was provided by the Photographic Division, Deputy for Test and Engineering, Air Force Special Weapons Center. Heavy equipment and operators were provided by the Kirtland Air Force Base Civil Engineering Division.

This technical report has been reviewed and is approved.


HARRY E. AULD
Captain USAF
Project Officer


THOMAS J. LOWRY, JR.
Colonel USAF
Chief, Civil Engineering
Branch


R. A. HOUSE
Colonel USAF
Chief, Development Division

ABSTRACT

Results from the Phase II, Long-Duration High-Explosive Simulation Technique (LDHEST) experiment are presented. This experiment simulates the air-blast-induced ground motions from a large-yield nuclear weapon over a plan area 96 feet by 150 feet. A specially designed matrix of primacord was utilized to produce the desired explosion in a confined volume of air. An overburden, or mass of material, was placed over the explosion to provide a reaction force to shape the resulting wave pulse and to provide the required long durations. The experiment produced an air pressure pulse which had a peak overpressure of 312 psi, a time to one-half peak pressure of 13.2 msec, and a total duration of 170 msec. The shock front traveled at an average velocity of 5,120 ft/sec. On the basis of these results, recommendations are made for future simulation experiments. The measured earth free-field motions and stresses are compared with theoretical calculations, and the validity of the technique for simulating the desired nuclear environment is established.

This page intentionally left blank.

CONTENTS

PART 1

SIMULATION TECHNIQUE

| <u>Section</u> | | <u>Page</u> |
|----------------|---------------------------------|-------------|
| I | INTRODUCTION | 3 |
| | 1. Objectives | 3 |
| | 2. Background | 3 |
| | 3. Nuclear Blast Environment | 4 |
| | 4. Theory | 5 |
| II | PROCEDURE | 30 |
| | 1. Operations | 30 |
| | 2. Instrumentation | 36 |
| III | RESULTS | 53 |
| IV | DISCUSSION | 56 |
| V | CONCLUSIONS AND RECOMMENDATIONS | 63 |

PART 2

AIR FREE FIELD

| | | |
|------|-----------------------|----|
| VI | INTRODUCTION | 67 |
| | 1. Objectives | 67 |
| | 2. Background | 67 |
| | 3. Predictions | 67 |
| VII | PROCEDURE | 69 |
| | 1. Instrumentation | 69 |
| | 2. Gage Placement | 70 |
| | 3. Gage Locations | 70 |
| VIII | RESULTS | 74 |
| | 1. Air Pressure Gages | 74 |
| | 2. Break Wires | 75 |
| | 3. Microbarographs | 75 |

CONTENTS (cont'd)

PART 2 (cont'd)

| <u>Section</u> | | <u>Page</u> |
|-------------------------|--------------------------------------------|-------------|
| IX | DISCUSSION | 76 |
| | 1. Pressure-Time History | 76 |
| | 2. Shock Front Velocity | 77 |
| | 3. End Wall Reflections | 77 |
| | 4. Shock Pressure Vented to the Atmosphere | 78 |
| X | CONCLUSIONS AND RECOMMENDATIONS | 89 |
| PART 3 | | |
| EARTH FREE FIELD | | |
| XI | INTRODUCTION | 93 |
| | 1. Objectives | 93 |
| | 2. Background | 93 |
| | 3. Soil Survey | 93 |
| | 4. Predictions | 94 |
| XII | PROCEDURE | 107 |
| | 1. Instrumentation | 107 |
| | 2. Gage Placement | 109 |
| | 3. Gage Locations | 110 |
| XIII | RESULTS | 120 |
| | 1. Soil Stress Gages | 120 |
| | 2. Accelerometers | 120 |
| | 3. Velocity Gages | 121 |
| | 4. Long-Span Displacement Gages | 121 |
| | 5. Slope-Indicator Gage | 121 |
| | 6. Time-of-Arrival System | 123 |

CONTENTS (cont'd)

PART 3 (cont'd)

| <u>Section</u> | | <u>Page</u> |
|----------------|------------------------------------|-------------|
| XIV | DISCUSSION | 140 |
| | 1. Soil Stress | 140 |
| | 2. Acceleration | 141 |
| | 3. Velocity | 141 |
| | 4. Displacement | 145 |
| | 5. Horizontal Motions and Stresses | 146 |
| XV | CONCLUSIONS AND RECOMMENDATIONS | 159 |
| | APPENDIX A | 165 |
| | Instrumentation Equipment List | 165 |
| | APPENDIX B | 175 |
| | Air Blast Records | 175 |
| | APPENDIX C | 187 |
| | Free-Field Ground Motion Records | 187 |
| | REFERENCES | 213 |
| | DISTRIBUTION | 214 |

ILLUSTRATIONS

| <u>Figure</u> | | <u>Page</u> |
|---------------|--------------------------------------------------------------------|-------------|
| I-1 | Pressure-Time History for 300 psi Wave from 1 MT Surface Burst | 18 |
| I-2 | Air-Blast-Loading from a 1 MT Surface Burst | 19 |
| I-3 | Stresses on an Element Under One-Dimensional Wave Conditions | 20 |
| I-4 | Pressure-Time History at Depth, z | 20 |
| I-5 | Rarefaction Waves | 21 |
| I-6 | Stress Waves in an Elastic Half Space | 22 |
| I-7 | Air-Blast-Induced Ground Motions in Superseismic Region | 23 |
| I-8 | Primacord Matrix | 24 |
| I-9 | Peak Shock Overpressure versus Load Density | 25 |
| I-10 | Shock Front Velocity versus Wrap Angle | 26 |
| I-11 | Model for Overburden Calculations | 27 |
| I-12 | Results of Overburden Calculations | 28 |
| I-13 | Comparison of Pressure-Time Histories for Primacord and Nuclear | 29 |
| II-1 | Plan View of Detonation Facility | 39 |
| II-2 | Cross Section of Detonation Facility | 40 |
| II-3 | Cross Section of Detonation Facility | 41 |
| II-4 | Cross Section of Steel Support Structure | 42 |
| II-5 | Early Stage of the Facility Construction | 43 |
| II-6 | Details of the Steel Construction | 44 |
| II-7 | Primacord Rack Placement | 45 |
| II-8 | Typical Primacord Rack Construction | 46 |
| II-9 | Primacord Wrapping | 47 |

ILLUSTRATIONS (cont'd)

| <u>Figure</u> | | <u>Page</u> |
|---------------|-----------------------------------------------------------------------------------------------------------|-------------|
| II-10 | Primacord Cross Tying | 48 |
| II-11 | Primacord Entrances into Detonation Facility | 49 |
| II-12 | Primacord Detonation | 49 |
| II-13 | General Project and Instrumentation Layout | 50 |
| II-14 | Instrumentation Recording System Schematic | 51 |
| II-15 | Target Stands | 52 |
| III-1 | Maximum Overburden Height | 54 |
| III-2 | Overburden Motion | 55 |
| IV-1 | Peak Shock Overpressure versus Load Density (Corrected) | 57 |
| IV-2 | Shock Front Velocity versus Wrap Angle (Corrected) | 58 |
| IV-3 | Comparison of Pressure-Time Histories for Primacord and Nuclear | 59 |
| IV-4 | Overburden Motion | 60 |
| IV-5 | Duration Efficiency Factors | 61 |
| IV-6 | Corrected Overburden Calculations | 62 |
| V-1 | Overburden versus Cavity Depth Required to Simulate a 300 psi Shock Wave from a One- Megaton Weapon | 64 |
| VII-1 | Pressure Transducer Mount | 72 |
| VII-2 | Instrumentation Locations | 73 |
| IX-1 | Composite Pressure-Time History Curve | 80 |
| IX-2 | Shock Front Velocities--North Gage Line | 81 |
| IX-3 | Shock Front Velocities--Central Gage Line | 82 |
| IX-4 | Shock Front Velocity--South Gage Line | 83 |
| IX-5 | Shock Front Velocity--Break Wires | 84 |
| IX-6 | Summary of Shock Front Velocities | 85 |

ILLUSTRATIONS (cont'd)

| <u>Figure</u> | | <u>Page</u> |
|---------------|---------------------------------------------------------------------|-------------|
| IX-7 | Shock Front Positions | 86 |
| IX-8 | Attenuation of Reflected Pressure | 87 |
| IX-9 | Reflected Shock Front Velocity | 87 |
| IX-10 | Overpressure versus Distance | 88 |
| XI-1 | Soil Profile | 99 |
| XI-2 | Stress-Strain Curves from Constrained Modulus Tests | 100 |
| XI-3 | Predicted Attenuation Factor | 101 |
| XI-4 | Predicted Peak Vertical Accelerations | 102 |
| XI-5 | Predicted Peak Vertical Velocity | 103 |
| XI-6 | Idealized Bilinear Stress-Strain Curve | 104 |
| XI-7 | Predicted Total Displacements for Various Depths | 105 |
| XI-8 | Predicted Relative Displacements Between Surface and Various Depths | 106 |
| XII-1 | Sandia Velocity Gage and Protective Cover | 113 |
| XII-2 | Statham Model A69TC Accelerometer and Protective Cover | 113 |
| XII-3 | Soil-Stress Gage | 114 |
| XII-4 | Long-Span-Displacement Gage Mounted on Calibration Device | 114 |
| XII-5 | Scratch Gage | 115 |
| XII-6 | Slope-Indicator Instrument and Accessories | 116 |
| XII-7 | Depth Probe | 117 |
| XII-8 | Instrumentation Locations | 118 |
| XII-9 | Typical Gage Installation | 119 |
| XIII-1 | Near-Surface Vertical Soil Stress | 124 |

ILLUSTRATIONS (cont'd)

| <u>Figure</u> | | <u>Page</u> |
|---------------|---------------------------------------------------------------------------|-------------|
| XIII-2 | Near-Surface Vertical Soil Stress | 125 |
| XIII-3 | Peak Vertical Accelerations | 126 |
| XIII-4 | Peak Vertical Velocities | 127 |
| XIII-5 | Times of First Arrival, Hole 12 | 128 |
| XIII-6 | Times of First Arrival, Hole 21 | 129 |
| XIII-7 | Times of First Arrival, Hole 25 | 130 |
| XIII-8 | Times of Arrival (Peak Velocity) | 131 |
| XIII-9 | Peak Vertical Displacements | 132 |
| XIII-10 | Survey Data for Slope Indicator | 133 |
| XIII-11 | Slope Indicator Lateral Movement (East-West) | 134 |
| XIII-12 | Slope Indicator Lateral Movement (North-South) | 135 |
| XIII-13 | Plan View Showing Ball Switch Placement and Shock Wave at Surface of Soil | 136 |
| XIII-14 | Time-of-Arrival Contours, Plane 1 | 137 |
| XIII-15 | Time-of-Arrival Contours, Plane 2 | 138 |
| XIII-16 | Time-of-Arrival Contours, Plane 3 | 139 |
| XIV-1 | Attenuation Factors | 147 |
| XIV-2 | Near-Surface Vertical Soil Stress | 148 |
| XIV-3 | Near-Surface Vertical Soil Stress | 149 |
| XIV-4 | Peak Vertical Accelerations | 150 |
| XIV-5 | Peak Vertical Velocities | 151 |
| XIV-6 | Foundation on an Elastic Soil | 152 |
| XIV-7 | Influence of Rarefaction Waves | 153 |
| XIV-8 | Propagation Velocities, Hole 12 | 154 |
| XIV-9 | Propagation Velocities, Hole 21 | 155 |

ILLUSTRATIONS (cont'd)

| <u>FIGURE</u> | | <u>Page</u> |
|---------------|----------------------------------------|-------------|
| XIV-10 | Propagation Velocities, Hole 25 | 156 |
| XIV-11 | Propagation Velocities (Peak Velocity) | 157 |
| XIV-12 | Peak Vertical Displacements | 158 |
| XV-1 | Peak Vertical Stresses | 161 |
| XV-2 | Peak Vertical Accelerations | 162 |
| XV-3 | Peak Vertical Velocities | 163 |
| XV-4 | Mass of Material Realistically Loaded | 164 |
| B-1 | Air Pressure versus Time | 177 |
| B-2 | Air Pressure versus Time | 178 |
| B-3 | Air Pressure versus Time | 179 |
| B-4 | Air Pressure versus Time | 180 |
| B-5 | Air Pressure versus Time | 181 |
| B-6 | Air Pressure versus Time | 182 |
| B-7 | Air Pressure versus Time | 183 |
| B-8 | Air Pressure versus Time | 184 |
| B-9 | Air Pressure versus Time | 185 |
| C-1 | Vertical Acceleration versus Time | 189 |
| C-2 | Vertical Velocity versus Time | 190 |
| C-3 | Vertical Acceleration versus Time | 191 |
| C-4 | Vertical Velocity versus Time | 191 |
| C-5 | Vertical Acceleration versus Time | 192 |
| C-6 | Vertical Velocity versus Time | 192 |
| C-7 | Vertical Acceleration versus Time | 193 |
| C-8 | Vertical Velocity versus Time | 194 |
| C-9 | Vertical Acceleration versus Time | 195 |

ILLUSTRATIONS (cont'd)

| <u>Figure</u> | | <u>Page</u> |
|---------------|-----------------------------------|-------------|
| C-10 | Vertical Velocity versus Time | 195 |
| C-11 | Vertical Velocity versus Time | 196 |
| C-12 | Vertical Displacement versus Time | 196 |
| C-13 | Vertical Velocity versus Time | 197 |
| C-14 | Vertical Displacement versus Time | 197 |
| C-15 | Vertical Velocity versus Time | 198 |
| C-16 | Vertical Displacement versus Time | 198 |
| C-17 | Vertical Velocity versus Time | 199 |
| C-18 | Vertical Displacement versus Time | 200 |
| C-19 | Vertical Velocity versus Time | 201 |
| C-20 | Vertical Displacement versus Time | 202 |
| C-21 | Vertical Velocity versus Time | 203 |
| C-22 | Vertical Displacement versus Time | 203 |
| C-23 | Vertical Velocity versus Time | 204 |
| C-24 | Vertical Displacement versus Time | 204 |
| C-25 | Vertical Velocity versus Time | 205 |
| C-26 | Vertical Displacement versus Time | 206 |
| C-27 | Vertical Velocity versus Time | 207 |
| C-28 | Vertical Displacement versus Time | 208 |
| C-29 | Vertical Velocity versus Time | 209 |
| C-30 | Vertical Displacement versus Time | 209 |
| C-31 | Vertical Velocity versus Time | 210 |
| C-32 | Vertical Displacement versus Time | 210 |
| C-33 | Vertical Velocity versus Time | 211 |

ILLUSTRATIONS (cont'd)

| <u>Figure</u> | | <u>Page</u> |
|---------------|-----------------------------------|-------------|
| C-34 | Vertical Displacement versus Time | 211 |
| C-35 | Vertical Velocity versus Time | 212 |
| C-36 | Vertical Displacement versus Time | 212 |

TABLES

| <u>Table</u> | | <u>Page</u> |
|--------------|--------------------------------------------------------------|-------------|
| I-1 | Summary of One-Dimensional Wave Propagation Quantities | 10 |
| II-1 | Notch Spacing | 33 |
| VII-1 | Instrumentation List | 71 |
| VIII-1 | Shock Front Time of Arrival at Pressure Transducer Locations | 74 |
| VIII-2 | Shock Front Time of Arrival at Break Wire Locations | 75 |
| VIII-3 | Microbarograph Results | 75 |
| IX-1 | Reflection Results | 78 |
| XI-1 | Seismic Profile | 94 |
| XI-2 | Physical Properties for Displacement Calculations | 97 |
| XII-1 | Instrumentation Coding System | 110 |
| XII-2 | Instrumentation Listing | 111 |
| XIII-1 | Permanent Vertical Displacement with Depth (Slope Indicator) | 122 |
| XIV-1 | Rise Times | 142 |

This page intentionally left blank.

PART 1

SIMULATION TECHNIQUE

This page intentionally left blank.

SECTION I

INTRODUCTION

The Phase II, Long-Duration High-Explosive Simulation Technique (LDHSEST) shot, was fired at 1315 hours, MST, on 15 December 1964, at Kirtland Air Force Base, New Mexico.

1. Objectives

The primary objective of this test was to simulate the air-blast-induced ground motions from a large-yield nuclear surface explosion. The specific requirement was to simulate the environment at the 300-psi overpressure range from a large-yield nuclear explosion. Secondary objectives were to observe the response of a scaled structural model and to proof test a hardened cable complex in the simulated environment.

2. Background

A great deal of interest has been recently generated in the development of various techniques to simulate nuclear weapon effects. Much of the impetus for this increased interest resulted from the moratorium on atmospheric testing which was imposed by the Nuclear Test Ban Treaty. Air Force requirements exist to conduct nuclear tests on actual hardened systems as well as to conduct basic research on nuclear weapon effects. Since atmospheric testing is no longer possible, these requirements must now be met through simulation programs. To meet a portion of these requirements, the Air Force Weapons Laboratory began a two-phase program in February 1964 to develop a technique to simulate the air-blast-induced ground motions from a large-yield nuclear explosion. Phase I (reference 1) of this program consisted of a thorough study of various simulation techniques and the actual field testing of the two most promising explosive techniques. The techniques tested were (1) a detonable gaseous mixture and (2) a matrix of primacord to produce the desired explosion in a confined volume. An overburden, or mass of material, was placed over the explosive to provide a reaction force which would shape the resulting wave pulse to provide the required long durations.

The application of an overburden to increase explosion durations was first attempted by the Stanford Research Institute (reference 2). They fired a number of simulation shots on a small scale, 5-1/2 feet x 11-1/2 feet in plan, utilizing a detonable gaseous mixture. These preliminary results indicated that the overburden concept for increasing durations was a practical scheme if the experiment was conducted on a large enough scale. However, the gaseous mixtures which they utilized did not simulate the traveling wave characteristics of a shock wave in air, i.e., the correct pressure/frontal velocity relationships.

The primacord matrix concept, also utilizing the overburden to increase durations, was developed under contract (reference 3) for the Air Force Weapons Laboratory. Two shots were conducted on an area 15 feet x 30 feet in plan. These efforts were not successful in producing the desired environment of a 300-psi overpressure wave from a large-yield nuclear weapon.

Seven shots were fired under the Phase I study on an area 20 feet x 40 feet in plan. These tests further developed the two explosive techniques and refined the overburden concept for increasing durations. Either technique appeared to be capable of simulating the desired environment. However, the primacord matrix, officially designated the Long-Duration High-Explosive Simulation Technique (LDHEST), was selected as the more promising for application on larger scales. It was easier to field, safer, and more economical than the detonable gas technique.

The Phase II test was a direct follow-on of the Phase I effort. This test was conducted to demonstrate the feasibility of simulating air-blast-induced ground motions from a large-yield nuclear weapon utilizing the LDHEST. The test was conducted on a plan area 96 feet x 150 feet, which was much larger than any experiment previously conducted. Conventional construction techniques and practices were utilized to demonstrate the feasibility of conducting even larger experiments.

3. Nuclear Blast Environment

This experiment was planned to simulate the nuclear blast environment at the 300-psi peak overpressure level from a 1-MT surface explosion. This

peak overpressure will occur at a ground range of 2,250 feet from the detonation point and will have an associated shock front velocity of 4,600 feet per second (reference 4). The overpressure decays rapidly from the peak value at the shock front and reaches a value of 150 psi in 37 msec. However, the total positive phase duration will be approximately 1 second.

Figure I-1 illustrates the pressure-time history of a 300-psi peak overpressure shock wave from a 1-MT surface burst. The impulse contained in this pulse can be computed by taking the time integral of the pressure over the entire positive phase duration. In this instance, it is 32 psi-sec.

When the history of the shock wave is studied (figure I-2) it can be seen that the peak overpressure and the shock front velocity both decay monotonically with ground range. This is caused by the expansion taking place as the air blast loads increasingly larger disks of material.

The curvature of the shock front also decreases with ground range. At a distance of 2,000 feet from the detonation point, the curvature of the shock front is considered to be insignificant. Therefore, this simulation technique utilizes a plane wave front to simulate the actual case.

The air-blast parameters that were considered in the development of the environment to be simulated are

- (1) Peak overpressure
- (2) Shock front velocity
- (3) Overpressure duration, pulse shape and impulse
- (4) Peak overpressure and shock front velocity decay

The effects of these parameters on the air-blast-induced ground motions are discussed in the next section.

4. Theory

a. Air-Blast-Induced Ground Motions

When large surface areas are loaded nearly uniformly, such as occurs at moderate ranges from a large-yield nuclear detonation, one-dimensional wave theory can be used as an approximation. In one-dimensional wave theory, only vertical motions occur and simple relationships can be established among stress, displacement, strain, velocity, and acceleration.

Although this situation is highly idealized, the theory provides an understanding of the basic relationships between the air-blast parameters and the stresses and motions induced in the soil. These results can then be corrected to take account of the other factors which influence the free-field behavior.

Figure I-3 shows a uniform elastic medium, extending to an infinite depth, which is loaded uniformly at its free surface by a time dependent pressure, $P(t)$. A unit cylinder of soil, extending from the surface to an infinite depth, can be examined and will be representative of all the surrounding material. The strains in all directions except depth, z , are equal to zero.

For equilibrium the summation of forces in the z direction must be equal to zero, and

$$(\rho dz) \left(\frac{\partial^2 u}{\partial t^2} \right) - \frac{\partial \sigma_z}{\partial z} dz = 0$$

which simplifies to

$$\rho \frac{\partial^2 u}{\partial t^2} = \frac{\partial \sigma_z}{\partial z}$$

where

- ρ = mass density of the medium
- z = undisturbed location of a given particle
- u = displacement of a given particle in the z direction, a function of z and t
- t = time variable
- σ_z = normal stress in z direction, tension considered positive

Define strain as

$$\epsilon_z = \frac{\partial u}{\partial z}$$

and stress as

$$\sigma_z = M \epsilon_z$$

where

$$M = \frac{E(1-\nu)}{(1+\nu)(1-2\nu)}$$

= constrained modulus

E = Young's modulus

ν = Poisson's ratio

Then making appropriate substitutions into the wave equation,

$$\rho \frac{\partial^2 u}{\partial t^2} = M \frac{\partial}{\partial z} \left(\frac{\partial u}{\partial z} \right) = M \frac{\partial^2 u}{\partial z^2}$$

Define

$$c^2 = M/\rho$$

Then the wave equation reduces to

$$\frac{\partial^2 u}{\partial t^2} = c^2 \frac{\partial^2 u}{\partial z^2}$$

The solution to this equation is of the form

$$u = f(t - z/c) + g(t + z/c)$$

where

$f(t - z/c)$ describes a forward moving wave
 $g(t + z/c)$ describes a backward moving wave

Since the medium is considered to have an infinite depth, only the forward moving wave solution is required.

The wave shape is unaltered as it propagates through the medium. Figure I-4 shows a pressure pulse propagating through the medium with the time variable, $(t - z/c)$. z/c is the time it takes the wave to propagate from the surface to the depth being studied.

Stress has been previously defined as

$$\sigma_z = M \epsilon_z$$

With appropriate substitutions

$$\sigma_z = C^2 \rho c_z = C^2 \rho \frac{\partial u}{\partial z} = -\rho C f'(t - z/C)$$

where

$$u = f(t - z/C)$$

$$\frac{\partial u}{\partial z} = -\frac{1}{C} f'(t - z/C)$$

$$f' = \frac{d[f(t - z/C)]}{d(t - z/C)}$$

strain has been previously defined as

$$c_z = \frac{\partial u}{\partial z}$$

which from above is

$$c_z = -\frac{1}{C} f'(t - z/C)$$

Particle velocity is defined as

$$\dot{u} = \frac{\partial u}{\partial t} = f'(t - z/C)$$

At the surface ($z = 0$) the stress is equal to

$$\sigma_z = -P(t)$$

Then from above

$$\sigma_z = -P(t) = -\rho C f'(t - z/C)$$

and

$$f'(t - z/C) = \frac{P(t)}{\rho C}$$

At a depth, z

$$f'(t - z/C) = \frac{P(t - z/C)}{\rho C}$$

Making the appropriate substitutions

$$\sigma_z = -P(t - z/C)$$

$$\epsilon_z = -P(t - z/C)/\rho C^2$$

$$\dot{u} = P(t - z/C)/\rho C$$

Acceleration is defined as the partial derivative of the particle velocity with respect to time

$$\ddot{u} = \frac{\partial \dot{u}}{\partial t} = \frac{1}{\rho C} \frac{\partial}{\partial t} [P(t - z/C)]$$

Thus, the peak acceleration is dependent on the shape of the overpressure-time curve.

The absolute displacement of a point, z , at a specific time, τ , can be obtained by an integration of the particle velocity at the point, z

$$u(z, t) = \frac{1}{\rho C} \int_0^\tau P(t - z/C) dt$$

and

$$u(z, t) = \frac{1}{\rho C} I$$

where

$$I = \int_0^\tau P(t - z/C) dt$$

This integral is equal to the area under the overpressure-time curve $P(t - z/C)$ between the times 0 to τ . See figure I-4. This integration can be conveniently performed graphically on the overpressure-time curve.

Table I-1 summarizes the one-dimensional wave propagation quantities.

Table I-1

SUMMARY OF ONE-DIMENSIONAL WAVE PROPAGATION QUANTITIES

| Quantity | Equation |
|--------------|------------------------------------------------------------------------|
| Stress | $\sigma_z = -P(t - z/C)$ |
| Strain | $\epsilon_z = -P(t - z/C)/\rho C^2$ |
| Velocity | $\dot{u} = P(t - z/C)/\rho C$ |
| Acceleration | $\ddot{u} = \frac{1}{\rho C} \frac{\partial}{\partial t} [P(t - z/C)]$ |
| Displacement | $u = I/\rho C$ |

The one-dimensional wave theory has shown that the stress in the soil propagates with a wave shape unaltered from the air-blast input. In reality, three major changes will take place as the stress wave propagates with depth. The rise time will increase, the impulse duration will be spread out, and the peak stress will decrease. Nonlinearities in the stress-strain curves of earthen materials are the primary cause of the first two factors. The variation of stress intensity with depth is caused by three separate phenomena. First, most earthen materials have highly nonelastic stress-strain curves which result in energy absorption. Secondly, when finite areas are loaded by transient inputs, rarefaction waves propagate inward from the boundaries (see figure I-5). Thirdly, spatial attenuation, or the spreading out of the load, and reinforcing of the load by areas that have been loaded by higher pressures play conflicting roles. As previously described, the peak overpressure and shock velocity of the air-blast input are both decaying with ground range (see figure I-2). If this air-blast is used as the loading input for an elastic half space, ray theory can be used to examine the problem (see figure I-6). Each peak overpressure level has a ray path along which

it propagates, and spatial divergence causes it to attenuate as it propagates. If a vertical section is examined, it can be shown that energy from higher overpressure regions will be feeding into and locally reinforcing the stress level at any ground range of interest. For megaton yields, the air-blast parameters are changing at the appropriate rate to balance the effect of the spatial divergence and no attenuation due to this phenomenon should occur.

When the test area is small (<500 feet), in comparison with the area loaded by a 1-MT weapon, the air-blast parameters are nearly uniform (see figure I-2). In addition, when depths of a few hundred feet or less are of interest, the raying effect is minimal. Because of these factors, the decay of peak overpressure and shock front velocity have not been further considered as an important parameter to the simulation technique.

The one-dimensional wave theory has also shown that the strain and particle velocity are affected by the magnitude and wave shape of the air-blast input and the properties of the medium. These free field quantities are also affected by the same parameters which cause the attenuation of stress with depth. Acceleration has been previously shown to be extremely sensitive to the shape of the air-blast input, particularly the rise time, which increases with depth. Displacement has been shown to be dependent on the integral of the stress-time history at the depth of interest. To achieve significant displacements, the impulse must grossly match that of the nuclear explosion and the area loaded must be significantly large, in relationship to the depth of interest, to minimize the effect of rarefaction waves.

Only vertical components have been discussed thus far. A traveling wave must be considered to study the relationship between vertical and horizontal stresses and motions. Figure I-7 illustrates a typical air-blast input, $P(t)$, traveling over the surface of the earth with a shock velocity, U . The velocity of propagation of the stress wave into the earth, C , is determined by the intensity of the air-blast input and the properties of the earth material. It is given by

$$C = \sqrt{M/\rho}$$

where

M = constrained modulus at the stress level of interest
 ρ = mass density

For the sake of simplicity only the air-blast input in the superseismic region will be discussed. This is a good assumption for facilities which are constructed in soil or soft rock to withstand overpressures of several hundred psi. In this region, the stress wave trails behind the air-blast shock front and enters the ground with an angle, α , which can be determined by

$$\sin \alpha = C/U$$

As indicated in figure I-7, the initial stresses and motions propagate in a direction perpendicular to the stress wave front. However, behind the wave front these directions change. At very late times the problem can be considered static and the motions and stresses must now be vertical. The direction of the motions and stresses thus change with time, having an initial direction perpendicular to the compression wave front and a final direction on a vertical line. As an approximation, the components of the motions and stresses can be computed by assuming that the entire stress wave propagates in a direction perpendicular to the compression wave front. For this assumption the horizontal components and vertical components are

Horizontal component = value perpendicular to front $\times \sin \alpha$

Vertical component = value perpendicular to front $\times \cos \alpha$

Thus, the value of the horizontal and vertical components of both the initial stresses and motions induced in the soil are a function of the material properties as well as the shock front velocity. To achieve appropriate horizontal and vertical components, the shock front velocity produced by the simulation technique must closely duplicate that of the nuclear environment at the overpressure level of interest.

The previous discussion of air-blast-induced ground motion has shown that the peak overpressure, shock front velocity, overpressure duration pulse shape, and impulse are significant parameters in defining the environment to be simulated. The Phase II test attempted to generate a peak overpressure of 300 psi and a shock front velocity of 4,800 ft/sec. The duration

to one-half peak pressure was used as a criterion for defining the correctness of the overpressure decay behind the shock front. In addition, the gross matching of the impulse was attempted.

b. Primacord Matrix

Figure I-8 illustrates the general concept of the primacord matrix. A continuous strand of primacord has been laced into a matrix which approximates the uniform properties of a solid sheet explosive. This approximation is required since sheet explosives with the appropriate detonation properties are not currently commercially available. Primacord, on the other hand, has the appropriate detonation properties when it is placed in a specially designed matrix. In addition, it is commercially available, fairly economical, and safe to work with.

There are two parameters which may be adjusted to control the characteristics of the shock wave produced by this technique. These parameters are the load density and the primacord wrap angle. To understand the effect of these two parameters, the process that produces the shock wave must be considered. The wrap angle determines the rate at which the combustion products are formed along the length of the facility. These combustion products act like a piston which loads a cylinder of air in front of the detonation. This process forms a shock wave in the air which moves out ahead of the piston, and the particle velocity of the air behind the shock wave is equal to the velocity of the piston. The problem is further complicated by the intense, short-duration shocks that are produced by the detonation of the individual strands of primacord and the reflection of these shocks with one another and the boundaries of the cavity. These secondary shocks move forward at a faster velocity and overtake the main shock. The net effect is a reinforcement of the main shock with a corresponding increase in pressure and shock velocity. The interaction of shocks creates a natural pressure decay immediately behind the shock front. If the cavity were perfectly insulated and had rigid boundaries, the gases inside would eventually come to some equilibrium pressure. However, the overburden begins to move upward at early times, which increases the cavity volume and causes a corresponding decrease in pressure.

(1) Peak Shock Pressure

The theoretical prediction of the peak shock pressure proved to be intractable. Therefore, an experimental approach was used in Phase I (reference 1) to determine the peak pressure. This approach was guided by a theoretical thermochemical analysis where isentropic, equilibrium pressures were computed for a fixed volume (reference 3). These calculations considered the combustion of the primacord and its case and the disassociation of the combustion products. Figure I-9 presents a logarithmic least-square fit of the four experimental data points which were available from previous experiments. The peak shock overpressure has been plotted as a function of load density. Load density is defined as the total weight of explosive, in pounds, divided by the initial confined volume of air, in cubic feet. According to figure I-9, a load density of 0.076 lbs/ft³ is required to produce a peak shock overpressure of 300 psi.

(2) Shock Front Velocity

Figure I-8 also illustrates a plane shock front propagating in the desired direction of travel. The primacord has a detonation velocity far in excess of the 4,800 ft/sec shock front which is to be simulated. Therefore, the primacord matrix must be designed to have a wrap angle which produces a shock front having the appropriate velocity. Simple trigonometric theory suggests that the wrap angle, θ , should be defined by the following formula:

$$\sin \theta = \frac{\text{shock front velocity}}{\text{detonation front velocity}}$$

Experimental data from Phase I indicate that this simple theory does not explain the observed results. The problem is complicated by all of the factors discussed in section I.4.b. Therefore, the results of the experimental program must be utilized to predict the required wrap angle for a desired shock front velocity.

Figure I-10 presents a curve of shock front velocity versus wrap angle. This curve was obtained from a least squared fit of the four data points which were available. There was a great deal of scatter in the experimental results and the curve is only accurate to ± 500 ft/sec. According to figure I-10, a wrap angle of 9.2 degrees will produce a shock front velocity of 4,800 ft/sec.

c. Overburden Calculations

A pressure pulse of extremely short duration would be produced if the primacord matrix were exploded in the open air. However, the total duration can be significantly increased and the major portion of the decay behind the front controlled if an overburden is utilized. The overburden will move upward after the detonation takes place and the explosion products will expand into the increasing volume. The initial volume of the explosion cavity, the peak overpressure, the overburden mass, and the expansion process all control the movement of the overburden. A number of simplifying assumptions must be made before the movement of the overburden can be calculated.

Figure I-11 illustrates the model which was used for the overburden calculations. A time-varying pressure is confined in a cavity of infinite lateral extent which has an initial height of x_0 . The lower boundary of the cavity is assumed to be a rigid surface. The upper boundary of the cavity, which is formed by the overburden, is assumed to move only in the vertical direction with rigid body motion. The overburden is defined by a mass per unit area, m . Only one coordinate is required to define the rigid body motion of the overburden. Thus:

$$x(t) = \text{displacement}$$

$$\frac{d^2 x}{dt^2} = \text{acceleration}$$

The expansion of the gases in the cavity can be described by

$$P(t) = (P_0 + a) \left(\frac{x + x_0}{x_0} \right)^{-\gamma}$$

where

$$P_0 = \text{peak shock overpressure}$$

$$a = \text{atmospheric pressure}$$

$$x = \text{displacement}$$

$$x_0 = \text{initial cavity height}$$

$$\gamma = \text{ratio of specific heats} = 1.3$$

Using Newton's second law,

$$F = m \frac{d^2 x}{dt^2}$$

the following equation can be derived:

$$\frac{d^2 x}{dt^2} - \left(\frac{P_0 + w}{m} \right) \left(\frac{x + x_0}{x_0} \right)^{-\gamma} + \frac{w}{m} + g = 0$$

This nonlinear differential equation was solved by numerical integration.

Figure I-12 presents the results of the overburden calculations for an initial overpressure of 300 psi. The time to one-half peak pressure has been plotted as a function of the two variables: overburden weight and initial cavity height. It can be seen that increasing either the initial cavity height or the overburden weight will increase the time to one-half pressure.

Results from Phase I indicate that the duration to one-half pressure is approximately 44 percent of the theoretical value. However, the effect of experiment size on this factor was not known, since all of the previous tests had been conducted in approximately the same size facility. It was postulated that edge effects played an important role in the Phase I experiments, and on the basis of judgment, a correction factor of 90 percent was selected rather than the experimental value of 44 percent. Figure I-12 was then used to select an initial cavity height of 36 inches and an overburden weight of 500 lbs/ft² to give an expected time to one-half pressure of 37 msec.

Figure I-13 presents the theoretical overpressure-time history calculated for the selected parameters. The results for a 1-MT nuclear weapon have also been plotted on the same figure for comparison. It can be seen that the primacord curve matches the nuclear curve only in the neighborhood of the one-half peak pressure. However, it must be realized that the theoretical primacord curve accounts only for the pressure decay caused by overburden motion, and the interaction of shocks at the front will cause a decay immediately behind the shock, which is not considered in these calculations. When this is taken into account, the general characteristics of the two curves should be quite similar down to one-half peak pressure. The

primatord curve has a total duration of 160 msec and a total impulse of 15 psi-sec. The nuclear curve has a total impulse of 32 psi-sec; however, in the first 160 msec, it has an impulse of approximately 18 psi-sec.

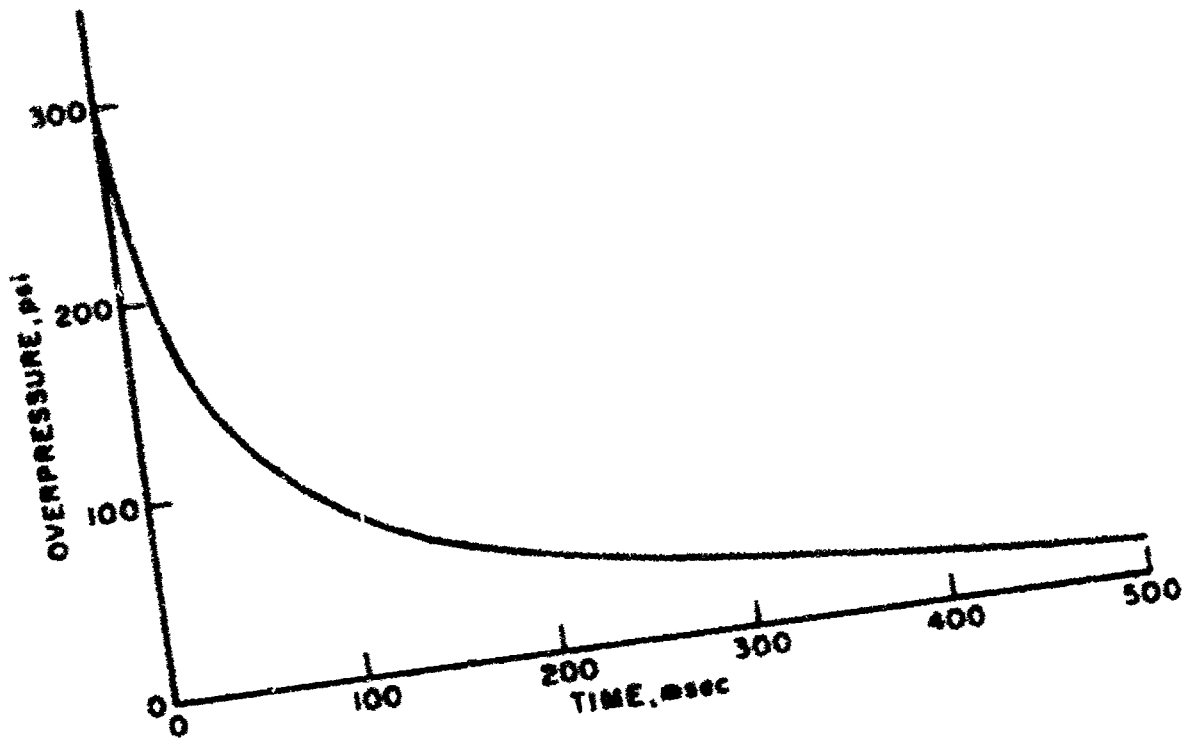


Figure I-1. Pressure-Time History for 300 psi Wave from 1 MT Surface Burst

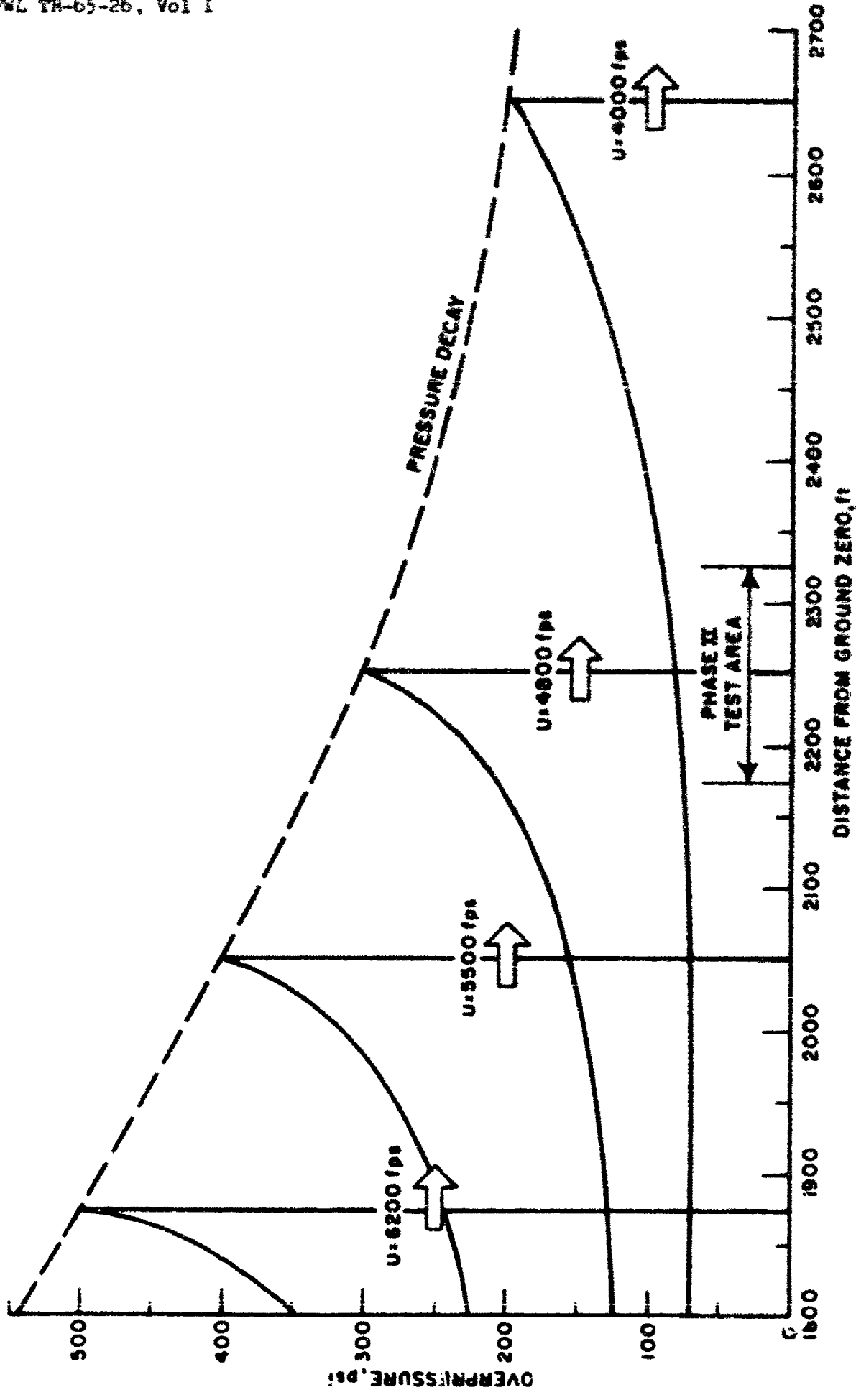


Figure I-2. Air-Blast-Loading from a 1 MT Surface Burst

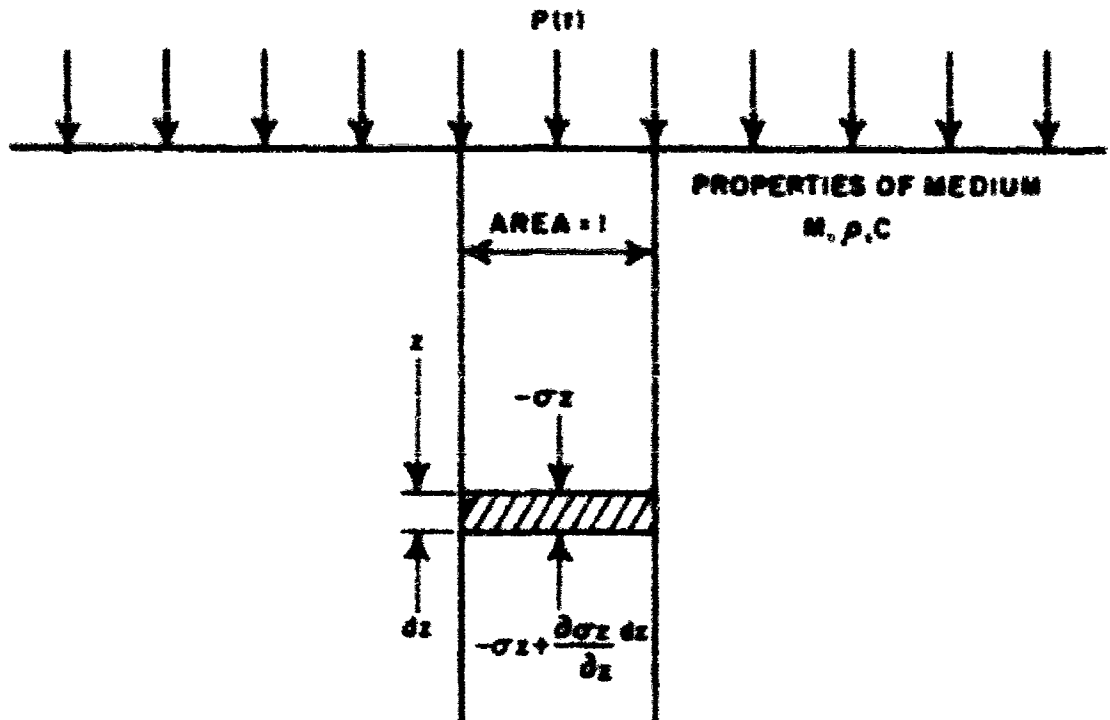


Figure I-3. Stresses on an Element Under One-Dimensional Wave Conditions

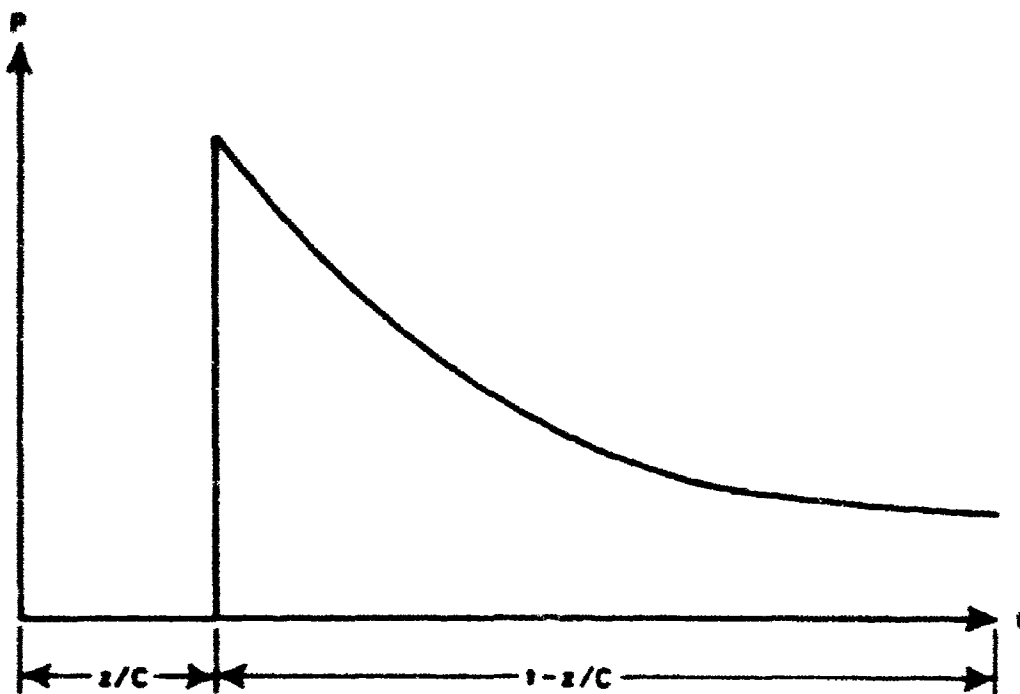


Figure I-4. Pressure-Time History at Depth, z

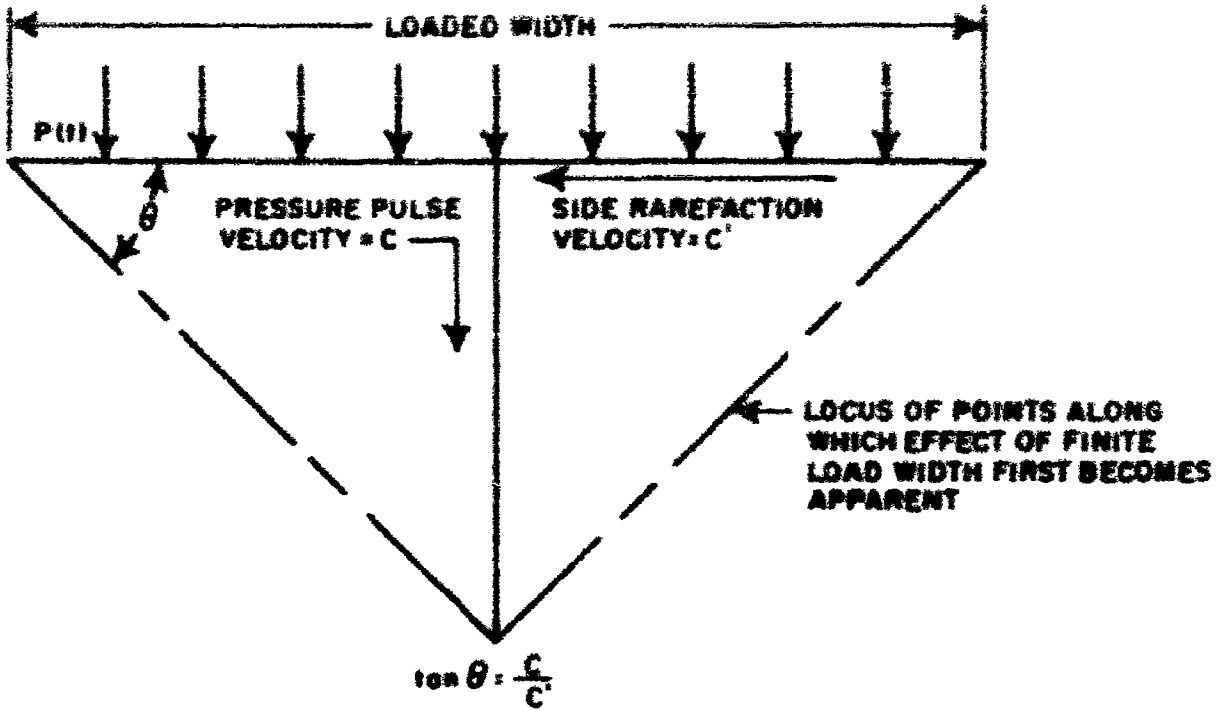


Figure I-5. Rarefaction Waves

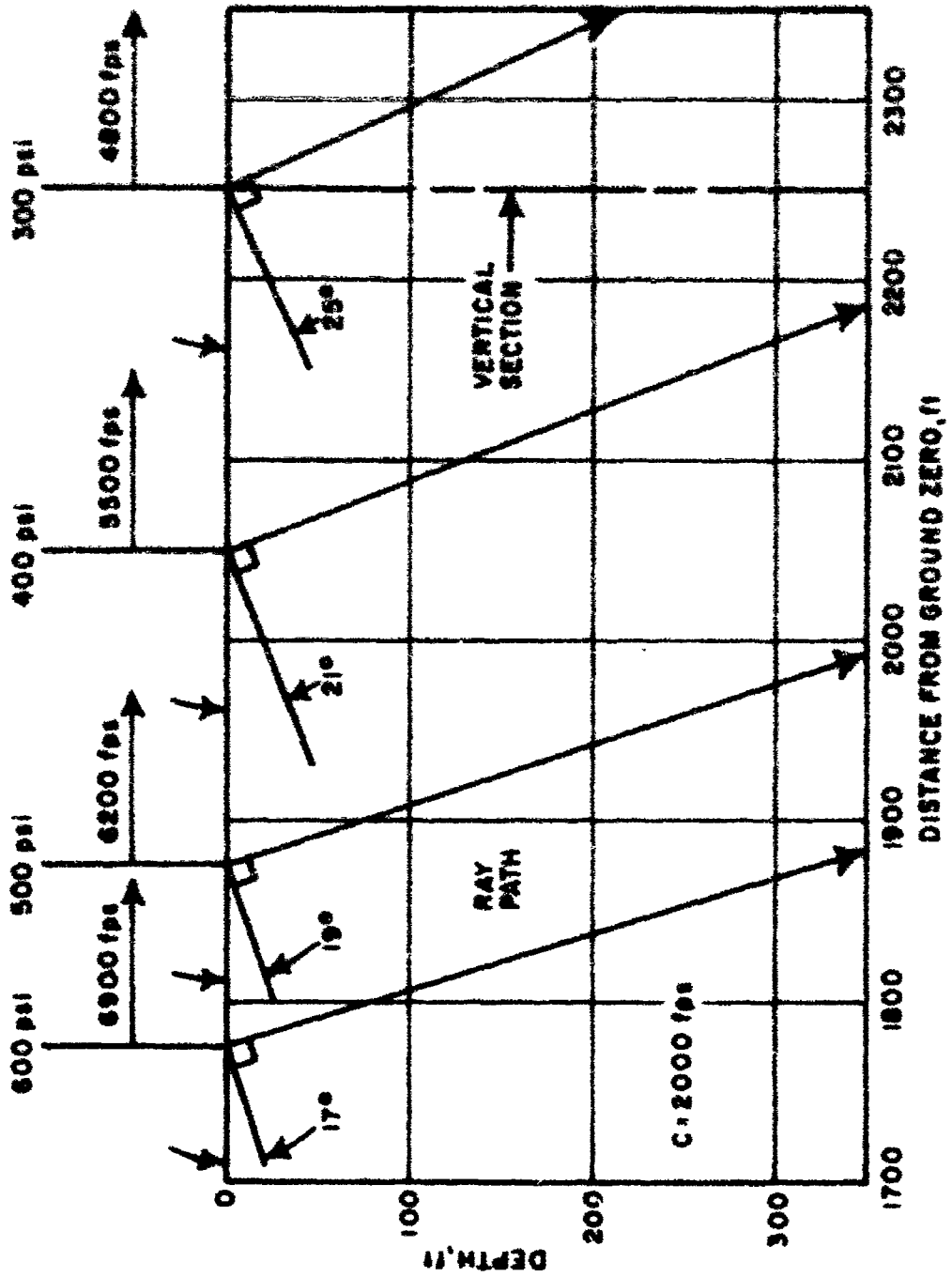


Figure I-6. Stress Waves in an Elastic Half Space

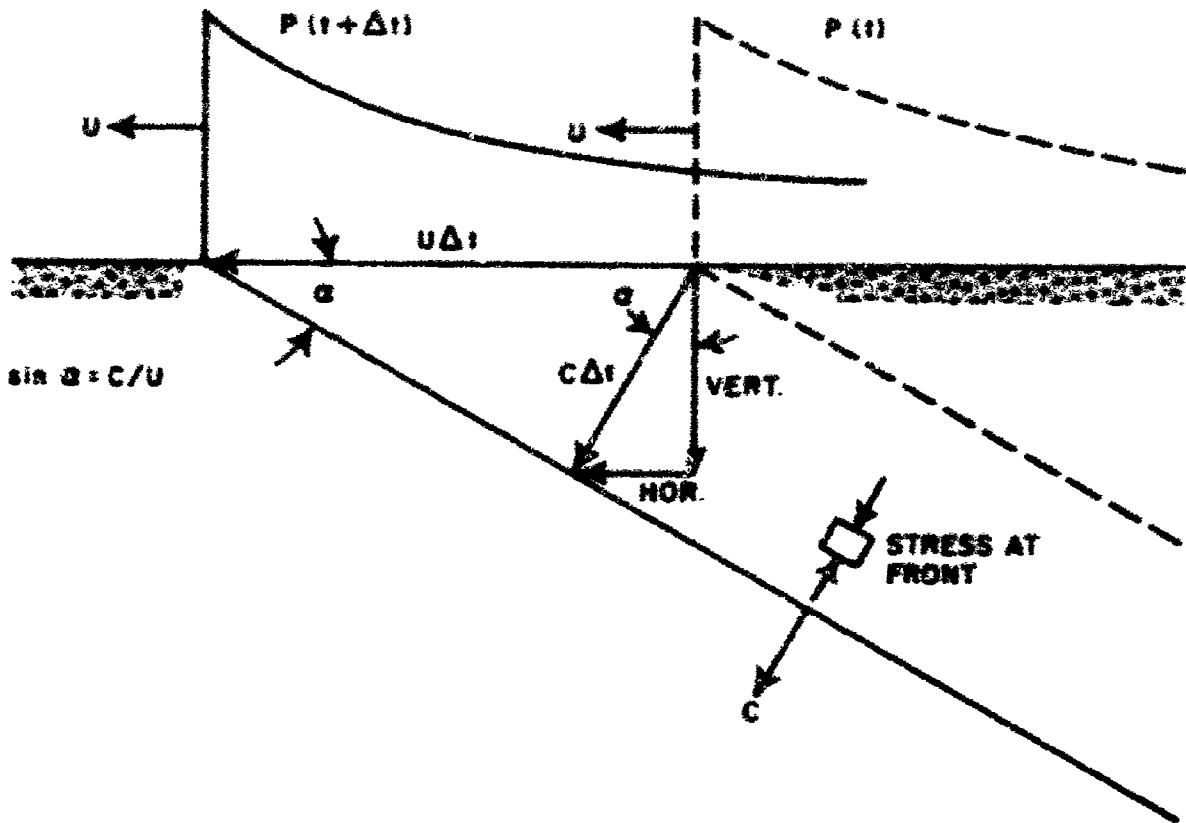


Figure I-7. Air-Blast-Induced Ground Motions in Superseismic Region

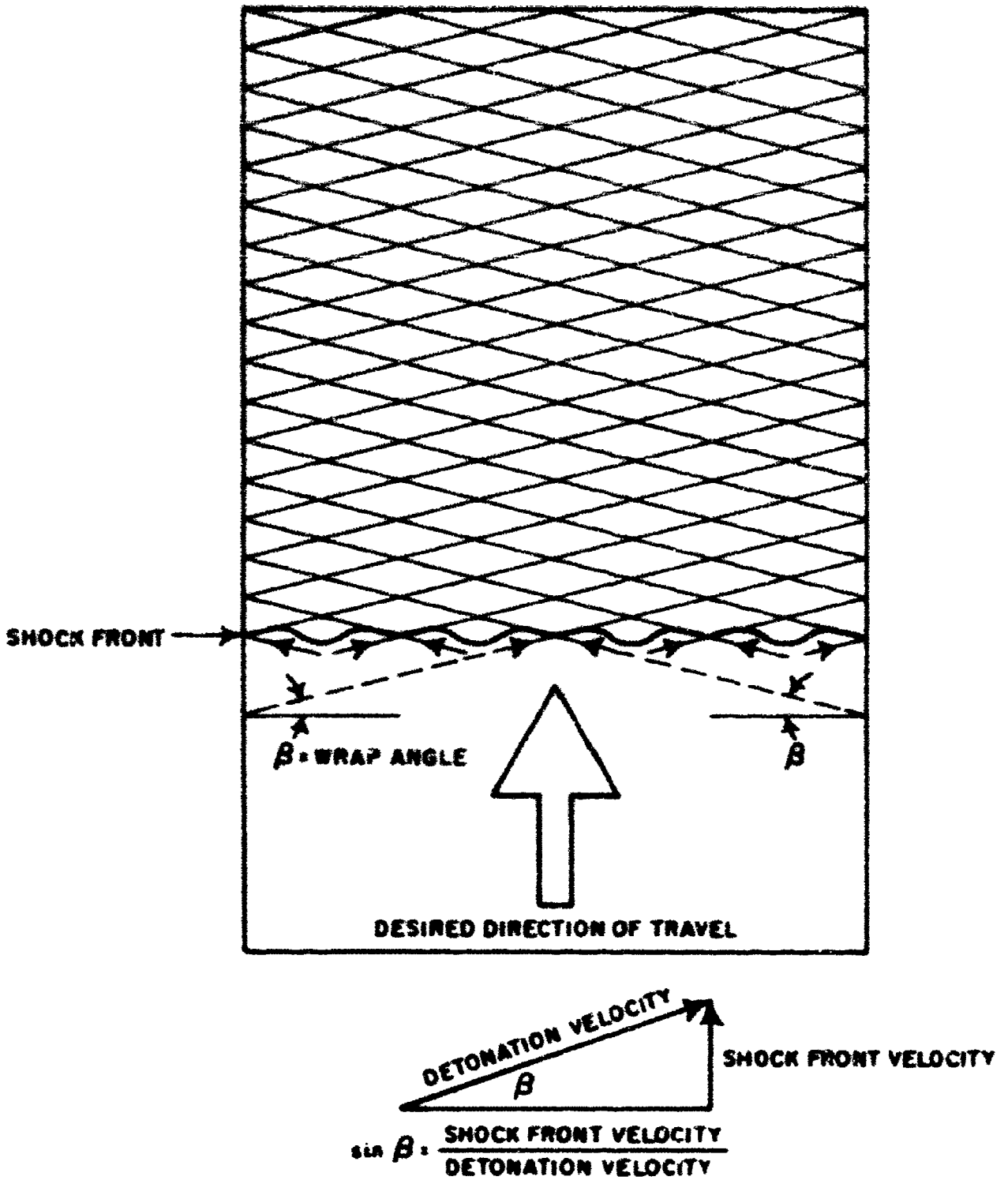


Figure I-8. Primacord Matrix

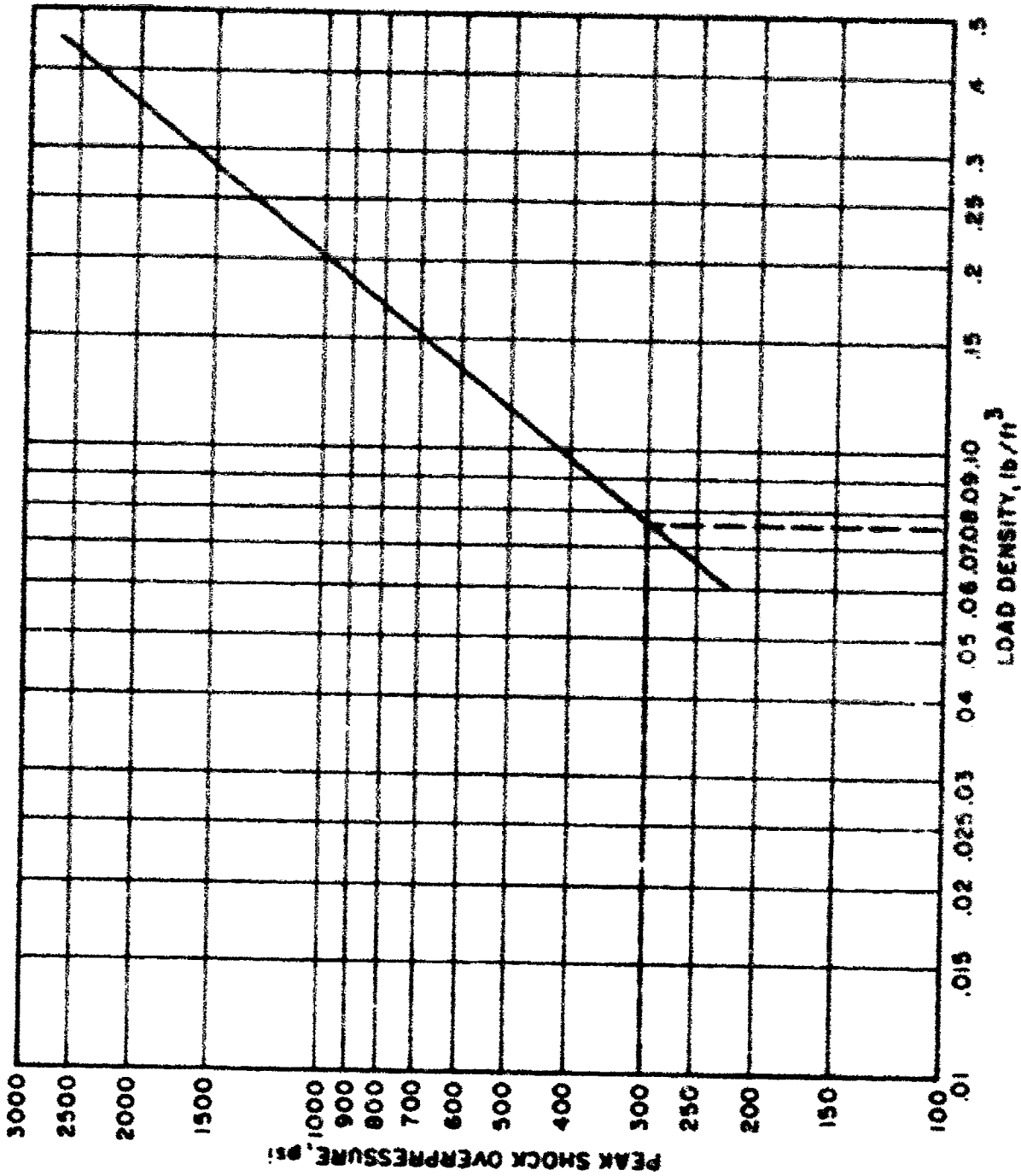


Figure I-9. Peak Shock Overpressure versus Load Density

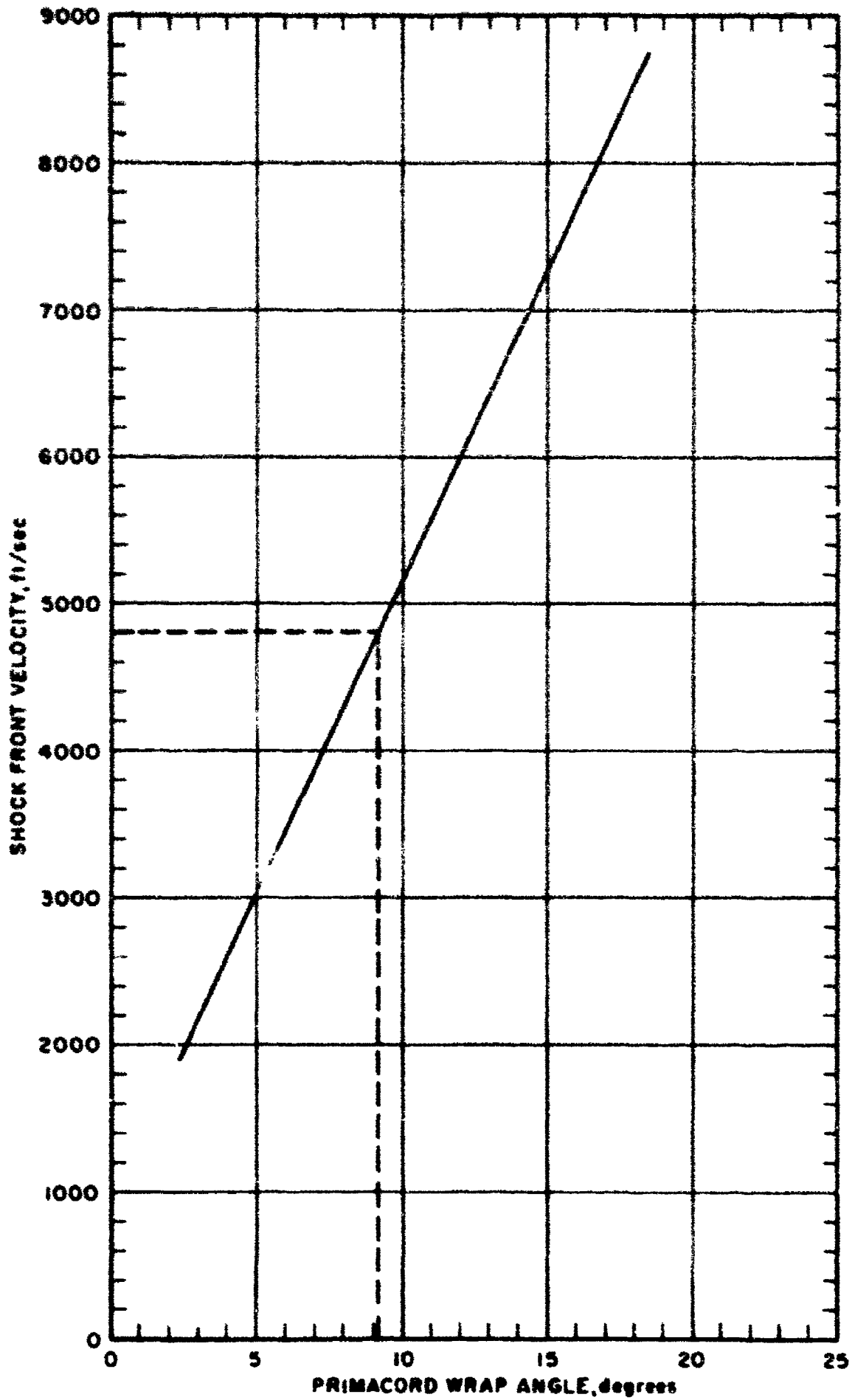


Figure I-10. Shock Front Velocity versus Wrap Angle

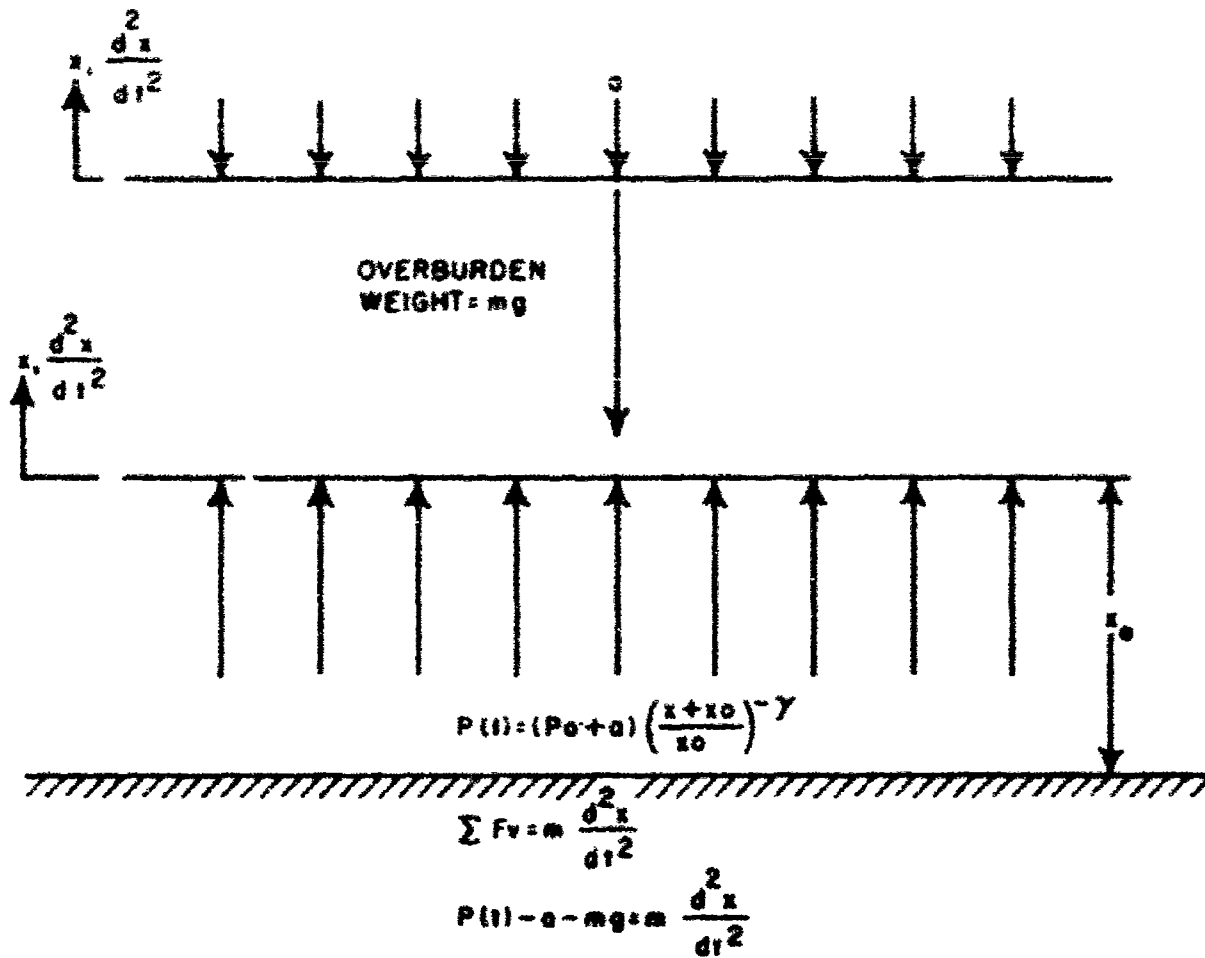


Figure I-11. Model for Overburden Calculations

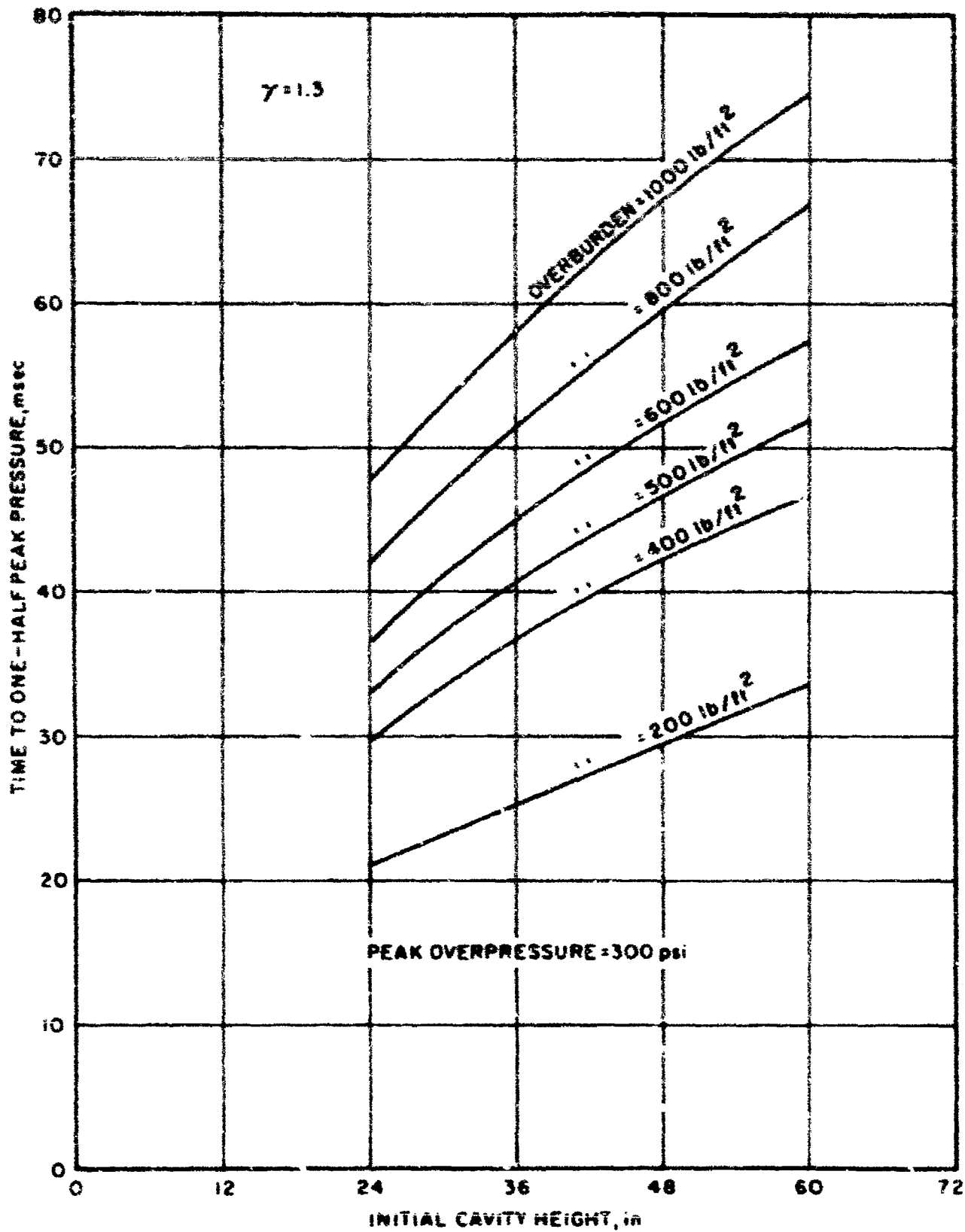


Figure I-12. Results of Overburden Calculations

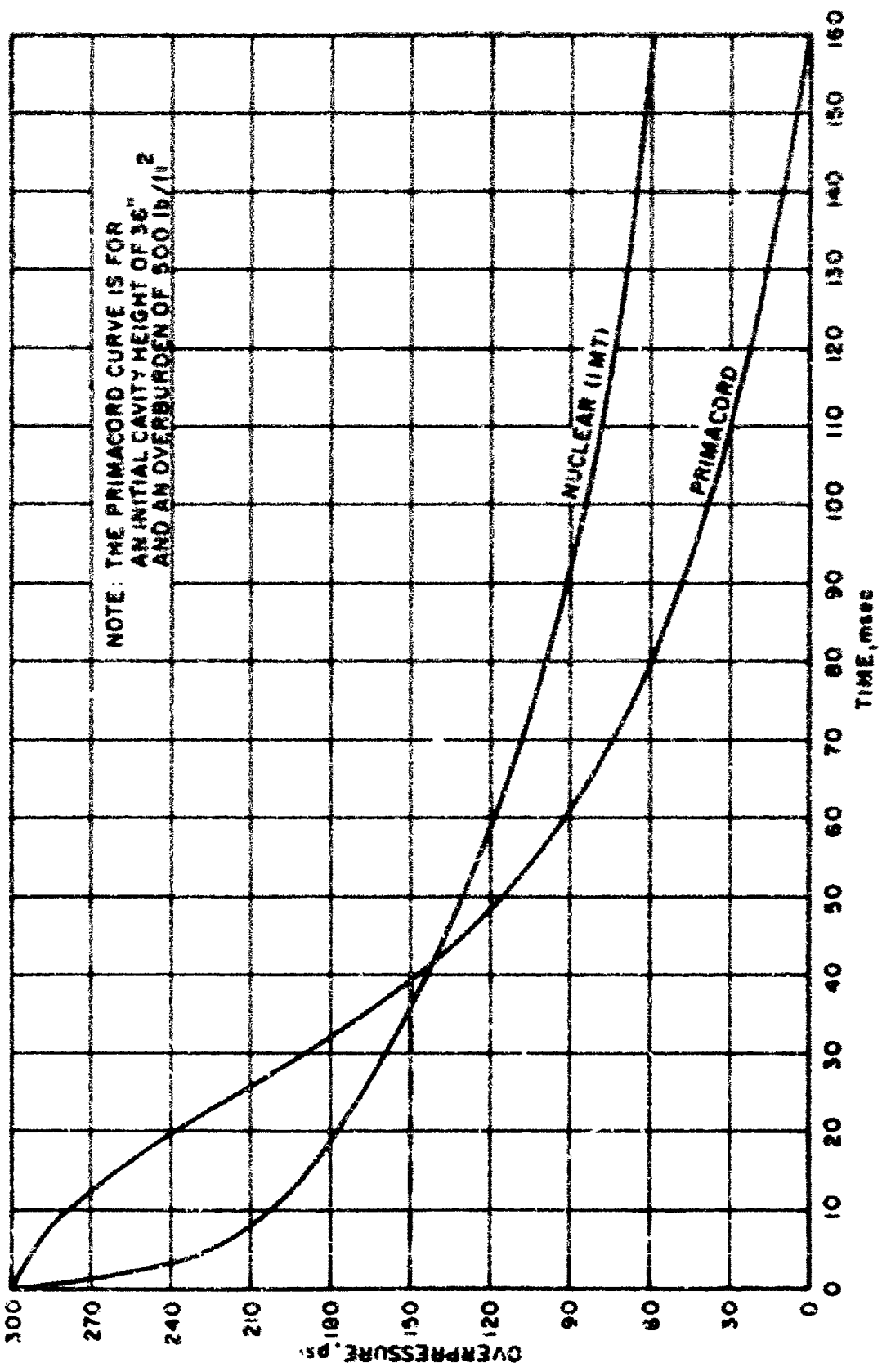


Figure I-13. Comparison of Pressure-Time Histories for Primacord and Nuclear

SECTION II

PROCEDURE

1. Operations

a. Detonation Facility Construction

The detonation facility consists of steel sheet piling and earth retaining walls, a wood and steel support structure, and sand overburden. Figure II-1 is a general plan view. Figures II-2, II-3, and II-4 are three typical sections which illustrate the major components of the facility.

The construction of the detonation facility was accomplished in the following major steps:

- (1) The test area was excavated to the required dimensions.
- (2) Steel sheet piling was driven around the perimeter of the facility, except for a small access roadway.
- (3) Steel H piles were driven, and WF beams, to span the model section, were positioned and welded in place.
- (4) The rows of prefabricated footings, columns, and girders were set into place and nailed together.
- (5) The remaining steel sheet piling was driven to close the roadway.
- (6) The primacord racks were installed, tied together, and connected to the plane wave detonation generator.
- (7) The partially prefabricated wood panels were positioned on top of the girders, nailed in place, and filled with sand; and the top plywood members were stapled to the floor joists.
- (8) Sand fill was placed between the steel sheet piling and the wooden support structure.
- (9) Finally, the sand overburden was placed simultaneously with the earth backfill which surrounds the facility.

The facility was constructed in a rectangular excavation approximately 120 feet by 170 feet in plan and 10 feet deep. As originally conceived, the

facility would have been constructed on a level area with the earth retaining wall in a bermed configuration. However, a 10-foot cut was required for this test in order to place the floor of the facility at an elevation below rock layers which were present at the site.

The steel sheet piling was driven around the perimeter of the test area with a 6-inch space between the support structure and the inside face of the sheet piling. This 6-inch space was later filled with sand to provide additional lateral stability to the facility. The steel sheet piling was driven to a depth of 5 feet and was cut off at a height of 10 1/2 feet. This was to provide a vertical working face and to support the unbalanced horizontal force which results from the different heights between the overburden and the backfill.

The earth retaining wall is required to prevent side venting after the detonation takes place. Side venting would release energy from the experiment, distort the one-dimensional motion of the overburden, and present additional safety hazards. The earth retaining wall was constructed by backfilling between the sheet piling and the side of the open cut. The backfill material was placed uncompacted. It consisted of a predominately silty material which was present at the site. The backfill operation was accomplished simultaneously with the placement of the sand overburden to avoid excessive bending of the sheet piling.

The support structure serves three purposes simultaneously: it provides the initial cavity in which the explosion takes place, it positions the primacord in a horizontal plane above the ground surface, and it supports the overburden. The initial cavity height, from the surface of the ground to the bottom of the floor panels, is 3 feet. After the detonation takes place, the explosion products fill this initial cavity and create the required peak overpressure.

Figures II-2 and II-3 are typical sections which illustrate the construction of the wood portion of the support structure. The bays of footings, columns, and girders were placed in rows which span the length of the facility. The exterior bays were located on 4-foot centers while the interior bays were located on 8-foot centers. The columns were placed on 5-foot centers along the length of each row.

The two rows, which make up the central bay, were broken across a 20-foot span at the model location, and steel construction was used in place of the wood. Steel H piles were driven to depths of approximately 35 feet at the four corners, and steel WF beams were used to span the distance between the piles in each row. Figure II-4 illustrates this portion of the construction. The overburden weight is transferred to the H piles which distribute the load along their length instead of to the surface of the ground. This avoids the preloading of the upper portion of the structural model, including the door.

The wood panels, which span the rows of girders, were partially prefabricated prior to placement; i.e., the bottom plywood sheets were stapled to the wood joists. After the panels were nailed into position in the facility, the space between the joists was filled with a dense commercial concrete sand at a density of approximately 105 lb/ft^3 . The dense sand controls the initial movement of the overburden by preventing compaction of the lower surface. This is to ensure that rigid body motions, which have been assumed for the overburden calculations, actually take place. After the sand was leveled, the top plywood sheets were stapled in place.

The sand for the remainder of the overburden was obtained from a local borrow pit. It was selected on the basis of obtaining an uncompacted density of approximately 100 lb/ft^3 or greater. The high-density requirements are again to ensure that rigid body motions take place and to produce the minimum height for a given weight of overburden. The sand overburden was placed from the exterior of the test area utilizing a long boomed crane. The final leveling was accomplished by a small tractor and hand labor. The total weight of overburden, including the panel sand, was $500 \pm 5 \text{ lb/ft}^2$.

Figures II-5 through II-7 show the construction sequence. Figure II-5 shows the detonation facility in an early stage of the construction. The sheet piling around the perimeter of the facility can be seen in the background. The workmen are trenching for the footings, and portions of the columns are already in place. Figure II-6 shows the upper portion of one of the H piles and the WF beam which spans the model section. Figure II-7 shows the completed rows of footings, columns and girders. The primacord racks are being installed before placement of the partially prefabricated

wood panels. These panels can be seen stacked in the background.

b. Primacord Installation

175-grain, plastic-coated primacord manufactured by the Ensign-Bickford Company was utilized for this test. Tests were conducted on 300-foot elements of this primacord and it was determined that the detonation velocity was 21,000 ft/sec \pm 1 percent.

(1) Primacord Rack Fabrication

The primacord matrix parameters were selected from the data presented in section I. A load density of 0.076 lb/ft³ and a wrap angle, θ , of 9.2 degrees were selected to respectively produce a peak equilibrium overpressure of 300 psi and a shock front velocity of 4,800 ft/sec.

The primacord matrices were fabricated on wooden racks. The racks were constructed of 2-inch by 4-inch lumber with 22-gage metal braces at all joints and corners (see figure II-8). Two rack sizes were required to match the girder spacings which were utilized in the construction of the detonation facility. The larger racks, type A, were 7 feet 2 inches by 24 feet 10 inches and the smaller racks, type B, were 2 feet 9 inches by 24 feet 10 inches.

Notches were cut around the entire perimeter of the racks to position the primacord. The notch spacing was determined on a trial and error basis in an attempt to simultaneously match the two parameters of load density and wrap angle. Table II-1 summarizes the notch spacings which were utilized. This notch spacing produced a wrap angle of 8.5 degrees.

Table II-1

NOTCH SPACING

| Rack type | Side spacing (inches) | End spacing (inches) |
|-----------|-----------------------|----------------------|
| A | 2.625 | 17.2 |
| B | 2.54 | 16.5 |

The wrapping of the primacord was accomplished with the primacord racks supported at their center line with a chain hoist. This provided a clearance for free passage of the primacord. The primacord was initially secured to a top corner of the rack with tape and stretched to the opposite side (bottom) of the rack and placed in the proper notch. The cord was then passed under the rack and again stretched to the opposite side (top) and placed in the proper notch. The cord was alternately passed under and thrown over the top of the rack to enable the wrappers to use a continuous strand of primacord. Each succeeding wrap cycle was a repeat of the previous operation until the center line of the rack was reached. At this point, the person throwing the cord over the rack proceeded to the opposite end of the rack where he continued his operations. This procedure continued until the entire rack had been wrapped with primacord. Figure II-9 is a sketch of this operation.

One hundred eighteen thousand feet of primacord were used in fabricating the racks and lacing them together after they were positioned in the facility. The total volume of the explosion cavity minus the volume of the wood in the cavity was 40,700 ft³. The actual loading density was

$$\rho = \frac{(118,000 \text{ ft}) \left(175 \frac{\text{grain}}{\text{ft}} \right)}{\left[7,000 \frac{\text{grain}}{\text{lb}} \right] \left(40,700 \text{ ft}^3 \right)} = 0.0725 \frac{\text{lb}}{\text{ft}^3}$$

(2) Primacord Rack Placement

The racks were wrapped with primacord in advance of their placement in the detonation facility. During the interim period, they were stored in an off-site explosive ordnance bunker. Transportation to the site and installation in the detonation facility were accomplished in consecutive steps. Some of the primacord racks were loaded on a flatbed trailer, transported to the site, and unloaded onto pallets. The pallets were lifted into the detonation facility by a crane and the racks were placed by workmen while the flatbed trailer returned for another load. Figure II-7 shows the placement of a rack. The tops of the columns provided a ledge which positioned the primacord racks in a horizontal plane 2 feet above the ground surface.

The primacord on the end of each rack was laced to its mate on the end of the adjacent rack with 175-grain primacord. In addition, transverse ties were made with short lengths of 175-grain primacord. These ties were made between the primacord on the sides of adjacent racks at 5-foot intervals. Figure II-10 shows the tying operation.

(3) Primacord Detonation

A 96-foot strand of 400-grain primacord was connected to each individual piece of primacord across the entire width of the matrix on the detonation end of the facility. Forty-eight strands of 175-grain primacord were connected to the 400-grain primacord on 2-foot centers. Each of the 48 strands was placed in a plastic casing which passed through the plywood bulkhead, sheet piling, and backfill material to the original ground surface (see figure II-11).

Figure II-12 illustrates the geometric pattern of equal-length 175-grain primacord strands which were utilized to fabricate the plane-wave generator. Duplicate blasting caps were used to initiate detonation. The detonation wave traveled down the plane wave generator and simultaneously detonated the 400-grain primacord at 48 separate points. Phase I results indicate that this detonation scheme will generate a wave which is plane across the width of the facility within a few microseconds.

c. Detonation Sequence

A dry-run of the countdown procedure was conducted before the test to ensure that all instrumentation, timing, and firing circuits were properly functioning. The countdown procedure consisted of the following steps:

- (1) At T-1 hours, the test area was cleared of all personnel.
- (2) The blasting caps were installed on the plane wave generator and the firing lines were connected to the blasting caps.
- (3) The firing lines were connected to the safety box at the command center. Before the firing circuit could be energized from the power supply, a plug had to be physically inserted into the safety box and a button depressed and held down.
- (4) At T-15 minutes, the area was visually checked by guards to

ensure that the area was still clear of personnel.

- (5) At T-5 minutes, all instrumentation circuits were energized.
- (6) At T-2 minutes, the firing system programmer was initiated.
- (7) At T-1 minute, a siren was sounded. The plug was inserted into the safety box and the button was depressed.
- (8) At T-15 seconds, a verbal countdown was started.
- (9) At T-10 seconds, the manual calibration switch was thrown.
- (10) At T-8 seconds, the calibration switch was opened.
- (11) At T-2 seconds, the cameras were turned on.
- (12) At T-0 seconds, the explosives were detonated.
- (13) The facility was visually inspected for undetonated explosives and the "All Clear" siren was sounded.

4. Safety

The command center was located approximately 500 feet from the edge of the detonation facility. Only essential personnel were allowed in the command center. Spectators were not allowed to approach within 1,000 feet of the detonation facility from T-1 hours until after the "All Clear" siren was sounded.

The weather criteria were based on a maximum wind velocity of 10 miles per hour with a heading such that sand or debris would not be blown toward an active portion of the Kirtland Air Force Base.

Because of the siting on an Air Force base, close coordination was required with the FAA tower to ensure that aircraft did not pass over the facility in their landing and take off patterns during the firing sequence.

2. Instrumentation

a. General Layout

Figure II-13 illustrates the general instrumentation layout. The locations of the structural model and the hardened cable project are indicated. The general location of the air pressure gages, the near-surface soil pressure gages, and the drill holes for the earth free-field gages are also shown.

The specific instrumentation details are reported in Parts 2 and 3. A detailed instrumentation list is provided in appendix A.

All the instrumentation cables were brought out of the detonation facility in five major trenches which has a minimum depth of cover of 3 feet of earth. The sheet piling immediately over the cable trenches was driven to 1-foot depth instead of the normal 5 feet to prevent shearing of the cables at this discontinuity. The cables were further protected by being placed in plastic conduits which ran continuously from all instrumentation locations to the exterior of the detonation facility. The cables were brought to the surface approximately 30 feet from the north edge of the facility and from this point they ran above ground to the instrumentation vans.

b. Instrumentation Recording

The electronic signals produced by the free-field gages in this experiment were recorded in the Air Force Weapons Laboratory Field Instrumentation Trailer which was located approximately 500 feet to the north of the test site. The CEC "System D" (3-kc carrier) was used for signal conditioning of the velocity gages. The remaining free-field gages were operated by Allegheny Instrument "Sensor Analogue Modules" (SAM-1) signal conditioning equipment. The SAM-1 is a DC system incorporating a power supply and a DC wide band amplifier for each gage. Four ampex CP-100 and two CEC PR-3300 tape recorders were used to record all free-field instrumentation with the exception of the earth time of arrival system, which was recorded by Fastax camera. A time code generator was used to place an IRIG time code on each tape. Simulated calibration signals were sent through each recording channel immediately before and after the shot by shunting selected resistors across one arm of the transducer bridge. Figure II-14 is a schematic of the instrumentation recording system.

c. Camera Coverage

High-speed motion picture and Fastax cameras were utilized to photograph the event. These cameras were mounted on two wooden stands, one to the north and one to the west of the detonation facility. Wooden targets were positioned to give the relative movement between the top and bottom of the overburden as illustrated in figure II-15. The camera coverage was

planned to give data on the overburden motion and any venting of the explosion products as well as to provide total pictorial coverage of the event.

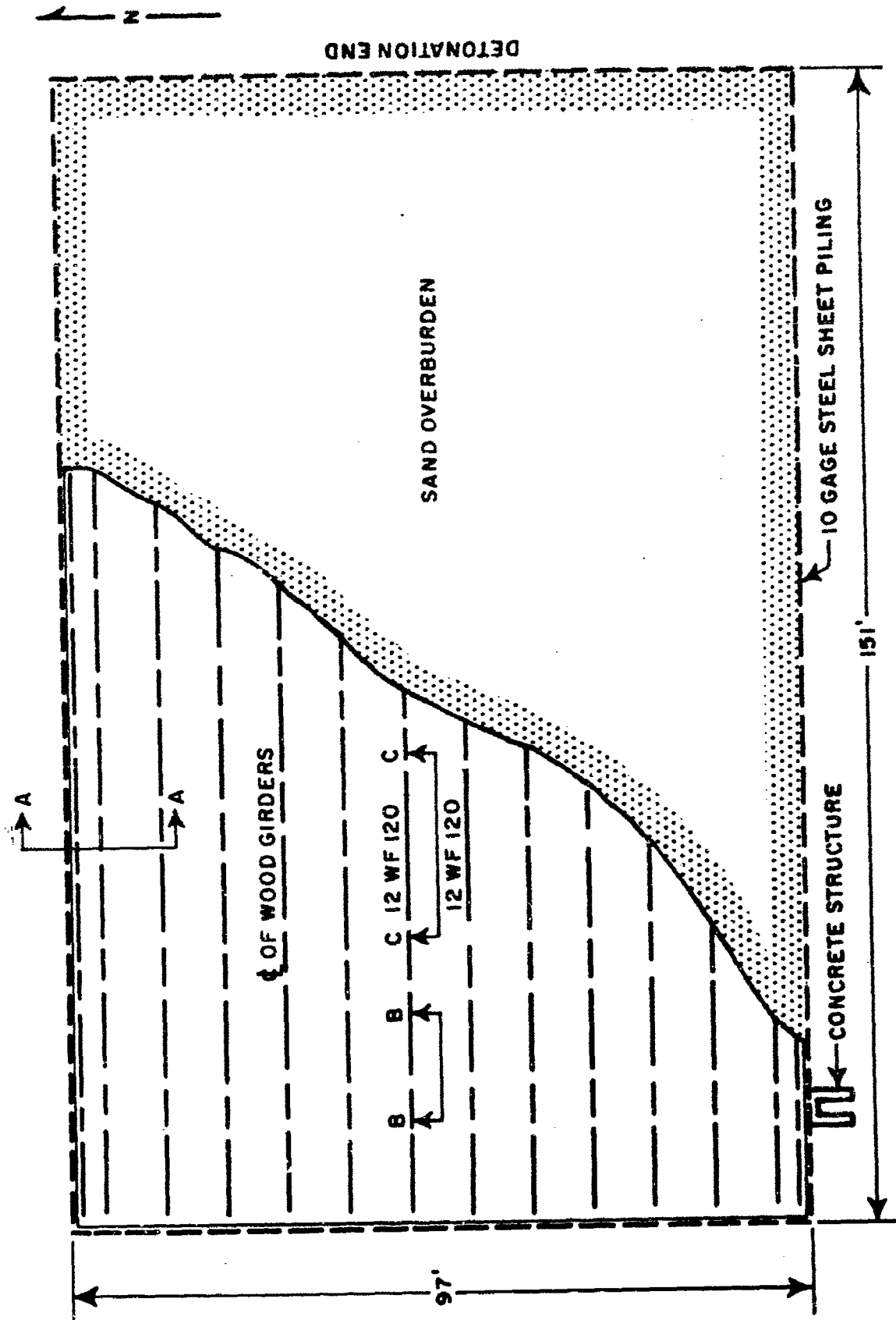


Figure II-1. Plan View of Detonation Facility

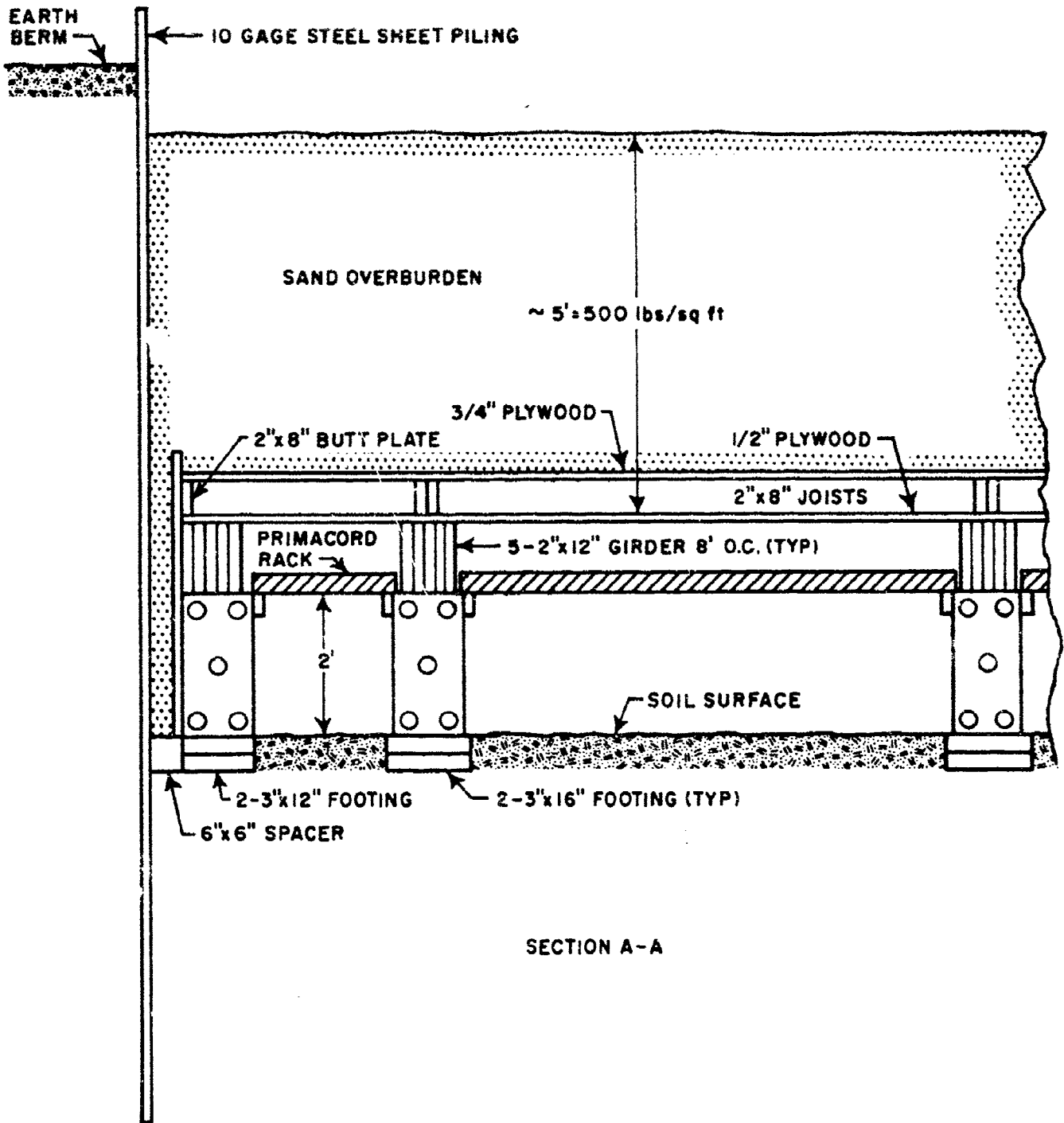


Figure II-2. Cross Section of Detonation Facility

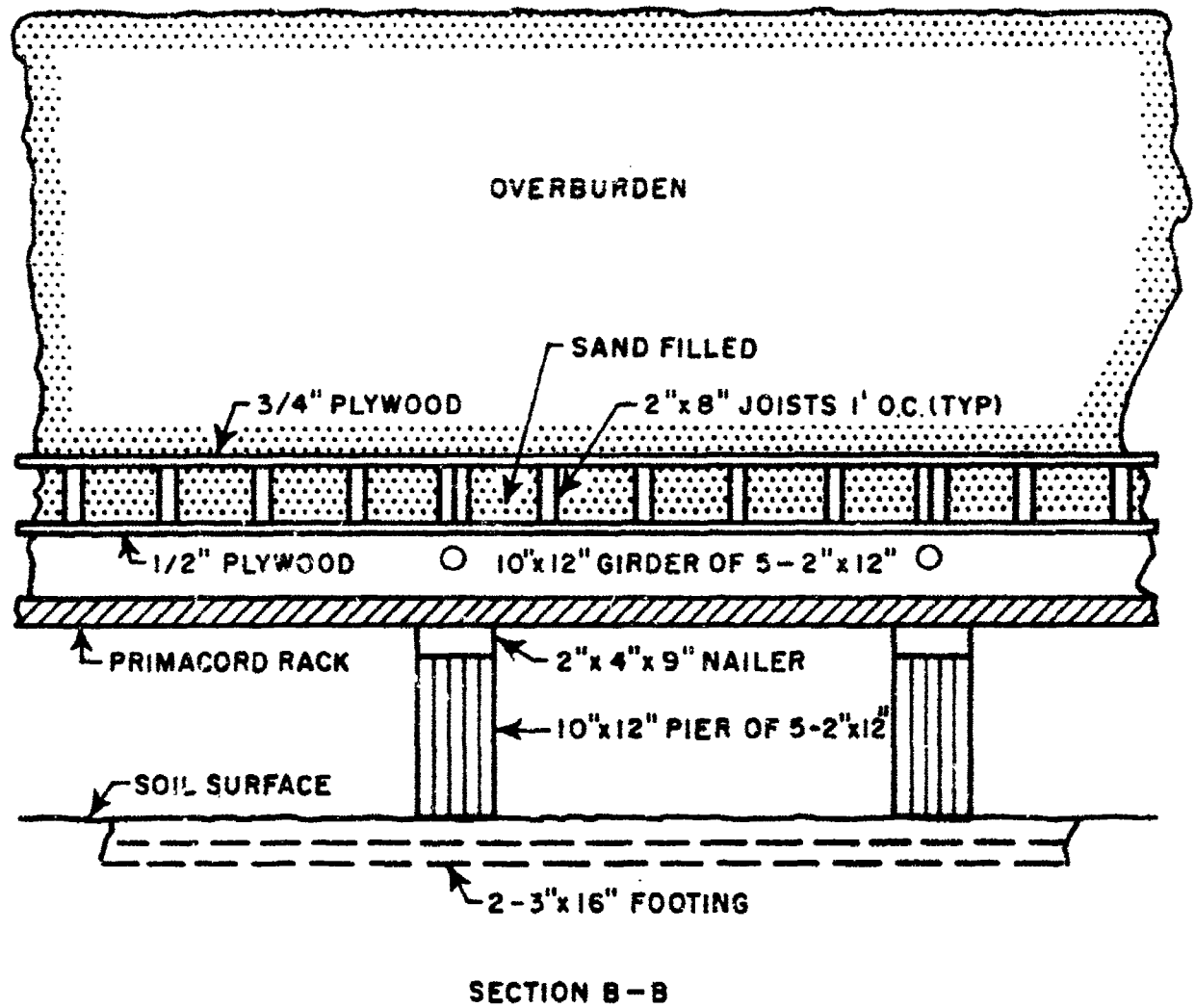


Figure II-3. Cross Section of Detonation Facility

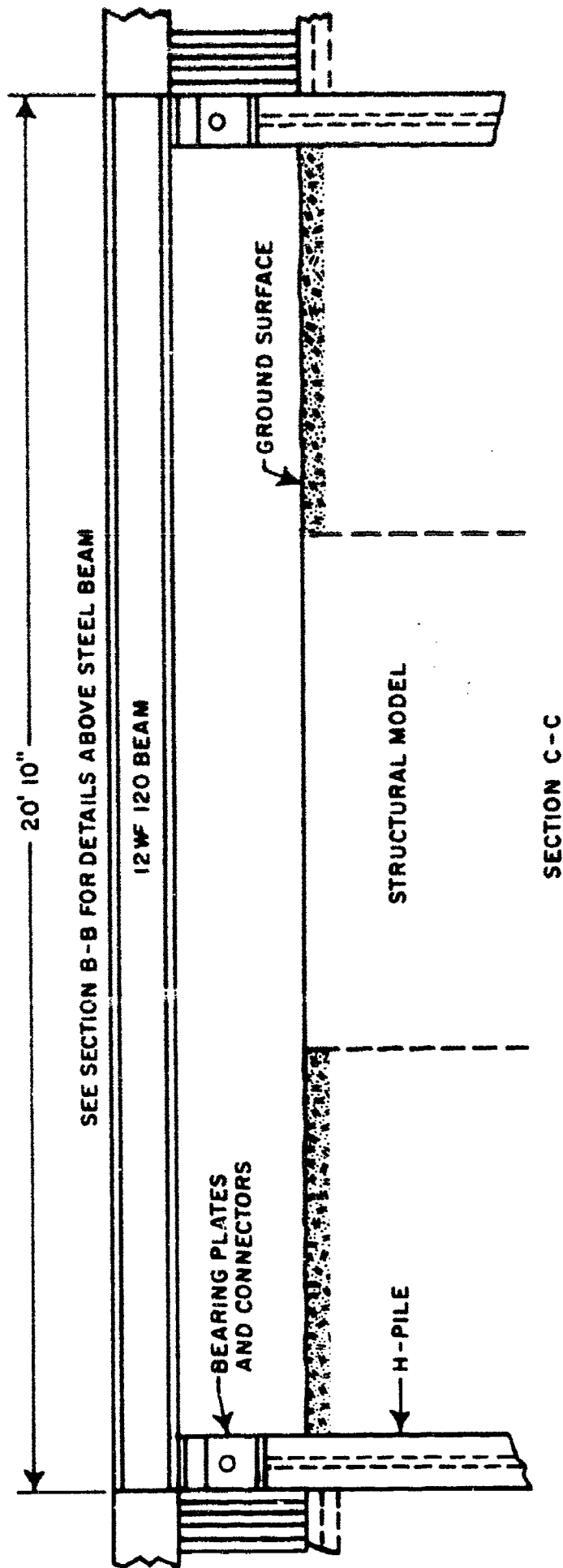


Figure II-4. Cross Section of Steel Support Structure

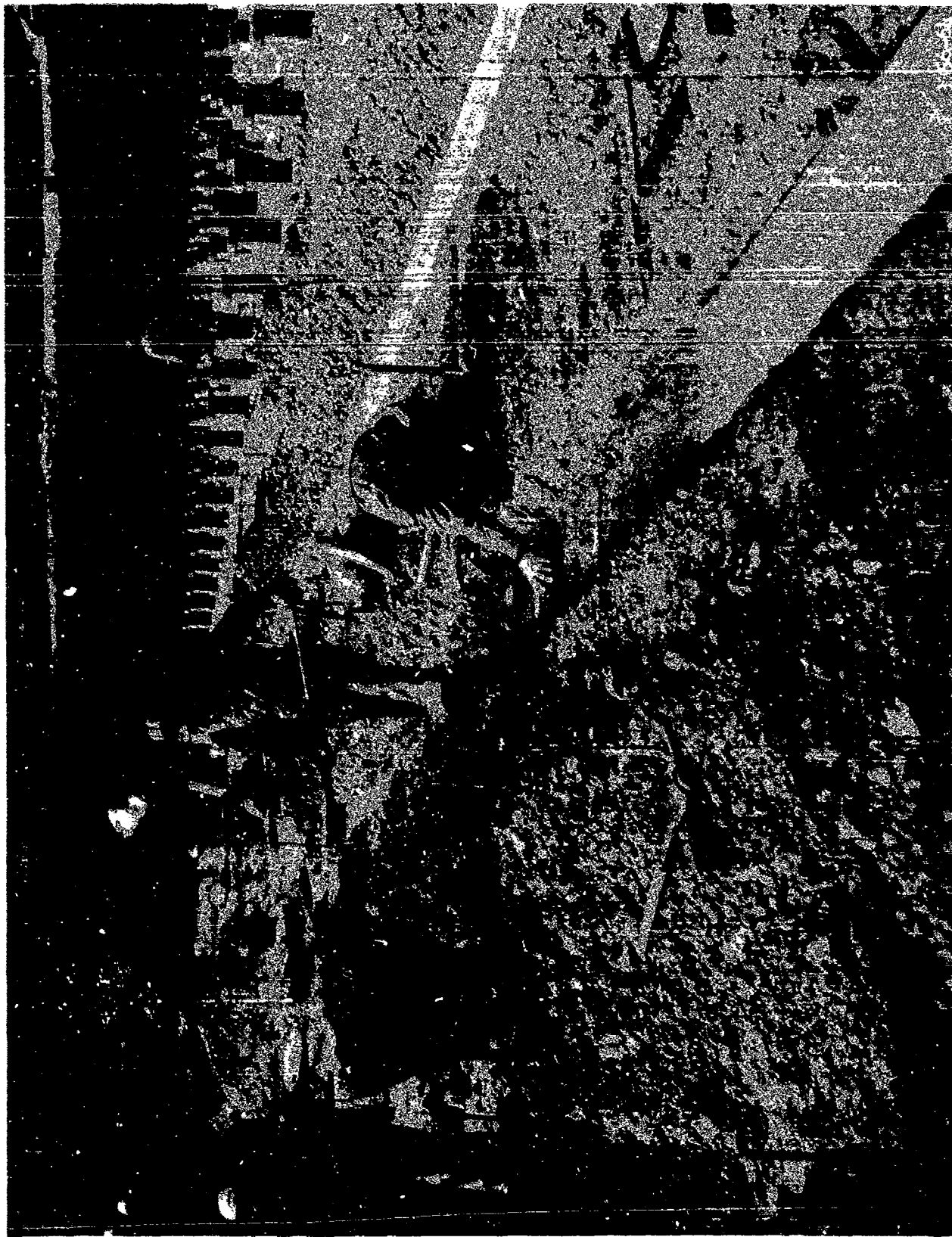


Figure II-5. Early Stage of the Facility Construction



Figure II-6. Details of the Steel Construction

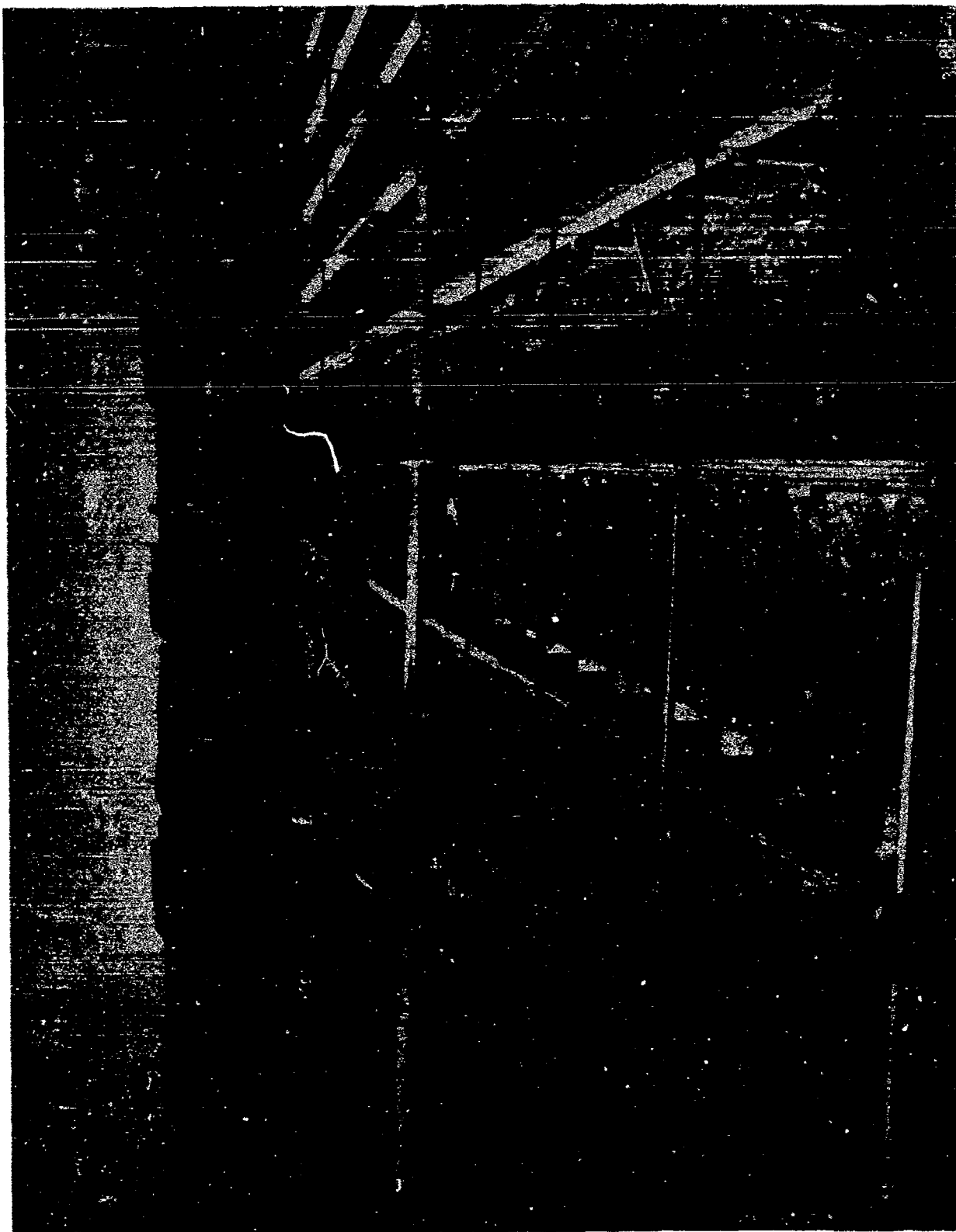
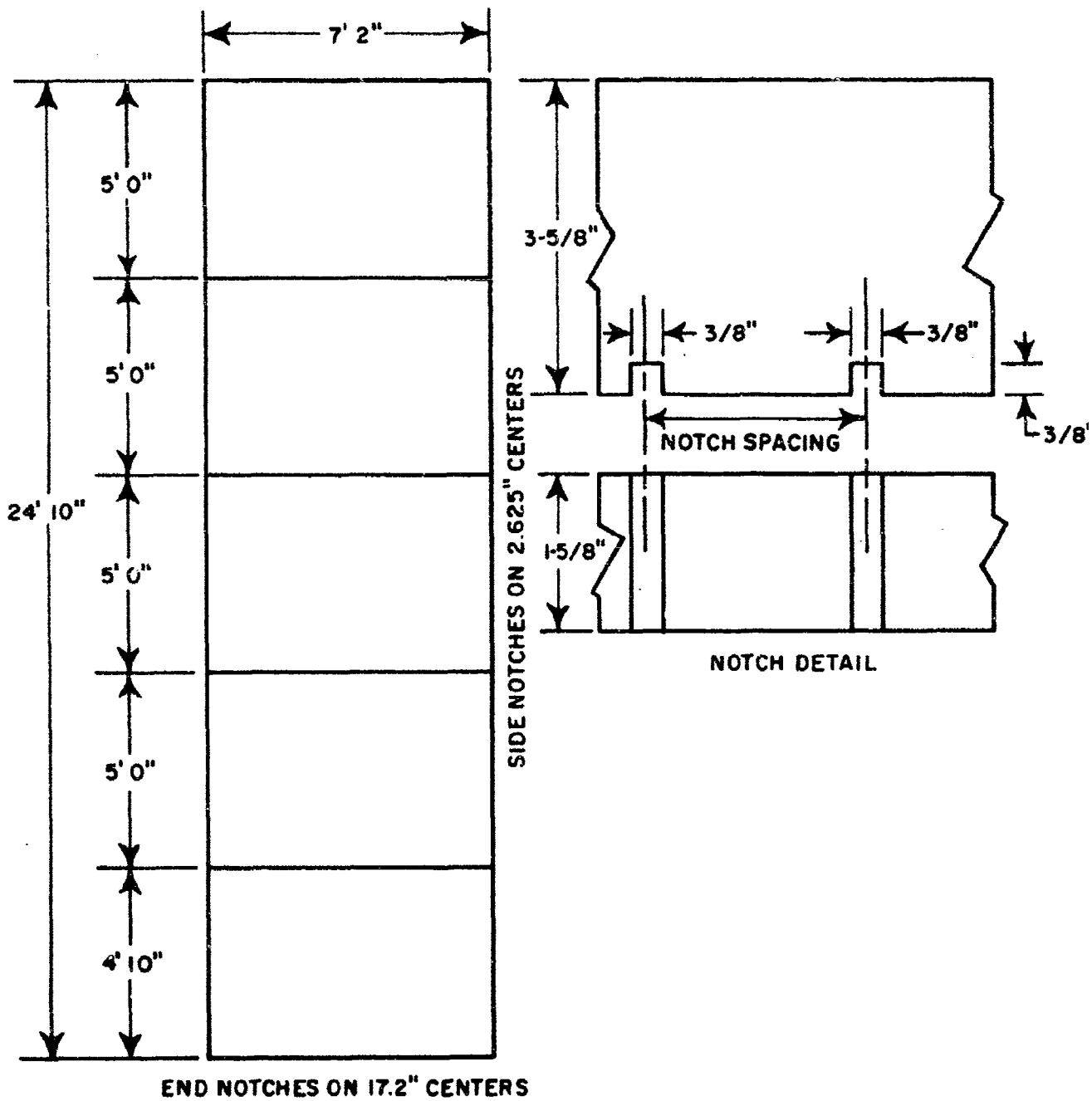


Figure II-7. Primacord Rack Placement



NOTE: PRIMACORD RACKS CONSTRUCTED FROM 2" x 4" LUMBER WITH 22 GAGE METAL STIFFENERS AT ALL JOINTS AND CORNERS

Figure II-8. Typical Primacord Rack Construction

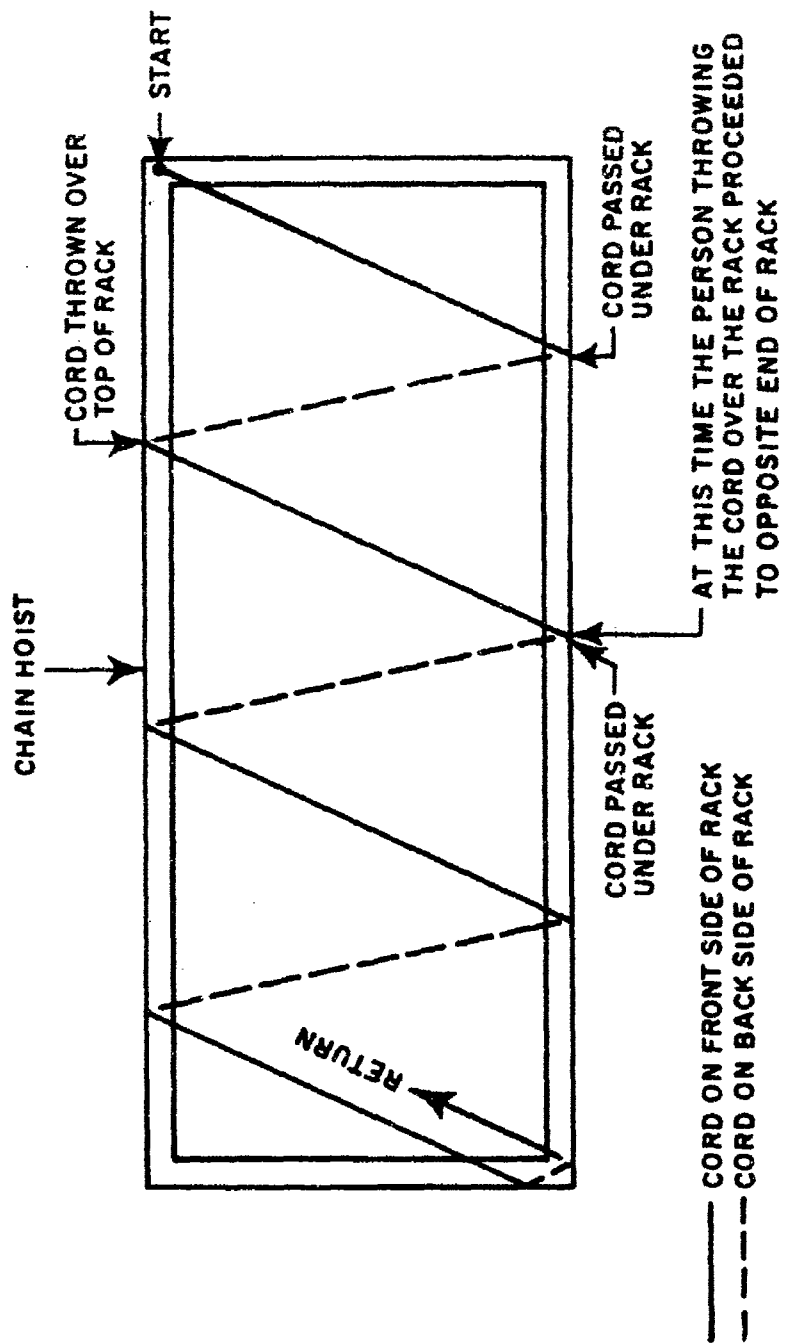


Figure II-9. Primacord Wrapping

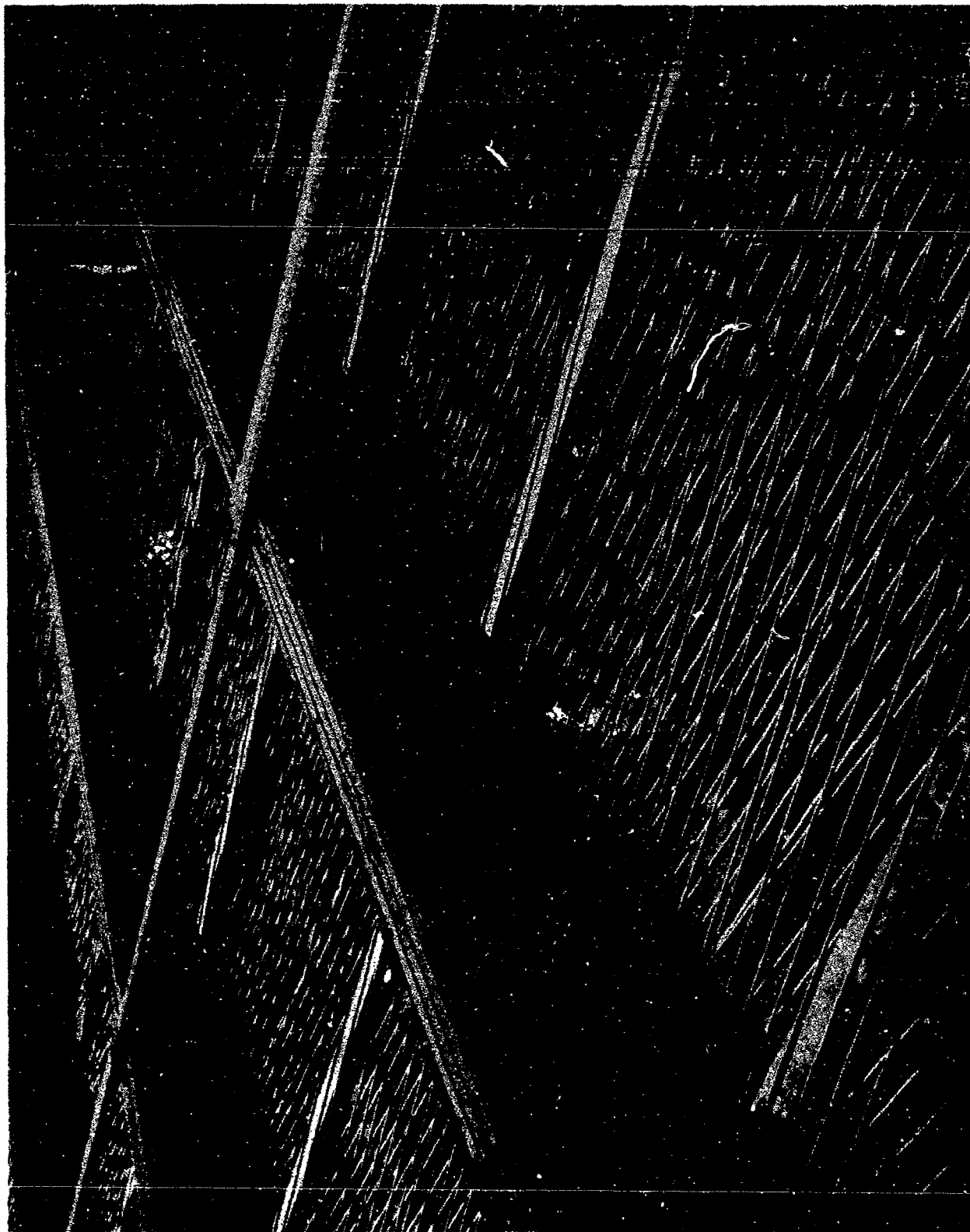


Figure II-10. Primacord Cross Tying

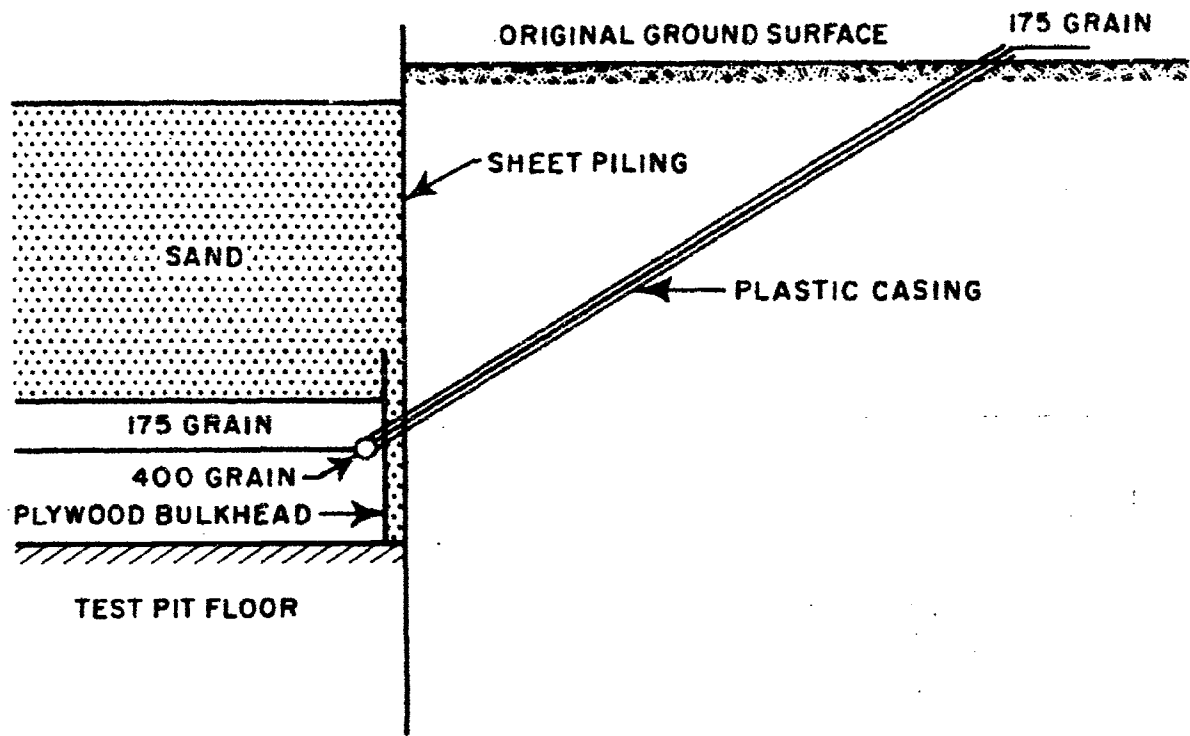


Figure II-11. Primacord Entrance into Detonation Facility

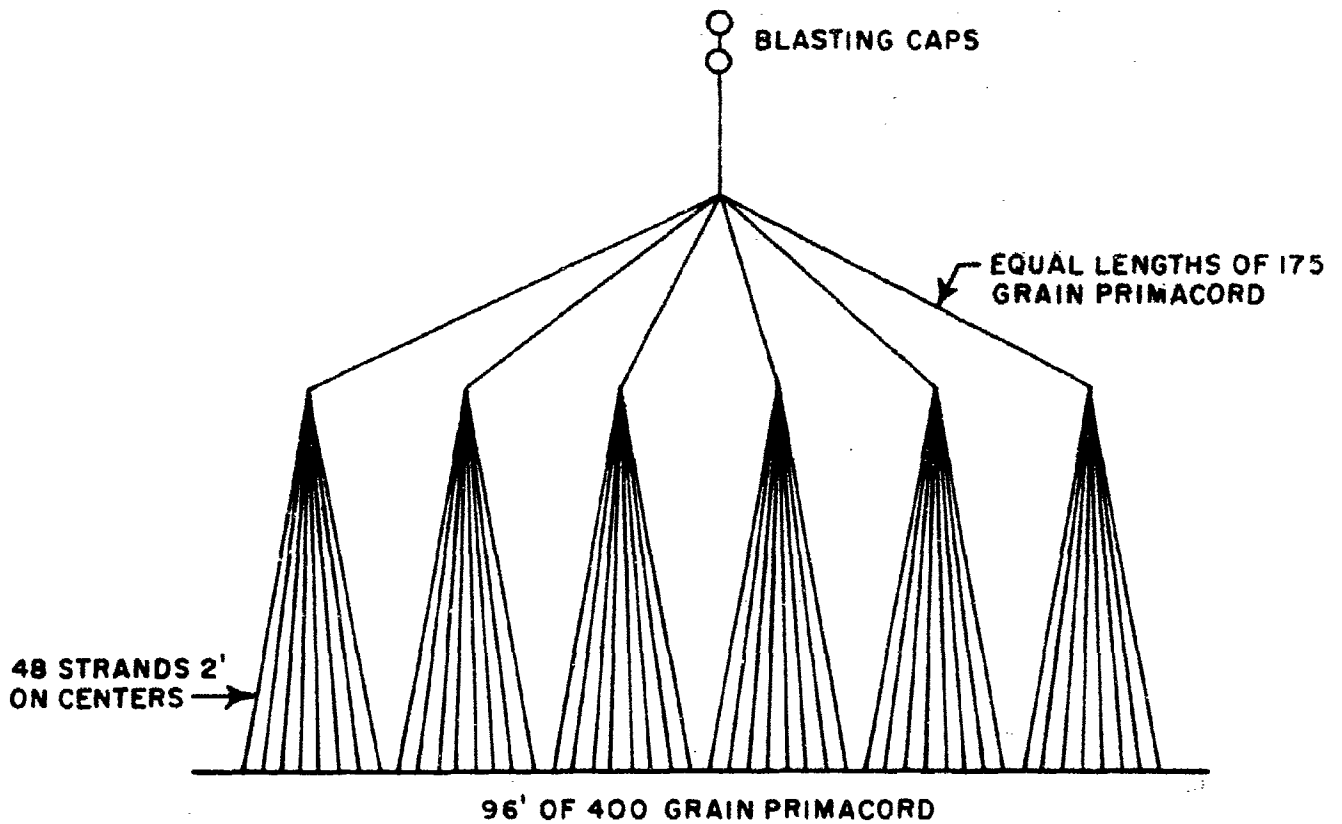


Figure II-12. Primacord Detonation

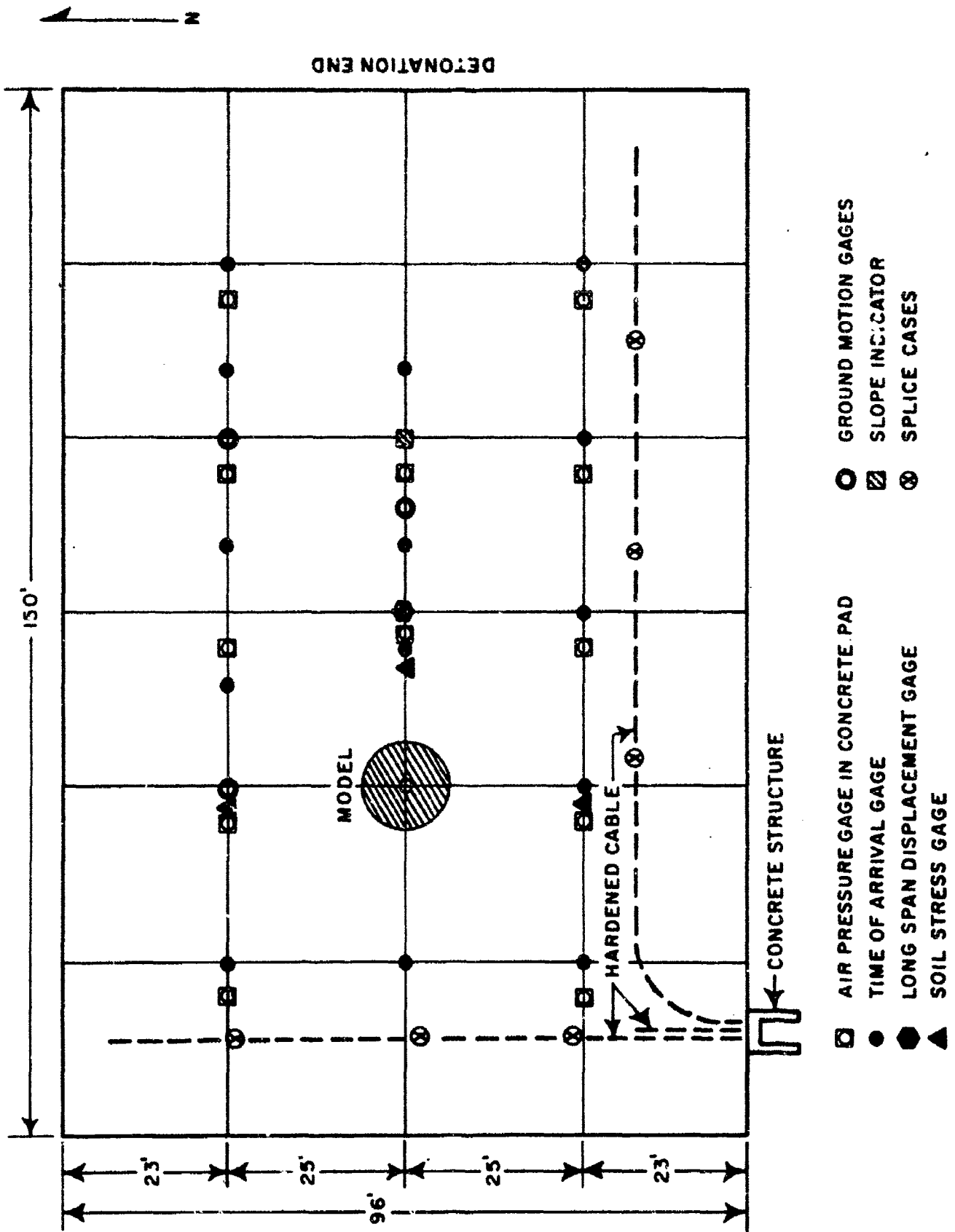
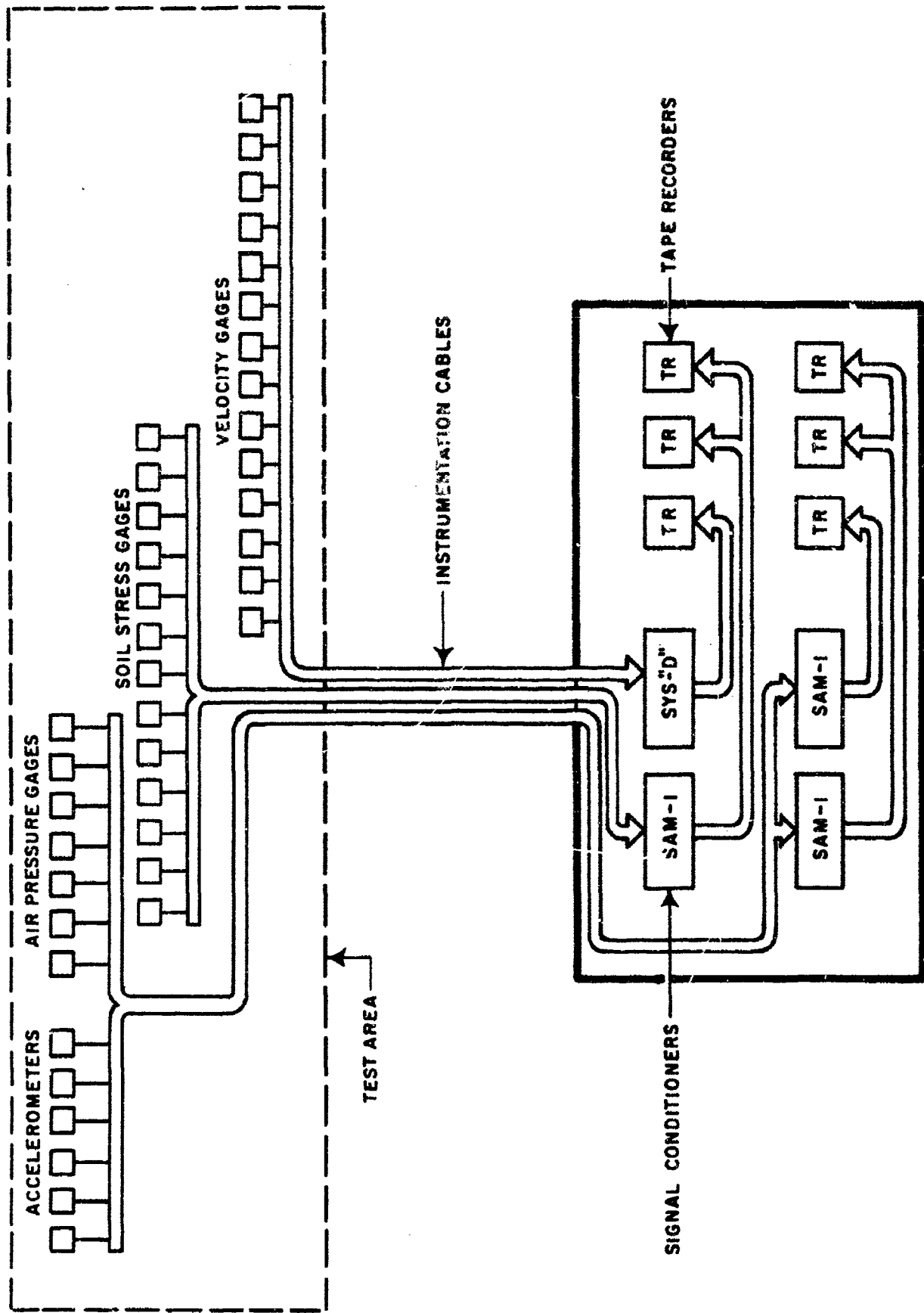


Figure II-13. General Project and Instrumentation Layout



FIELD INSTRUMENTATION TRAILER

Figure II-14. Instrumentation Recording System Schematic

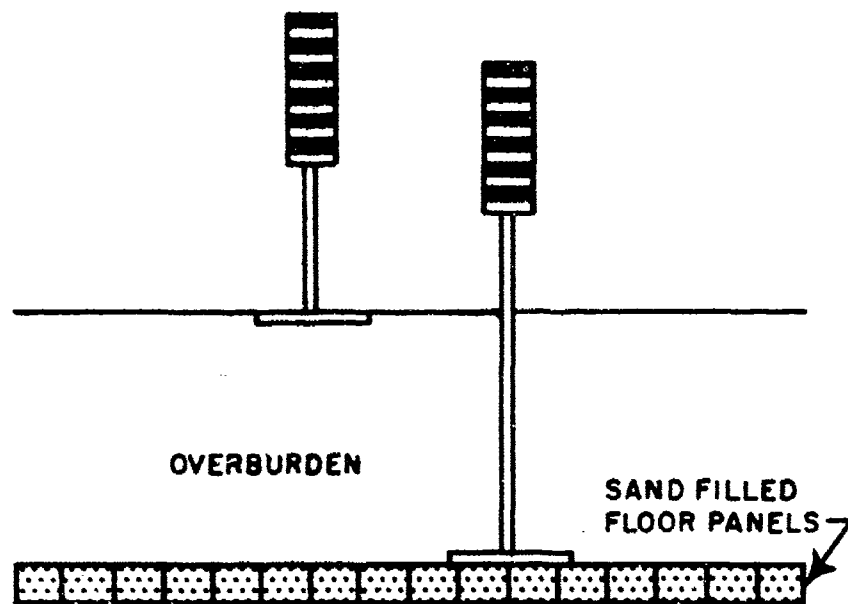


Figure II-15. Target Stands

SECTION III

RESULTS

This experiment produced a peak overpressure of 312 psi, a time to one-half peak pressure of 18.2 msec and a total duration of 170 msec. A composite pressure-time history curve is given in figure IX-1 which defines the air free field environment. The impulse contained under this curve is approximately 10.4 psi-sec. The average shock front velocity was 5,120 ft/sec \pm 11 percent. and the wave front was essentially plane, across the central portion, as it traveled the length of the facility.

The overburden moved upward with rigid body motions until it cleared the top of the metal sheet piling. The overburden continued to move upward as a mass until it reached a height of approximately 125 feet at the firing end (see figure III-1). At this point, the individual particles of sand began to break up and a dust cloud continued to rise to nearly twice this height. The overburden displacement versus time measurements taken from the Fastax camera coverage of the target stands are presented in figure III-2. No differential motions between the top and the bottom of the overburden could be detected in the target stand data.

A small amount of sidewall venting was first detected at the southeast corner of the facility. This venting progressed across the detonation end of the facility and then proceeded down the sidewalls and across the reflection end of the facility. Major venting did not occur until the bottom of the overburden had cleared the top of the sheet piling.

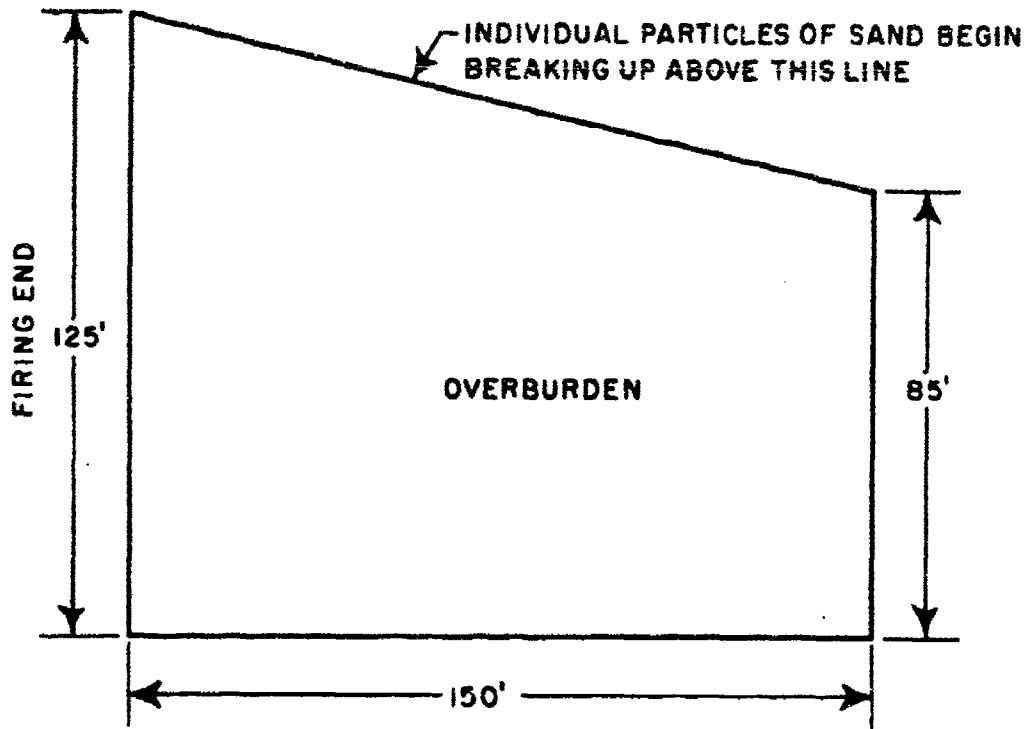


Figure III-1. Maximum Overburden Height

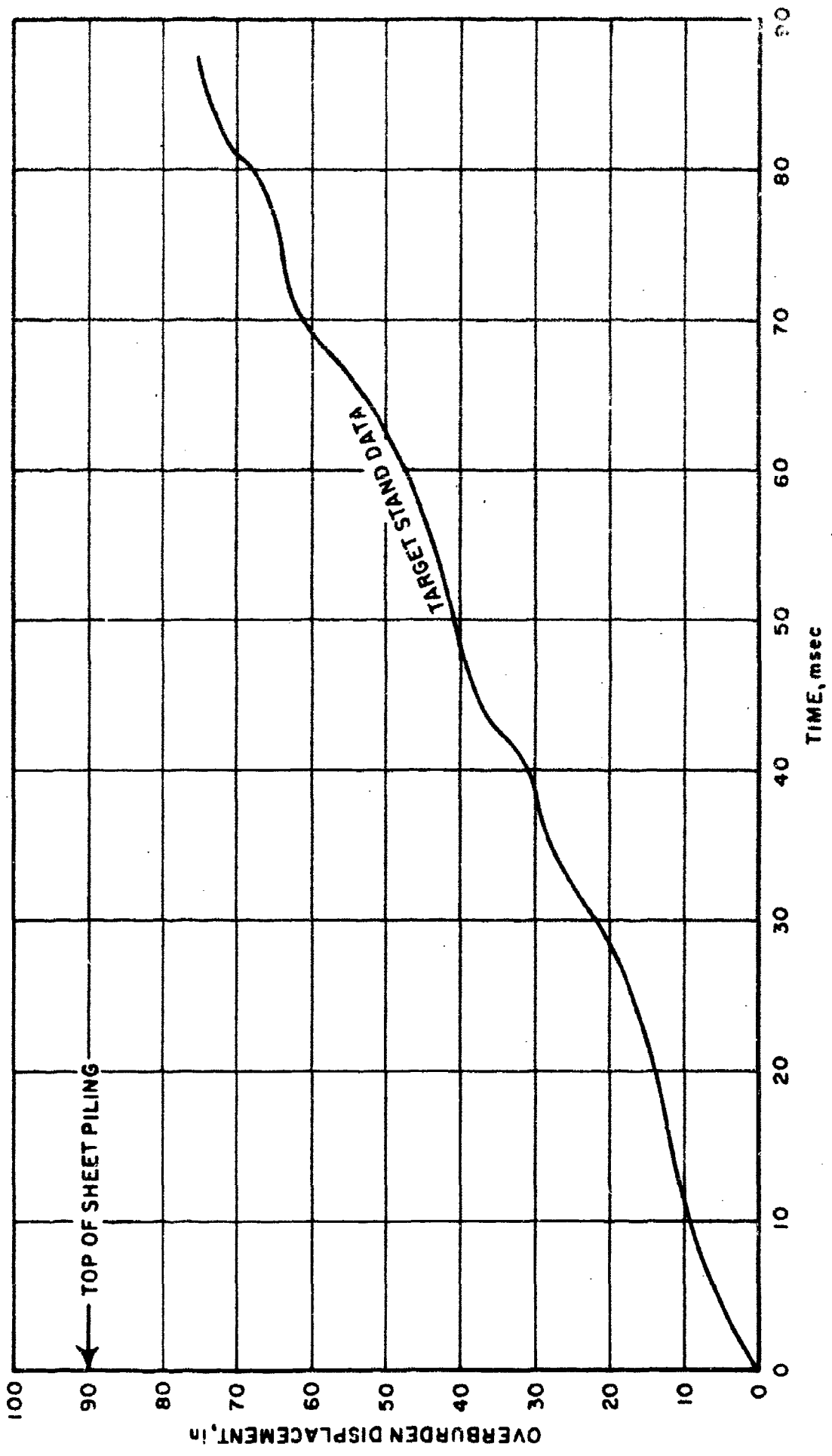


Figure III-2. Overburden Motion

SECTION IV

DISCUSSION

The peak overpressure and shock front velocity curves developed during Phase I (figures I-9 and I-10) have been corrected to include the Phase II data. These corrections were quite small. Figures IV-1 and IV-2 present the corrected peak overpressure versus load density, and shock front velocity versus wrap angle prediction curves.

The composite air-pressure curve obtained from this experiment is compared with the results from a 1-MT nuclear weapon in figure IV-3. It can be seen that the desired durations were not obtained in this experiment. The observed duration to one-half peak pressure was 49.2 percent of the desired duration and 44.4 percent of the computed duration. This agrees well with the 43.9 percent observed in the Phase I experiments. It had been postulated that edge effects played a major role in producing the observed low efficiency factor. However, this does not now appear to be the case since the perimeter length to plan area ratio was decreased from 0.15 for the Phase I facilities to 0.0342 for the Phase II facility with no substantial increase in the efficiency factor.

Figure IV-4 presents the displacement-time history of the overburden motion. A comparison of the theoretical and observed time histories reveals that the overburden was initially accelerated much more rapidly than was computed, while at late times there is fair agreement. The observed high initial acceleration will cause a much faster decay of pressure than was computed.

Since the duration efficiency factors from both Phase I and Phase II agree and experimental results clearly indicate that the overburden calculations are in error, it is obvious that these calculations must be adjusted in order to successfully make predictions for future experiments. Figure IV-5 has been extracted from reference 1. It is a plot of duration efficiency factors to one-half peak pressure for various cavity heights. The results in figure I-12 have been corrected to include the efficiency factors given in figure IV-5. The corrected set of curves are presented in figure IV-6.

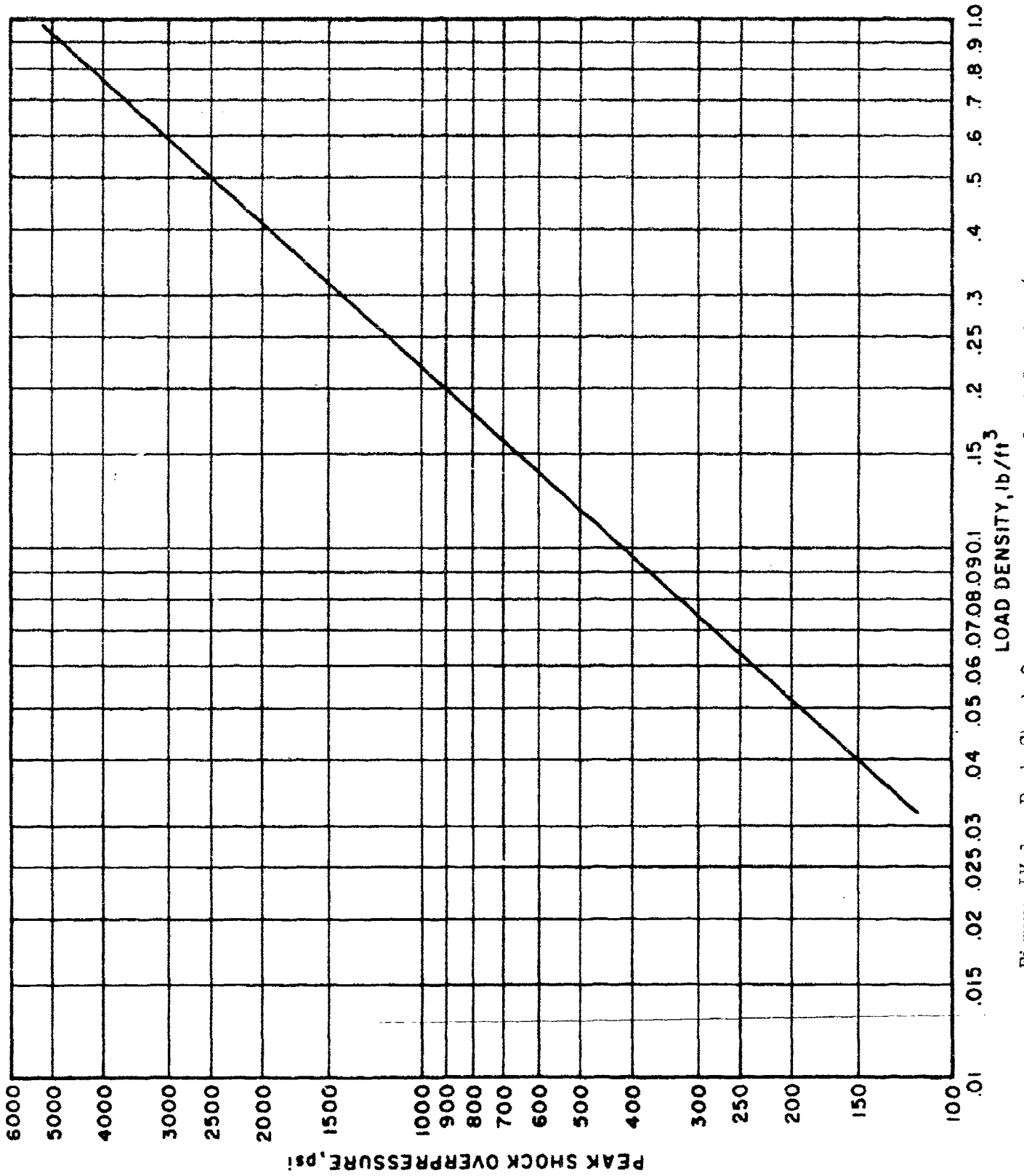


Figure IV-1. Peak Shock Overpressure versus Load Density (Corrected)

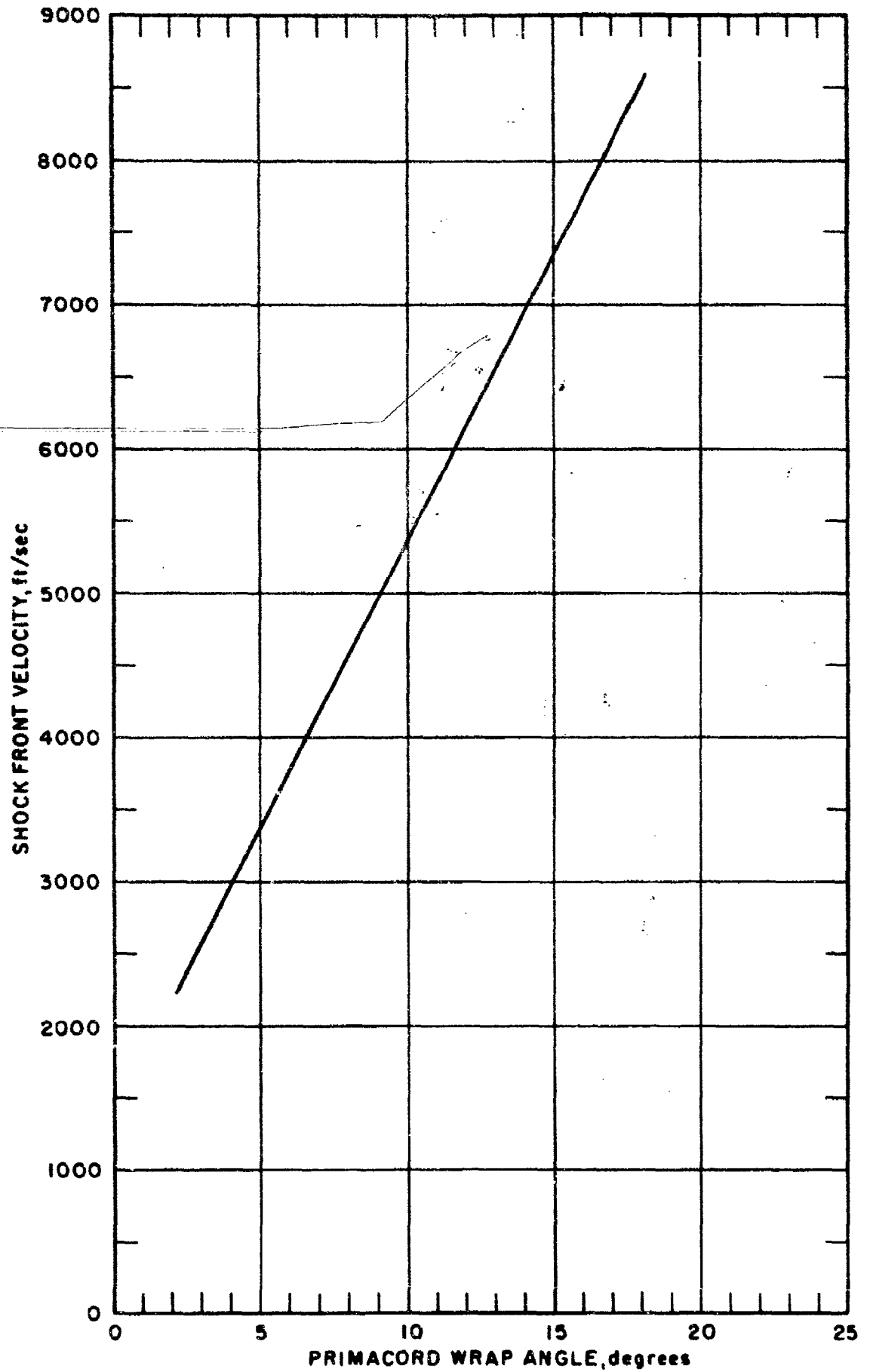


Figure IV-2. Shock Front Velocity versus Wrap Angle (Corrected)

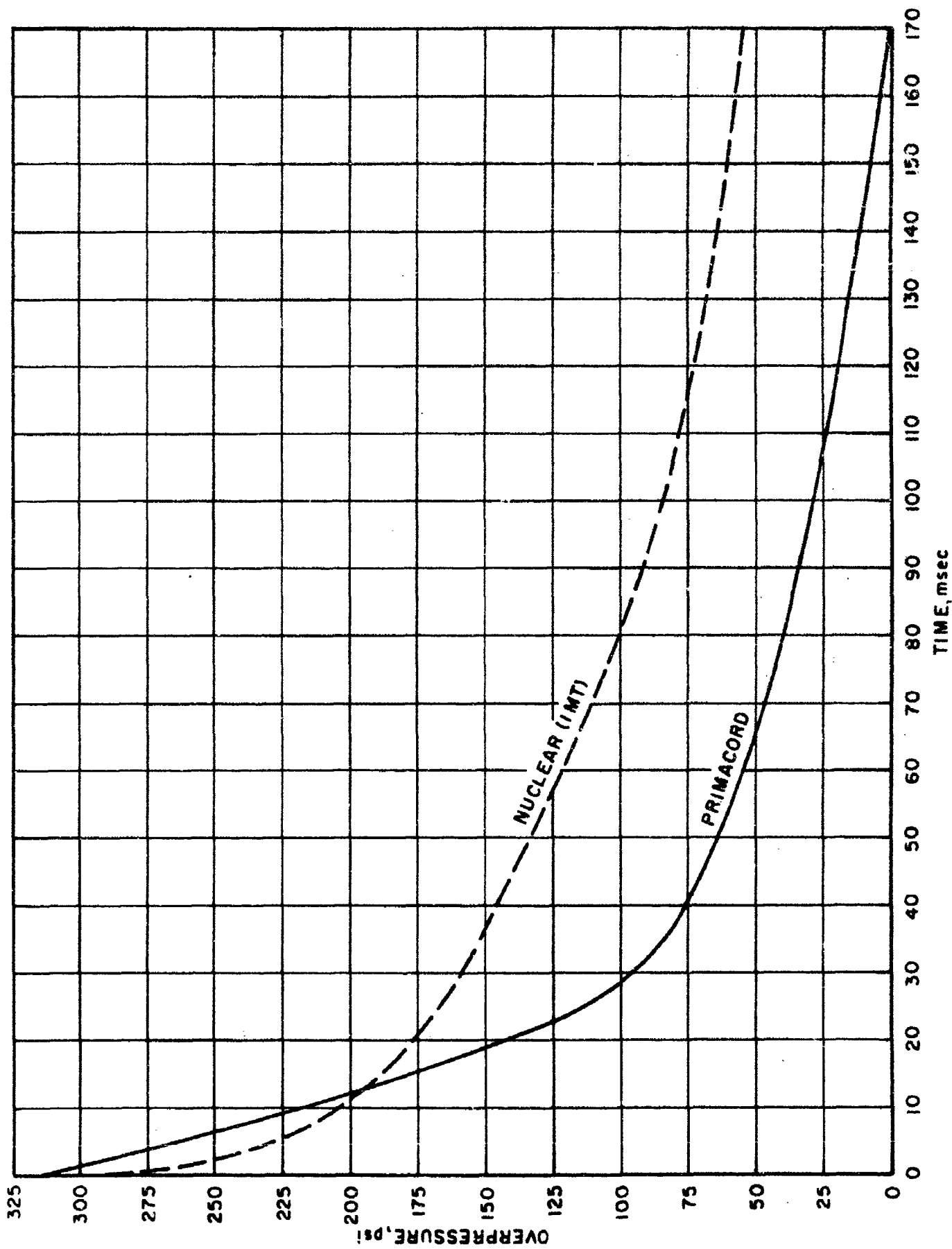
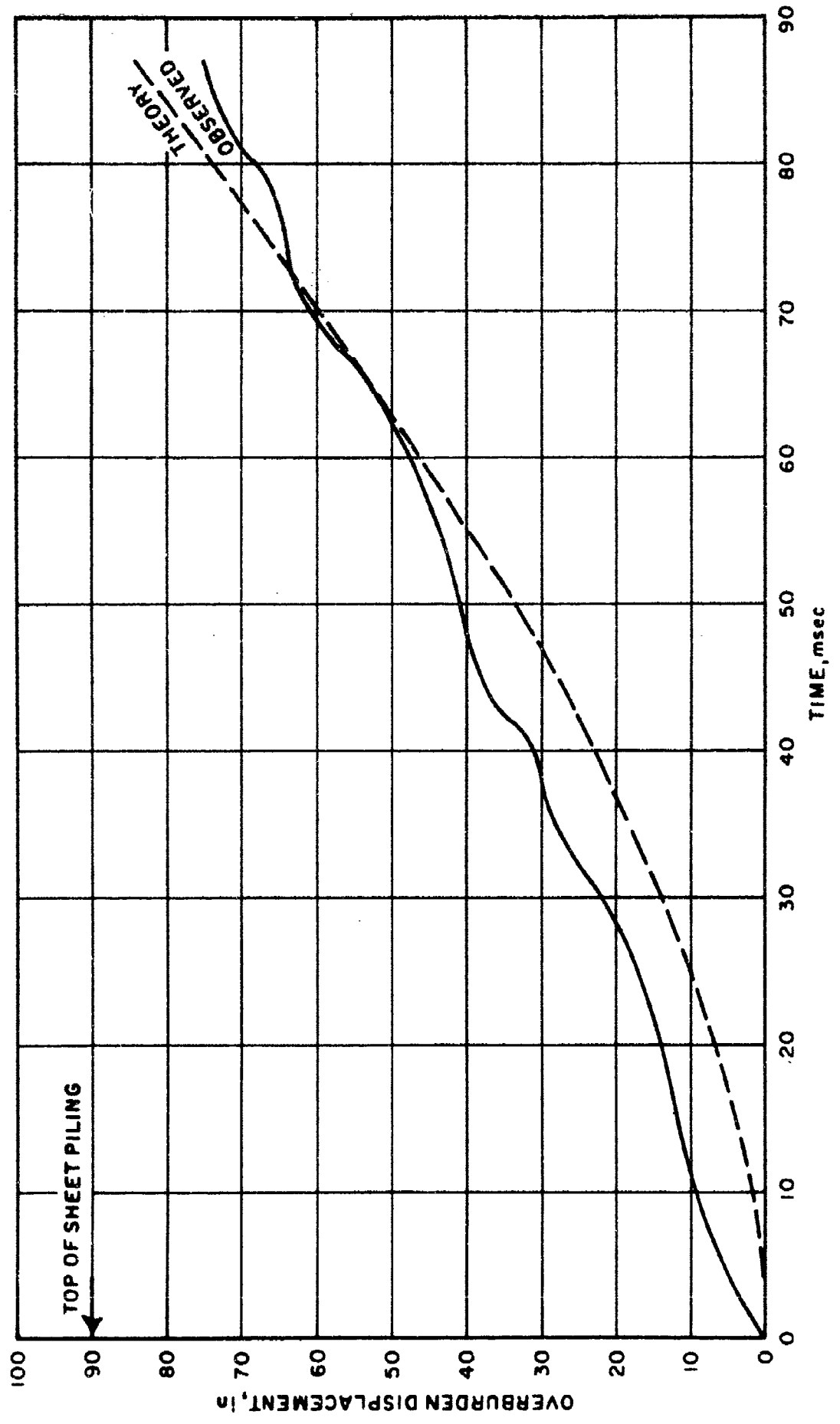


Figure IV-3. Comparison of Pressure-Time histories for Primacord and Nuclear



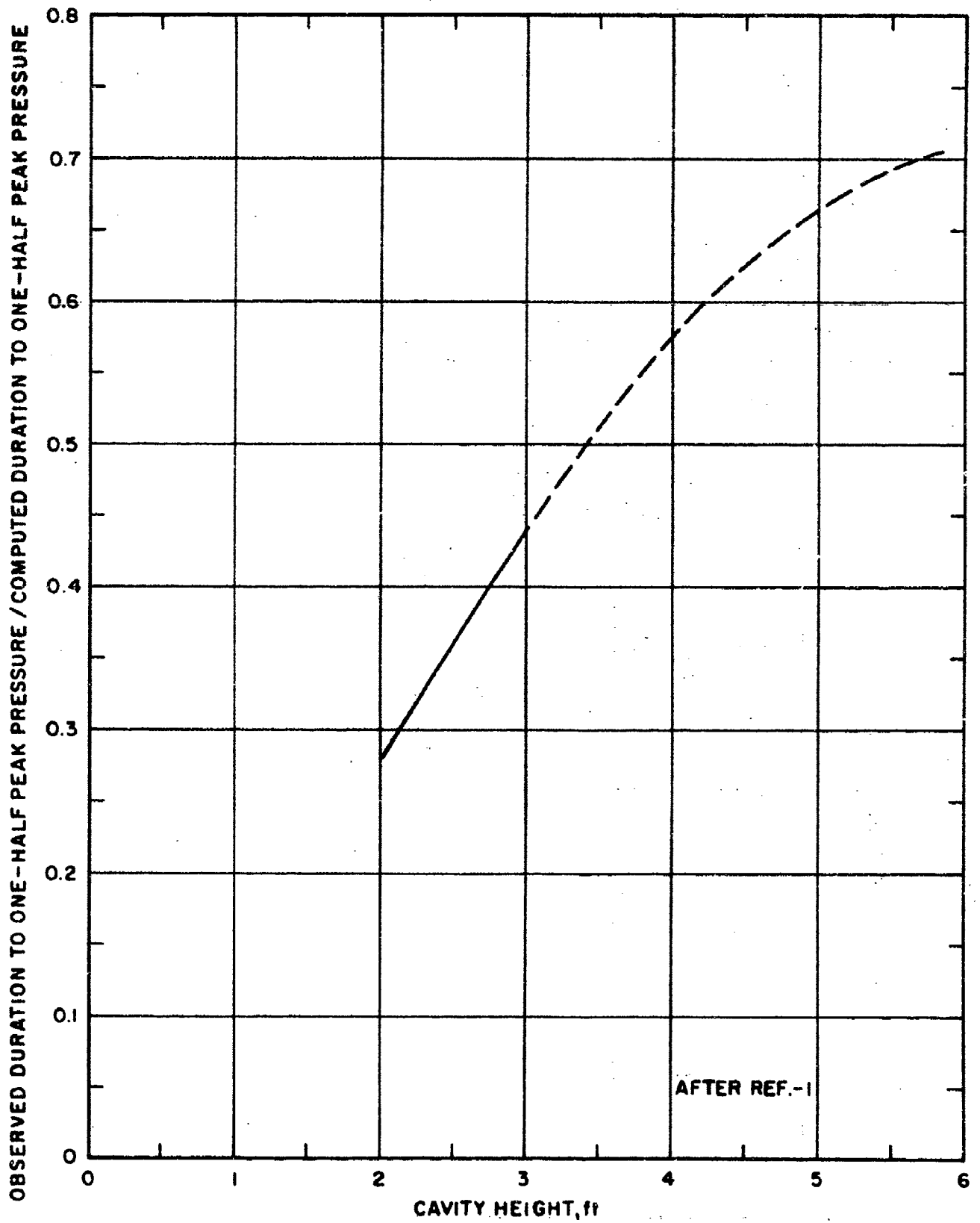


Figure IV-5. Duration Efficiency Factors

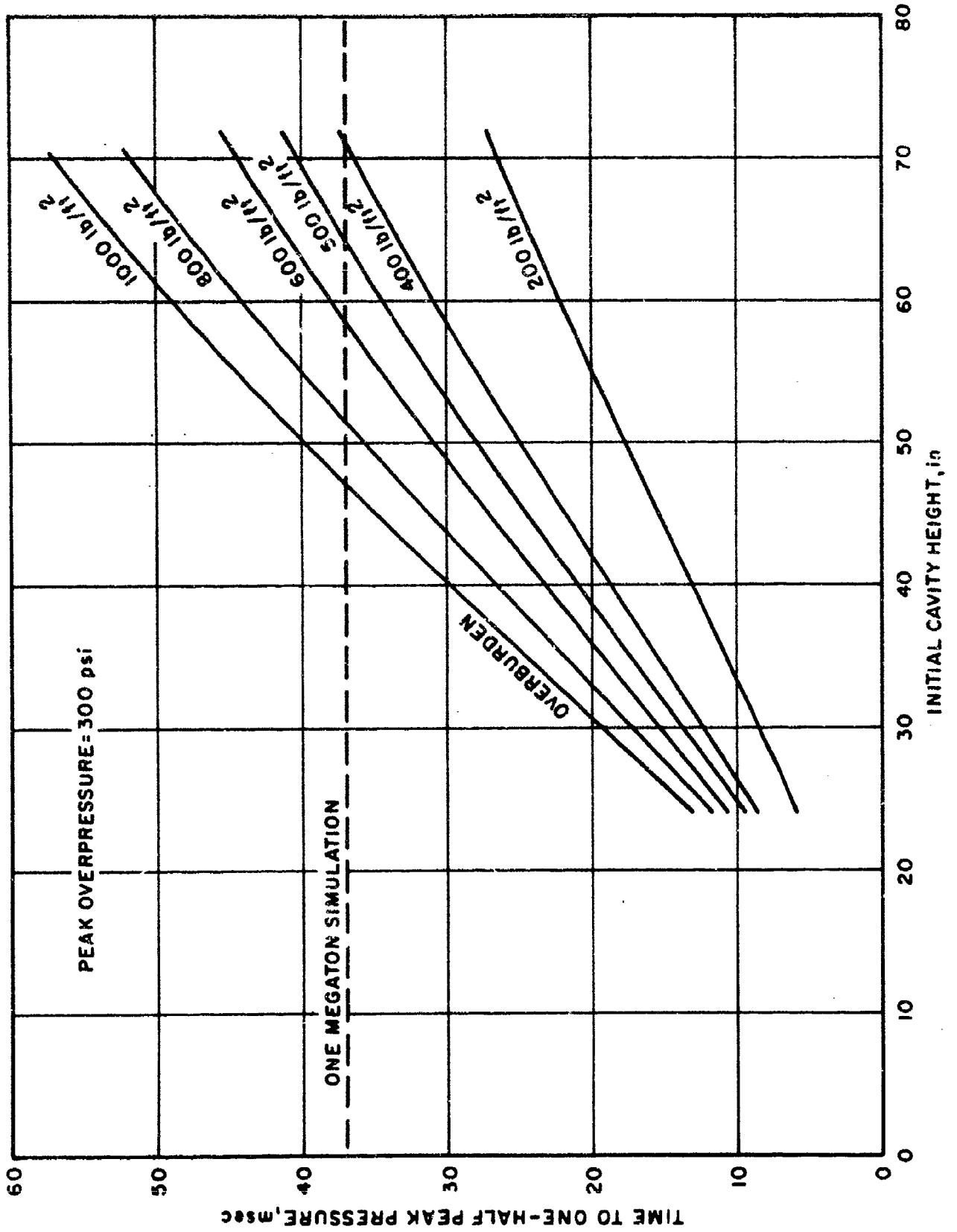


Figure IV-6. Corrected Overburden Calculations

SECTION V

CONCLUSIONS AND RECOMMENDATIONS

The parameters of the simulation technique scaled exactly between the small Phase I tests and the large Phase II test. The peak overpressure and shock front velocity prediction curves, which were developed during Phase I, appear to be valid within approximately 10 percent and only small corrections were required to include the Phase II data.

The observed durations to one-half peak pressure were only 49.2 percent of those desired. Duration efficiency factors have been applied to the theoretical calculations to account for this discrepancy. Figure V-1 summarizes these calculations and illustrates the overburden versus initial cavity height required to simulate a 300-psi shock wave for a 1-MT detonation.

For future 300-psi simulations, it is recommended that a load density of 0.0720 pound of PETN/ft³ and a wrap angle of 8.6 degrees be used. The initial cavity height and the overburden mass should be selected from the values given in figure V-1. The primacord matrix should be positioned 24 inches above the ground surface when a 36-inch cavity height is utilized. Similar recommendations cannot be made for larger cavity heights until additional tests are conducted.

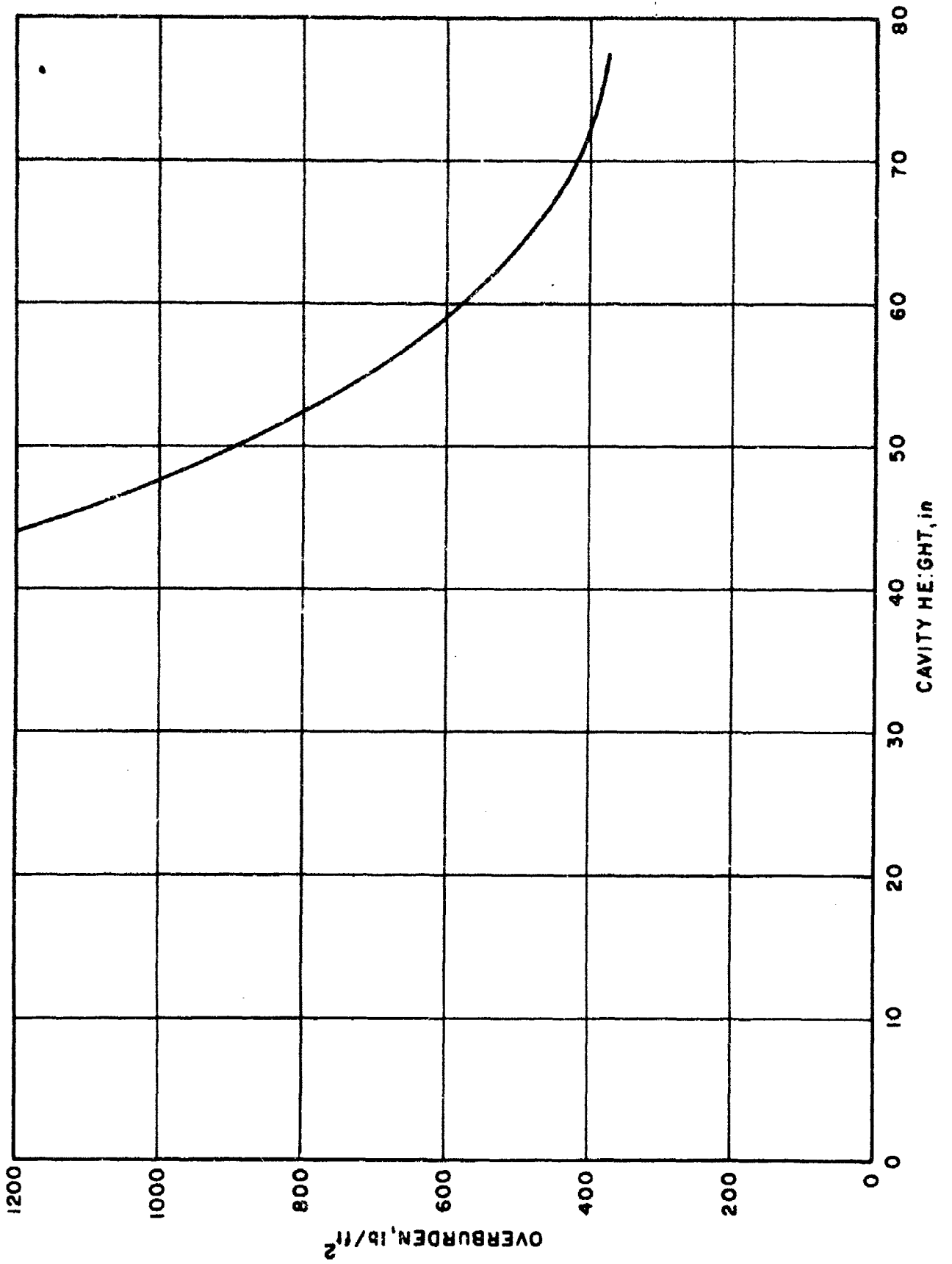


Figure V-1. Overburden versus Cavity Depth Required to Simulate

PART 2

AIR FREE FIELD

This page intentionally left blank.

SECTION VI
INTRODUCTION

1. Objectives

The air free-field measurements were made to determine the air-blast pulse produced by the experiment, to provide input data for the structural model and the earth free field, and to provide data to improve prediction techniques for future tests. In addition, measurements were made of the shock wave which was released to the atmosphere.

2. Background

The research performed during the first phase of this project was used as a basis to design this large-scale experiment. During Phase I, four primacord tests were conducted and experimental data were collected to determine the load density, primacord wrap angle, cavity height, and mass of overburden which are required to produce a desired simulation. As outlined in section I, an experimental approach was necessary since the analytical problem is nearly intractable.

Many of the Phase I conclusions were arrived at with a minimum of data points. Also, all of the previous experiments were conducted on a much smaller scale than the Phase II experiment. This experiment will, therefore, provide valuable data for improving the prediction techniques for future simulations. For example, it was found in Phase I that a 36-inch cavity would produce a duration which was 44 percent of the theoretically computed duration. The effect of scaling the loaded area on this parameter can be determined on the basis of the Phase II results.

3. Predictions

As discussed in section VI-2, the Phase I results were utilized to predict the parameters required to give the desired simulation. In addition, judgment was utilized to determine the effect of increasing the scale of the experiment. On this basis, the following predictions were made:

| | |
|---------------------------|---------|
| Peak overpressure | 300 psi |
| Time to one-half pressure | 37 msec |

| | |
|----------------------|--------------|
| Total duration | 160 msec |
| Shock front velocity | 4,800 ft/sec |

SECTION VII

PROCEDURE

1. Instrumentation

a. Air-Blast Gages

The prime instrumentation for this portion of the experiment consisted of flush-mounted pressure transducers. These gages provide pressure-time histories as well as shock front time-of-arrival data. Two types of pressure transducers were used, the Norwood Model 111 and the Scheavitz-Bytrex Model HFG-2000. The Norwood transducer is a conventional strain gage device selected because it proved to be dependable and rugged during the Phase I test series. The main weakness of this gage is its relatively low frequency response (20,000 cps) which causes a moderate amount of ringing when the gage is subjected to an air shock. The Scheavitz-Bytrex gage is a recently developed pressure transducer which uses a semiconductor strain gage to link a very stiff diaphragm to the transducer body. This gage was selected because of its relatively high frequency response (50,000 cps). Calibration was accomplished in the field with static air pressure.

b. Shock Front Time of Arrival

A line of break wires was placed along the length of the facility to provide additional shock front time-of-arrival data. The break wires were manufactured in the Air Force Weapons Laboratory from very lightweight foil. The break wires were connected to a DC circuit such that when a foil element was broken, a step increase in voltage was produced. The seven break wires were multiplexed into a single channel for recording.

c. Microbarographs

Microbarographs were used to measure the intensity of the shock wave formed in the surrounding air when the facility vents. These self-contained instruments had a variable-reluctance bridge pressure sensor head supplied by a 1,000-cps carrier, preamplifier, detector, DC amplifiers, and Brash recorders. The sensing head is a Wianko twisted Bourdon tube.

2. Gage Placement

The pressure transducers were mounted in concrete blocks which had a concave upper surface to facilitate the attachment of calibration fittings. The blocks were set in the field with the top of the gage flush with the ground surface. The gage leads were threaded through a flexible metal tubing which had been cast in the concrete. After exit from the concrete, the cables were protected by plastic conduit. The upper portion of the mounting block was grouted level with the ground surface when the calibration of each gage was completed. See figure VII-1.

3. Gage Locations

Figure VII-2 is a plan view of the test area showing the location of the air free-field instrumentation. It will be noted that each position containing a pressure transducer has been assigned a location number. The actual distance between various gage locations was surveyed, and these distances have been indicated in figure VII-2. The break wires were placed at 25-foot intervals, commencing at the detonation end of the facility. Their location will be designated by the letters D. E., plus a distance to the gage of interest, i.e., D.E. + 75 feet. Table VII-1 lists the transducers used at each of the locations shown in figure VII-2.

The microbarographs were located along a line at distances of 400, 800, and 1,200 feet from the north edge of the test facility.

Table VII-1
INSTRUMENTATION LIST

| <u>Location number</u> | <u>Instrument type</u> |
|------------------------|---------------------------------|
| 1 | Norwood Model 111 |
| 4 | Norwood Model 111 |
| 5 | Norwood Model 111 |
| 7 | Norwood Model 111 |
| 10 | Scheavitz-Bytrex Model HFG-2000 |
| 14 | Norwood Model 111 |
| 18 | Norwood Model 111 |
| 22 | Scheavitz-Bytrex Model HFG-2000 |
| 24 | Norwood Model 111 |
| 28 | Scheavitz-Bytrex Model HFG-2000 |
| 30 | Norwood Model 111 |
| 32 | Scheavitz-Bytrex Model HFG-2000 |
| 34 | Norwood Model 111 |
| D.E. | Break Wire |
| D.E. + 25 ft | Break Wire |
| D.E. + 50 ft | Break Wire |
| D.E. + 75 ft | Break Wire |
| D.E. + 100 ft | Break Wire |
| D.E. + 125 ft | Break Wire |
| D.E. + 150 ft | Break Wire |

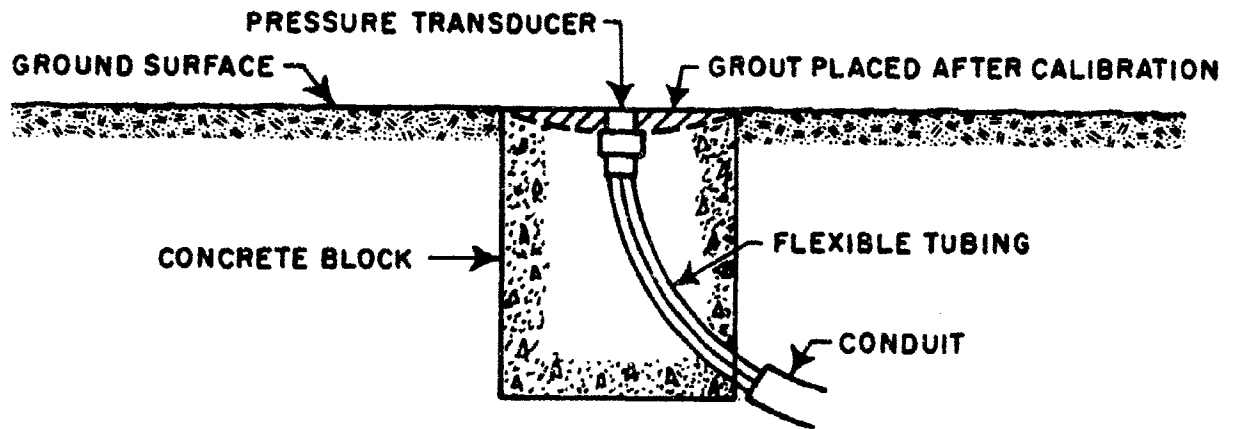
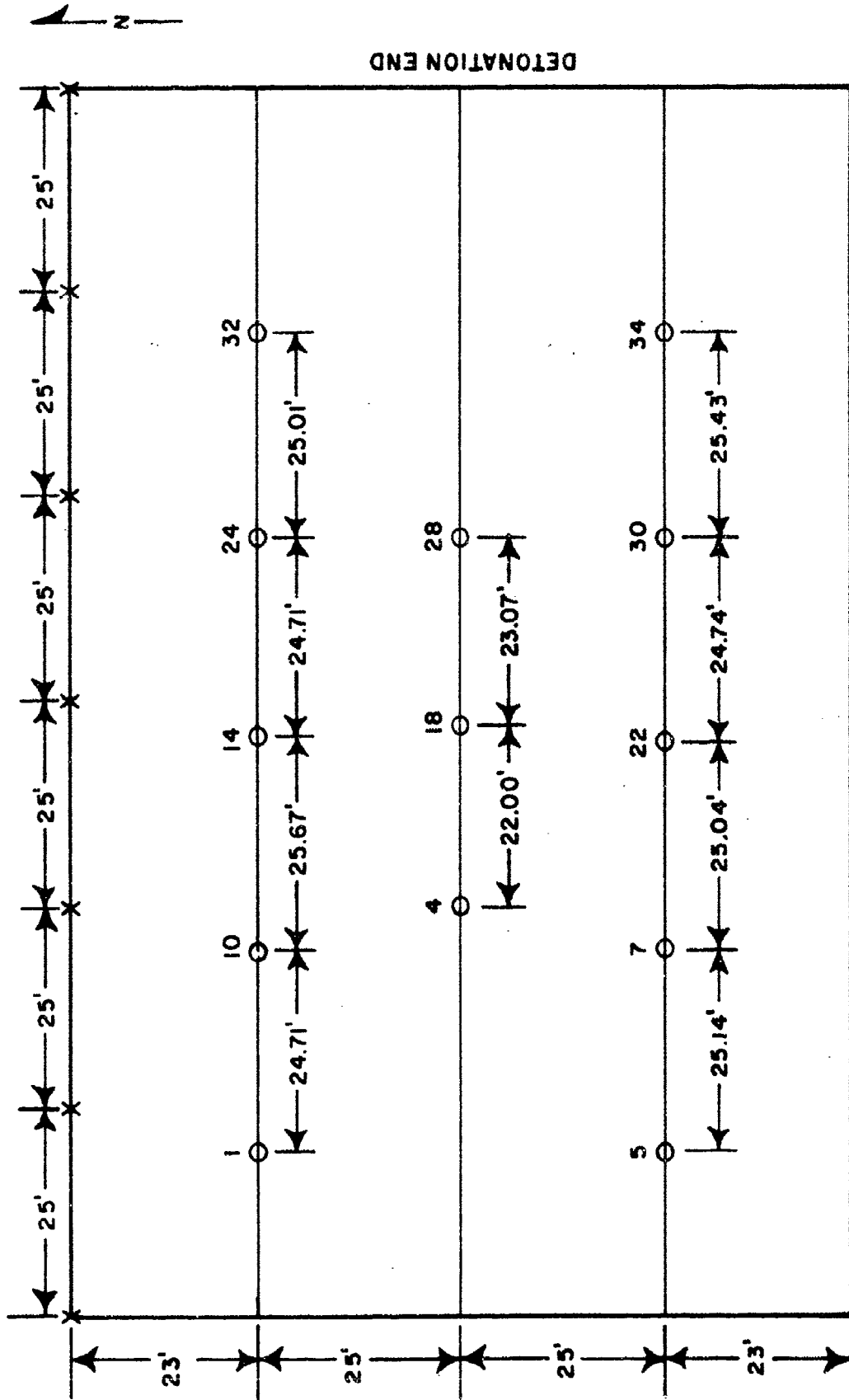


Figure VII-1. Pressure Transducer Mount



KEY: O PRESSURE TRANSDUCER
X BREAK WIRE

Figure VII-2. Instrumentation Locations

SECTION VIII

RESULTS

1. Air Pressure Gages

Nine pressure-time history traces were recorded from the 13 air pressure gages which were installed in the experiment. In addition, three of the channels (18, 22, and 28) contained time-of-arrival data, but pressure-time data could not be recognized or extracted from the excessive amount of noise which was recorded. The cause of this excessive noise has not been determined. The gage at position No. 30 was disconnected before the test because of faulty signal-conditioning equipment.

Appendix B contains the time history records for all of the air pressure gages which recorded usable data. Table VIII-1 is a summary of the shock front time of arrival at each of the gage locations.

Table VIII-1

SHOCK FRONT TIME OF ARRIVAL AT PRESSURE TRANSDUCER LOCATIONS

| <u>Location No.</u> | <u>Time of arrival (msec)</u> |
|-------------------------|-----------------------------------|
| 32 | 5.4 |
| 24 | 10.9 |
| 14 | 15.8 |
| 10 | 20.4 |
| 1 | 24.9 |
| 28 | 10.9 |
| 18 | 16.0 |
| 4 | 19.7 |
| 34 | 5.7 |
| 30 | --- |
| 22 | 15.8 |
| 7 | 20.4 |
| 5 | 25.3 |

2. Break Wires

All seven of the break wires performed satisfactorily and the times of arrival recorded at each location are summarized in table VIII-2.

Table VIII-2

SHOCK FRONT TIME OF ARRIVAL AT BREAK WIRE LOCATIONS

| <u>Location</u> <u>Dist from Detonation End (ft)</u> | <u>Time of Arrival</u> <u>(msec)</u> |
|---------------------------------------------------------|-----------------------------------------|
| Detonation End | 0.0 |
| Detonation End + 25 | 5.4 |
| Detonation End + 50 | 10.8 |
| Detonation End + 75 | 16.1 |
| Detonation End + 100 | 21.2 |
| Detonation End + 125 | 25.9 |
| Detonation End + 150 | 30.3 |

3. Microbarographs

The results obtained from the microbarographs are summarized in table VIII-3.

Table VIII-3

MICROBARAGRAPH RESULTS

| Range (feet) | Peak positive phase overpressure | | Peak negative phase overpressure | | Positive duration (sec) | Total duration (sec) |
|-----------------|-------------------------------------|--------|-------------------------------------|--------|-------------------------------|----------------------------|
| | (microbars) | (psi) | (microbars) | (psi) | | |
| 400 | 8,400 | 0.123 | 4,800 | 0.0705 | 0.20 | 0.53 |
| 800 | 3,900 | 0.0574 | 2,400 | 0.035 | 0.20 | 0.53 |
| 1,200 | 3,360 | 0.0495 | 1,680 | 0.025 | 0.20 | 0.53 |

SECTION IX

DISCUSSION

1. Pressure-Time History

A review of the pressure-time history records presented in appendix B will reveal the presence of many small shocks during the early portion of the record (approximately the first 10 msec). Originally, it was planned to ignore these minor shocks and to wait for thermal equilibrium before defining the peak overpressure. However, the shock portion of the curve represents too much of the impulse to be ignored. Since the soil tends to integrate or smooth out the pressure pulse, it was decided to substitute a smoothed curve for each observed pressure pulse, taking care to preserve impulse. To arrive at this smoothed curve, the early portion of each individual record was divided into a number of equal time increments. A mean pressure value was selected for each time increment such that the impulse was preserved. Finally, a smooth curve was constructed utilizing the mean values, and it was assumed that this fit represented the pressure pulse seen at a particular gage.

Figure IX-1 is a composite pressure-time history curve derived from the individual smoothed curves described above. The peak pressure of the composite curve was determined by averaging all of the peak pressures from the smoothed curves. To determine the wave shape of the composite curve, the smoothed curve representing each pressure-time history was normalized to the average peak pressure. These normalized curves were then averaged together to complete the composite curve.

Three of the pressure records indicated negative pressures at relatively early times. These curves were adjusted by linear base line shifts such that they reached a zero pressure at a time which agreed with the zero pressure from the composite curve.

Some justification exists for the rather complicated derivation of a composite air pressure curve. Figures XIV-2 and XIV-3 compare the pressure-time histories seen at two shallow buried soil stress gages with the composite air pressure curve. The shocks have already decreased in magnitude and the measured stress curve appears to be approaching the shape of the composite curve

2. Shock Front Velocity

Shock front velocities have been computed from the shock front time-of-arrival data and the results have been plotted in figures IX-2 through IX-5, respectively, for the north gage line, central gage line, south gage line and break wires. These plots contain interval velocities as well as average velocities. The distance between gages was measured to the nearest 0.01 foot; however, the physical location of the gages in the test facility was only known to ± 1 foot. A summary of the interval shock front velocities is presented in figure IX-6 along with an average shock front velocity of 5,120 ft/sec. It should be noted that there appears to be an increase in velocity with the distance traveled. The individual values agree with the average value within ± 16 percent. However, the central line of gages represents the largest deviation from the average value in both the plus and minus direction. These points are suspected to reflect surveying errors since their average velocity is exactly 5,120 ft/sec. If these points are disregarded, the individual values agree with the average value within ± 11 percent.

Figure IX-7 is a plot of equal time contours which define the position of the shock front in the test facility. The shock front is essentially plane across the central 50 feet of the test facility. The maximum distance deviation, for a given time, in the central area is 3 feet. This is equivalent to approximately 0.6 msec. There is a definite edge effect along the entire length of the facility. This may be due to the smaller primacord racks which were utilized at the edge positions.

3. End Wall Reflections

When the shock front reaches the end of the facility a reflected shock is formed which travels in a direction opposite to the initial flow and causes an increase in pressure. Table IX-1 contains a summary of the observed results.

Table IX-1

REFLECTION RESULTS

| Gage position no. | Dist from reflection end (ft) | t_r (msec) | P_r (psi) |
|----------------------|----------------------------------|-----------------|----------------|
| 1 | 20 | 9 | 190 |
| 5 | 20 | 9 | 185 |
| 10 | 44.71 | 20 | 80 |
| 4 | 50 | --- | --- |
| 7 | 45.14 | 19 | 70 |

where t_r = time of reflected shock arrival

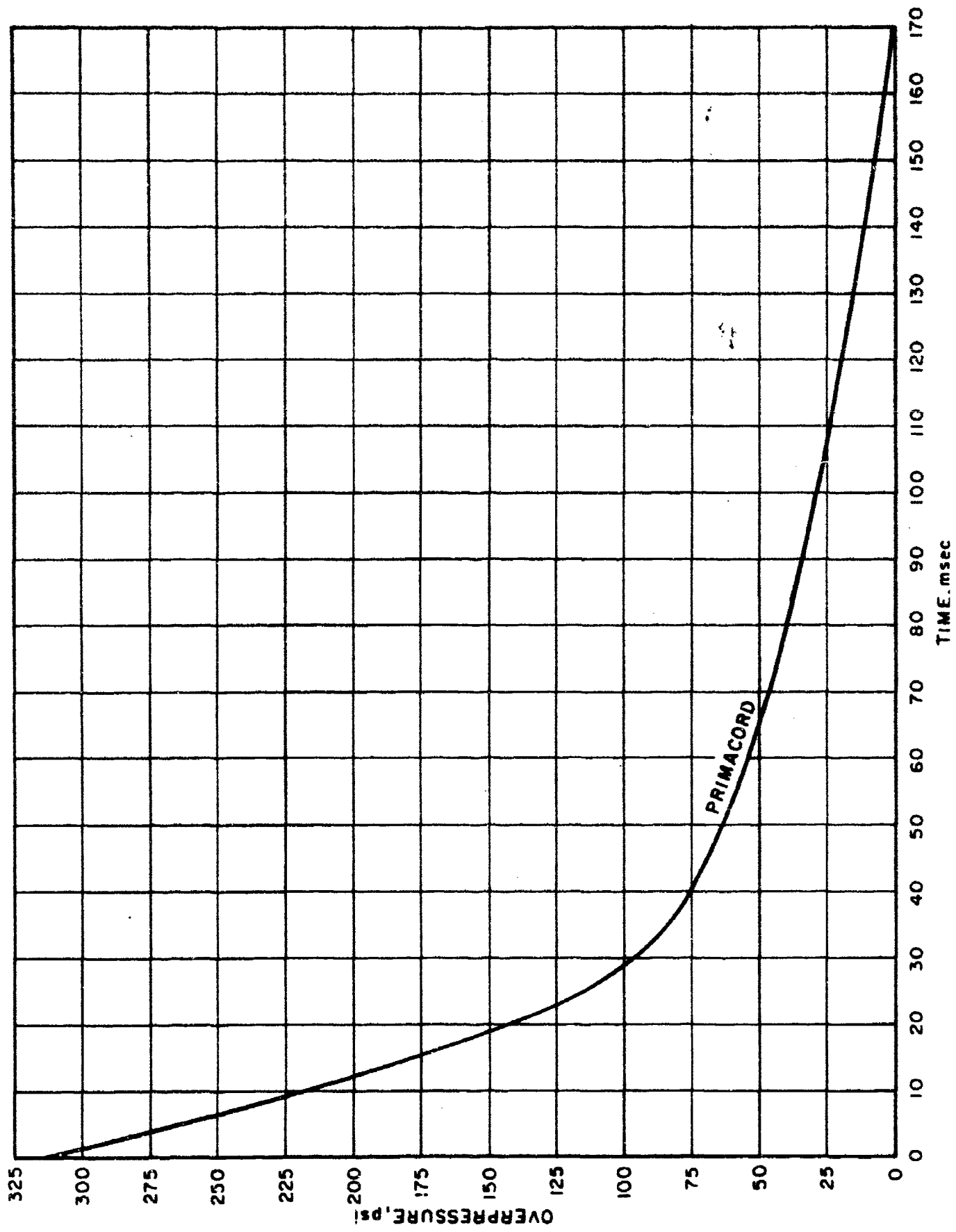
P_r = strength of reflected shock

The reflected shock pressures have been plotted as a function of travel distance in figure IX-8. If a linear fit to the data is assumed, a reflection factor of approximately 2 is obtained at the end wall (reflection factor = incident pressure plus reflected pressure divided by incident pressure). For a shock wave, the reflection factor from a perfectly rigid wall is 6.5. However, the detonation wave is not a true shock and the end wall provides an extremely soft boundary. Figure IX-8 also indicates that the reflected pressure should have died out by the time it has traveled 60 feet. No reflected pressures were observed on the pressure records at 70 feet from the reflection end. The average reflected shock front velocity has been obtained from time-of-arrival data in figure IX-9. The average velocity of 4,000 ft/sec corresponds to a pressure of 200 psi in air, which agrees fairly well with average measured reflected pressures.

4. Shock Pressure Vented to the Atmosphere

In figure IX-10 the air shock which was created by the venting into the atmosphere is compared with an equivalent unconfined hemispherical high explosive detonation with a total charge weight of 3,000 pounds. It can be seen that the Long-Duration High-Explosive Simulation Technique creates an

air shock which is at least an order of magnitude lower in peak overpressure than its equivalent charge weight of high explosives.



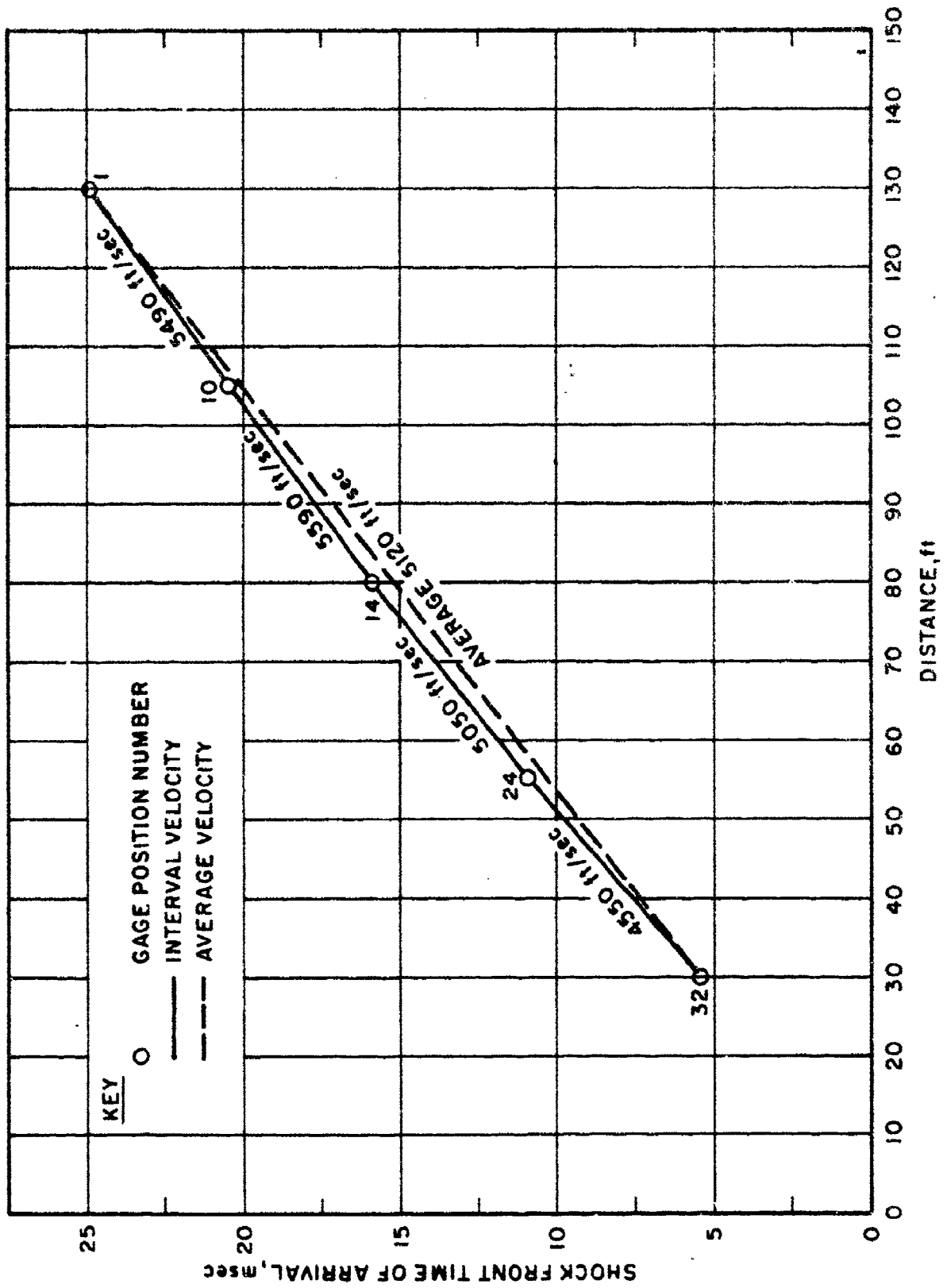


Figure IX-2. Shock Front Velocities--North Gage Line

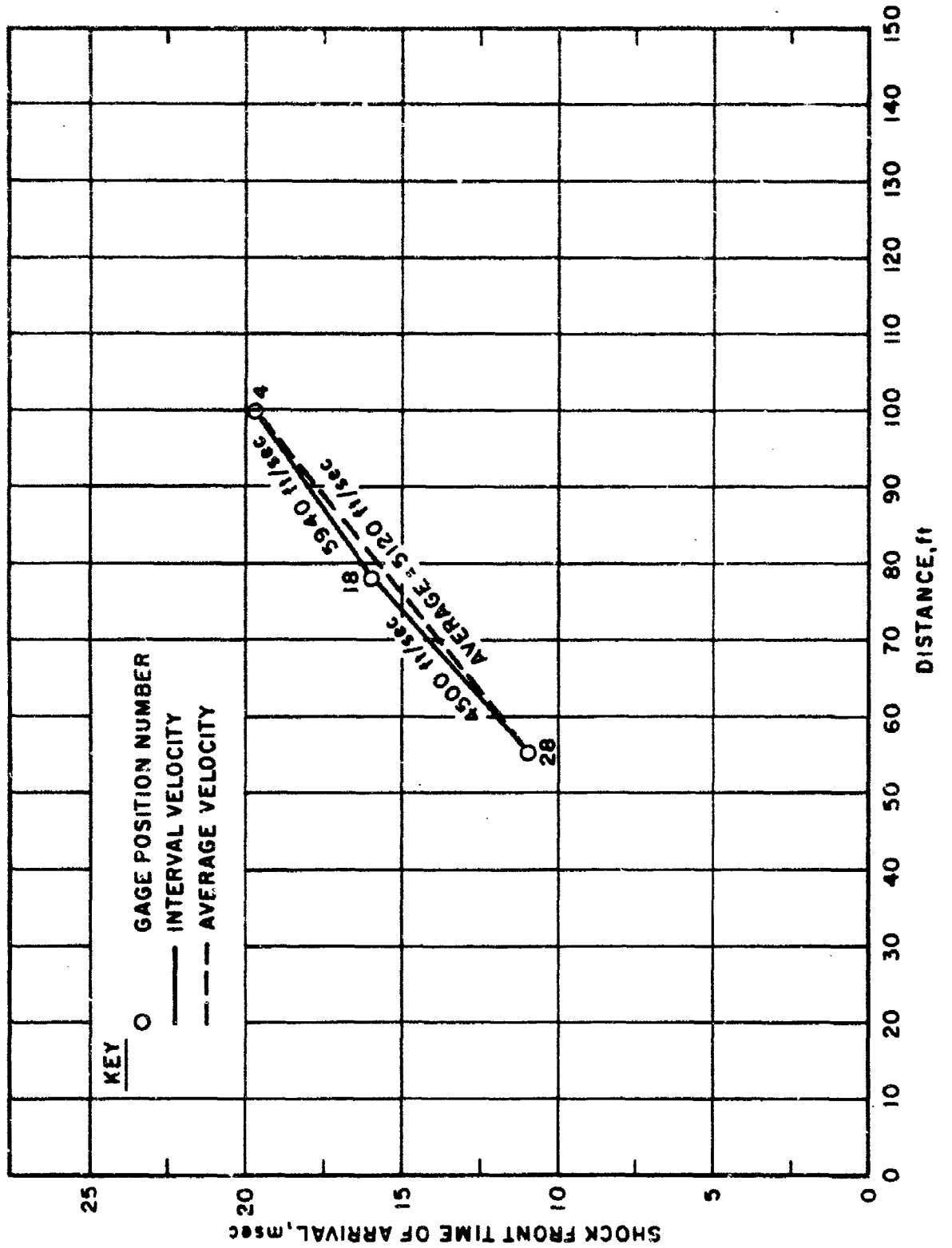


Figure IX-3. Shock Front Velocities--Central Gage Line

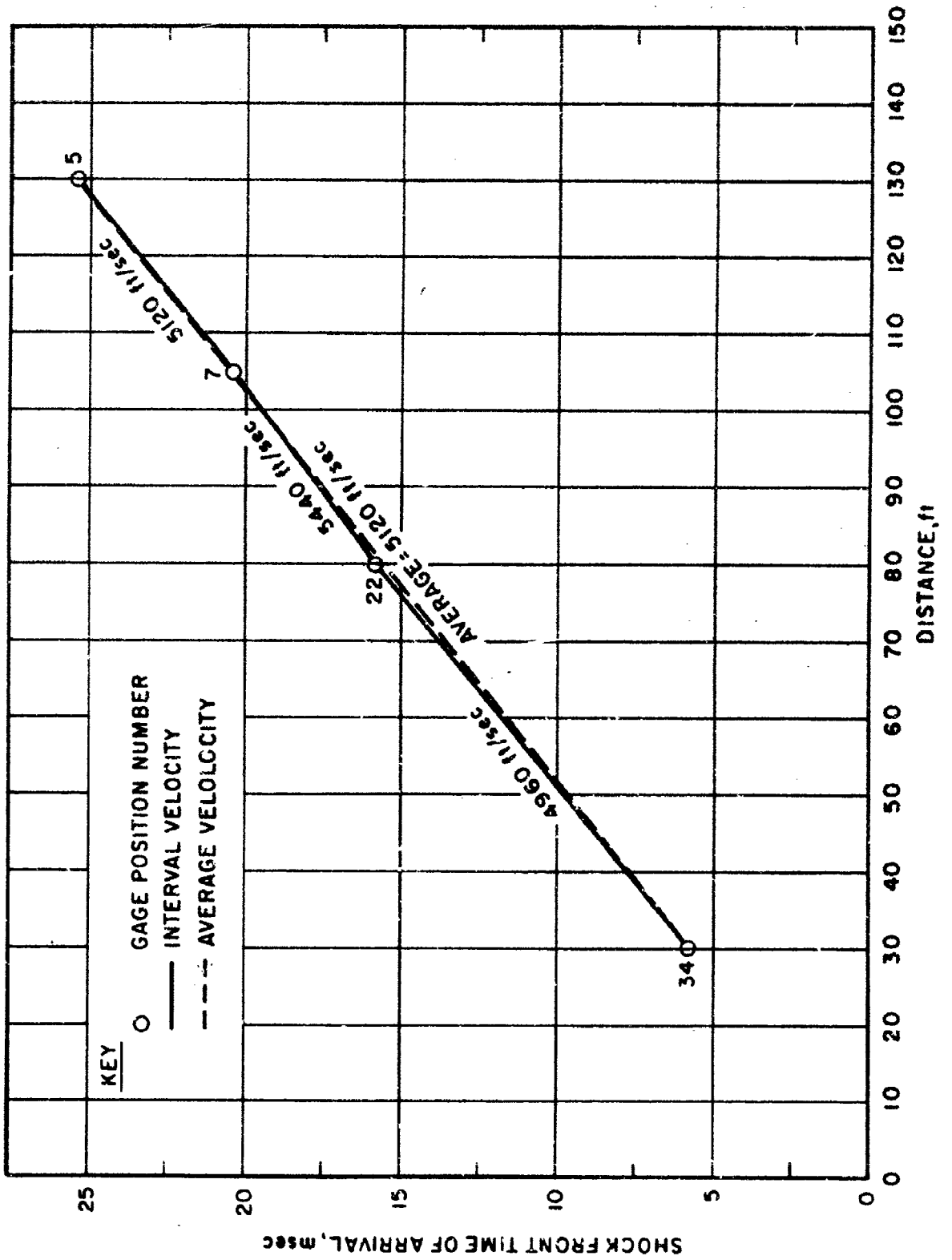
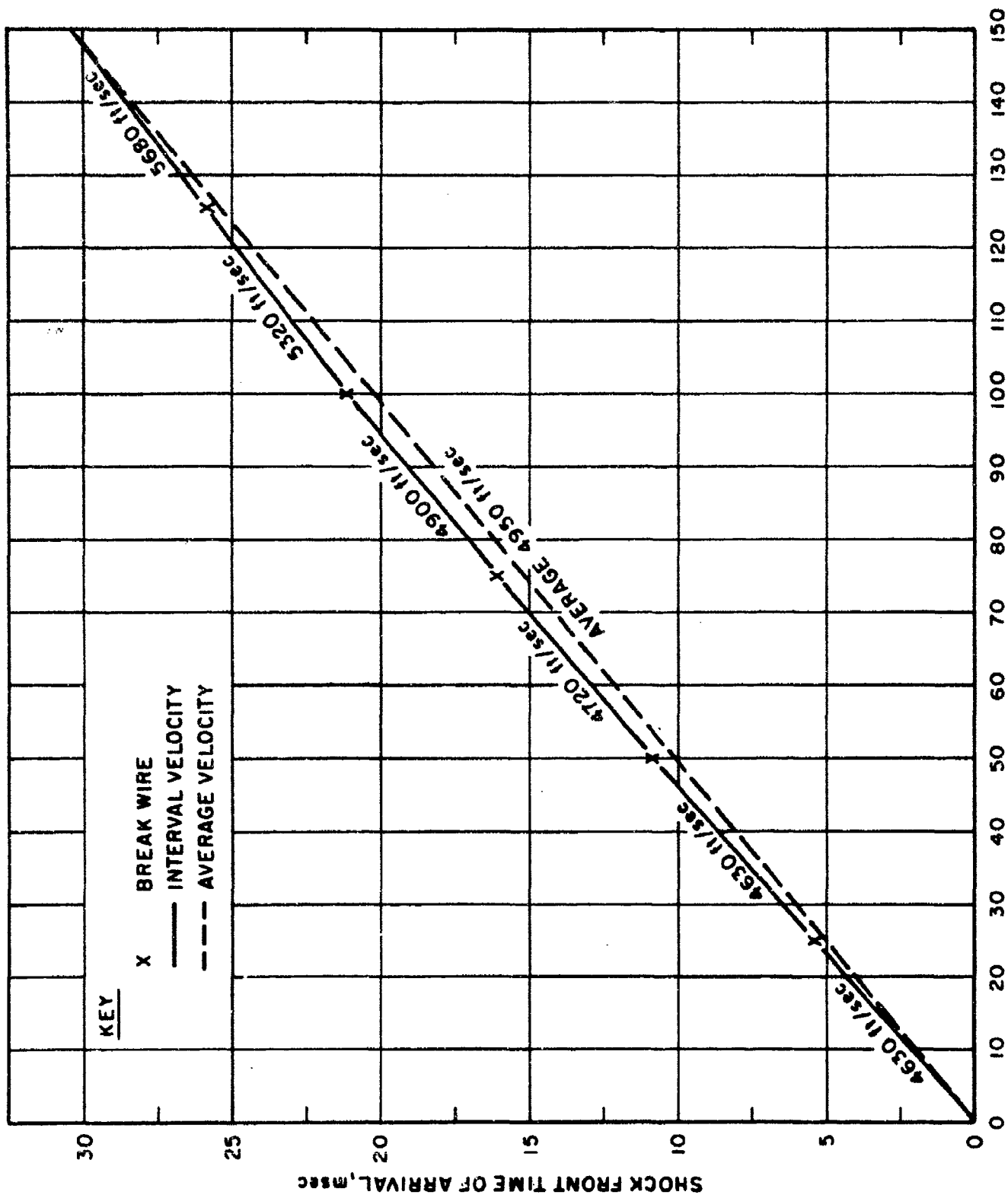


Figure IX-4. Shock Front Velocity--South Gage Line



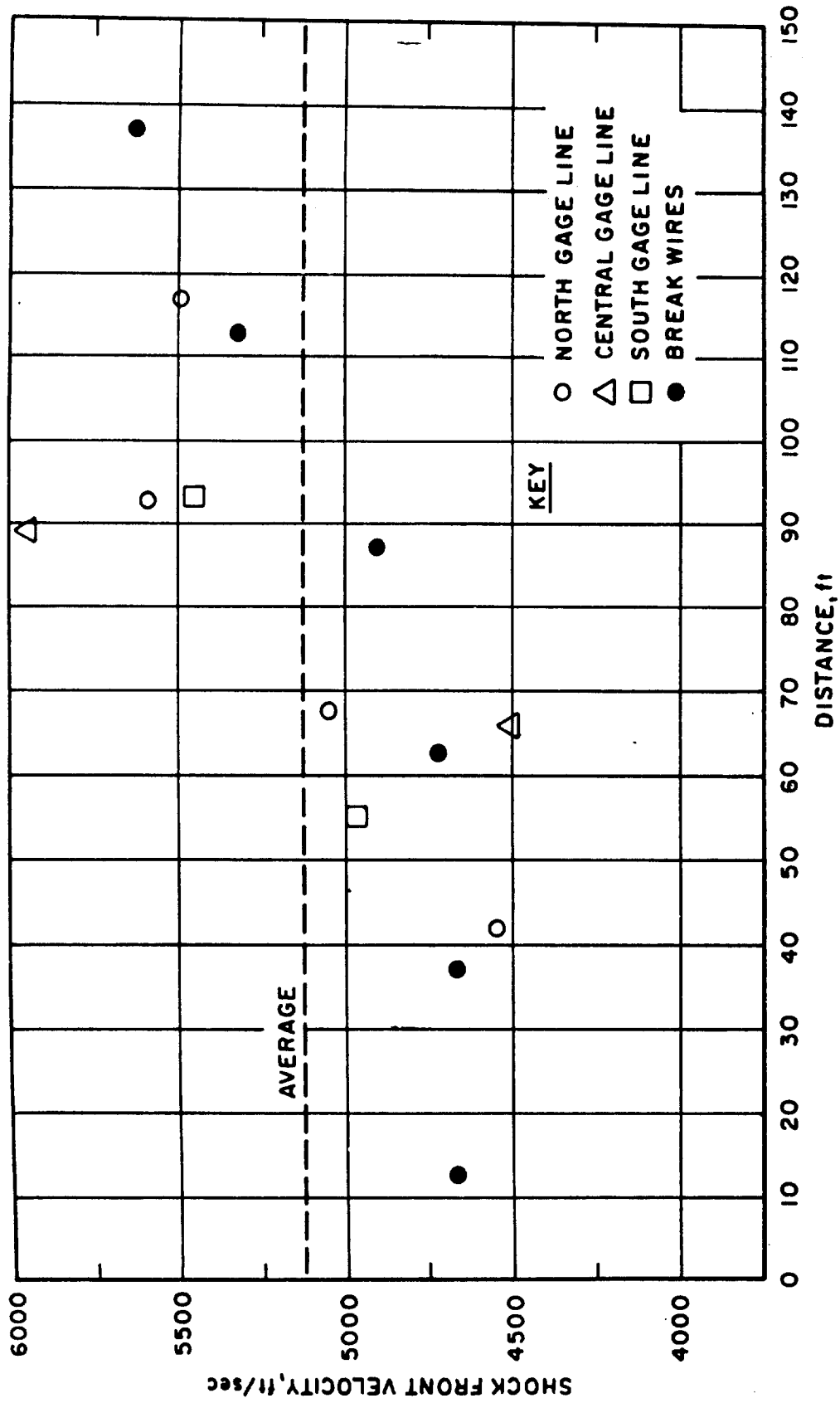


Figure IX-6. Summary of Shock Front Velocities

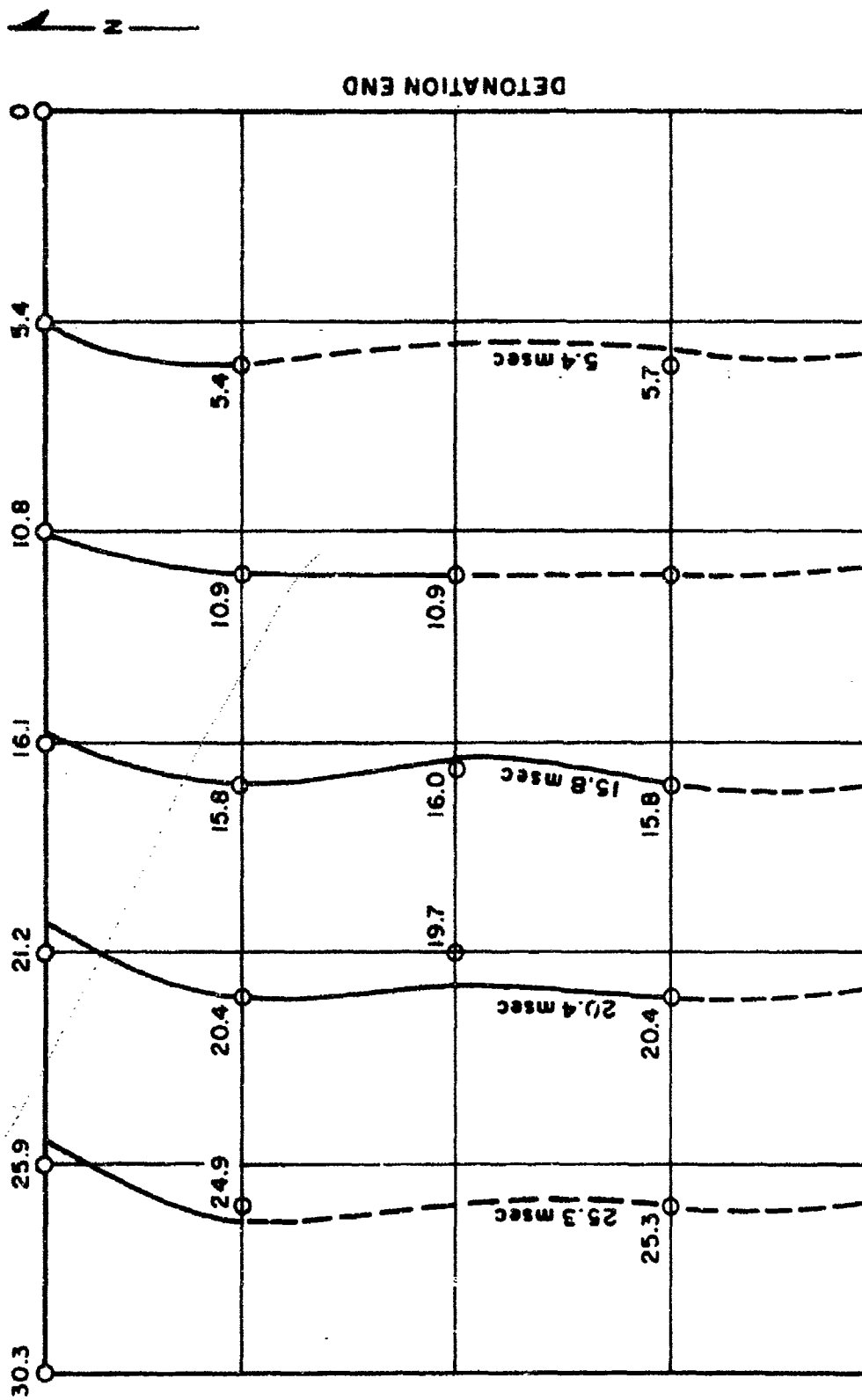


Figure IX-7. Shock Front Positions

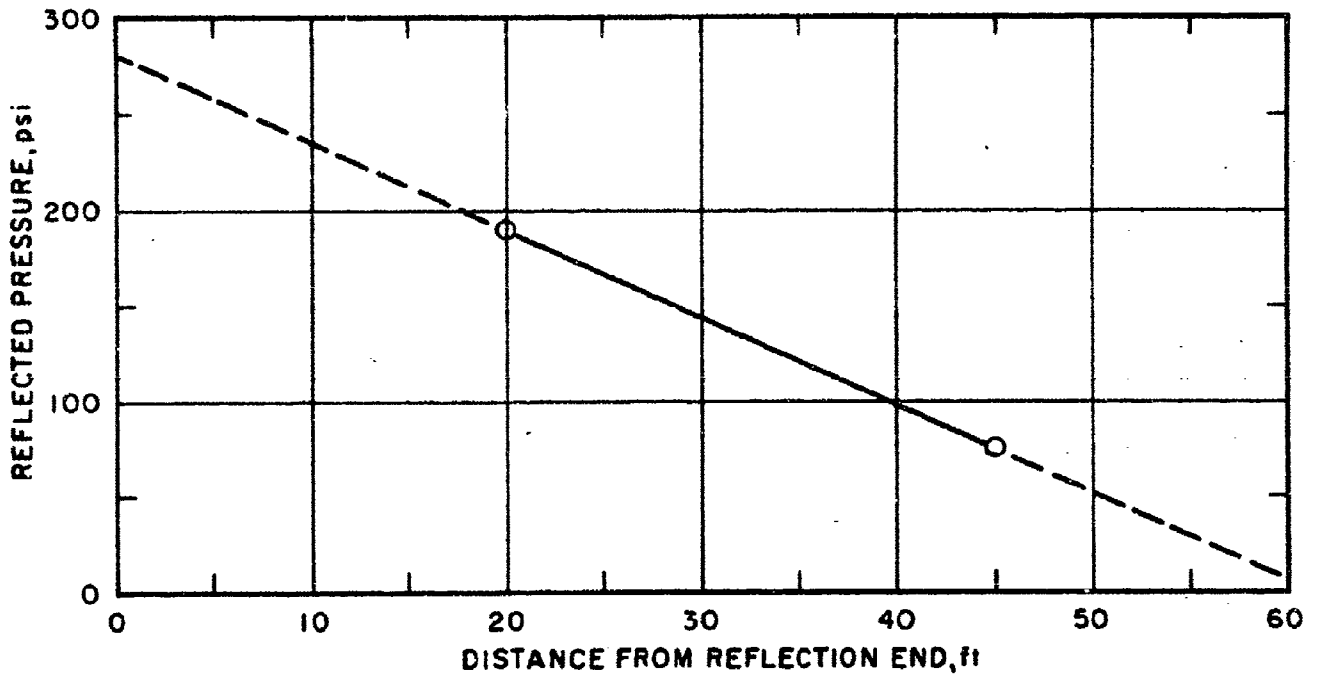


Figure IX-8. Attenuation of Reflected Pressure

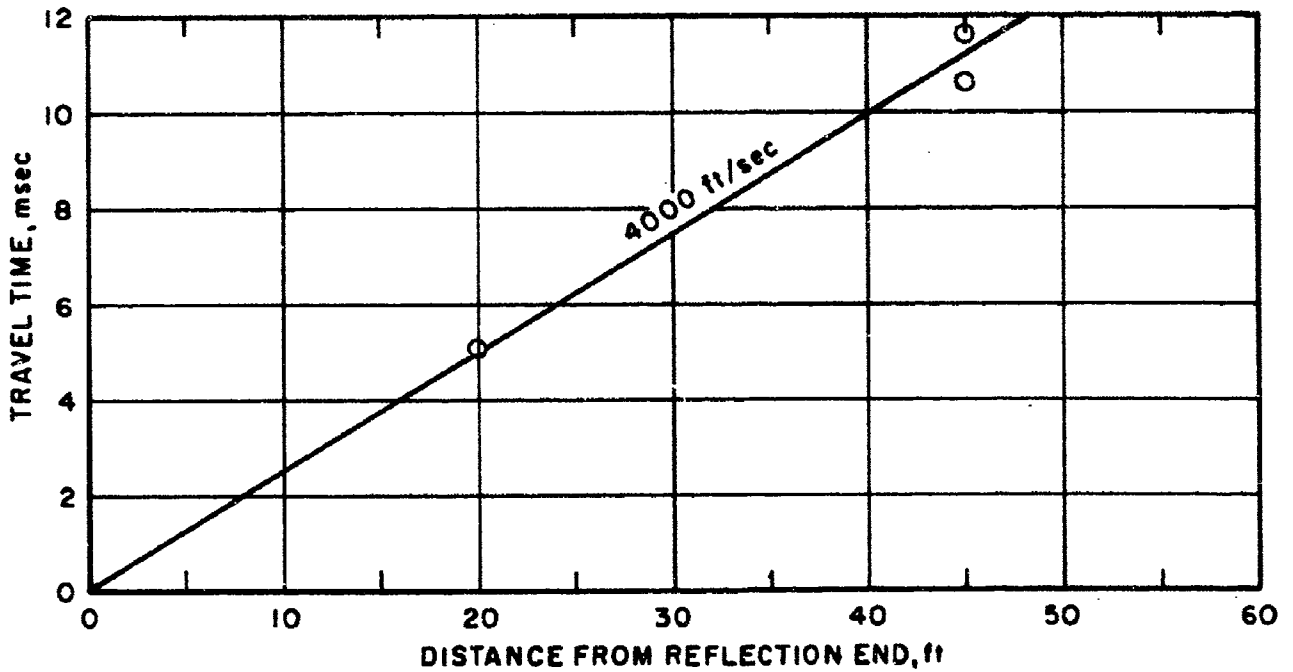
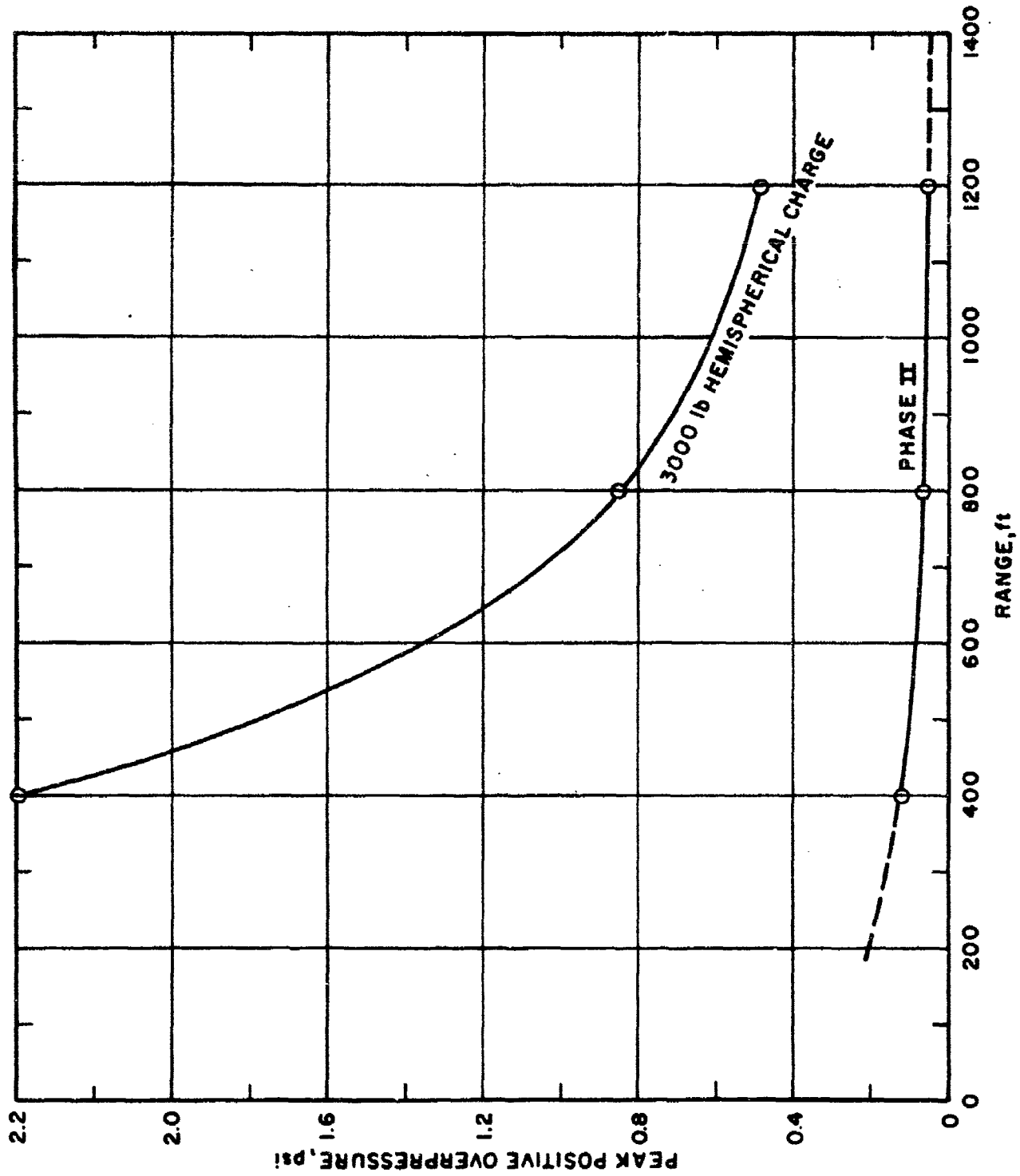


Figure IX-9. Reflected Shock Front Velocity



SECTION X

CONCLUSIONS AND RECOMMENDATIONS

The composite pressure-time history curve given in figure IX-1 defines the air free-field environment which was produced by this experiment. It indicates a peak overpressure of 312 psi, a time to one-half peak pressure of 18.2 msec, and a total duration of 170 msec. The impulse contained under this curve is approximately 10.4 psi-sec.

The shock front velocity produced in this experiment increased with travel distance and ranged from 4,550 ft/sec to 5,680 ft/sec. The average velocity was 5,120 ft/sec \pm 11 percent. The wave front was essentially plane in the central 50-foot portion of the loaded area.

The reflected pressure at the end wall is of the same order or larger than the incident pressure. The reflected pressure attenuates rapidly with distance, and for this experiment it had decayed to zero in 60 to 70 feet of travel.

The air shock which was created in the atmosphere when the experiment vented was an order of magnitude lower than that created by an equivalent weight of high explosives detonated unconfined in a hemispherical charge.

This page intentionally left blank.

PART 3

EARTH FREE FIELD

This page intentionally left blank.

SECTION XI
INTRODUCTION

1. Objectives

The earth free-field measurements were made to determine the response of a known medium to a controlled input, to determine the attenuation of free-field quantities with depth, to provide input data for the structural model, and to provide data for determining the mass of material realistically loaded so that larger follow-on experiments may be appropriately scaled.

2. Background

Earth free-field measurements have been made on numerous nuclear and high-explosive detonations. These data have been utilized to derive a number of empirical prediction techniques as well as to provide check points to verify analytical solutions. Any theory used to predict the motions and stresses induced in the earth from an air-blast loading requires a knowledge of the properties of the soil. Therefore, a comprehensive site exploration program was accomplished to determine the properties of the soil at the test site.

3. Soil Survey

The site exploration program consisted of seismic refraction and uphole velocity surveys, the obtaining of undisturbed samples and the laboratory testing of samples. Laboratory investigations included mechanical analysis, constrained modulus tests, triaxial tests, and moisture content and density determinations.

The results of the seismic survey are summarized in table XI-1 (reference 5). The nature of higher velocity interface detected at 268 feet is unknown but it is probably the surface of an older, denser alluvial material. No higher velocities were detected to a depth of 1,500 to 2,000 feet.

Table XI-1
SEISMIC PROFILE

| <u>Depth (ft)</u> | <u>Seismic velocity (fps)</u> |
|-----------------------|-----------------------------------|
| 0-58 | 1700 |
| 58-268 | 2550 |
| 268-2,000 | 6740 |

The test site consists of layered media ranging from a dense sand to medium gravel with some mixing of clay and caliche. There was no ground water table above 90 feet. The soil profile is shown on figure XI-1 (reference 6). The boring denoted by "NE" was sampled by using 5-inch Shelby tubes to obtain 1-foot undisturbed samples at 5-foot intervals to a depth of approximately 15 feet. The boring denoted by "C" was explored to a depth of 90 feet using 5-inch Shelby tubes sampling at 5-foot intervals. The "SW" boring was examined utilizing a split spoon sampler and standard penetration tool. No undisturbed samples were obtained, but density, moisture content, and soil types were obtained to a depth of 90 feet. The "C" hole is located approximately in the center of the test area.

Figure XI-2 is a summary of the stress-strain curves obtained from the constrained modulus tests. These tests were performed in a modified Karol-Warner Model 354 consolidometer. This apparatus provides a rise time to maximum load of approximately 200 msec and essentially zero lateral strains. The results show composite curves for all the samples tested. The bearing capacity of the surface material was determined from triaxial tests to be 5,000 to 6,000 lbs/ft².

Investigations of various sites in the area resulted in the selection of a borrow pit in the area of the experiment. It was found that the native material could be placed at an average density of 98 lbs/ft³ by conventional earth-moving equipment with no compactive effort.

4. Predictions

The peak vertical stress acting at any depth below the surface of the loaded area was calculated using the approximate method developed by Newmark (reference 7).

This method utilizes influence charts to solve the classic Boussinesq spatial attenuation problem (i.e., a distributed static load applied to the surface of an elastic half-space). Inherent in the method is the assumption that the stresses propagate at an infinite velocity and thus a disturbance at the surface immediately influences the entire body.

The idealized pressure-time curve given in figure I-13 was utilized as the loading function with the smooth curve replaced by many steps of uniform pressure. Each step contained the same impulse as the portion of the curve that it replaced. A time dependent trial and error solution was then performed with the load positioned at various points over the 96 x 150 foot area until the maximum stress at the depth of interest was found. This process was continued until the maximum stress at several depths was found and then the points were connected with a smooth curve.

Figure XI-3 presents the computed theoretical attenuation of maximum stress with depth for the center of the loaded area. The results for the idealized primacord air-blast input and a 1-MT nuclear air-blast input are shown for comparison.

The prediction of peak vertical acceleration as a function of depth is shown in figure XI-4. Reference 7 was used as the basis for these calculations. At the surface the peak acceleration was computed from the formula

$$A_p = 150g \left(\frac{P_{so}}{100} \right) \left(\frac{1000}{C} \right)$$

where

A_p = peak vertical acceleration, g

P_{so} = peak overpressure applied at the surface, psi

and

C = seismic velocity, ft/sec

At depth, the peak accelerations were computed from the formula

$$A_{pz} = 5g \left(\frac{P_{so}}{100} \right) \left(\frac{100}{z} \right) \alpha_z$$

where

A_{pz} = peak vertical acceleration at
depth of interest, g

z = depth of interest, ft

α_z = attenuation factor, figure XI-3

The peak vertical acceleration at a depth of 10 feet was connected to the surface value with a straight line to interpolate between these two values.

The prediction of peak vertical velocity as a function of depth is shown in figure XI-5. References 7 and 8 were used as the basis for these calculations. Reference 7 gives the following equation for computing the peak vertical velocity

$$V_{pz} = 4 \text{ ft/sec} \left(\frac{P_{so}}{100} \right) \left(\frac{1000}{C} \right) \alpha_z$$

where

C = propagation velocity, ft/sec

The variations in results are obtained by using different values for C . The change in seismic velocity at 58 feet, as noted in table XI-1, was not taken into account. The lower range of values is obtained by letting C equal the seismic velocity of 1,700 ft/sec. The upper range of values is obtained by letting C equal a propagation velocity determined from the constrained modulus tests (885 ft/sec). It should be noted that the attenuation with depth is determined by α_z . Reference 8 gives the following equation for computing the peak vertical velocity at a depth of 5 feet.

$$V_{5'} = \frac{75P_{so}}{sC_1} \text{ ft/sec } \pm 20 \text{ percent}$$

where

$V_{5'}$ = peak vertical velocity at a depth
of 5 ft, ft/sec

s = specific gravity

C_1 = $3/4$ of the seismic velocity, ft/sec

This calculation contains an uncertainty of ± 20 and this entire range has been indicated on figure XI-5.

The predicted curve was drawn approximately midway between the range of values obtained from reference 7. It should be noted that the predicted curve also agrees quite well with the value obtained from reference 8 for a depth of 5 feet.

A computer program was available to calculate both relative and total displacements for various depths. This program is patterned after the computational scheme presented in reference 7. Tabulated values of α_z and $P(t)$ are required for each class of problems. In addition, the physical properties of the medium must be supplied. Table XI-2 contains a summary of the physical properties used for this calculation.

Table XI-2

PHYSICAL PROPERTIES FOR DISPLACEMENT CALCULATIONS

| Depth (ft) | Density (lb/ft ³) | Seismic velocity (ft/sec) | Wave peak velocity (ft/sec) | Recovery ratio (%) |
|------------|-------------------------------|---------------------------|-----------------------------|--------------------|
| 0-58 | 110 | 1,700 | 885 | 5 |
| 58-268 | 110 | 2,550 | 1,300 | 100 |
| 268- ∞ | 110 | 6,740 | 3,400 | 100 |

The wave peak velocity is the velocity at which the peak stress propagates; this value should be determined from laboratory tests. For the deeper layers the wave peak velocity was assumed to be approximately one-half of the seismic velocity. The recovery ratio is a measure of the materials nonelasticity. The recovery ratio equals the recovered strain divided by the peak strain or

$$R.R. = \frac{\epsilon_{\text{peak}} - \epsilon_{\text{permanent}}}{\epsilon_{\text{peak}}} = \frac{\epsilon_{\text{recovered}}}{\epsilon_{\text{peak}}}$$

(See figure XI-6.)

Figure XI-7 presents the prediction of total displacements as a function of time for various depths. Figure XI-8 presents the prediction of relative displacements between the surface and various depths as a function of time. It should be noted that the majority of the displacements are predicted to occur in the upper 75 feet of material.

The angle of entry of the stress wave into the ground, α , was computed from the formula

$$\sin \alpha = \frac{C}{U}$$

where

U = air shock velocity, 4,800 ft/sec

The value of α ranges between approximately 10 and 20 degrees depending on whether C equals the seismic velocity or a peak stress propagation velocity.

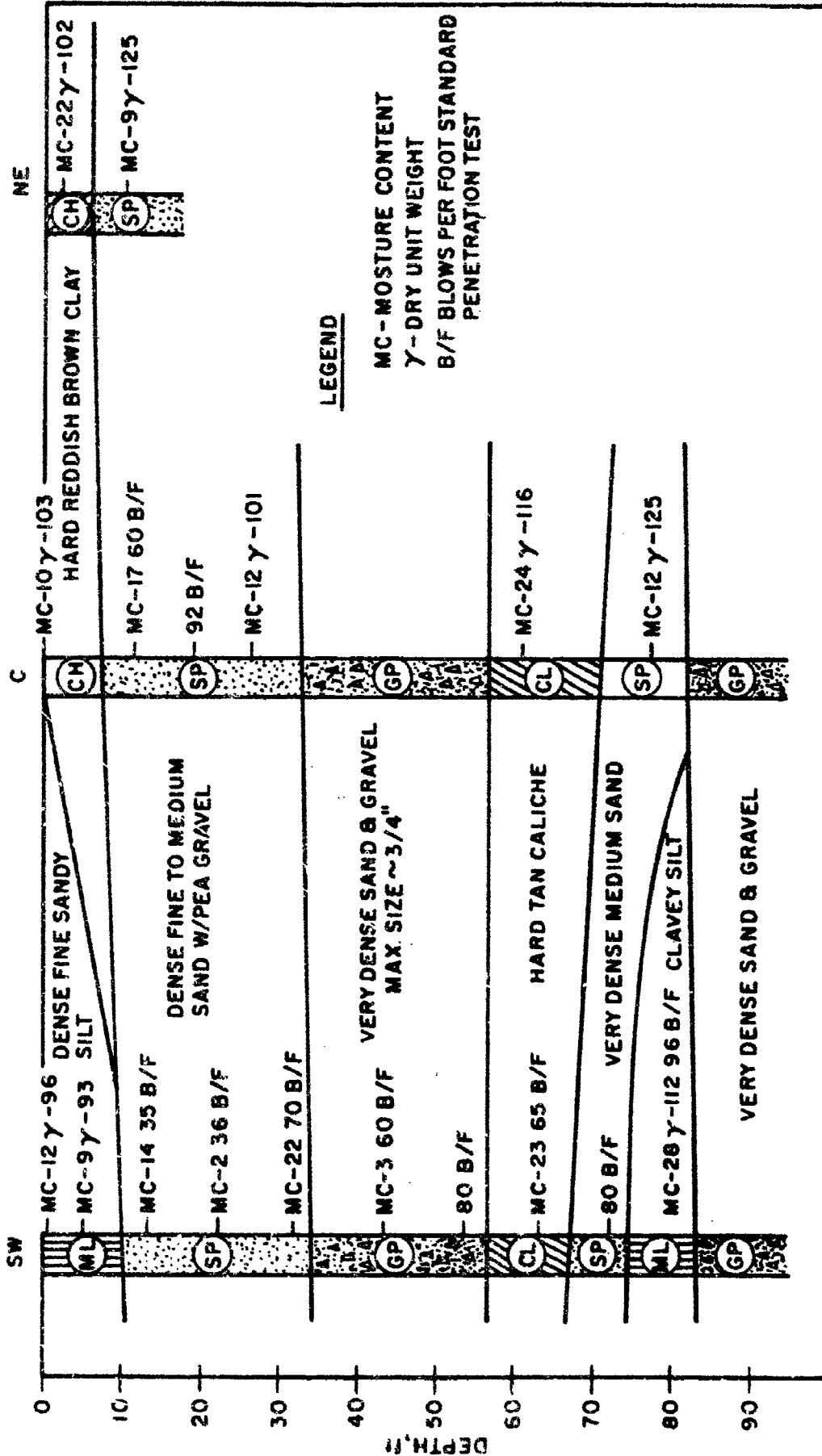


Figure XI-1. Soil Profile

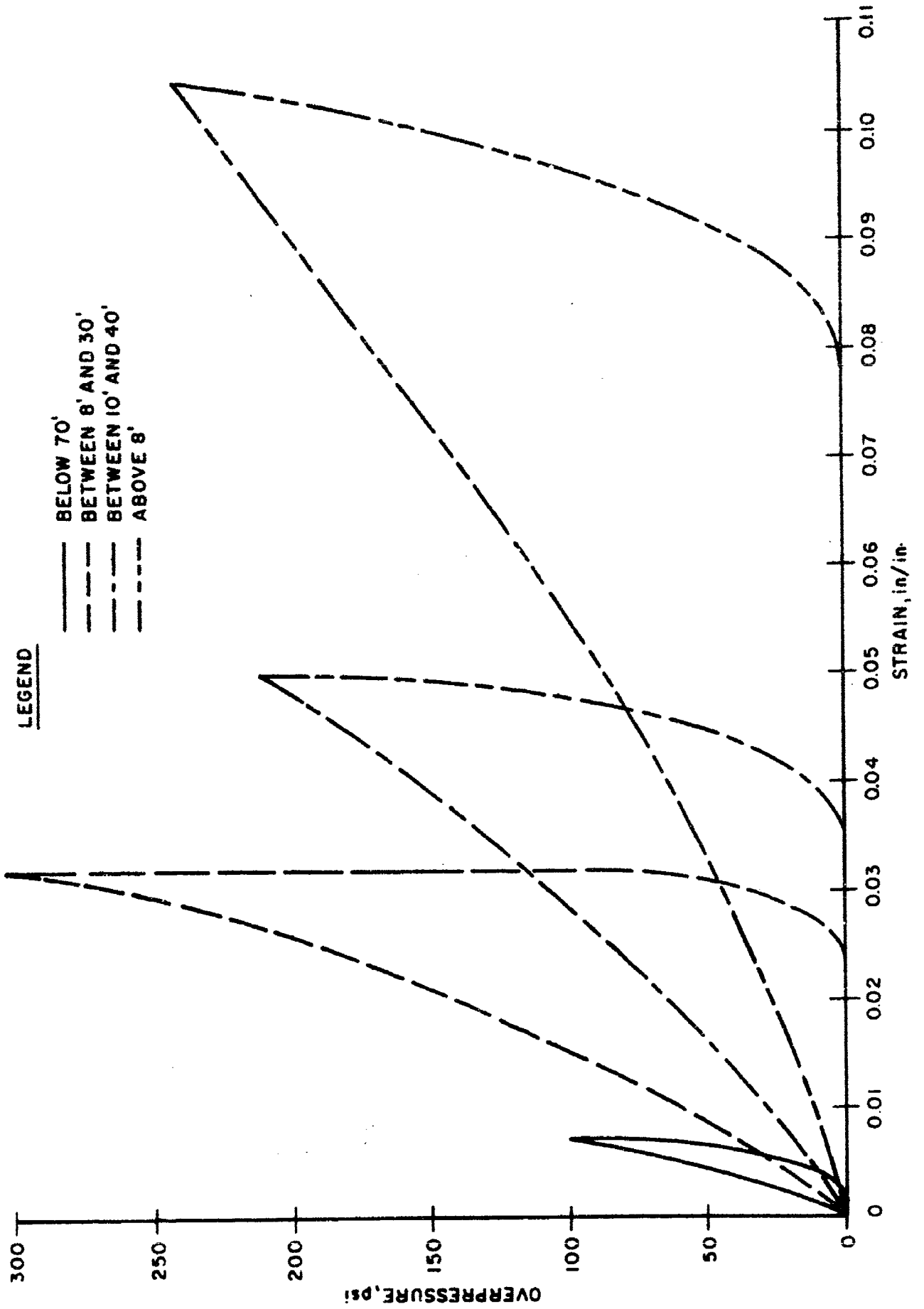


Figure XI-2. Stress-Strain Curves from Constrained Modulus Tests

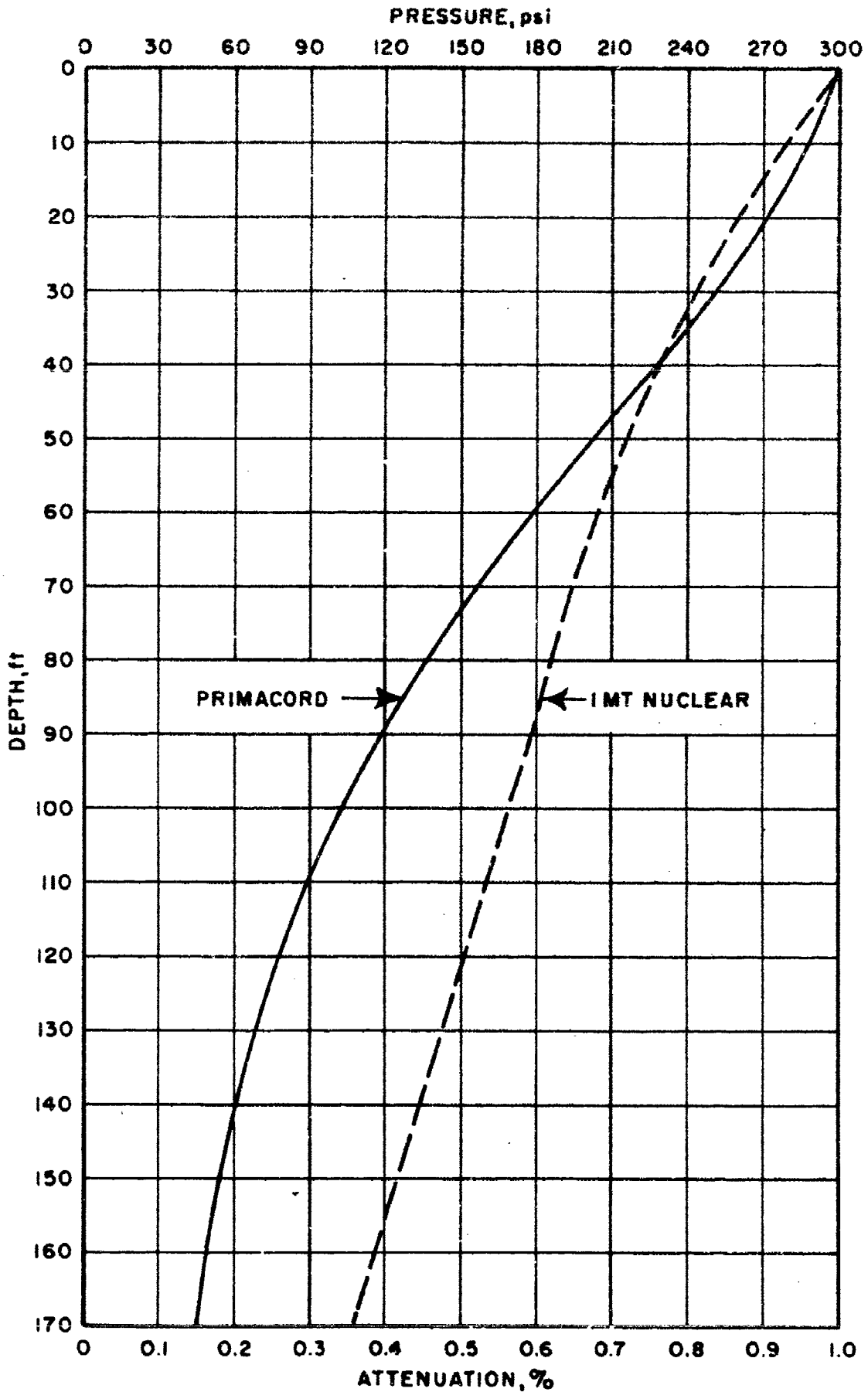


Figure XI-3. Predicted Attenuation Factor

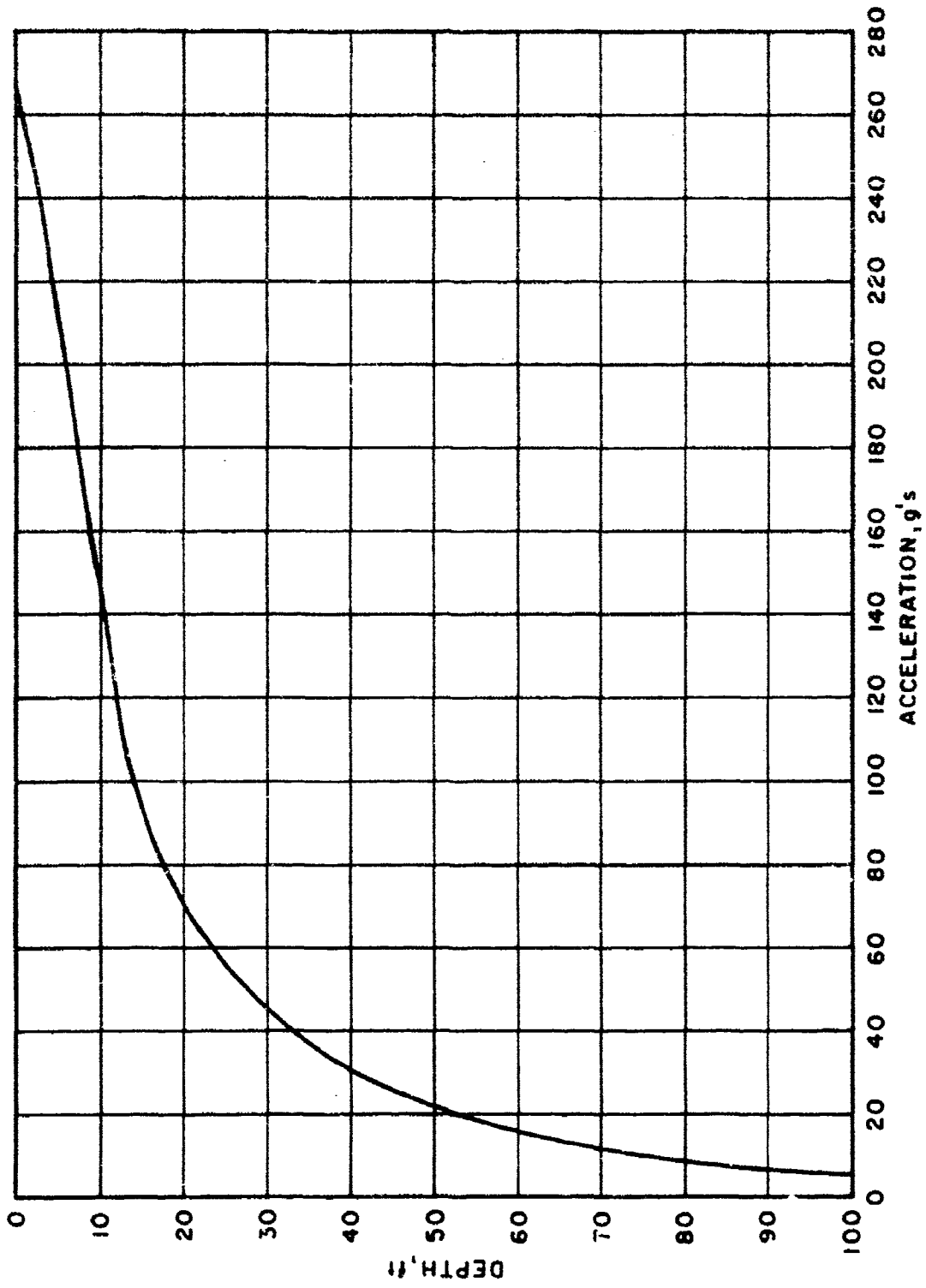


Figure XI-4. Predicted Peak Vertical Accelerations

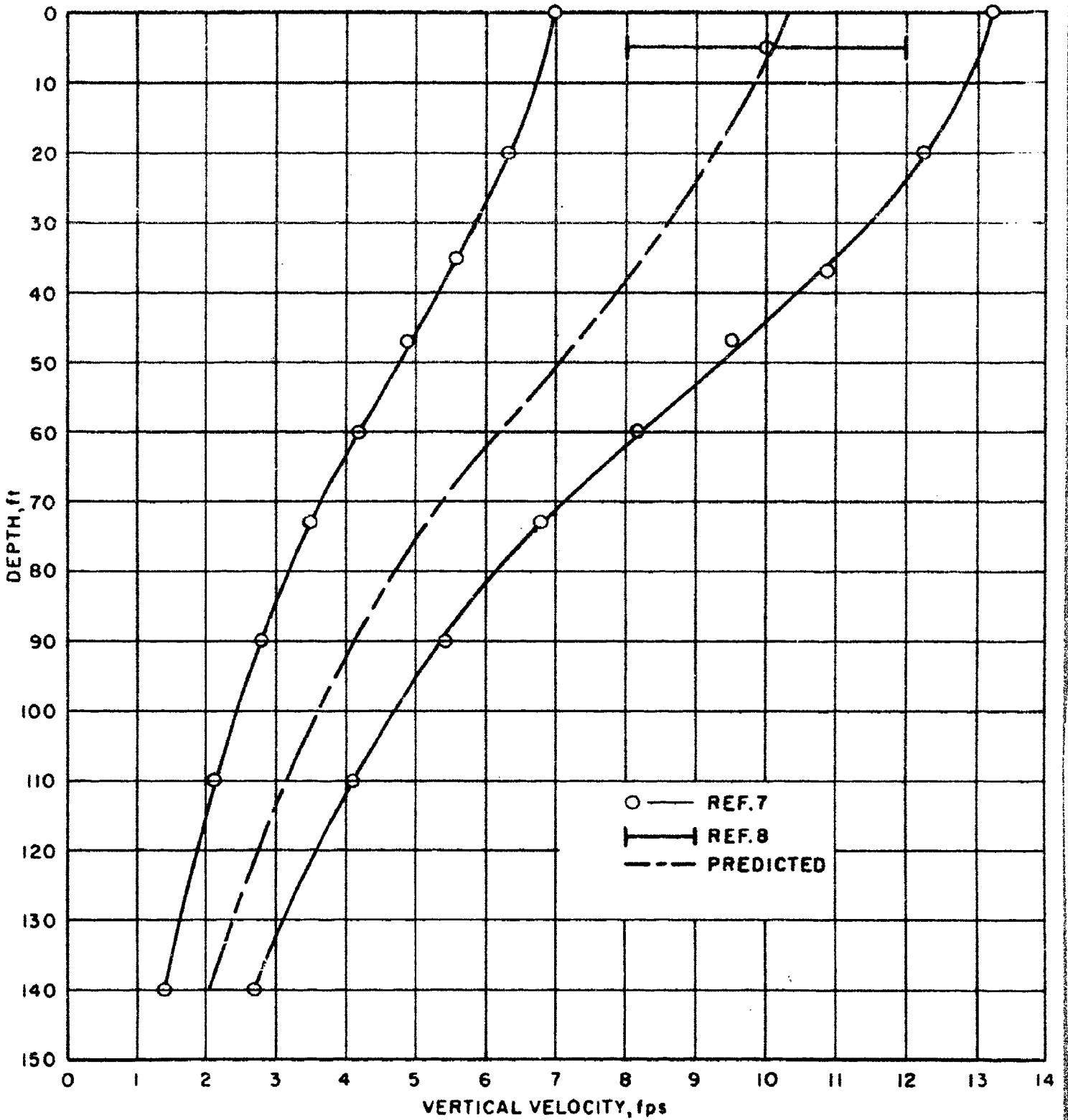


Figure XI-5. Predicted Peak Vertical Velocity

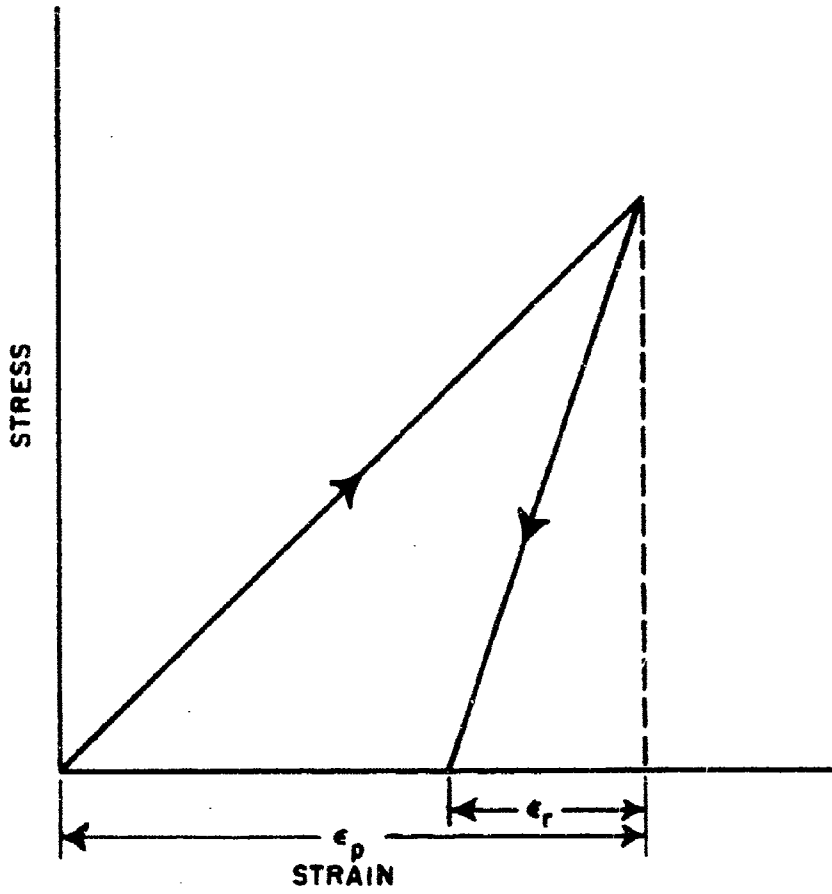


Figure XI-6. Idealized Bilinear Stress-Strain Curve

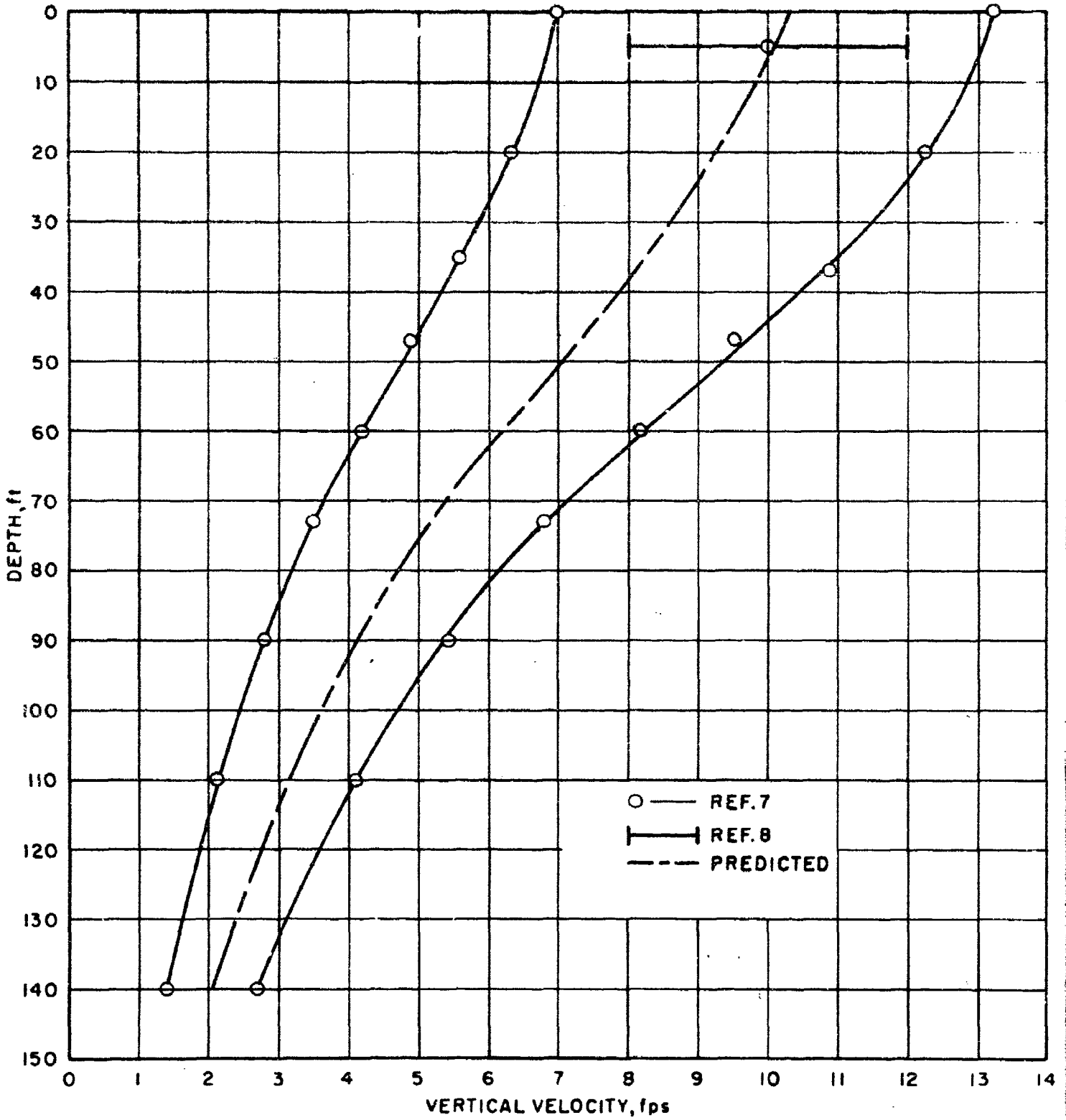


Figure XI-5. Predicted Peak Vertical Velocity

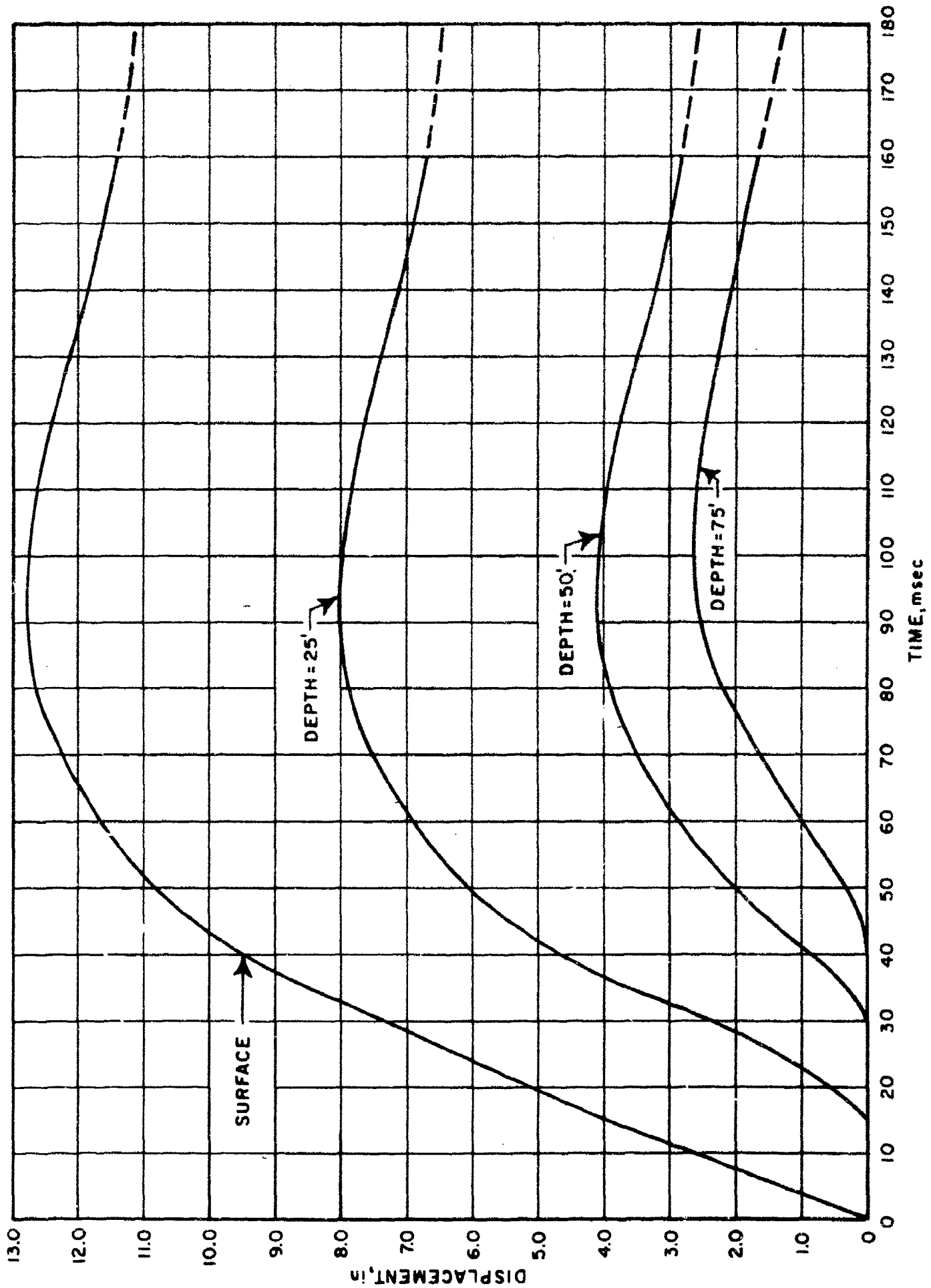


Figure XI-7. Predicted Total Displacements for Various Depths

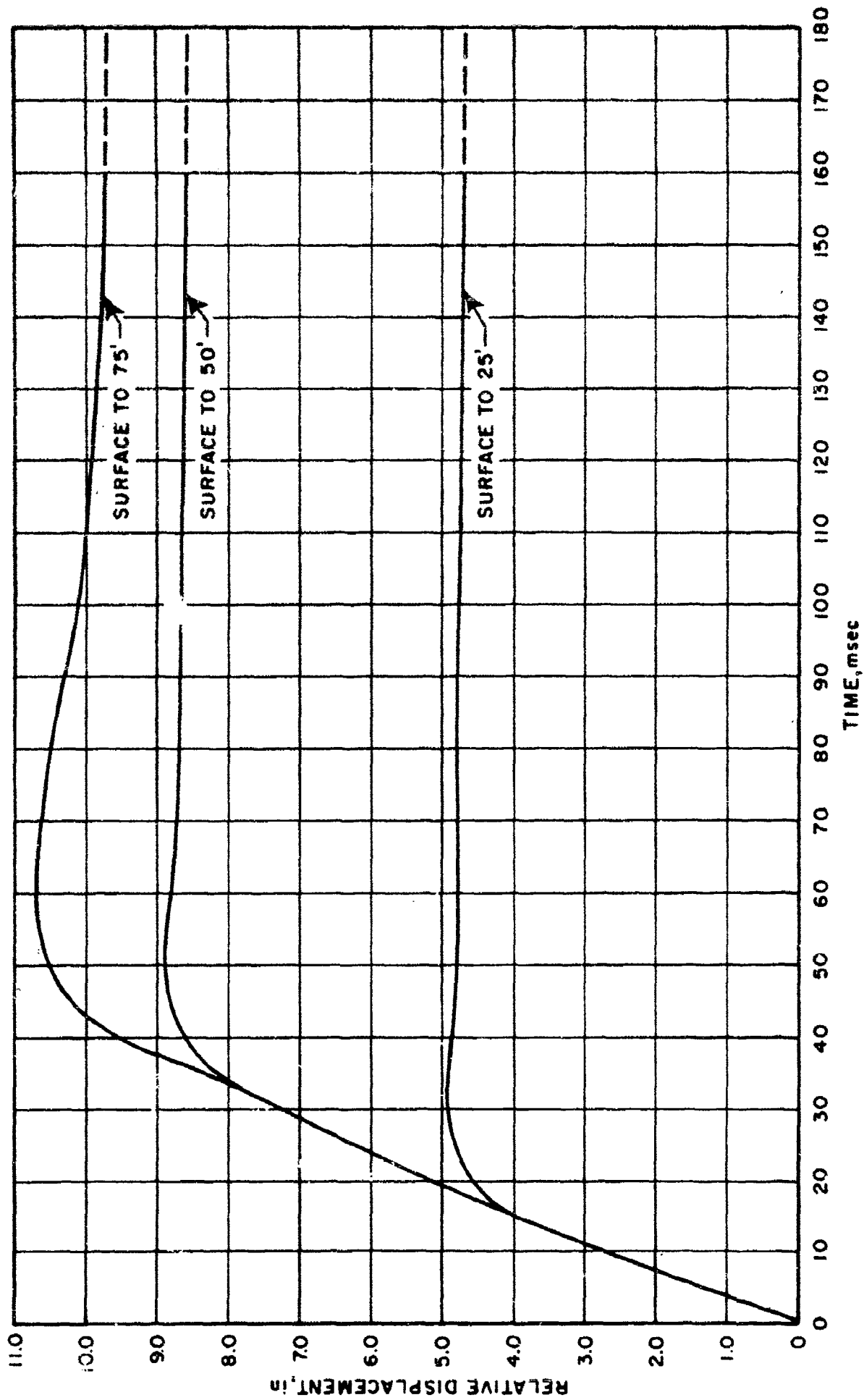


Figure XI-8. Predicted Relative Displacements Between Surface and Various Depths

SECTION XII

PROCEDURE

1. Instrumentation

The instrumentation used in this experiment was selected to be compatible with the recording equipment available at the Air Force Weapons Laboratory. Piezoelectric devices were avoided because of difficulties with long lines and with moisture. Further, because of the long duration of the loading pulse in the experiment, it was felt that piezoelectric concepts would not give sufficient static response characteristics. Wherever possible, balanced full-bridge transducers were used. DC signal conditioning equipment was preferred over carrier systems.

a. Velocity Gages

The primary earth free-field measurement in this experiment was vertical particle velocity at various depths. The velocity gage developed by the Sandia Corporation was used to observe this motion. This gage is a 3-kc carrier-driven device using a pendulum blade moving through a viscous damping fluid to provide the velocity measurement. The gage was encased in an exterior aluminum shell to protect it from the soil stress environment. Figure XII-1 shows the velocity gage and protective cover. Calibration was accomplished in the laboratory by displacing the blade pendulum from its zero position with a magnet and then letting the 1-g gravitational force return the pendulum to its zero position, thus producing a velocity versus electrical output curve.

b. Accelerometers

The Statham Model A69TC fluid damped accelerometer was used to measure vertical accelerations in the earth free field at various depths. This gage was selected because of its high frequency response. The accelerometer was sealed in a waterproof aluminum cup to protect it from moisture and soil stress. The void space inside the aluminum cup was filled with dry Ottawa sand to improve the density match of the accelerometer with the soil. Figure XII-2 shows the accelerometer and protective cover.

The accelerometers were calibrated in the laboratory on a centrifuge prior to packaging for placement in the ground.

c. Soil Stress Gages

A newly developed soil stress gage was used to measure the vertical stress in the soil at various depths. This gage, developed at the Air Force Shock Tube Facility, utilizes semiconductor strain gages to measure the load applied to a small aluminum cylinder. The gage was calibrated with static air pressure. This method of calibration has shown excellent agreement with results when the gage is placed in a dense (112-113 lbs/ft³) Ottawa sand and subjected to a static load. No dynamic results are available. Figure XII-3 shows the soil stress gage.

d. Long Span Displacement Gage

A long span displacement gage was used to measure the relative displacement between the surface and various depths. This gage was developed and has been previously used by the Sandia Corporation. The device consists of a long wire connected to concrete deadmen at various depths in a drill hole. The wire is isolated from the soil by flexible metal tubing. The upper end of the wire is connected to a spring-loaded reel whose axle is connected to a rotary potentiometer. This reel is attached to the interior surface of a cylindrical concrete structure near the surface of the ground. As the surface is depressed, the reel moves downward and the rotation of the potentiometer gives an electrical signal proportional to the deflection. Figure XII-4 shows the long span displacement gage mounted on its calibration device.

e. Time of Arrival System

A modified version of a previously developed time-of-arrival system was used to monitor the movement of the pressure pulse front through the earth. The system consisted of 100 omnidirectional "ball switches" positioned in a three-dimensional array in the ground. As the pressure pulse passes, the switch is moved and gives a switch closure. These switches are connected to a remote console where the switch closure triggers a multivibrator which momentarily lights a small neon light. A high-speed camera photographs the light bank to give a record of the switch closures as a function of time.

f. Slope-Indicator Gage

This installation was used to measure the permanent vertical and horizontal displacements and the vertical transient displacement from the ground surface to a depth of 50 feet. The gage consists of sections of extruded aluminum casing, 2 feet long and 3 inches in diameter with instrument grooves 90° apart, joined together with 12-inch aluminum couplings. The couplings permit relative vertical movement between the segments and form a 50-foot-long composite casing. A first-order survey was performed pre- and post-shot to determine the absolute motion of the top of the casing. The change in inclination of the casing and the vertical movement of the segments relative to the top are measured with an inclinometer or slope indicator instrument and depth probe lowered down the inside of the casing in the instrument grooves. These measurements were made pre- and post-shot; the difference between the two sets of readings represents the permanent horizontal and vertical movement of the casing.

In an attempt to measure vertical transient displacements, a 50-foot section of continuous blued aluminum tubing 2 1/2 inches in diameter was inserted inside the outer casing and secured to the bottom. This tubing was installed after the initial set of inclinometer and depth probe measurements had been made. Spring-loaded hinges with a scratch point were affixed to the inside of each coupling on the outside casing and were held open with a continuous length of piano wire. After the inside blued tubing was installed, the piano wire was withdrawn, allowing the hinges with their scribes to snap against the blued tubing. Figures XII-5, XII-6, and XII-7 illustrate the slope indicator instrument and the depth probe.

2. Gage Placement

With the exception of three near-surface soil stress gages, all free-field soil transducers were placed in 8-inch diameter drill holes at various depths ranging from 1 foot to 80 feet depth of burial. The holes were drilled using a special drilling mud which formed a starch liner around the interior surface of the holes. This liner added virtually no strength, but prevented water from penetrating into the surrounding soil and provided enough stability to the loose granular material to keep the holes open until the instrumentation was placed.

Each transducer was arranged on its cable so as to be properly oriented when it was lowered into the drill hole. Short sections of copper tubing were installed over the soil stress gage cables to ensure vertical alignment. In addition, a light was lowered into the hole immediately following the gage to permit visual inspection of the positioning of the gage. After the placement of each gage, the hole was filled to the next level with a dry native sand. A wire-screen box was placed over the top of the hole to provide a uniform method of raining the sand into the hole. This method gave a density of backfill material very nearly equal to that of the surrounding soil. The three near-surface soil stress gages were placed in hand-dug holes. The gage holes were backfilled with a native sand.

During placement, each gage was connected to its respective signal conditioning equipment. All gages were monitored for operation and balance to ensure their proper functioning.

The slope indicator casing was installed in a 9-inch-diameter drill hole and backfilled with a dry native sand. The sand backfill was compacted with a pneumatic vibrator to ensure that the casing would closely follow the motion of the surrounding soil.

3. Gage Locations

Figure XII-8 is a plan view of the test area showing the location of all of the earth free-field instrumentation. It will be noted that each position containing active instrumentation has been assigned a location number. The location number, gage type and depth of burial have been combined into a coding system which is illustrated in table XII-1.

Table XII-1

INSTRUMENTATION CODING SYSTEM

| <u>Code</u> | <u>Description</u> |
|-------------|--------------------------------------------------|
| 19D-75 | Hole 19 - Long Span Displacement - 75 ft depth |
| 21S-5 | Hole 21 - Soil Stress Gage - 5 ft depth |
| 25V-1 | Hole 25 - Velocity Gage - 1 ft depth |
| 12A-70 | Hole 12 - Accelerometer - 70 ft depth |
| 8S-g | Hole 8 - Soil Stress Gage - near surface (3 in.) |
| 6T-20 | Hole 6 - Time of Arrival - 20 ft depth |

Figure XII-9 is a cross section of the typical instrumentation installation. Hole 21 contained accelerometers, velocity gages, and soil stress gages. Holes 12 and 25 were identical to hole 21 with the exception that all of the soil stress gage locations were deleted. The time-of-arrival system was normally installed in either a 25- or 50-foot deep hole as illustrated in figure XII-9. The three near surface (3 inches deep) soil stress gages were installed at locations 8, 11, and 16. The long span displacement gage had three depths: 25 feet, 50 feet, and 75 feet. All of the electronic instrumentation, with the exception of the time-of-arrival system, responded to only the vertical component of the input.

Table XII-2 contains a complete earth free-field instrumentation listing.

Table XII-2
INSTRUMENTATION LISTING

| <u>Hole no.</u> | <u>Gage type</u> | <u>Depths (ft)</u> |
|-----------------|------------------------|----------------------------------|
| 2 | Time of Arrival | 5,10,15,20,25 |
| 3 | Time of Arrival | 5,10,15,20,25 |
| 6 | Time of Arrival | 1,5,10,15,20,25 |
| 8 | Soil Stress | 0.25 |
| 9 | Time of Arrival | 5,10,15,20,25, 30,35,40,45,50 |
| 11 | Soil Stress | 0.25 |
| 12 | Velocity | 1,20,40,60,80 |
| 12 | Accelerometer | 10,30,50,70 |
| 13 | Time of Arrival | 5,10,15,20,25, 30,35,40,45 |
| 15 | Time of Arrival | 5,10,15,20,25, 30,35,40,45 |
| 16 | Soil Stress | 0.25 |
| 17 | Time of Arrival | 5,10,15,20,25 |
| 19 | Long Span Displacement | 25,50,75 |
| 19 | Accelerometer | 75 |
| 20 | Time of Arrival | 5,10,15,20,25 |
| 21 | Velocity | 1,20,40,60,80 |
| 21 | Accelerometer | 10,30,50,70 |

Table XII-2 (cont'd)

| <u>Hole no.</u> | <u>Gage type</u> | <u>Depths (ft)</u> |
|-----------------|------------------|------------------------------------|
| 21 | Soil Stress | 5,15,25,35, 45,55,65 |
| 23 | Time of Arrival | 1,5,10,15,20,25, 30,35,40,45,50 |
| 25 | Velocity | 1,20,40,60,80 |
| 25 | Accelerometer | 10,30,50,70 |
| 26 | Time of Arrival | 5,10,15,20,25,30, 35,40,45 |
| 29 | Time of Arrival | 5,10,15,20,25 |
| 31 | Time of Arrival | 1,5,10,15,20,25 30,35,40,45 |
| 33 | Time of Arrival | 5,10,15,20,25 |
| 35 | Time of Arrival | 1,5,10,15,20,25 |

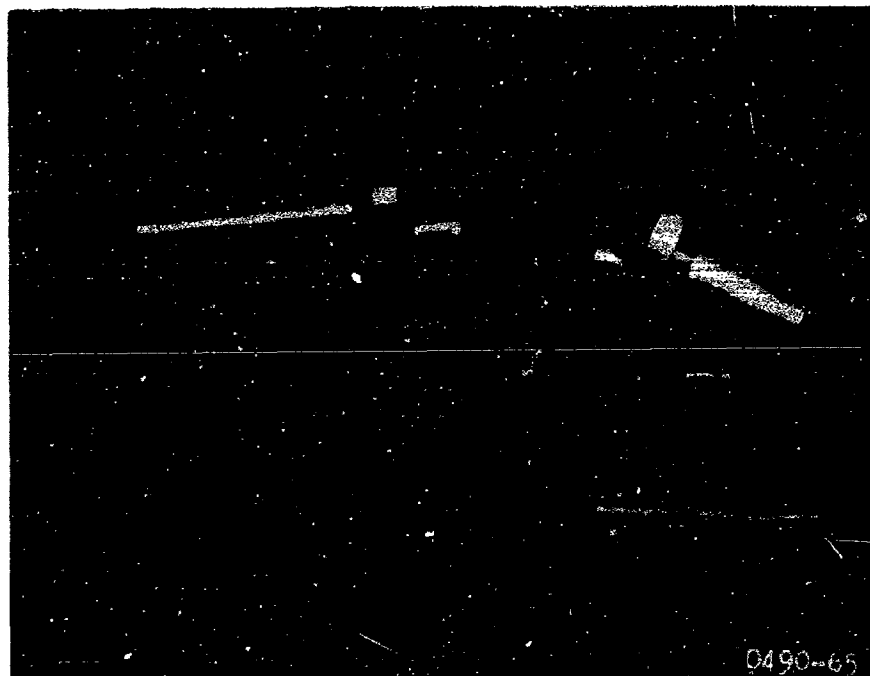


Figure XII-1. Sandia Velocity Gage and Protective Cover



Figure XII-2. Statham Model A69TC Accelerometer and Protective Cover

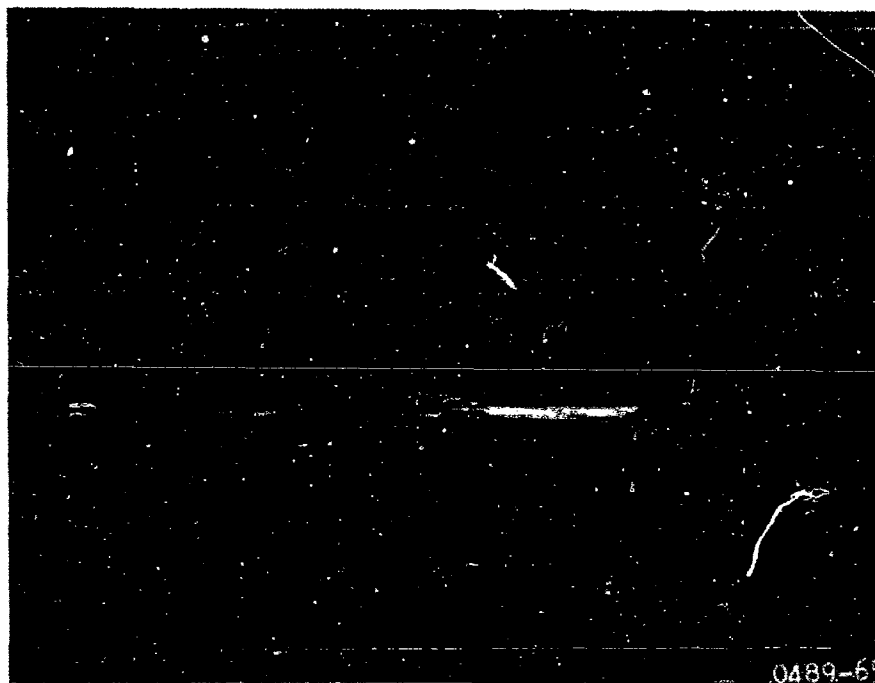


Figure XII-3. Soil-Stress Gage

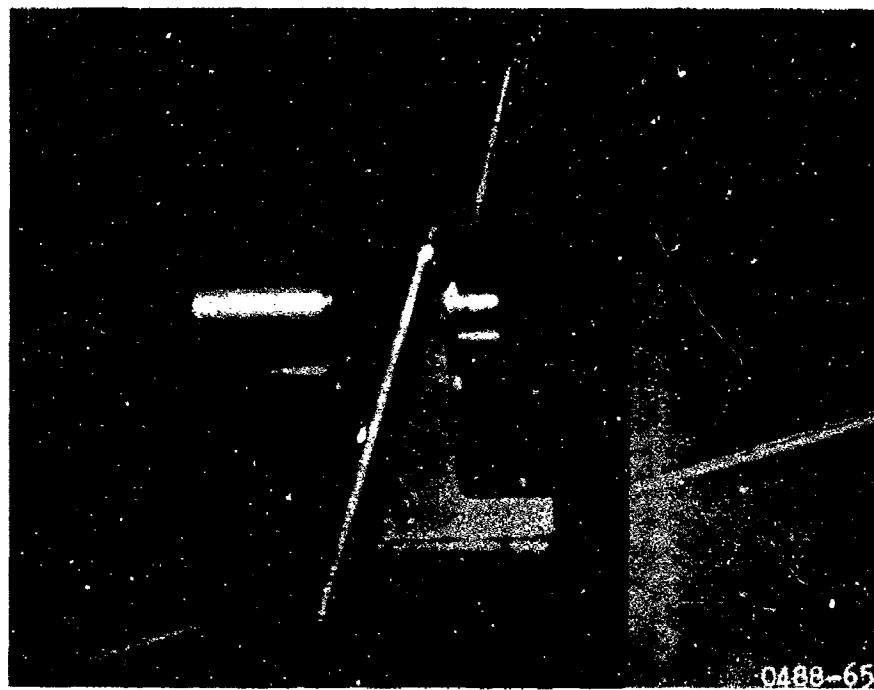


Figure XII-4. Long-Span-Displacement Gage Mounted on Calibration Device

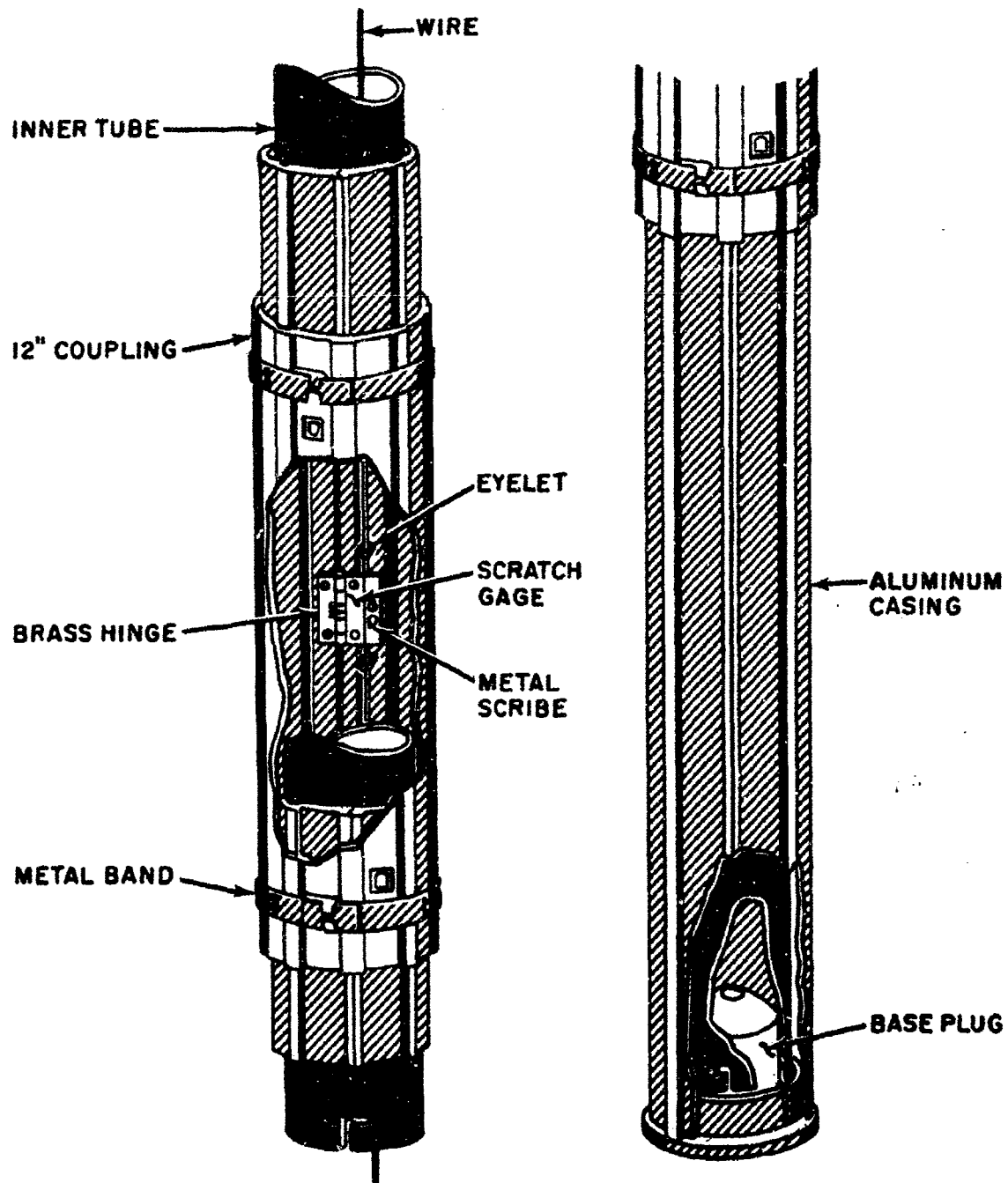


Figure XII-5. Scratch Gage

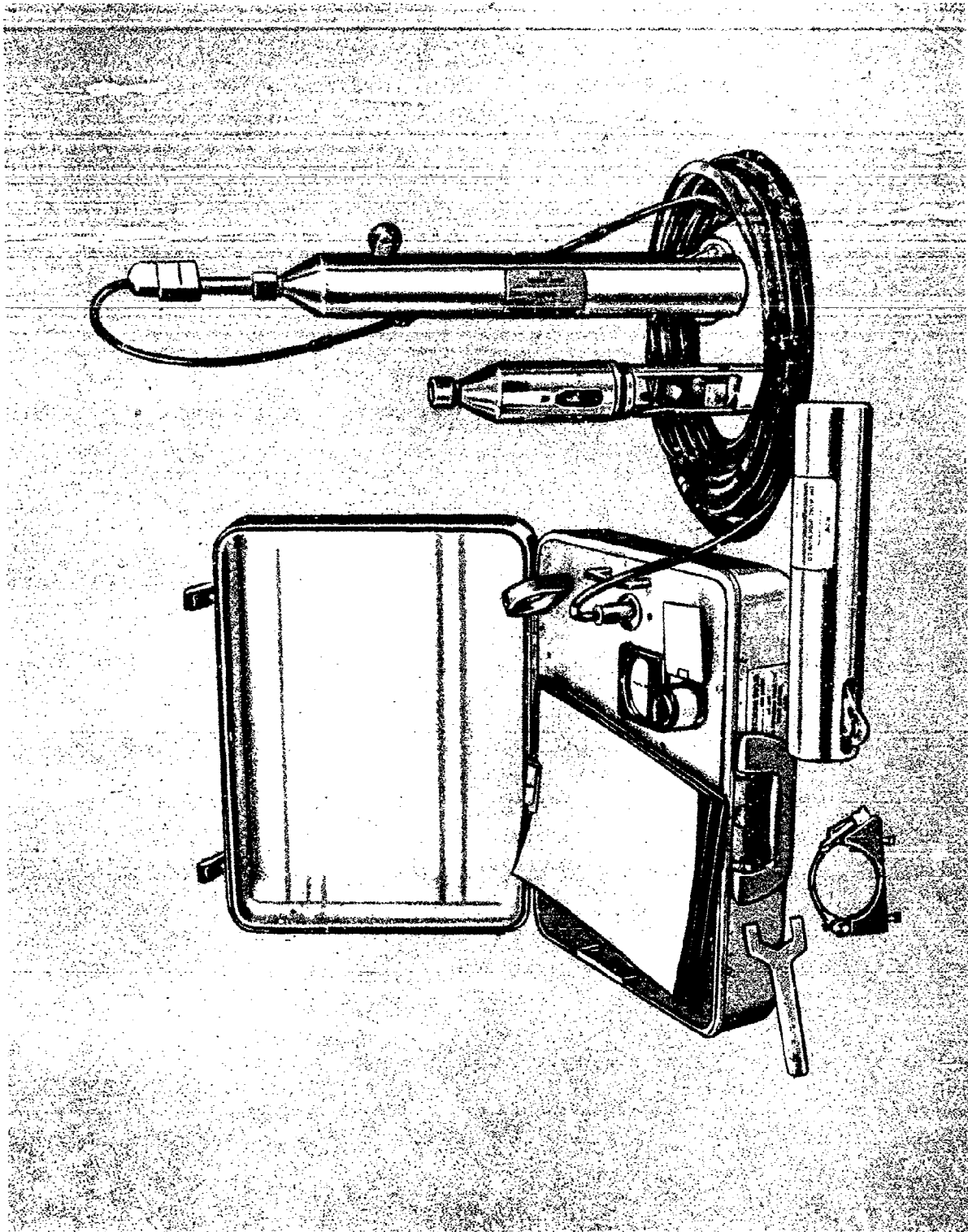


Figure XII-6. Slope-Indicator Instrument and Accessories

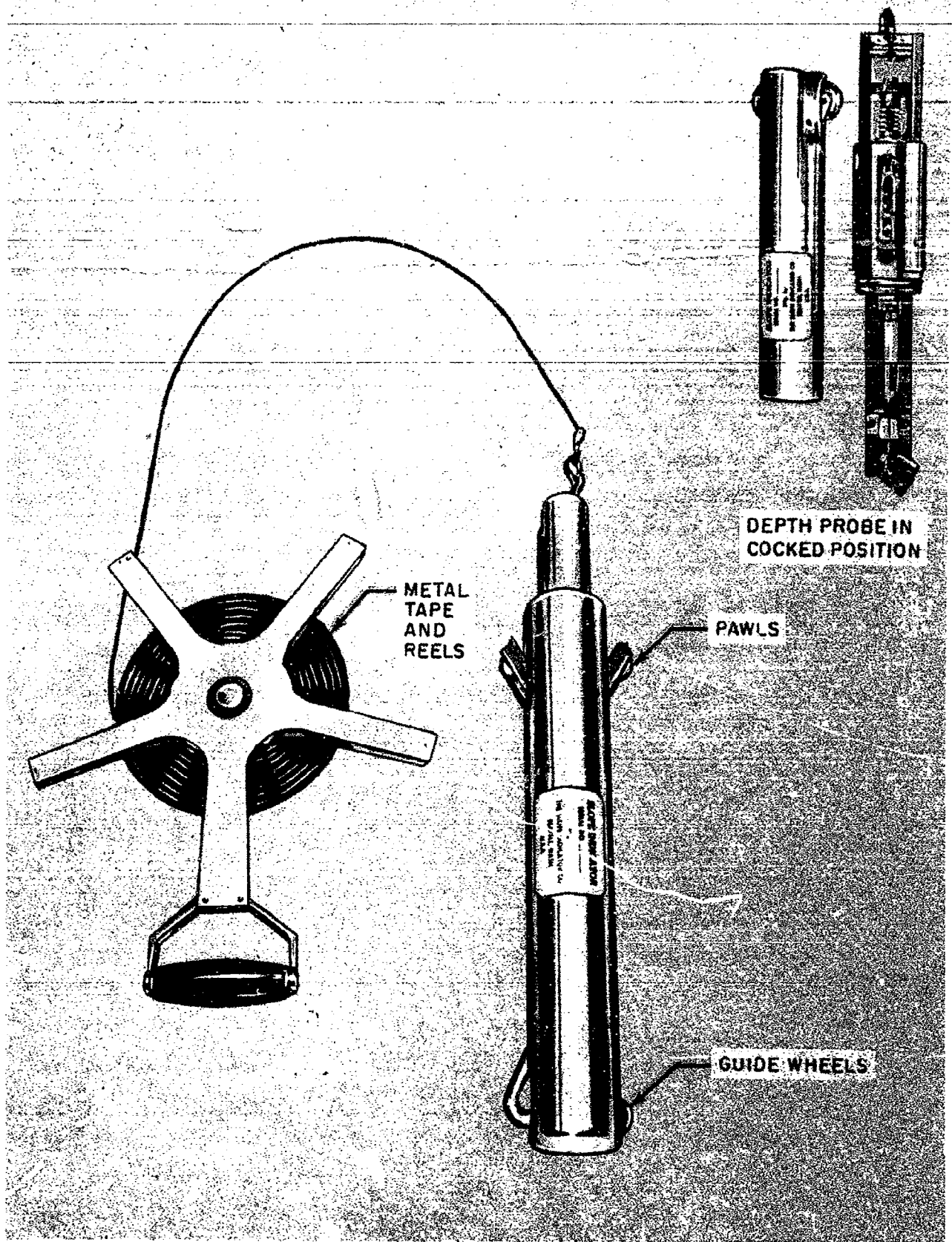


Figure XII-7. Depth Probe

SECTION XIII

RESULTS

1. Soil Stress Gages

Two data traces were recorded from the 10 soil stress gages which were installed in the experiment. All the soil stress gages installed in Hole 21 recorded an excessive amount of noise from which no useful data could be recognized or extracted. The noise on all of these records started at approximately 13 msec, which agrees with the first signal output from the top velocity gage in this hole. The cause of this excessive noise has not been positively identified. However, it is suspected that the noise was generated by the cables being squeezed as they exited from the protective conduit at the drill hole. The two data traces were obtained from gages installed with 3 inches of earth cover. The third near-surface gage (11S-g) appeared to saturate the amplifiers and no useful data were obtained. The measured near-surface vertical soil stress records for gages 8S-g and 16S-g are shown in figures XIII-1 and XIII-2 respectively.

2. Accelerometers

Five data traces were recorded from the 13 accelerometers which were installed to measure earth free-field motions. The remaining eight channels contained an excessive amount of noise from which no useful data could be recognized or extracted. The cause of this excessive noise has not been positively isolated; however, it is suspected that the tape recorders contributed significantly because of incorrect gain settings.

Appendix C contains the time history records for all of the accelerometers which contained data. Figure XIII-3 is a summary of the recorded peak downward vertical accelerations for the earth free field. Acceleration data from the interior of the structural model have also been included on this figure. Figure XIII-5 presents the times of first arrival of the acceleration pulses measured in Hole 12. Figure XIII-6 presents the time of first arrival of the acceleration pulse measured in Hole 21.

The acceleration-time records were integrated to obtain additional transient vertical velocity data and these results are presented in appendix C.

3. Velocity Gages

Thirteen data traces were recorded from the 15 velocity gages which were installed in the experiment. Gage 21V-1 was disconnected before the test because of a faulty signal conditioning unit. Gage 21V-60 appeared to saturate the amplifiers and no useful data were obtained.

Appendix C contains the time history records for all of the velocity gages which contained data. Figure XIII-4 is a summary of the recorded peak downward vertical velocities. Figure XIII-5 presents the times of first arrival for each of the velocity pulses measured in Hole 12. Figure XIII-6 presents the times of first arrival for each of the velocity pulses measured in Hole 21. Figure XIII-7 presents the times of first arrival for each of the velocity pulses measured in Hole 25. A summary of all the times of arrival of the peak vertical downward velocity are presented in figure XIII-8.

4. Long-Span Displacement Gages

The long span displacement gages did not provide any useful data. The overpressure caved in the protective cover over the gage housing and subjected the potentiometers to the free-field air blast environment. This drove all of the displacement records entirely off scale and saturated the amplifiers.

The velocity-time records were integrated to obtain an indication of the transient vertical displacement; these results are presented in appendix C. Base line shifts were required to integrate a portion of the velocity records and the adjustments that were made are indicated by dashed lines on the figures in appendix C. A summary of the first major downward peak vertical displacements obtained from the integration of the velocity records is presented in figure XIII-9.

5. Slope-Indicator Gage

Figure XIII-10 shows a plan view of the location of the top of the slope indicator gage both pre- and post-shot as determined from survey data. These data indicate that the top of the gage moved 3.72 inches downward, 1.20 inches to the east and 0.14 inch to the south. Figures XIII-11 and XIII-12 illustrate

the permanent lateral motion of the gage with depth. Table XIII-1 gives the permanent vertical displacement with depth.

The scratch gages installed to measure the transient vertical movement did not function as expected. Problems were encountered in the installation of the gage and the magnitude of the displacements appear to be lower than expected. These factors make the recognition of the data impossible and, therefore, no results are presented.

Table XIII-1

PERMANENT VERTICAL DISPLACEMENT WITH DEPTH
(SLOPE INDICATOR)

| Depth (ft) | Displacement surface to depth (in.) | Displacement between successive depths (in.) |
|---------------|-------------------------------------------|----------------------------------------------------|
| 2.00 | 1.32 | 1.32 |
| 4.50 | 1.80 | 0.48 |
| 7.02 | 2.16 | 0.36 |
| 9.52 | 2.70 | 0.24 |
| 12.04 | 2.40 | 0.00 |
| 14.54 | 2.52 | 0.12 |
| 17.05 | 2.70 | -0.12 |
| 19.55 | 2.52 | +0.12 |
| 22.06 | 2.52 | 0.00 |
| 24.57 | 2.64 (Max) | +0.12 |
| 27.08 | 2.52 | -0.12 |
| 29.58 | 2.52 | 0.00 |
| 32.09 | 2.64 (Max) | +0.12 |
| 34.60 | 2.52 | -0.12 |
| 37.09 | 1.32 | -0.12 |
| 39.60 | 2.28 | +0.96 |
| 42.09 | 2.40 | +0.12 |
| 44.62 | --- | --- |

6. Time-of-Arrival System

A plan view of the test area showing the location of the time-of-arrival gages and the shock wave at the surface of the soil is presented in figure XIII-13. As indicated in the figure, the time-of-arrival gages were installed along three lateral lines. The results obtained from the time-of-arrival system are presented in figures XIII-14, XIII-15, and XIII-16 for Planes 1, 2, and 3, respectively. Each plane represents an east-west profile of the test area. The time of arrival at each gage location is noted on the figure, and contour lines of equal times have been constructed to indicate the location and shape of the stress wave in the earth.

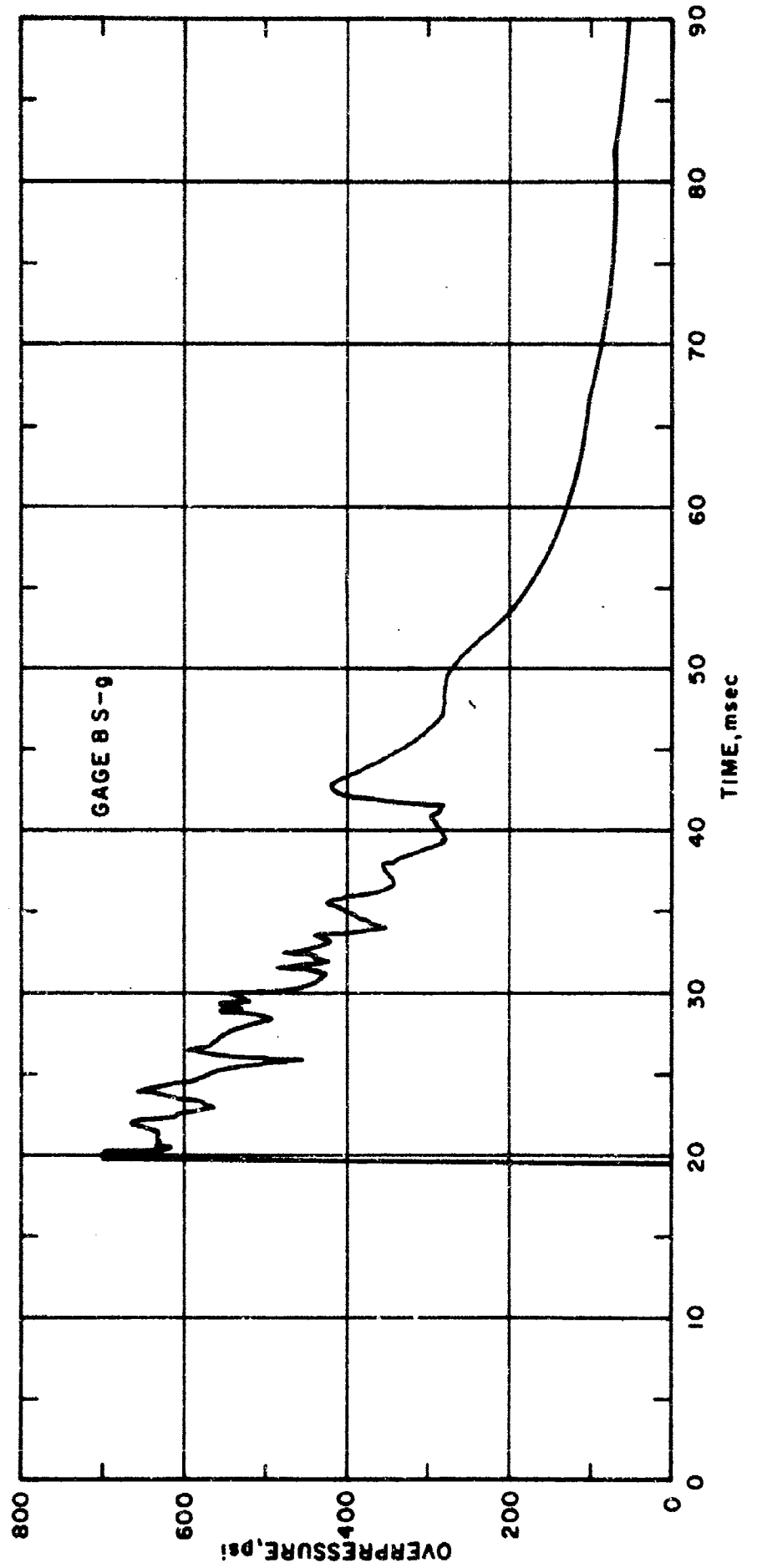


Figure XIII-1. Near-Surface Vertical Soil Stress

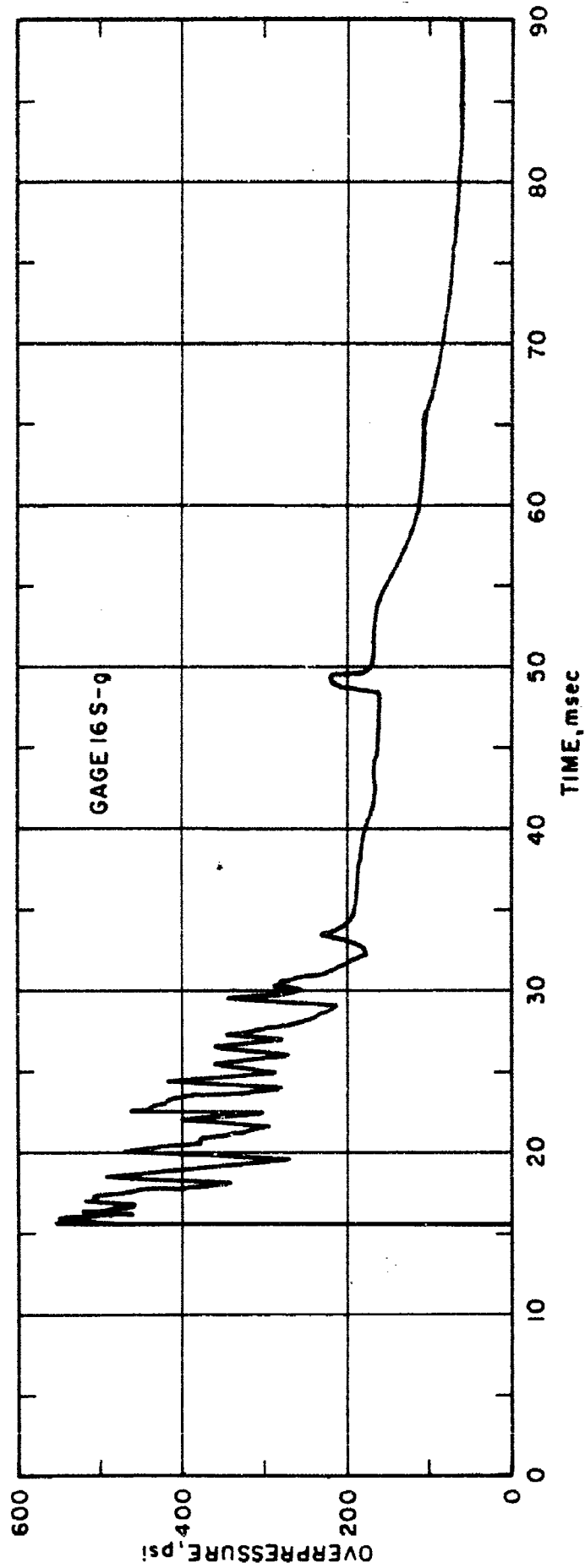


Figure XIII-2. Near-Surface Vertical Soil Stress

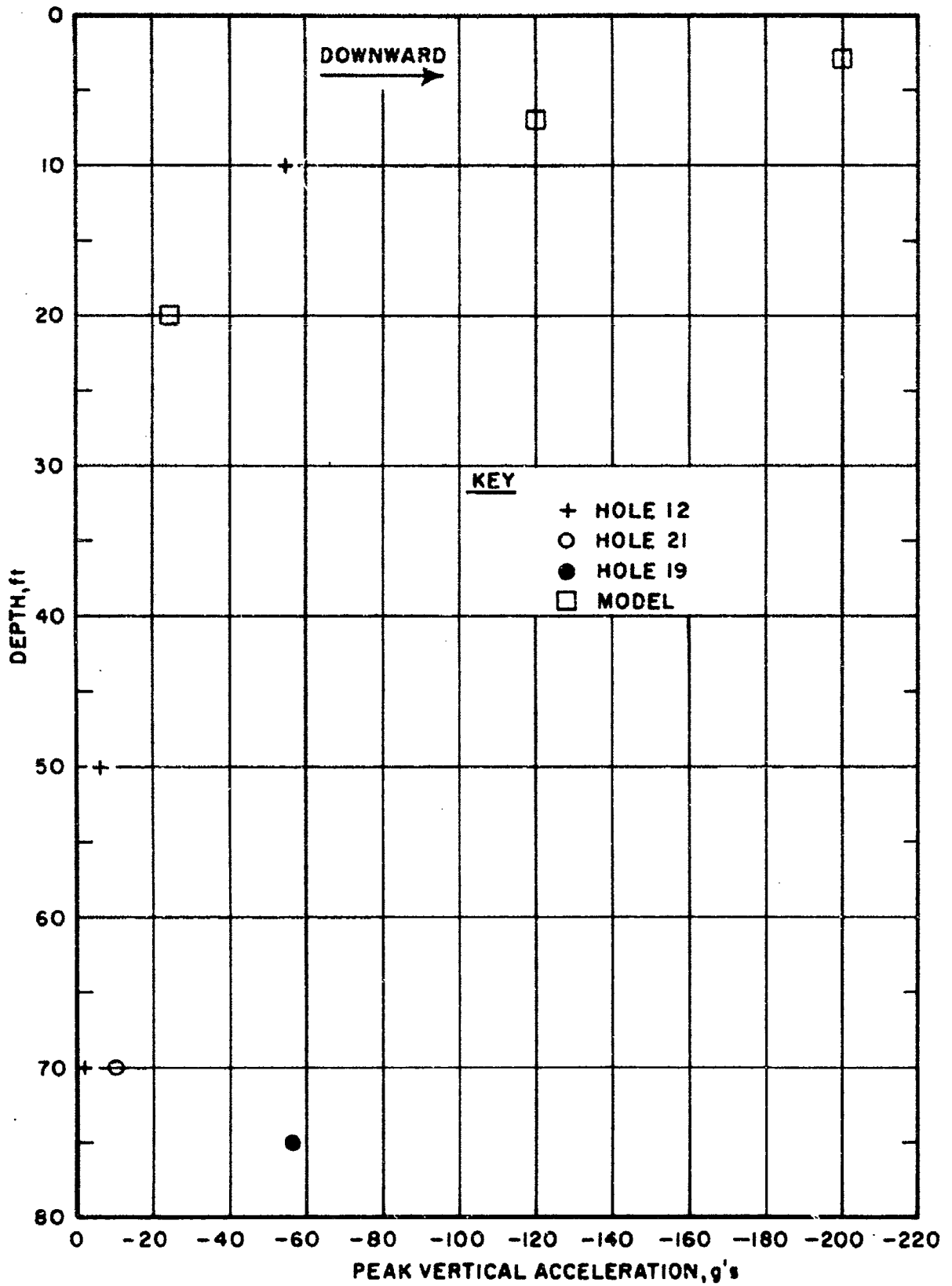


Figure XIII-3. Peak Vertical Accelerations

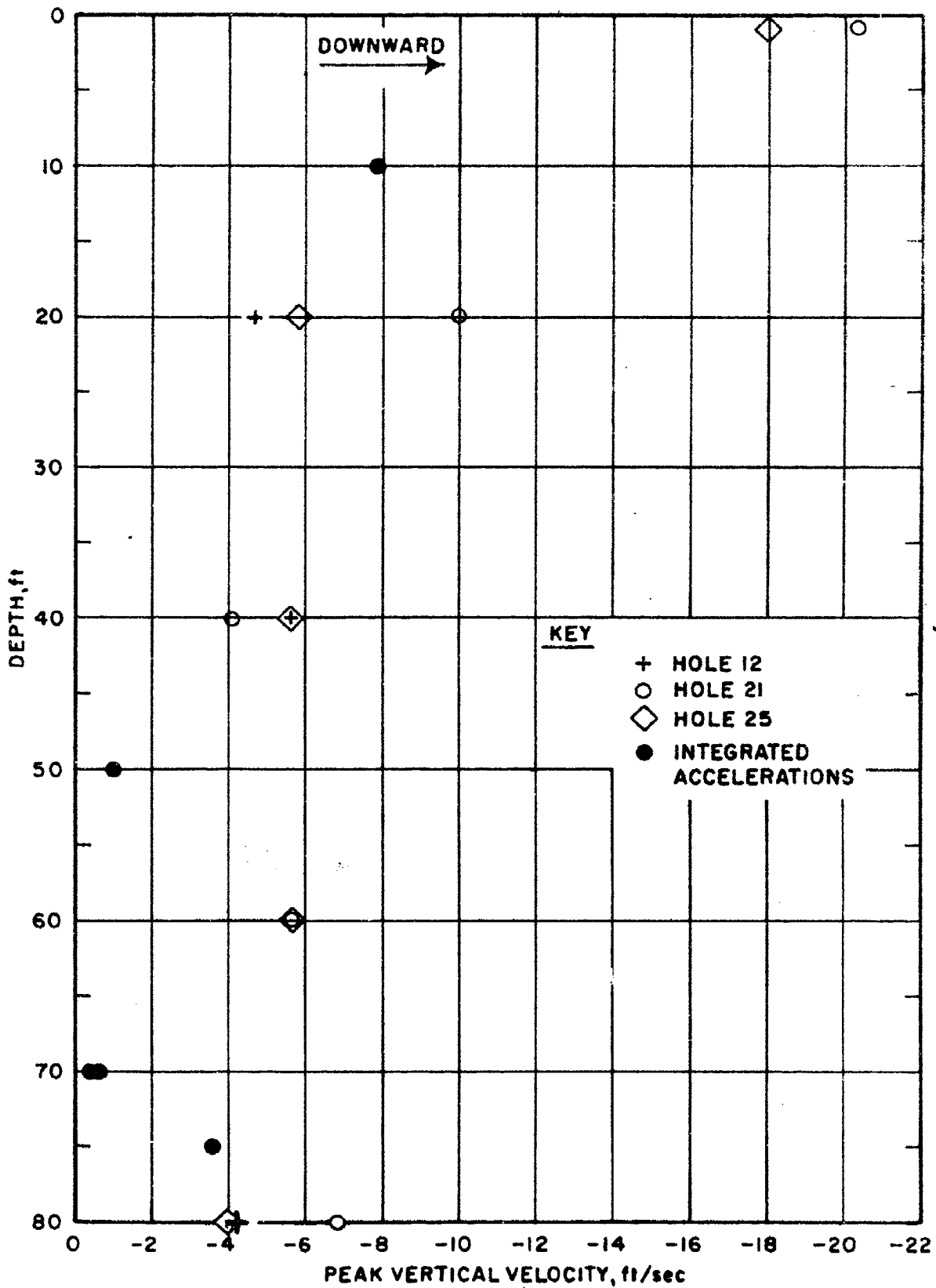


Figure XIII-4. Peak Vertical Velocities

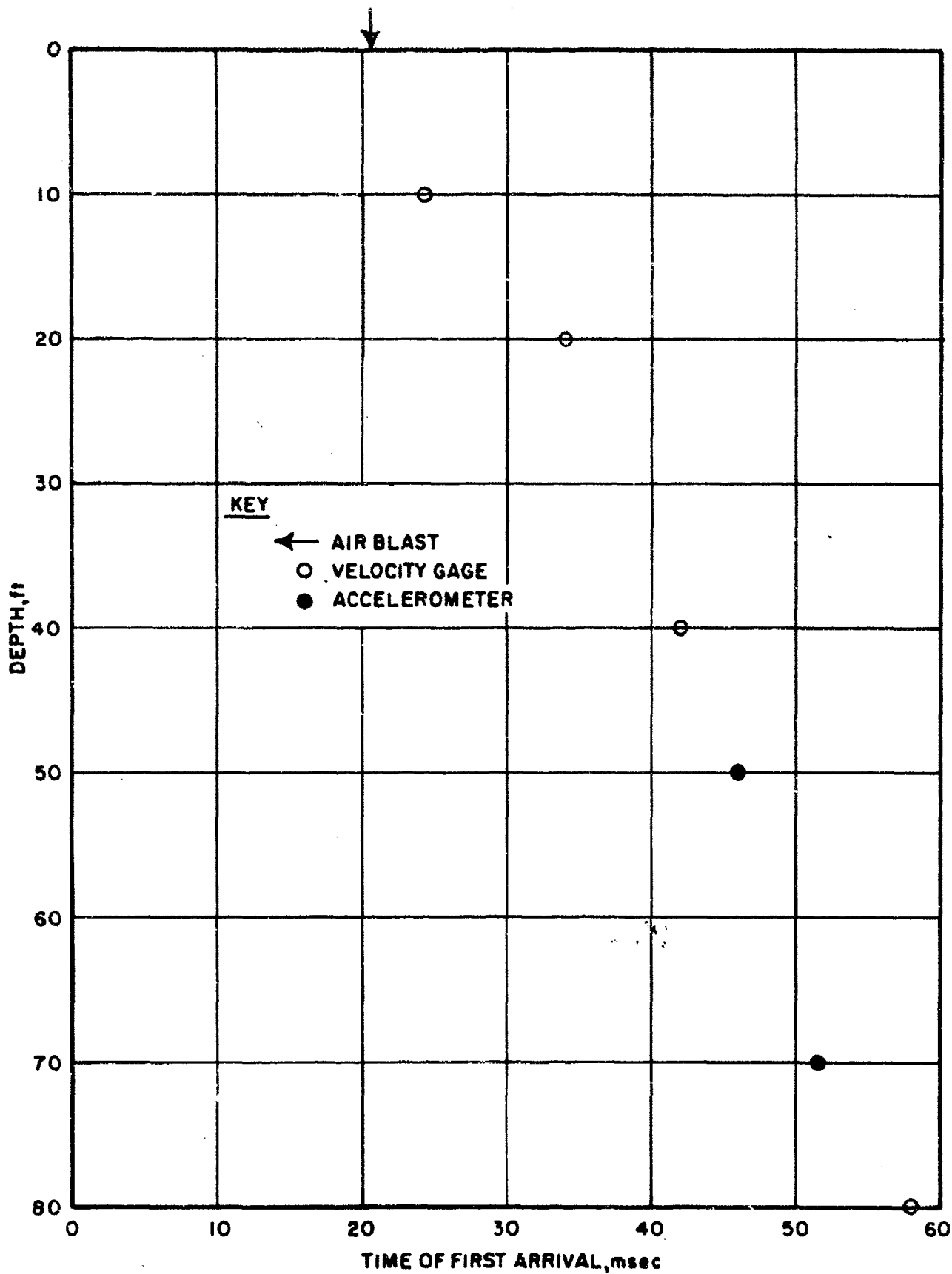


Figure XIII-5. Times of First Arrival, Hole 12

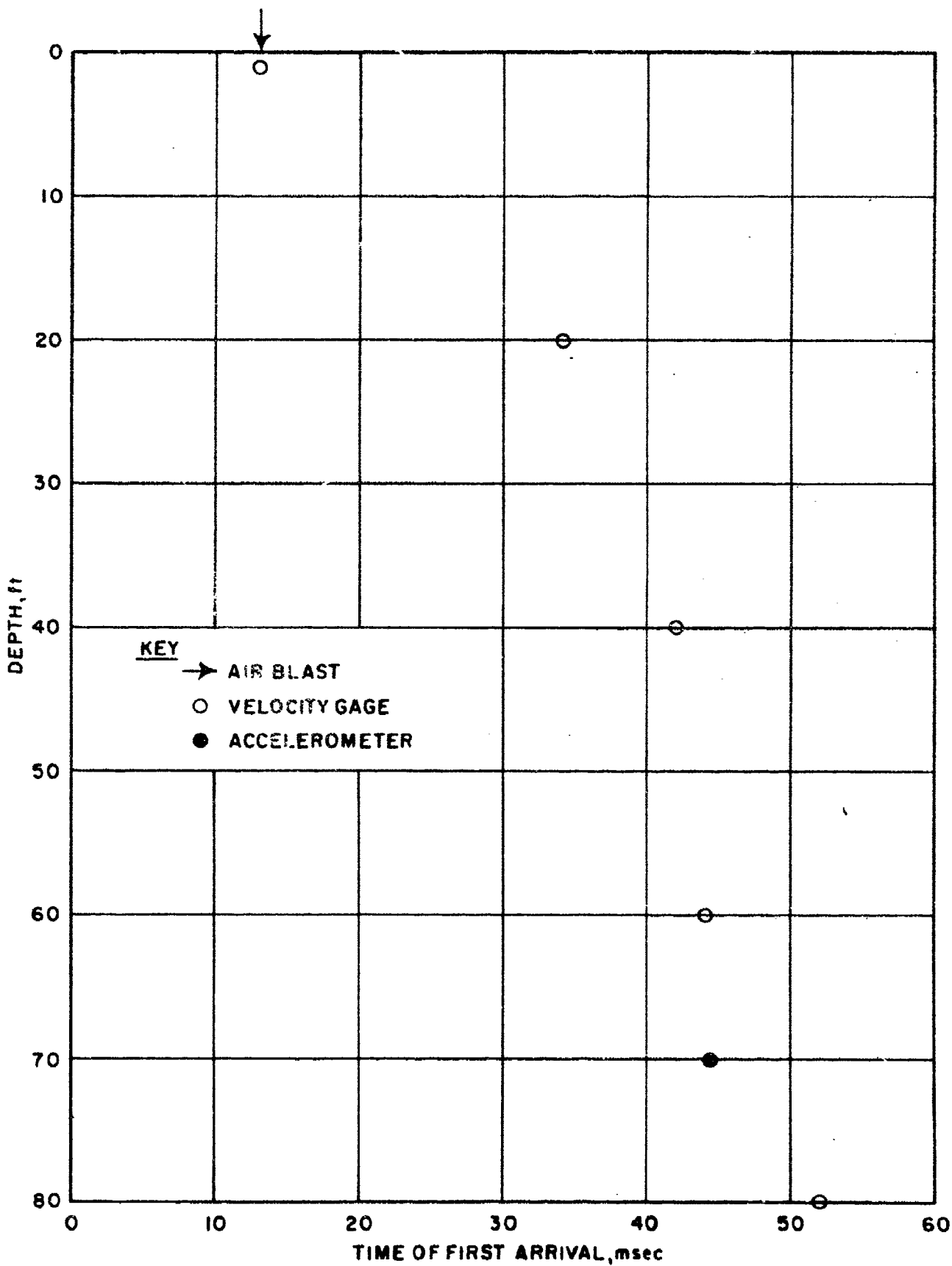


Figure XIII-6. Times of First Arrival, Hole 21

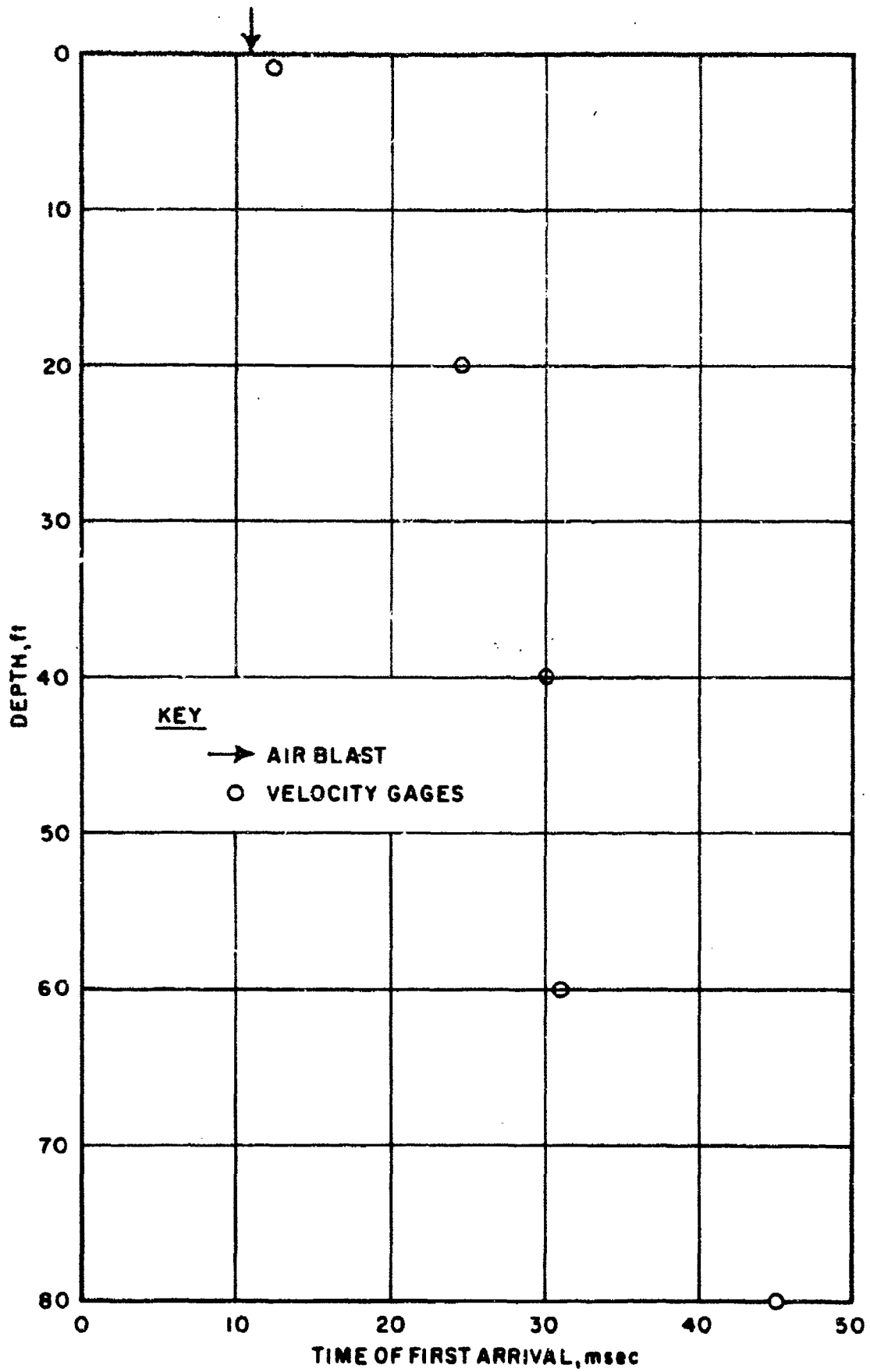


Figure XIII-7. Times of First Arrival, Hole 25

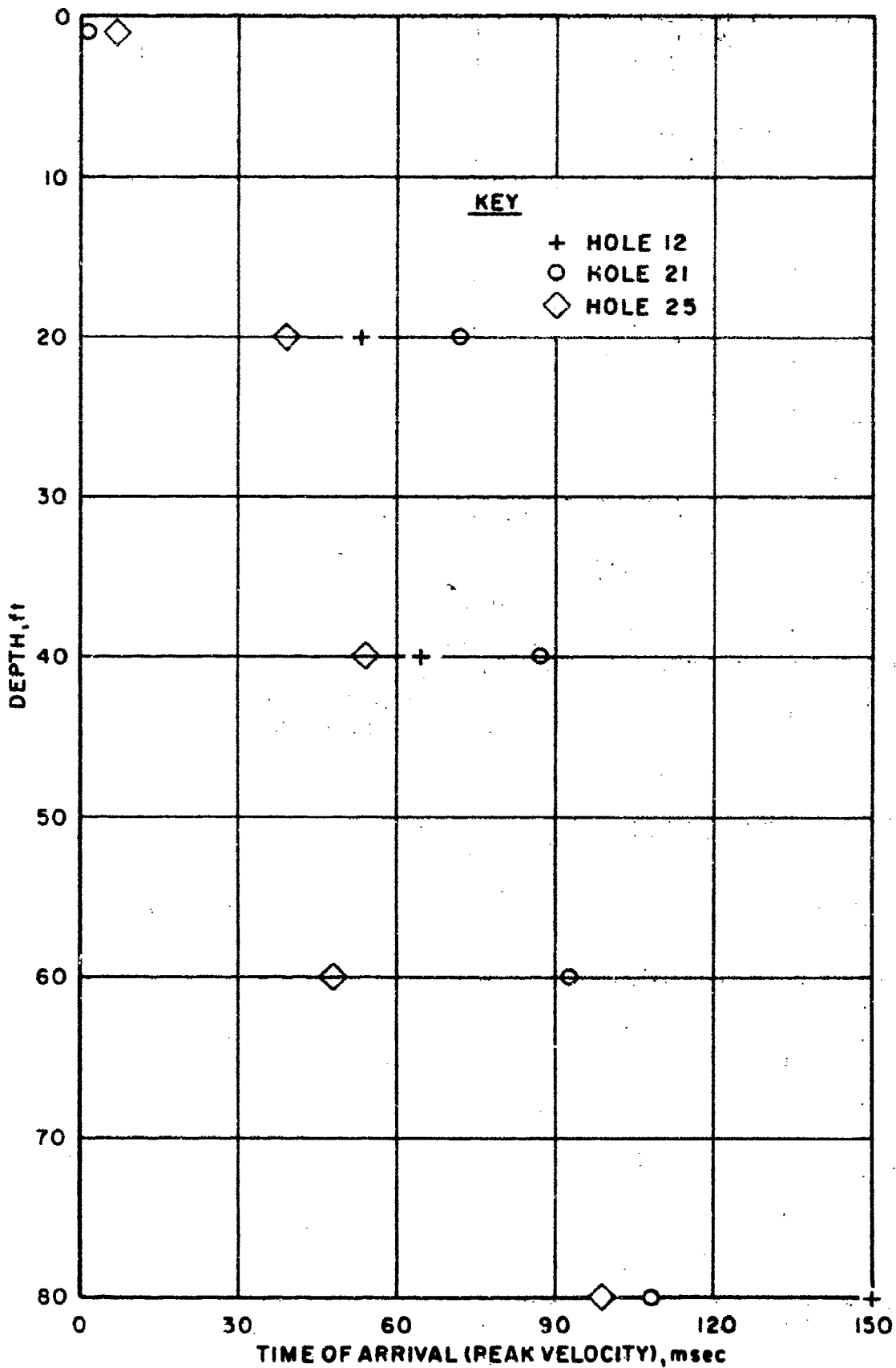


Figure XIII-8. Times of Arrival (Peak Velocity)

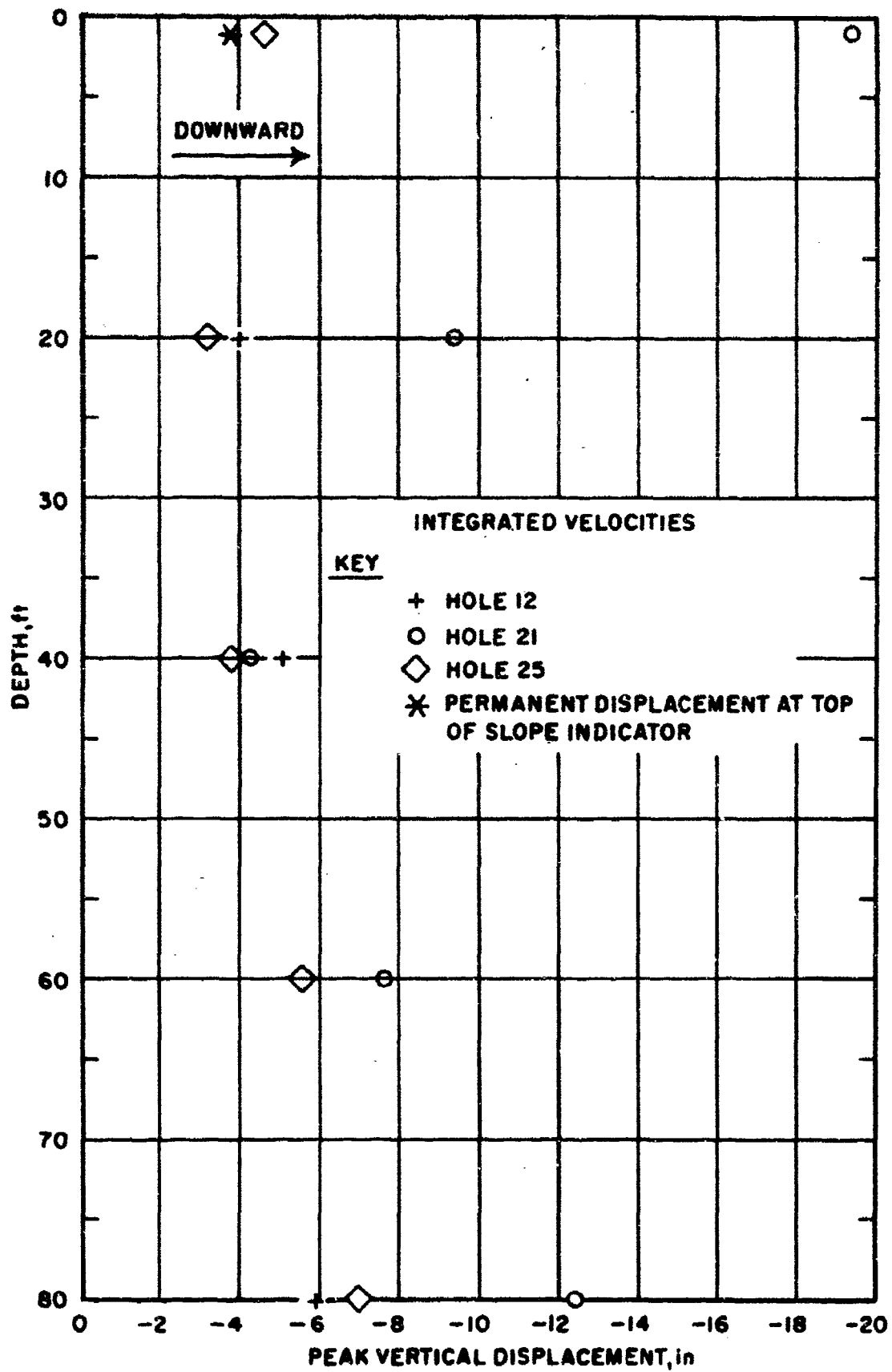


Figure XIII-9. Peak Vertical Displacements

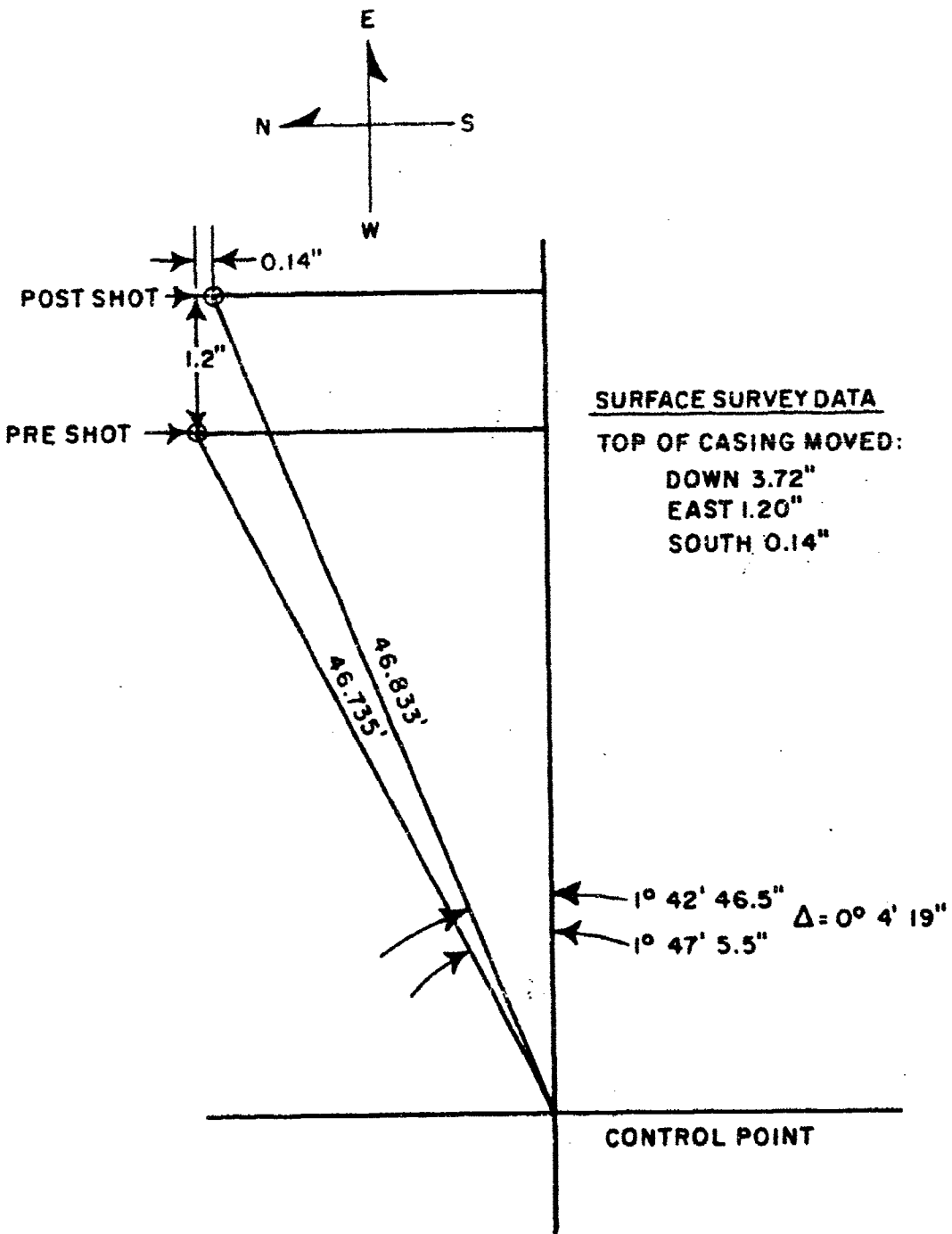


Figure XIII-10. Survey Data for Slope Indicator

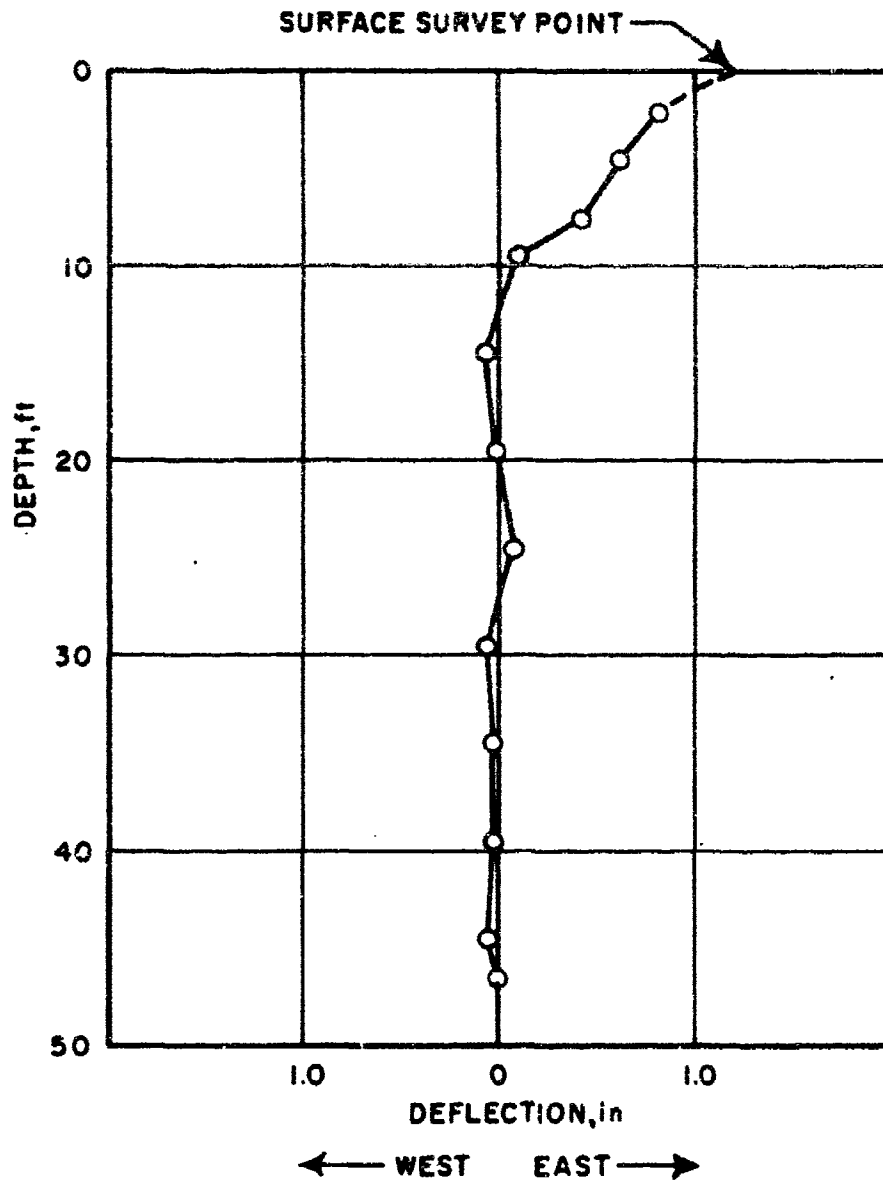


Figure XIII-11. Slope Indicator Lateral Movement (East-West)

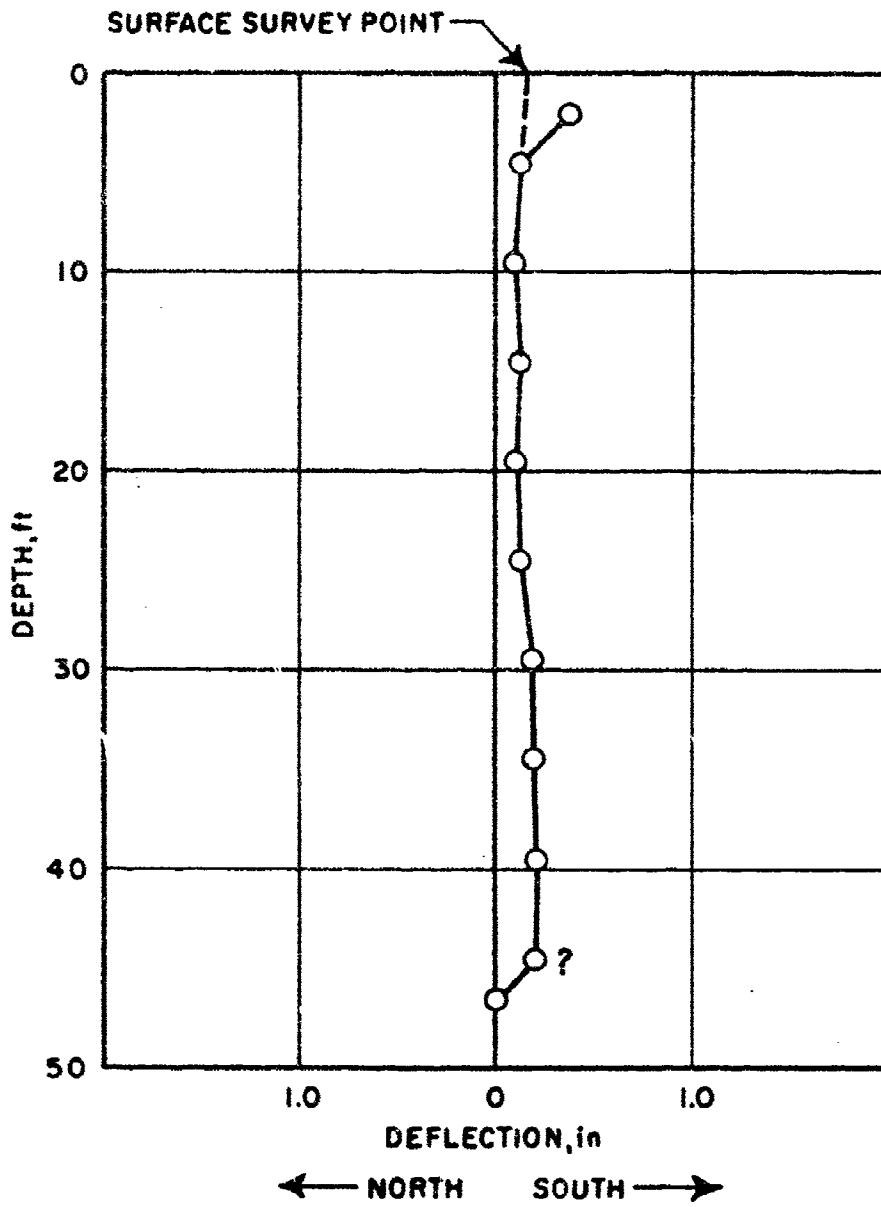


Figure XIII-12. Slope Indicator Lateral Movement (North-South)

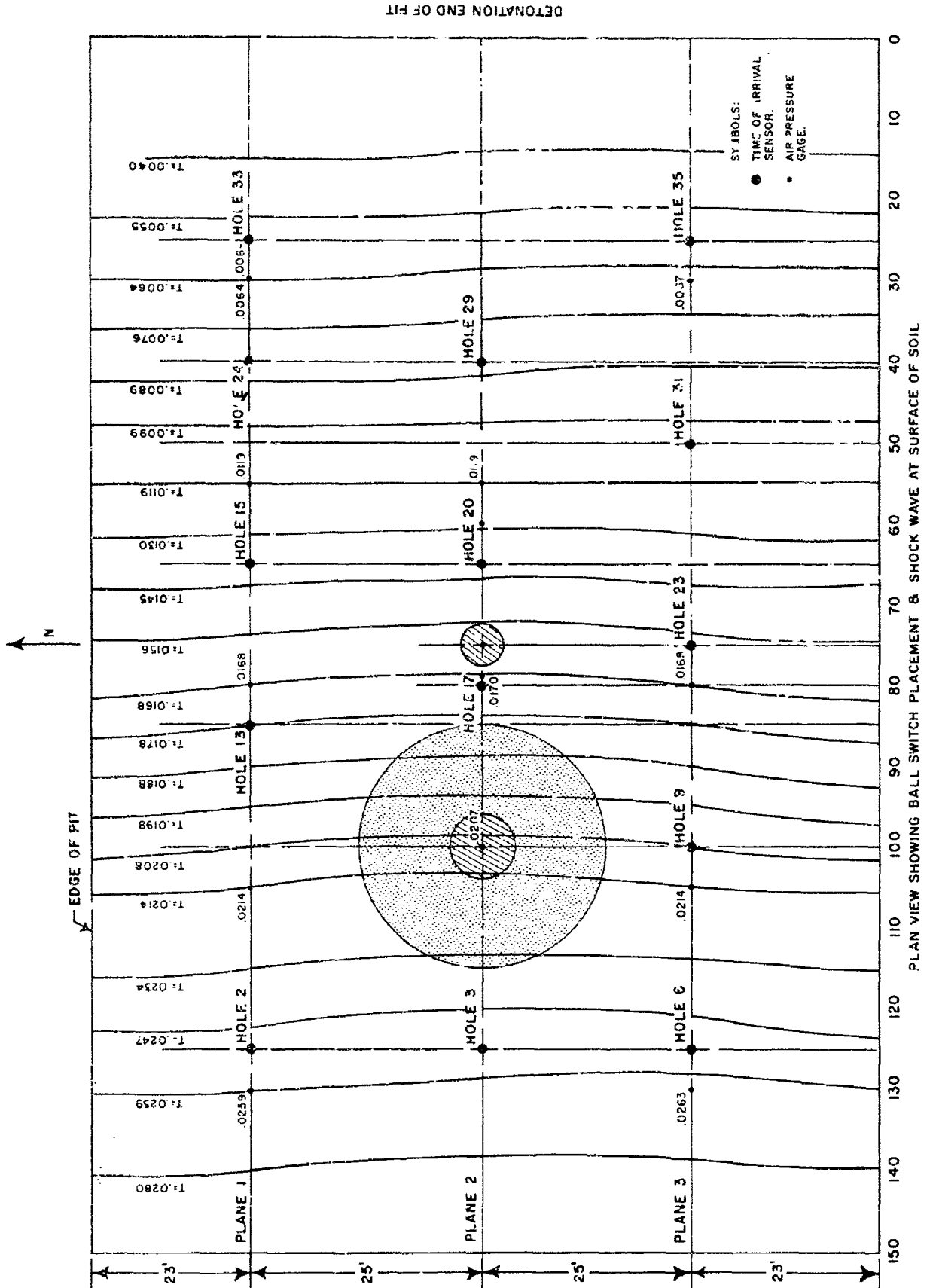


Figure XIII-13. Plan View Showing Ball Switch Placement and Shock Wave at Surface of Soil

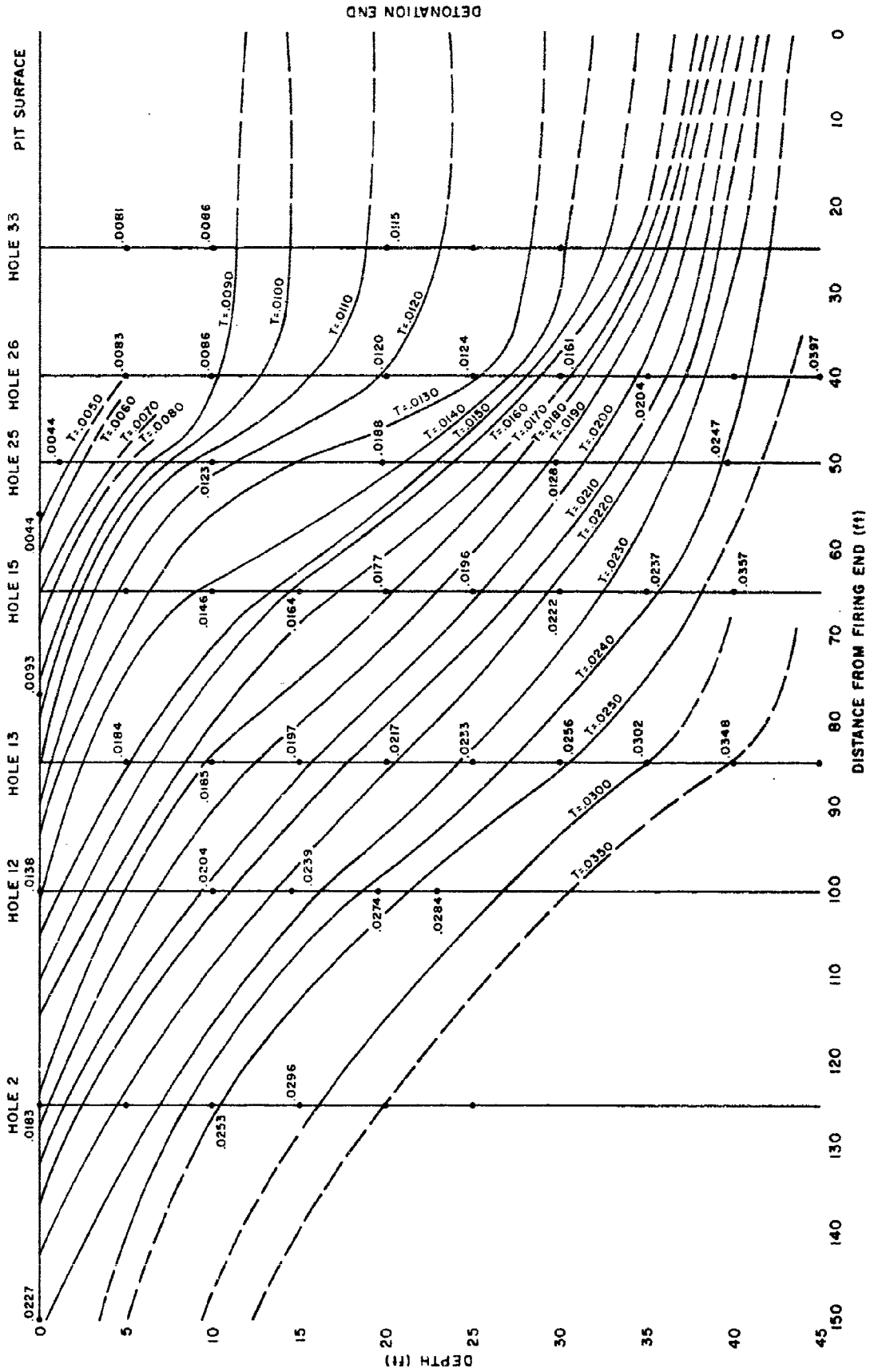


Figure XIII-14. Time-of-Arrival Contours, Plane 1

SECTION XIV

DISCUSSION

1. Soil Stress

As indicated in figure IX-1, The air-blast input had a different shape and considerably faster decay to one-half peak pressure than predicted. The shape of the air-blast curve influences the attenuation of stress with depth and, therefore, an after-the-fact calculation of the stress attenuation was accomplished utilizing the composite air-blast curve given in figure IX-1. The results of this calculation are presented in figure XIV-1 along with the predicted curve. Since there are considerable differences in the two curves, the attenuation of other earth free-field quantities was recomputed after-the-fact utilizing the new attenuation factors. Complete confidence cannot be placed in either calculated curve without supporting stress measurements, which were not available from this test.

The measured vertical stress in the soil near the ground surface (3 inches of cover) is presented in figures XIV-2 and XIV-3. These records indicate values of peak overpressure of 700 psi and 570 psi instead of the 312 psi obtained from a normalization of all the air pressure measurements (figure IX-1). The composite air pressure curve has been plotted on each of the soil stress records for comparison. The overpressure axis has been scaled such that the maximum values from each curve coincide. It should be noted that the shape of the two curves agrees quite well. If some adjustments were made for the small amount of attenuation which should take place in the 3-inch depth, the two curves would agree even better. Thus, it appears that the near surface stress gages reproduced the time history of the air-blast input closely while magnifying the intensity by a factor of approximately 2. These gages were calibrated with static air pressure. This method of calibration has been correlated with results in a dense (112-113 lbs/ft³) Ottawa sand, subjected only to static loads. The gages in this test, however, were placed in a native sand with a density of approximately 100 lbs/ft³ and were subjected to a dynamic load. A magnification factor of 2 is not unreasonable when the differences in density and loading are considered.

2. Acceleration

Figure XIV-4 presents all of the measured earth free-field peak accelerations along with after-the-fact calculations of attenuation with depth, which takes into account the composite air pressure curve (figure IX-1) and the after-the-fact attenuation factors given in figure XIV-1. Data from the interior of the structural model have also been included on this figure. The data obtained from the earth free-field accelerometers were of extremely poor quality since the signals were masked by a high-intensity noise. The only record for which this was not true was 19A-75; it gave a peak acceleration which was much higher than calculated. All of the acceleration data indicated pulses of extremely short duration. When these data were integrated to obtain velocity-versus-time histories, the results indicate that none of the velocities returned to zero (appendix C). This uncertainty about the integrated results also raises a question as to whether the peak velocity had been attained before the end of the data.

In spite of all the uncertainties, the data taken as a whole indicate that the shape of the attenuation of peak vertical acceleration curve with depth agrees fairly well with the calculated curve, although the measured values in the upper 20 feet were somewhat lower. A much larger quantity of reliable data would be required before the prediction technique could be radically changed.

3. Velocity

The vertical velocities measured at the near-surface locations had a characteristic shape that agreed quite well with the air-blast input, i.e., a short rise-time to the peak followed by a decay to zero in a time ranging from approximately 100 to 200 msec (see figures C-17 and C-27 in appendix C). The rise time increased monotonically with depth as indicated in table XIV-1.

Table XIV-1

RISE TIMES

| Hole | Depth (ft) | ta (msec) | tp (msec) | tp-ta (msec) |
|------|---------------|--------------|--------------|-----------------|
| 12 | 20 | 34 | 70 | 36 |
| 12 | 40 | 42 | 85 | 43 |
| 12 | 80 | 48 | 170 | 112 |
| 21 | 1 | 13 | 14 | 1 |
| 21 | 20 | 34 | 85 | 51 |
| 21 | 40 | 42 | 100 | 58 |
| 21 | 60 | 44 | 105 | 61 |
| 21 | 80 | 52 | 120 | 68 |
| 25 | 1 | 12.2 | 18 | 5.8 |
| 25 | 20 | 24.6 | 50 | 25.4 |
| 25 | 40 | 30 | 65 | 35 |
| 25 | 60 | 31 | 60 | 29 |
| 25 | 80 | 45 | 110 | 65 |

NOTE: ta = time of first arrival
 tp = time of peak arrival

In addition, the measured peak vertical velocity generally decreases with depth as shown in figure XIV-5. This figure presents all the measured peak vertical velocities and the after-the-fact calculated attenuation curve as well as the results obtained from the integration of acceleration records. The after-the-fact calculations were based on the formula from reference 7,

which is given in section XI $\left(V_{pz} = 4 \text{ ft/sec} \left[\frac{P_{so}}{100} \right] \left[\frac{1000}{C} \right] \alpha_z \right)$. A peak overpressure of 312 psi was used for P_{so} , C was taken as 3/4 of the seismic values given in table XI-1, and α_z was taken from the after-the-fact calculations given in figure XIV-1. Although there is considerable scatter, particularly when the velocities obtained by integration are included, the

data appear to fit the calculations reasonably well with the exception of the near surface values. Reference 8 does not predict velocity values above a depth of 5 feet because of the erratic results observed from nuclear field tests. The technique for predicting accelerations given in reference 7 takes this into account; near surface values and surface values are computed by two different equations which give widely different results. It is also possible that the velocities are much higher at the surface than at small depths of burial. This could be caused by low initial densities of the surface material or by a scouring effect immediately ahead of the air blast.

The data indicate that the velocity at a depth of 20 feet is much higher in Hole 21 (9.9 ft/sec) than in Holes 12 (4.7 ft/sec) and 25 (5.8 ft/sec). A first reaction would be to assume that this effect was caused by differences in the air pressure input at these locations. A review of the pressure-time records given in appendix B reveals that there was no record obtained from the gage near Hole 21. Both of the air pressure gages (10 and 24) near Holes 12 and 25 indicate that the pressure records required base line shifts to correct for negative pressures at relatively early times. In addition, the air pressure record from Position 24 was very spiked in appearance. However, there were not sufficient air pressure measurements taken to positively determine the variation in air pressure input at various locations within the loaded area. In addition, the near surface velocities had fair agreement, indicating similar air-blast inputs.

Another possible cause of these differences might be the side rarefactions as illustrated in figure I-5. However, this does not appear to be the case. Figure XIV-6 illustrates a gross simplification of the real problem, i.e., a static load applied by a foundation to a soil which is assumed to have elastic properties. In this case, the rarefactions have all interacted and static equilibrium has been reached. The unit width can be used to represent approximately 100 feet. Then the centerline represents Hole 21 and the one-quarter point represents Holes 12 and 25. At a scaled depth of 20 feet the stress intensity is 90 percent and 94 percent respectively. Thus the static representation of the rarefaction phenomenon does not explain the 60 percent or more differences in the measured velocities. Another argument can be used to negate the importance of the rarefaction waves. Figure XIV-7

illustrates the geometry and travel times involved. In this figure, t_a = time of first arrival for the signal generated at the surface, t_p = time of peak arrival for the signal generated at the surface, and t_r = time of first arrival for the rarefaction wave generated at the boundary of the loaded area. The fastest first-arrival velocity was utilized to compute the arrival times for the rarefaction waves. It is obvious from the figure that the rarefaction waves arrive at all holes after the first arrival from the surface but before the peak arrival from the surface. The arrival of a rarefaction wave cannot be observed on the velocity records given in appendix C between the first arrival and the peak arrival for the gages in question.

Another explanation for the differences in velocity measurements at the 20-foot depth is the difference in the in-situ material properties. The stratigraphy in Hole 21 consists of 10 feet of fractured hard clay followed by a thick layer of sand to a depth of 35 feet. The stratigraphy in Holes 12 and 25 consists of a foot or more of a very loose silt, a 4 to 5-foot layer of hard fractured clay and a thick layer of sand (see figure XI-1). It is also obvious from the blow counts on this figure that there were considerable variations in the density of the material in the sand layer. Thus the measured velocities at a depth of 20 feet may have been different because of differences in attenuation which took place above this depth and/or because of differences in the density of the material in which the gages were located.

The time-of-arrival data from the velocity records can be used to compute first-arrival propagation velocities as indicated in figures XIV-8, XIV-9, and XIV-10. The propagation velocities computed from the first arrivals agree with the uphole seismic data (table XI-1) with two exceptions. The propagation velocity in the upper 20 feet of material in Hole 21 is approximately 50 percent of the seismic value. In addition, both holes 21 and 25 indicate an exceedingly fast layer between 20 and 40 feet with propagation velocities in the range of 10,000 to 20,000 ft/sec. Referring to the Soil Profile (figure XI-1), the high velocity region appears to correspond to the very dense sand and gravel layer. It is very doubtful that a dense sand and gravel layer would be capable of providing velocities of this magnitude. The hard caliche in the lower layer should have a much faster

velocity than the sand and gravel, but the results again show good agreement with the seismic data.

The time-of-arrival data from the velocity records can also be used to compute peak arrival propagation velocities as indicated on figure XIV-11. These propagation velocities indicate that the peak velocity travels at one-half the front velocity or less. This agrees quite well with empirical rules of thumb ranging from $1/2$ to $3/4$ of the front velocity.

4. Displacement

No measured data were obtained on transient displacement since both the long span displacement gage and the transient measuring portion of the slope indicator failed to perform satisfactorily. The peak vertical displacements, derived from the integration of the velocity records, are compared on figure XIV-12 with after-the-fact calculations. The agreement is very poor and the data are very inconsistent. A detailed study of the displacement time records in appendix C will reveal that the majority of these data do not have the expected classic shape as illustrated in figure XI-7. The peak displacements from records which have the more classic shape also tend to fit the calculated curve on figure XIV-12 the best. These discrepancies may be caused by inaccuracies in the velocity-time records or by a poor selection of base-line shifts which were utilized for the integration.

Permanent displacement data are available from three sources: integrated velocity-time records, slope indicator measurements, and pre- and post-shot surveys. The permanent vertical displacements obtained from the integration of the velocity records were so inconsistent that the results are not presented. The permanent displacement of the top of the slope indicator installation was 3.72 inches according to the results obtained from the pre- and post-shot surveys. However, the depth probe readings indicate a value of 2.64 inches. These differences in results have not been reconciled. The survey also revealed that all of the near-surface monuments, such as the air pressure gage mounts, had essentially no permanent displacement. This can only be accounted for by elastic rebound near the free surface which would not affect deep structures to the same extent. The permanent lateral movement in the east-west direction was identical for the slope indicator and the survey data. The results indicate the surface

moved 1.2 inches to the east. The permanent lateral movement in the north-south direction varied between the slope indicator and the survey data. This difference appears to be due to an error in a slope indicator reading at a depth of 46.5 feet as shown in figure XIII-12. A permanent lateral movement to the east was also observed in the structural model. A movement in the direction opposite to the airblast travel was not expected since the stress wave induced in the ground will have a horizontal component whose direction is to the west. A surveying error can be immediately ruled out because of the excellent agreement between the two independent measuring techniques as illustrated in figure XIII-11. This motion can, however, be explained by an elastic rebound which overshoot the initial position during the unloading.

5. Horizontal Motions and Stresses

The time-of-arrival system indicated stress wave angles of entry (see figure I-7) ranging from 10° to 45°. However, the majority of the angles ranged from 15° to 25°, and 20° will be taken as a representative average. Combining the equations given in section I for the two components of motion gives

$$\frac{\text{Horizontal component}}{\text{Vertical component}} = \frac{\sin \alpha}{\cos \alpha} = \tan \alpha$$

and for 20°, $\tan \alpha = 0.364$. Thus the initial horizontal component of both motions and stresses behind the wave front, is equal to approximately 36 percent of the vertical component.

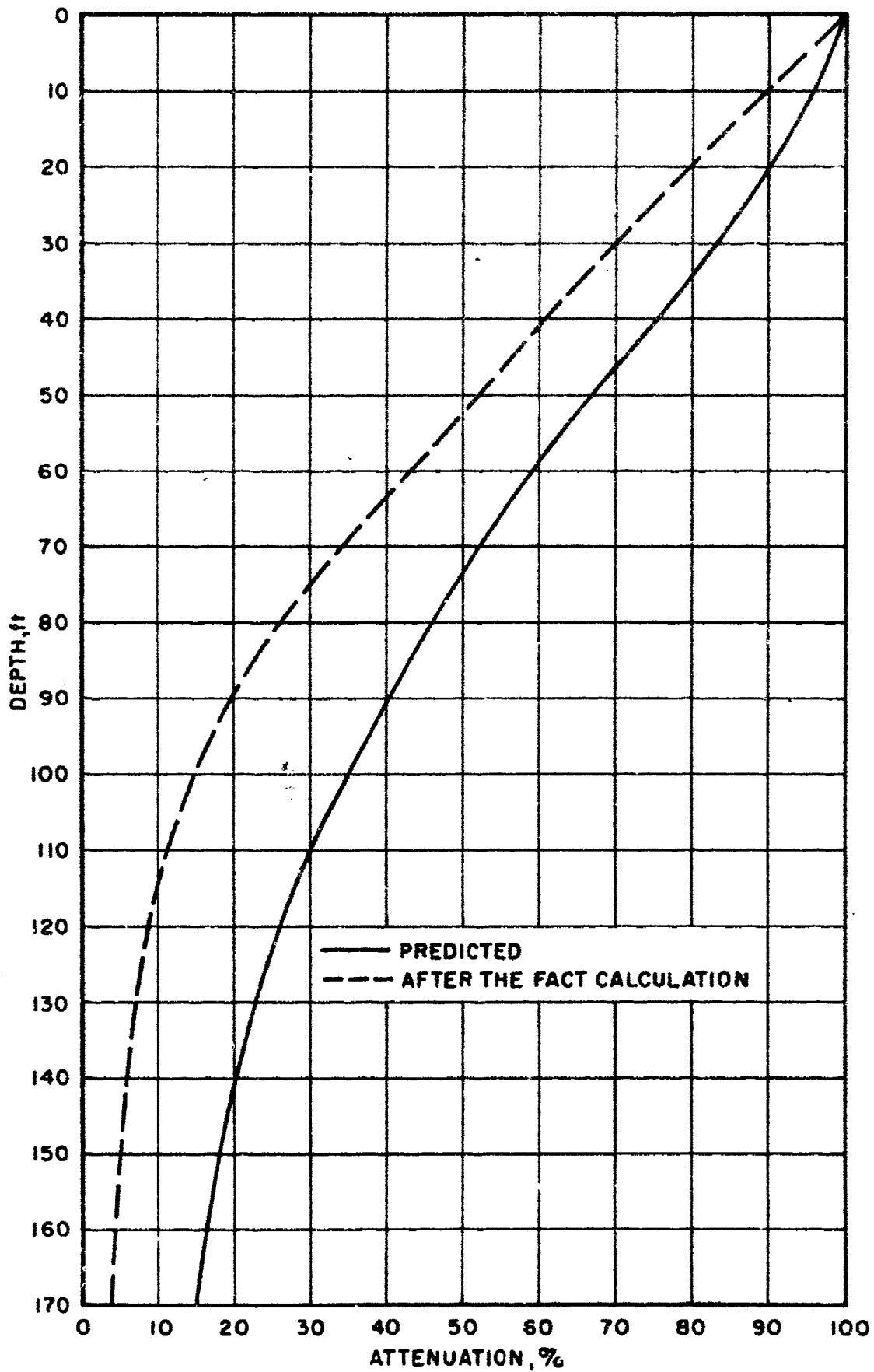


Figure XIV-1. Attenuation Factors

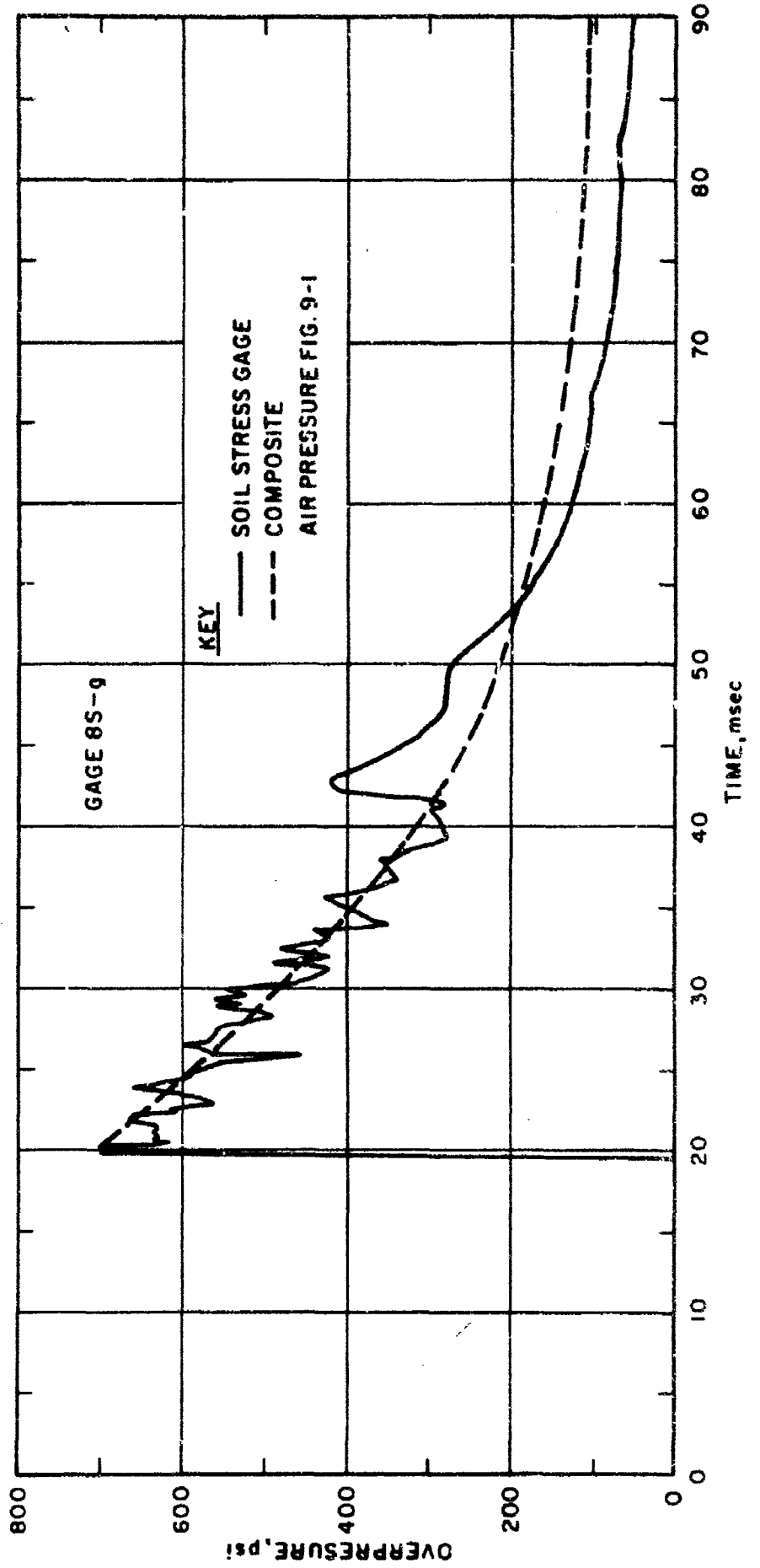


Figure XIV-2. Near-Surface Vertical Soil Stress

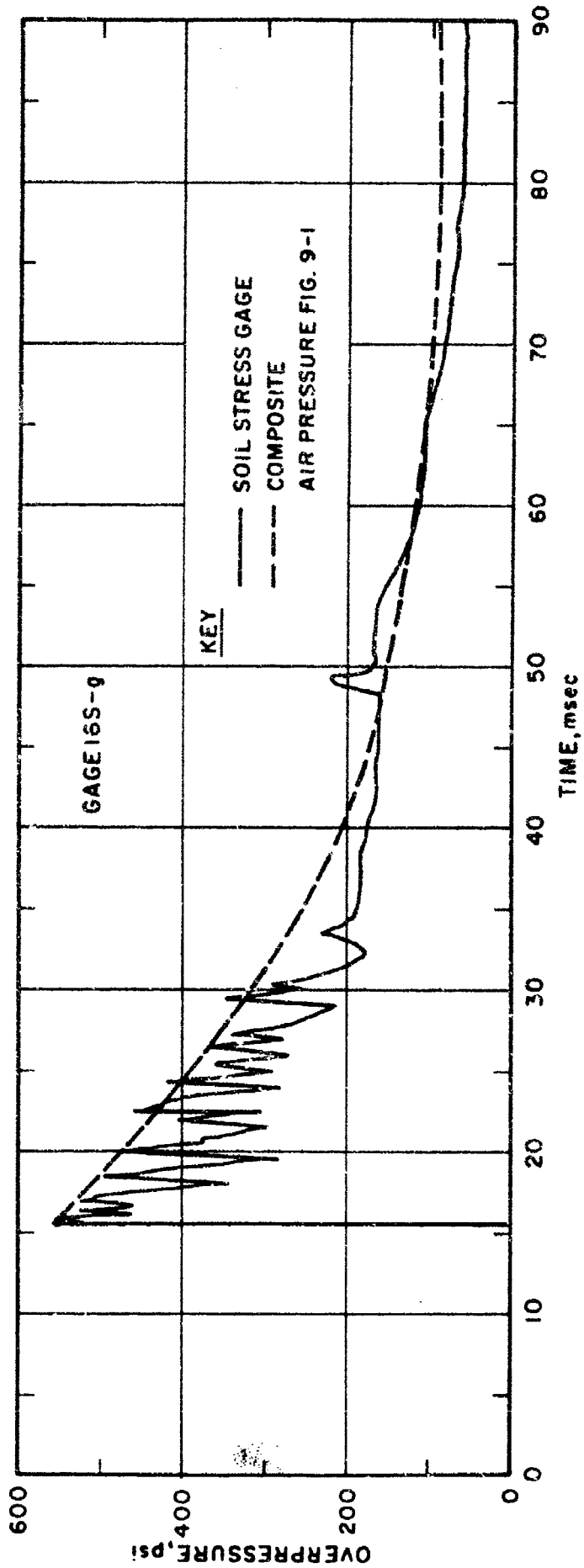


Figure XIV-3. Near-Surface Vertical Soil Stress

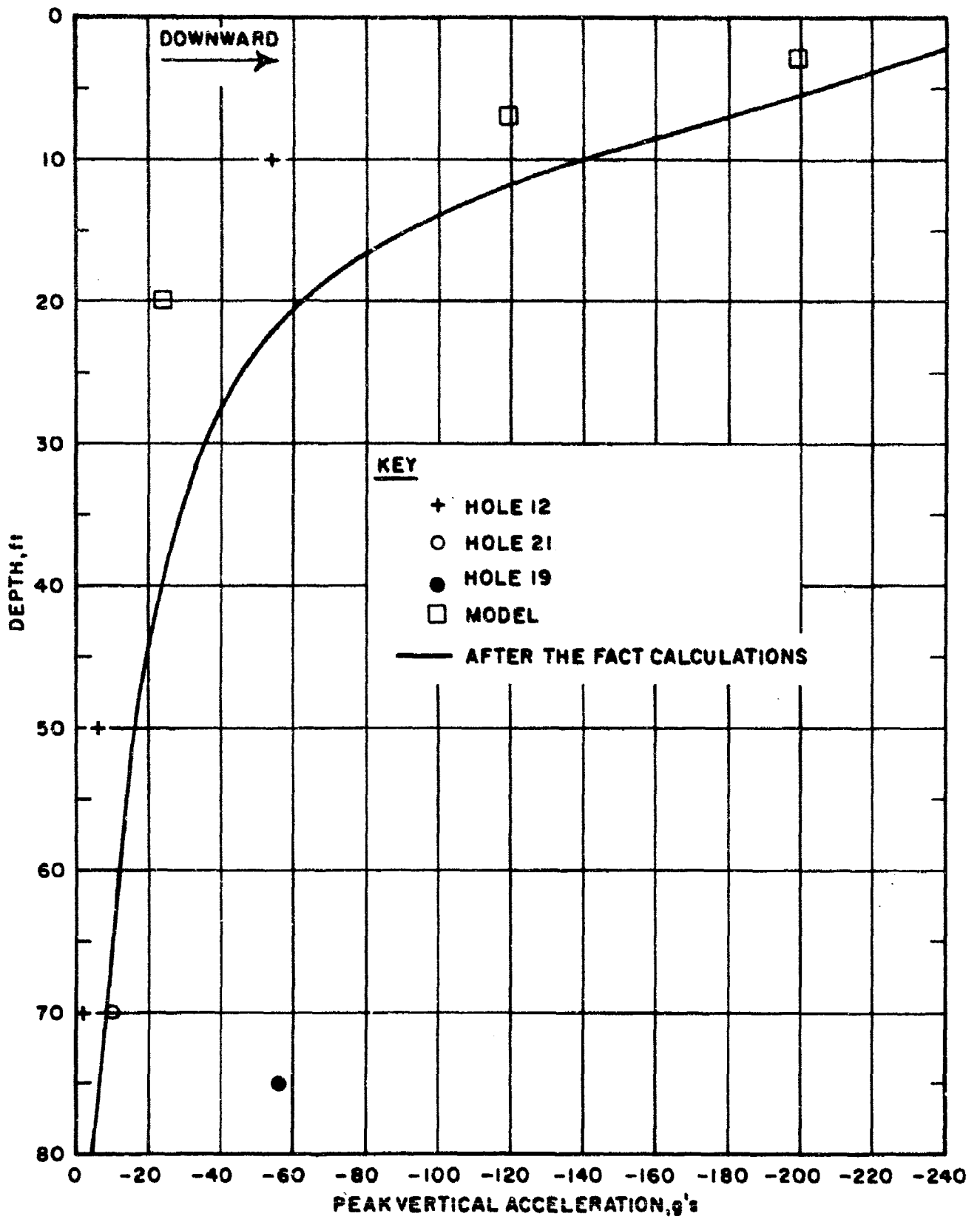


Figure XIV-4. Peak Vertical Accelerations

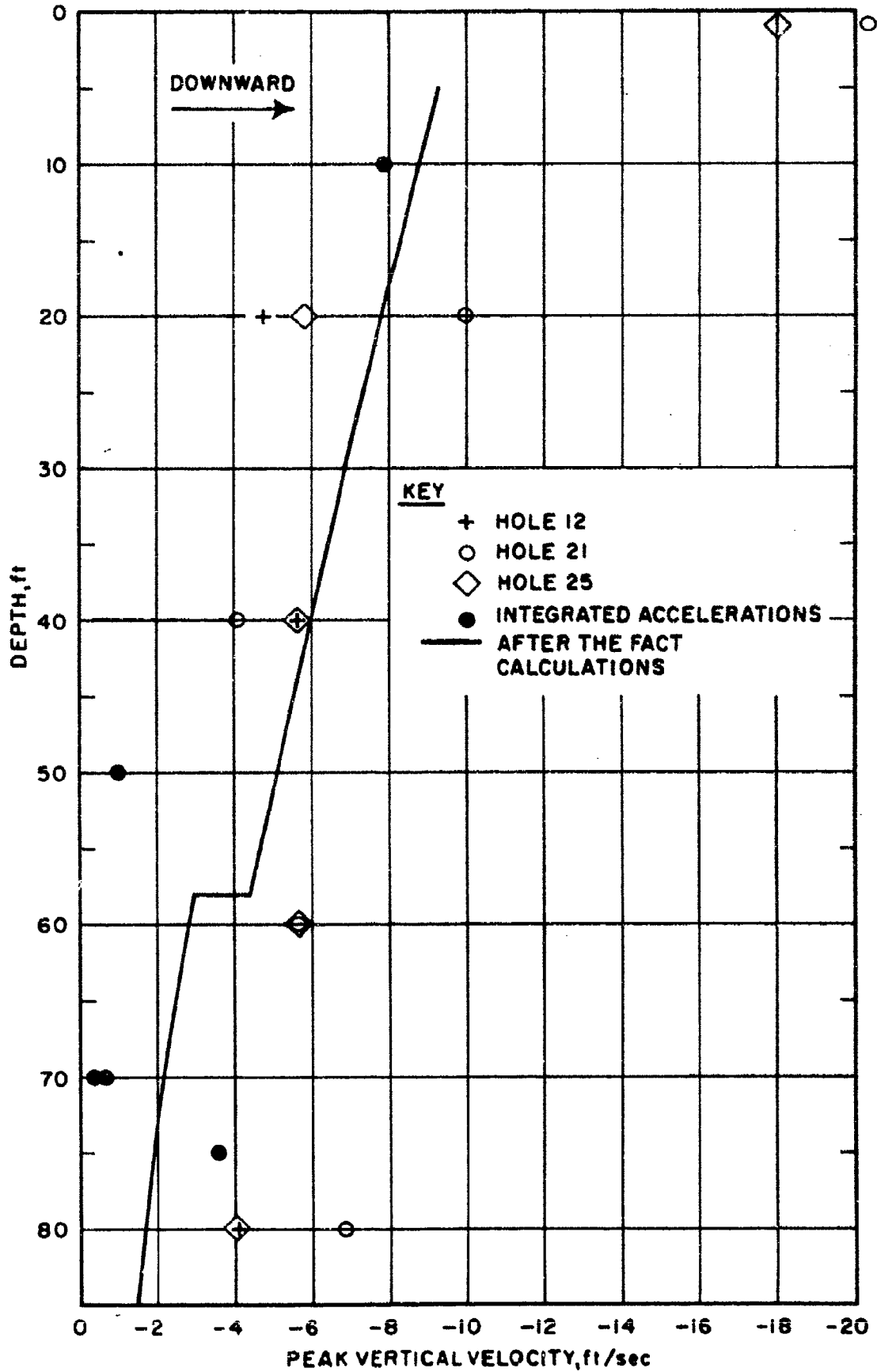


Figure XIV-5. Peak Vertical Velocities

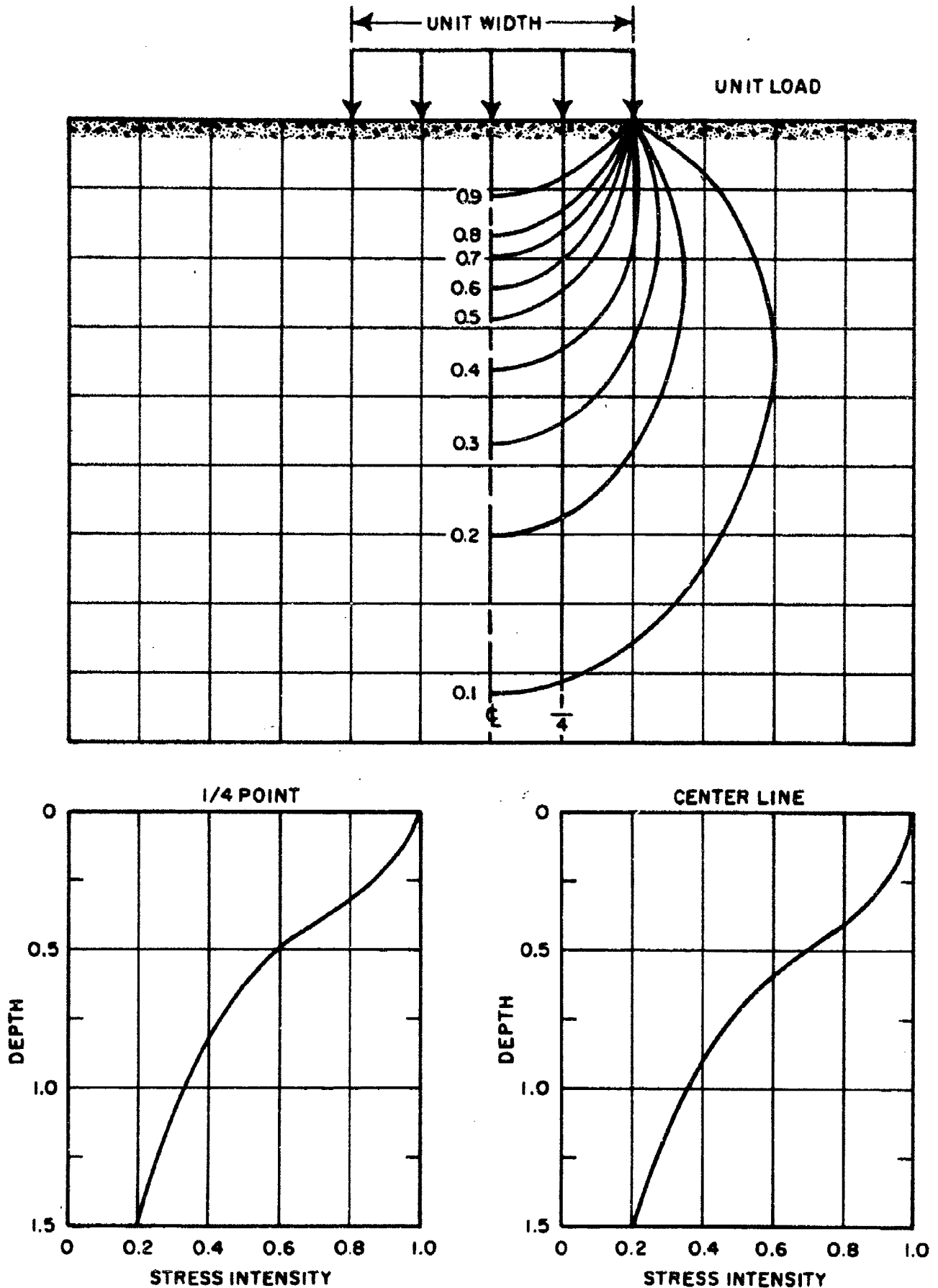


Figure XIV-6. Foundation on an Elastic Soil

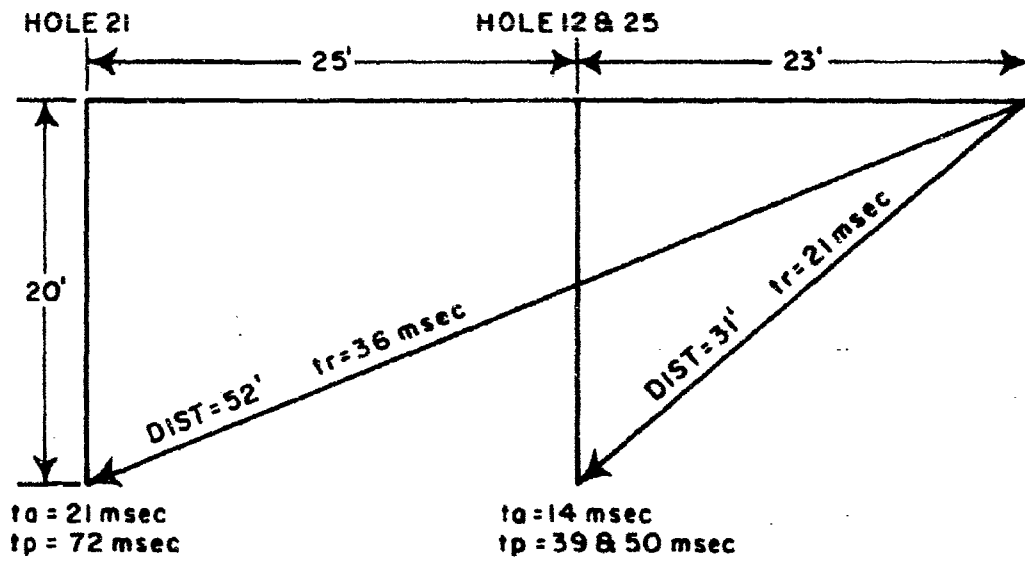


Figure XIV-7. Influence of Rarefaction Waves

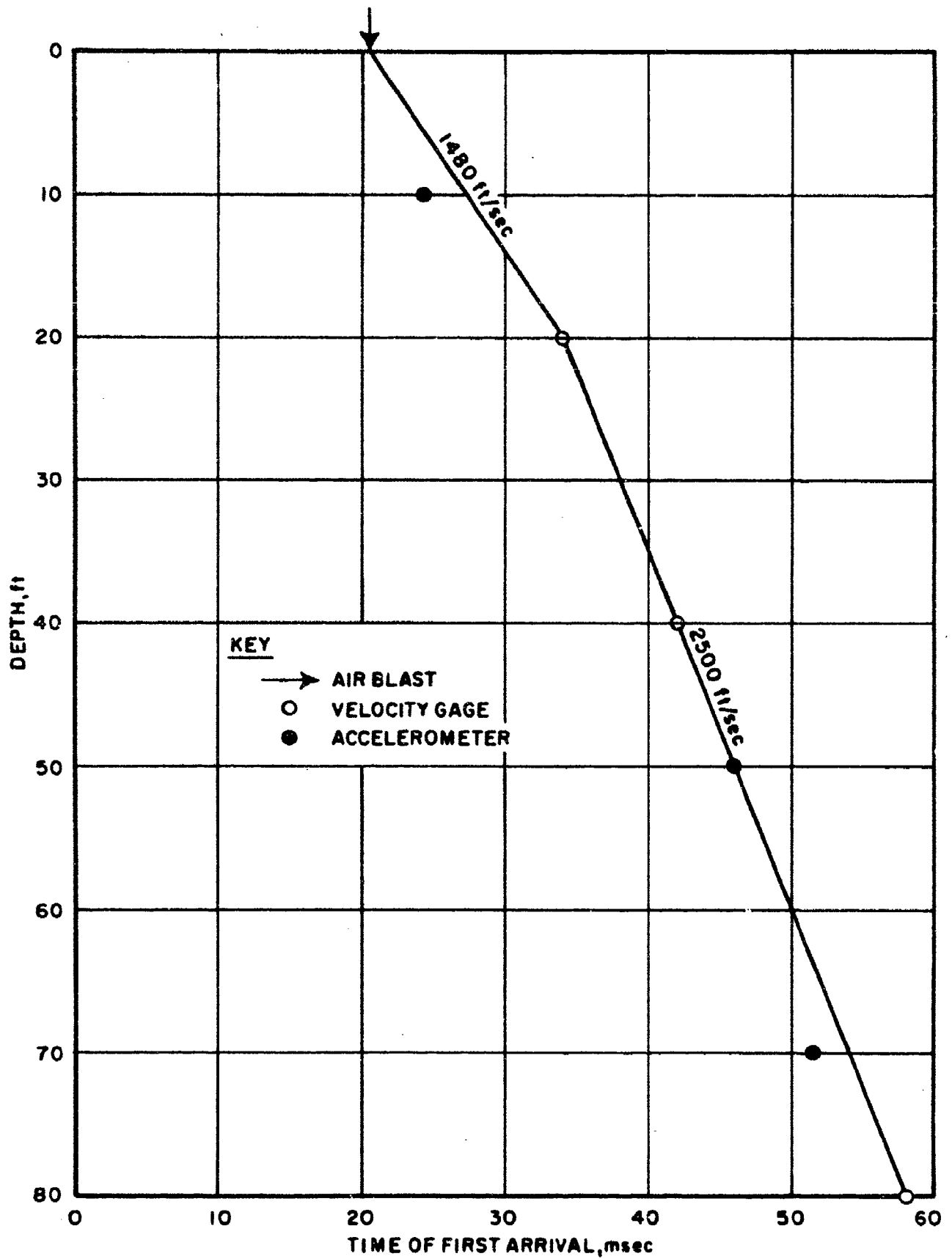


Figure XIV-8. Propagation Velocities, Hole 12

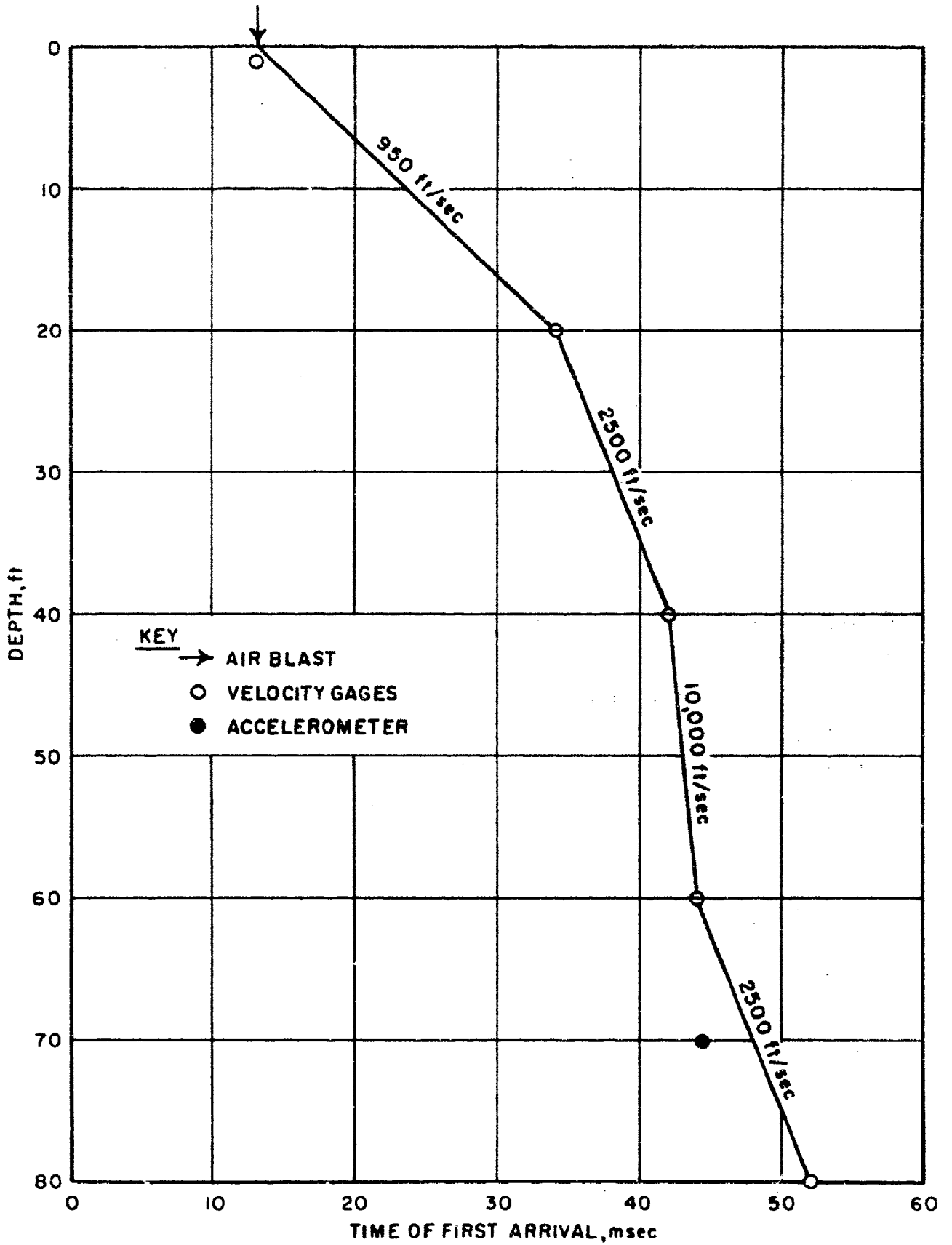


Figure XIV-9. Propagation Velocities, Hole 21

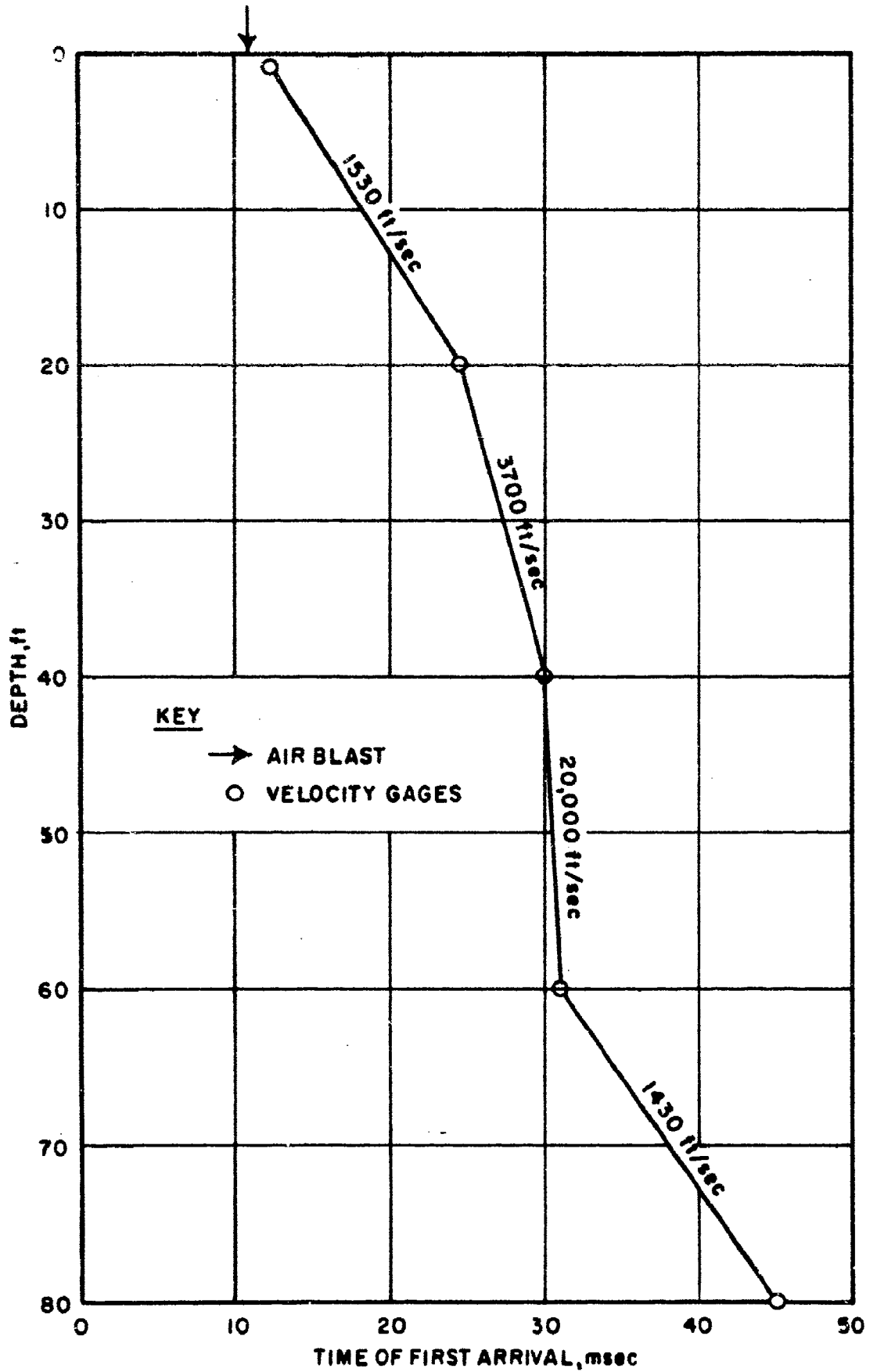


Figure XIV-10. Propagation Velocities, Hole 25

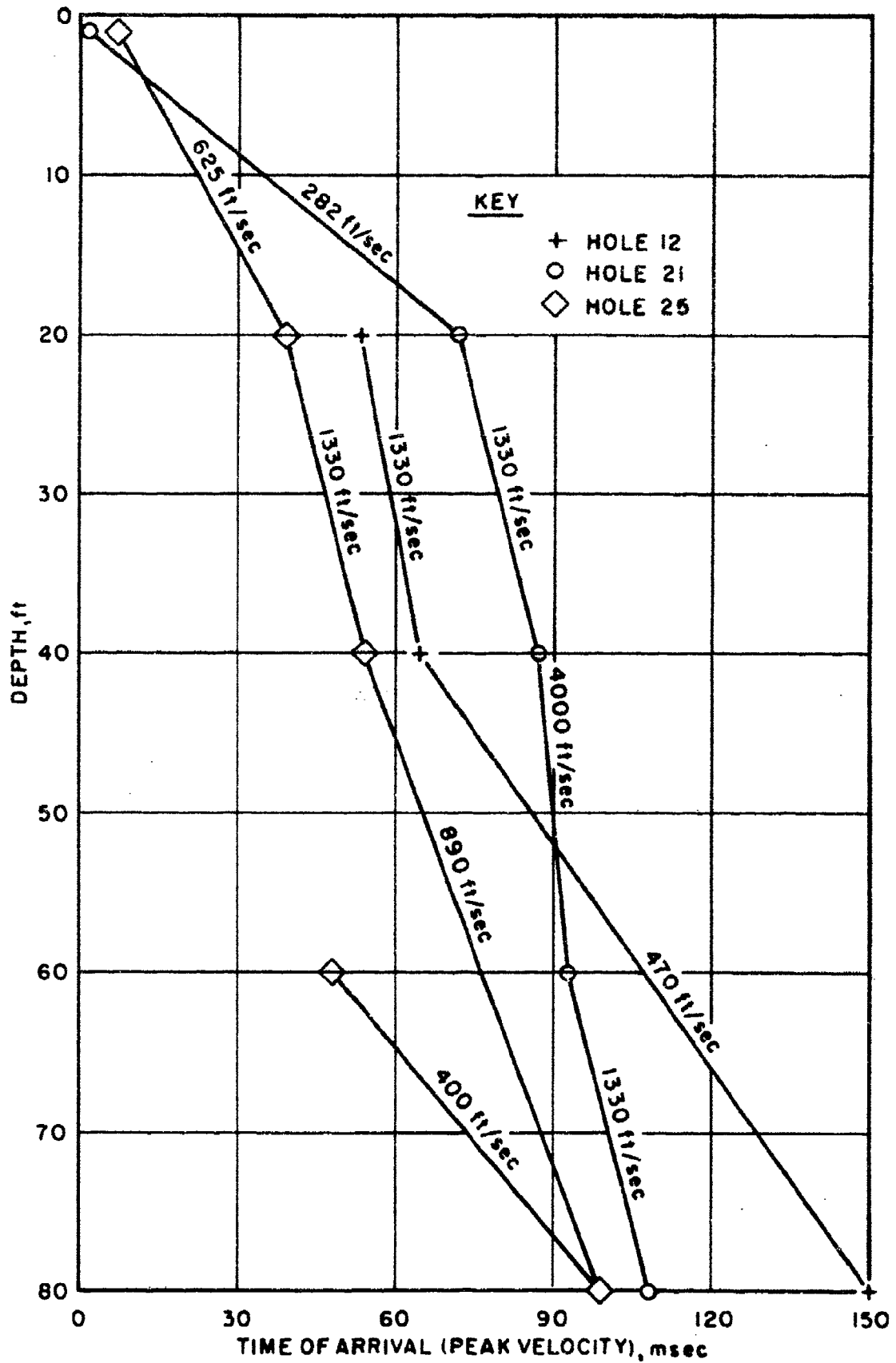


Figure XIV-11. Propagation Velocities (Peak Velocity)

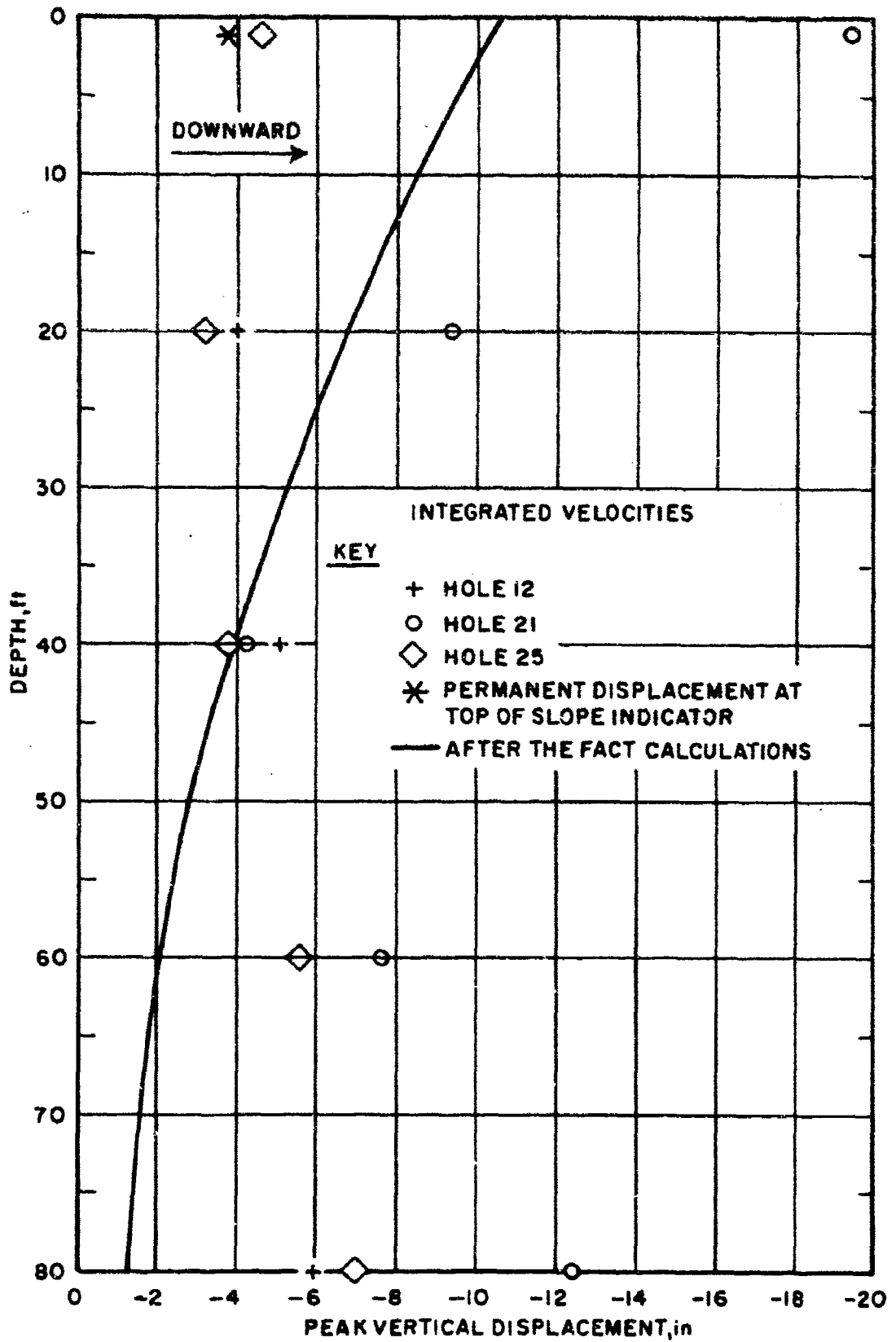


Figure XIV-12. Peak Vertical Displacements

SECTION XV

CONCLUSIONS AND RECOMMENDATIONS

The peak vertical stresses produced by this experiment are presented in figure XV-1. Since no stress data were obtained at depth, this curve was prepared utilizing the after-the-fact attenuation factors given in figure XIV-1. The peak vertical accelerations and velocities produced by this experiment are presented respectively in figures XV-2 and XV-3. The vertical velocities are the most reliable of all the transient earth free-field phenomena measured. These data reflect the nonhomogeneous nature of the soils which underlie the experimental area. The peak vertical displacements produced by this experiment were the most erratic of all the free-field quantities, and a great deal of reliance cannot be placed in the data. It is, therefore, recommended that the calculated curve presented in figure XIV-12 be utilized for defining the variation in peak vertical displacement with depth.

The ground surface experienced a permanent horizontal displacement of approximately 1 inch in a direction opposite to air-blast propagation, and a negligible amount of permanent vertical displacement. However, near-surface structures experienced permanent vertical displacements ranging from 2 to 4 inches. The magnitude and direction of the permanent displacements were primarily governed by elastic rebound phenomena.

The selection of gages for this experiment as regards type, number, and location should have been adequate to meet the project objectives if a high degree of data recovery had been realized. Mechanical and structural changes must be made to both the long-span displacement gage and the slope-indicator gage to successfully measure transient displacements. Electronic and recording problems must be corrected if the earth free-field accelerations and stresses are to be completely described.

The mass of material realistically loaded by this simulation technique is a function of both the size of the loaded area and the shape of the air-blast input. As a rule of thumb, the width of the loaded surface should be twice the depth of interest, and at this depth, the width of realistic simulation is limited to one-half the width of the loaded surface. This is

AFWL TR-65-26, Vol I

illustrated in figure XV-4. In addition, the actual air-blast input must simulate the overpressure-time history from the nuclear yield of interest as described in section I. These considerations should produce a simulated stress environment which does not deviate more than 20 percent from the desired nuclear environment.

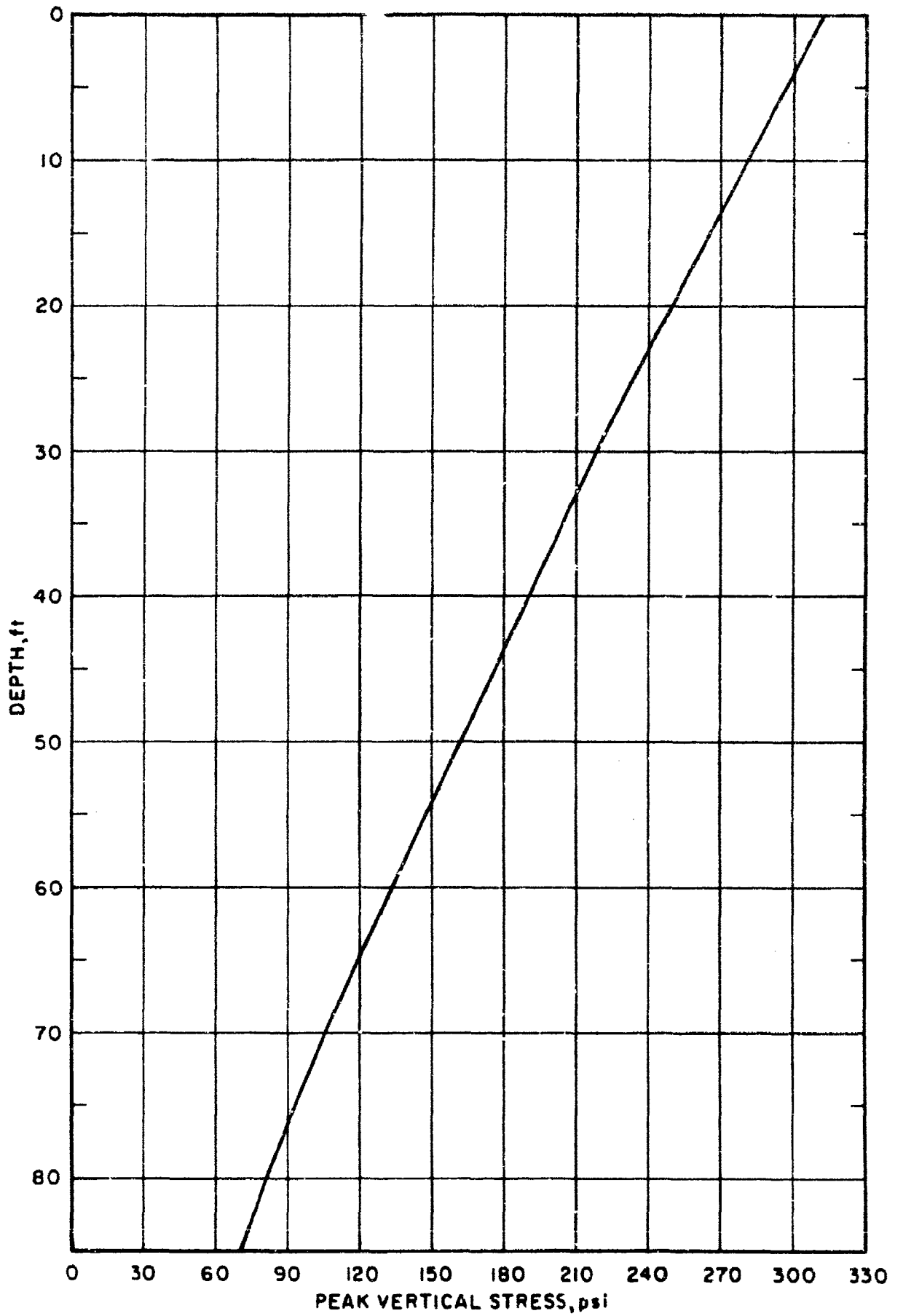


Figure XV-1 Peak Vertical Stresses

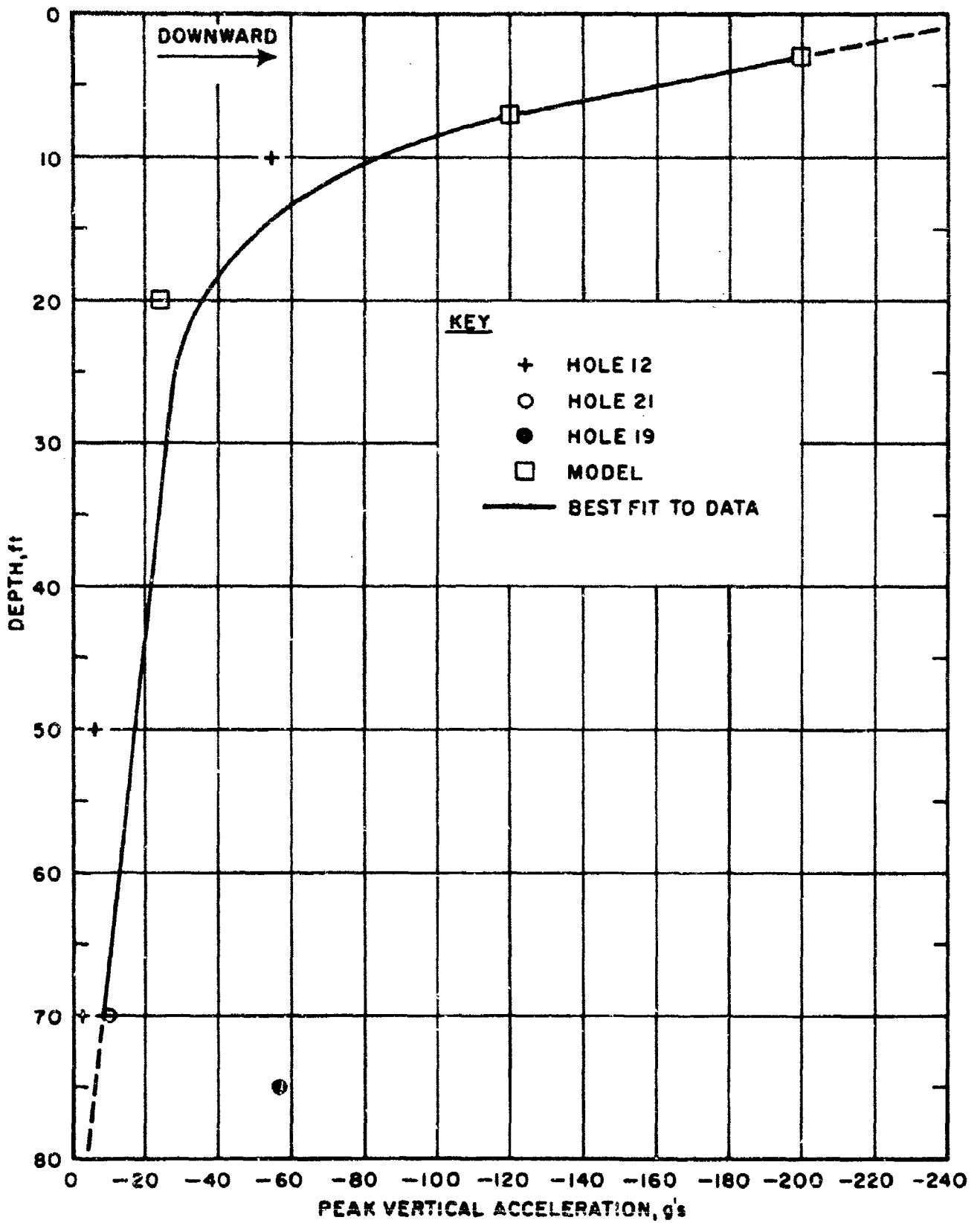


Figure XV-2. Peak Vertical Accelerations

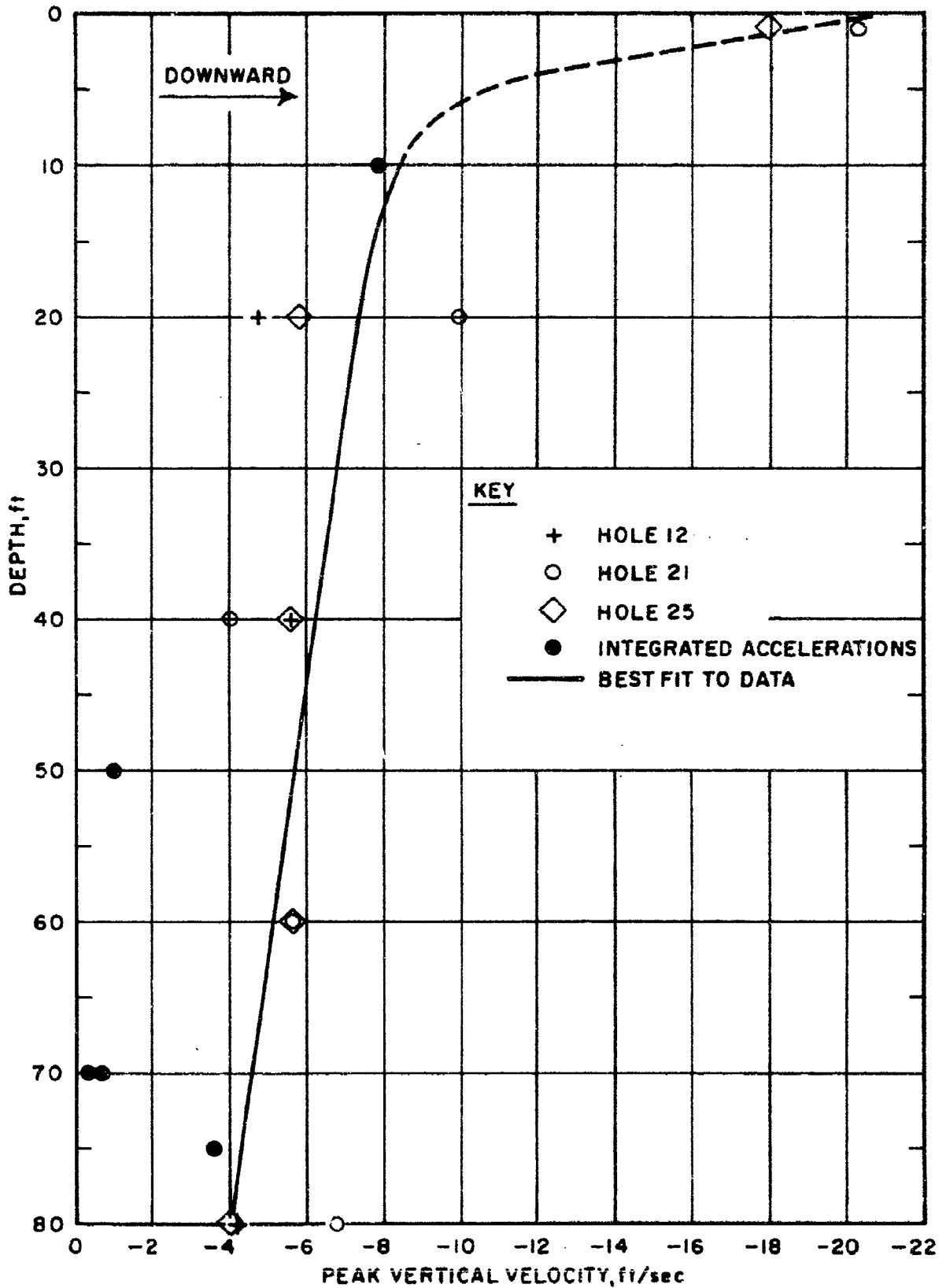


Figure XV-3. Peak Vertical Velocities

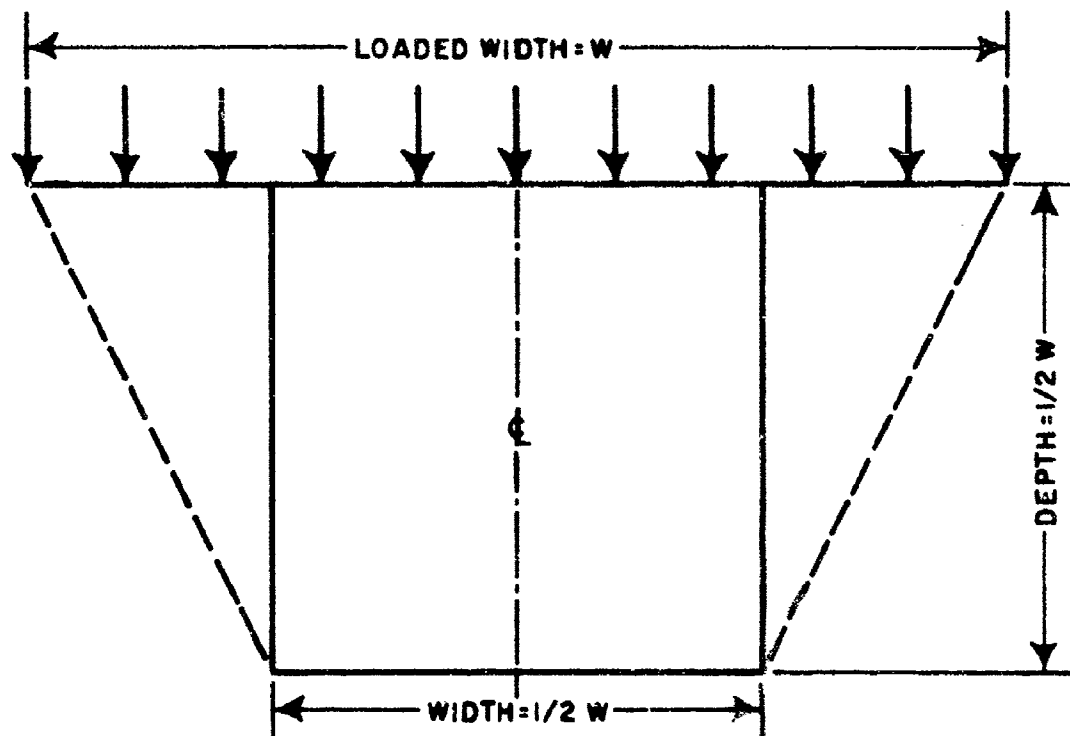


Figure XV-4. Mass of Material Realistically Loaded

APPENDIX A

INSTRUMENTATION EQUIPMENT LIST

This page intentionally left blank.

APPENDIX A
INSTRUMENTATION EQUIPMENT LIST

1. Tape Recorder

a. Make: Ampex

Model: CP-100

Ampex Corporation Instrumentation Products
934 Charter Street, Redwood City, Calif

List of Characteristics:

(1) Tape Transport

(a) Tape Speeds: 60, 30, 15, 7 1/2, 3 3/4, 1 7/8 ips standard

(b) Tape Speed Deviation: ± 0.35 percent maximum

(c) Start Time: 5 seconds or less at 60 ips or 30 ips

3 seconds or less at 15 ips or 7 1/2 ips

1.5 seconds or less at 3 3/4 ips or 1 7/8 ips

(d) Stop Time: Maximum of 2.0 seconds

(2) Direct Record/Reproduce System

(a) Frequency Response and RMS Signal-to-Noise Ratio:

| Tape speed (ips) | Bandwidth (cps) | RMS Signal to RMS Noise | |
|---------------------|---------------------------|----------------------------|--------------------------------|
| | | Bypass filtered (db) | Unfiltered wideband (db) |
| 60 | 300 to 250,000 ± 3 db | 30 | 25 |
| 30 | 200 to 125,000 ± 3 db | 30 | 24 |
| 15 | 200 to 60,000 ± 3 db | 30 | 23 |
| 7 1/2 | 200 to 25,000 ± 3 db | 28 | 21 |
| 3 3/4 | 200 to 12,500 ± 3 db | 28 | 19 |
| 1 7/8 | 200 to 6,250 ± 3 db | 28 | 19 |

(b) Input Consumption: Approximately 1375 recording level; operable from 0.7 to 10.0 volts rms.

(c) Input Impedance: Minimum 18,000 ohms resistive, in parallel with 275 micromicrofarads, unbalanced to ground.

(d) Output Level: 1.0 volt rms nominal across a 10,000 ohms or greater impedance.

(e) Output Impedance: Less than 100 ohms.

(f) Control Track Generator: Subcarrier frequency 17 kc or 18.24 kc. Modulating frequency 60 cps ± 0.02 percent. Modulation 50 percent ± 5 percent.

(3) Power Requirements

(a) Voltage: 105 to 125 volts, single phase, 48 to 62 cps or 380 to 420 cps AC; or 210 to 250 volts, single phase, 48 to 62 cps or 380 to 420 cps AC; or 26 to 30 volts DC, ripple 2 volts peak-to-peak maximum.

(b) Power Consumption: Approximately 375 watts for a 14 track system.

(4) Environment

(a) Temperature: Operating $+40^{\circ}\text{F}$ to $+125^{\circ}\text{F}$. Storage non-operating -20°F to 160°F .

(b) Altitude: Operating 10,000 feet; nonoperating 20,000 feet.

(c) Relative Humidity: Up to 95 percent without condensation space.

b. Make: Consolidated Electrodynamics

Model: PR-3300

Consolidated Electrodynamics Corporation
360 Sierra Madre Villa, Pasadena, Calif

List of Characteristics:

(1) Transport

(a) Tape Speeds: Six standard speeds in 3 pairs (60, 30 ips; 15, 7 1/2 ips; and 3 3/4, 1 7/8 ips)

(b) Tape Speed Accuracy: ± 0.25 percent

(c) Start Time: Less than 3 seconds at a speed of 60 ips and 2 seconds at lower speeds.

(d) Stop Time: Less than 2 seconds at 60 ips and 1 second at all other capstan controlled speeds.

(2) Direct Record and Reproduce System

(a) Frequency Response and Signal-to-Noise Ratio:

| Tape Speed (ips) | 60 | 30 | 15 | 7 1/2 | 3 3/4 | 1 7/8 |
|-----------------------|-------------------------|------------------------|------------------------|--------------------------|--------------------------|---------------------------|
| Bandwidth measured | 300 cps to 100 kc | 200 cps to 50 kc | 100 cps to 25 kc | 100 cps to 12.5 kc | 100 cps to 6.25 kc | 100 cps to 3.125 kc |

| | | | | | | |
|---------------------------------------|--------|--------|--------|--------|--------|--------|
| Frequency response ref to 1 kc | +3 db | +3 db | +3 db | +3 db | -3 db | +3 db |
| S-N-R(RMS) 300 cps to band edge | -35 db |

(b) Input Level: 1 volt rms nominal (0 db) to produce normal recording level.

(c) Input Sensitivity: 0.25 to 10 volts rms.

(d) Input Impedance: 20k ohms, unbalanced to ground.

(e) Output Level: 1 volt rms nominal (0 db) across a 600-ohm load impedance.

(f) Output Impedance: Less than 100 ohms in series with 25 mf unbalanced to ground.

(g) Distortion: 1 percent 3rd harmonic distortion of a one kc signal and less than 0.6 percent intermodulation distortion when recording and reproducing at normal record level (0 db) at 60 ips.

2. Timing Control System

a. Make: Hyperion

Model: Hi-140-12-S

Hyperion Industries, Inc.
Watertown, Mass

List of Characteristics

(1) WWV Synchronize: Automatically synchronizes time code generator with WWV with accuracy of 1 msec.

(2) Decimal time-of-day display; continuous decimal in-line display synchronized with output time codes. Time of day displayed in hours, minutes, seconds, tenths of seconds.

(3) Time Base: Internal 1 mc crystal controlled oscillator with stability of five parts in 10^9 per day.

(4) Serial Time Code Outputs:

(a) IRIG-A

(b) IRIG-B

(5) Serial Modulated Time Code Output:

0 to 5 volts P-P into 1 k

IRIG Modulated into 100 kc carrier

IRIG Modulated into 1 kc carrier

- (6) DC Level Shift Output: DC level shift code output is 0 to -6 volts P-P into 1 k ohm. Rise time 2 microseconds.
- (7) Power Requirements: 105 to 125 V, 60 to 440 cps.
- (8) Operating Environment: -25°C to +55°C in 95 percent humidity.

3. Signal Conditioning Equipment

a. Make: Consolidated Electrodynamics Corporation

Model: CEC System D (Type 1-113B Carrier Amplifier)

Consolidated Electrodynamics Corp., Data Recorders Division
360 Sierra Madre Villa, Pasadena, Calif

List of Characteristics:

- (1) Full Scale Output: ± 5 ma into a 26-ohm load.
- (2) Sensitivity: Input signal for maximum output, 1 mv with no attenuation, 1 volt maximum with full attenuation.
- (3) Input Impedance: Approximately 1,800 ohms.
- (4) Input Attenuator: 1 to 1,000 in 20 steps.
- (5) Bridge Balance System: Will accommodate four external bridge arms composed of wire strain gages or other resistance elements or two-arm variable-reluctance transducers suitable for use at 3 kc.
- (6) Linearity: Output current proportional to input voltage within 2 percent of maximum output.
- (7) Frequency Response: Galvanometer trace amplitude constant (+2 percent) for modulating frequencies from 0 to 600 pcs.

b. Make: Allegany

Model: Sensor Analogue Module (SAM-1)

Allegany Instrument Company, Division of Textron Electronics, Inc.
1091 Wills Mountain, Cumberland, Maryland

List of Characteristics:

- (1) Gain Range: 100 to 2,000, continuous with vernier
- (2) Amplifier Balance Control Range: ± 100 microvolts referred to the input.
- (3) Balance Range: ± 10 percent of scale standards.
- (4) Linearity: 0.02 percent of full scale at DC.
- (5) Frequency Response: DC to 40 kc. Down 3 db at 40 kc with vernier fully counterclockwise.
- (6) Noise: 7 microvolts rms, DC to 40 kc. Two microvolts peak-to-peak, DC to 3 cps.

- (7) Drift: 0.3 microvolt/°F referred to input.
- (8) Output Impedance: Less than 0.1 ohm at DC.
- (9) Output Voltage: 10 volts DC or peak AC to 20 kc.
- (10) Output Current: 100 ma DC.
- (11) Common Mode Rejection: 90 db at 60 cps.

4. Air Pressure Gage

a. Make: Norwood

Model: 111 Bonded Strain Gage Pressure Transducer

Advanced Technology Laboratories, A Division of American-Standard
360 Whisman Road, Mountain View, Calif

List of Characteristics:

- (1) Nonlinearity: Better than 0.5 percent of F.S. by terminal method or 0.25 percent by best straight line through zero method.
- (2) Hysteresis: Better than 0.5 percent of F.S.
- (3) Repeatability: Better than 0.1 percent of F.S.
- (4) Resolution: Infinite.
- (5) Acceleration Effect: Less than 0.1 percent F.S. per g in all planes.
- (6) Vibration Effect: Insensitive from 50 to 2,000 cps to 100 g in 3 planes.
- (7) Zero Pressure Output: Less than ± 2 percent of F.S. at rated excitation.
- (8) Resonant Frequency: Approximately 45,000 cps.
- (9) Frequency Response: Flat within \pm db from 0 to 20,000 cps.
- (10) Pressure Limit: 150 percent of F.S. for static pressure (125 percent for 100 psi range). Full scale for dynamic pressures.
- (11) Recommended Excitation: 10 volts DC or AC, 17 volts maximum.
- (12) Electrical Output: 3.5 mv/v ± 20 percent for -34 bridge, 3.0 mv/v ± 2 percent for -35 and -36 bridge.

b. Make: Scheavitz-Bytrex

Model: HFG-2000

Bytrex Corporation, Kulite-Bytrex Corporation
50 Hunt Street, Newton, Mass

List of Characteristics:

- (1) Output Signal: 100 mv F.S. minimum.

(2) Output Impedance: 1,300 ohms at 80°F, increases approximately 0.015 percent/°F.

(3) Input Impedance: 500 ohms at 80°F, increases approximately 0.06 percent/°F.

(4) Excitation: 20 volts DC or AC rms.

(5) Natural Frequency: 100 kc.

(6) Shock: Will Withstand more than 2,500 g on all axes.

(7) Acceleration Sensitivity: 0.002 percent per g.

(8) Operating Temperature Range: -65 to +300°F.

(9) Nonlinearity and Hysteresis: Less than 1 percent, combined.

(10) Maximum Allowable Pressure: 150 percent of range without damage, 200 percent of range without rupture.

(11) Measuring Range: 0 to 2,000.

5. Accelerometers

a. Make: Statham

Model: A69TC-350

Statham Instruments, Inc.

12401 West Olympic Blvd, Los Angeles, Calif

List of Characteristics:

(1) Acceleration Range: ± 100 g to ± 500 g.

(2) Bridge Resistance: 350 ohms.

(3) Excitation: 5 volts DC or AC rms.

(4) Full Scale Output: Approximately ± 20 mv.

(5) Operating Temperature Range: -40°F to +200°F.

(6) Direction of Sensitivity: Perpendicular to base.

(7) Overload: Three times rated range.

(8) Transverse Acceleration Response: Less than 0.02 g/g for transverse accelerations up to rated range.

(9) Nonlinearity and Hysteresis: Less than ± 1 percent of F.S. output.,

(10) Natural Frequency: Approximately 2,000 cps.

6. Soil Pressure Gages

a. Make: Lynch

Model: Developed and fabricated in Air Force Weapons Laboratory

List of Characteristics:

- (1) Frequency Response: Greater than 100 kc.
- (2) Range: 0 to greater than 2,000 psi.

7. Velocity Gage

a. Make: Sandia Corporation

Model: DX-B, variable reluctance type

List of Characteristics:

- (1) Frequency Response: 0.02 to 400 cps.
- (2) Maximum Range: 100 fps.
- (3) Excitation: 4 volts rms.

8. Time-of-Arrival System

100-channel digital display actuated by omnidirectional inertia switches. read out on 16-mm film run at 1,000 fps. Supplies a three-dimensional analog of energy transmission in soil.

9. Long-Span Strain Gage

a. Make: Developed and fabricated in Air Force Weapons Laboratory

Model: Helical potentiometer type

List of Characteristics:

- (1) Frequency Response: 12 cps.
- (2) Rise Time: 21 msec.
- (3) Range: Up to 100-ft length.

This page intentionally left blank.

APPENDIX B

AIR-BLAST RECORDS

This page intentionally left blank.

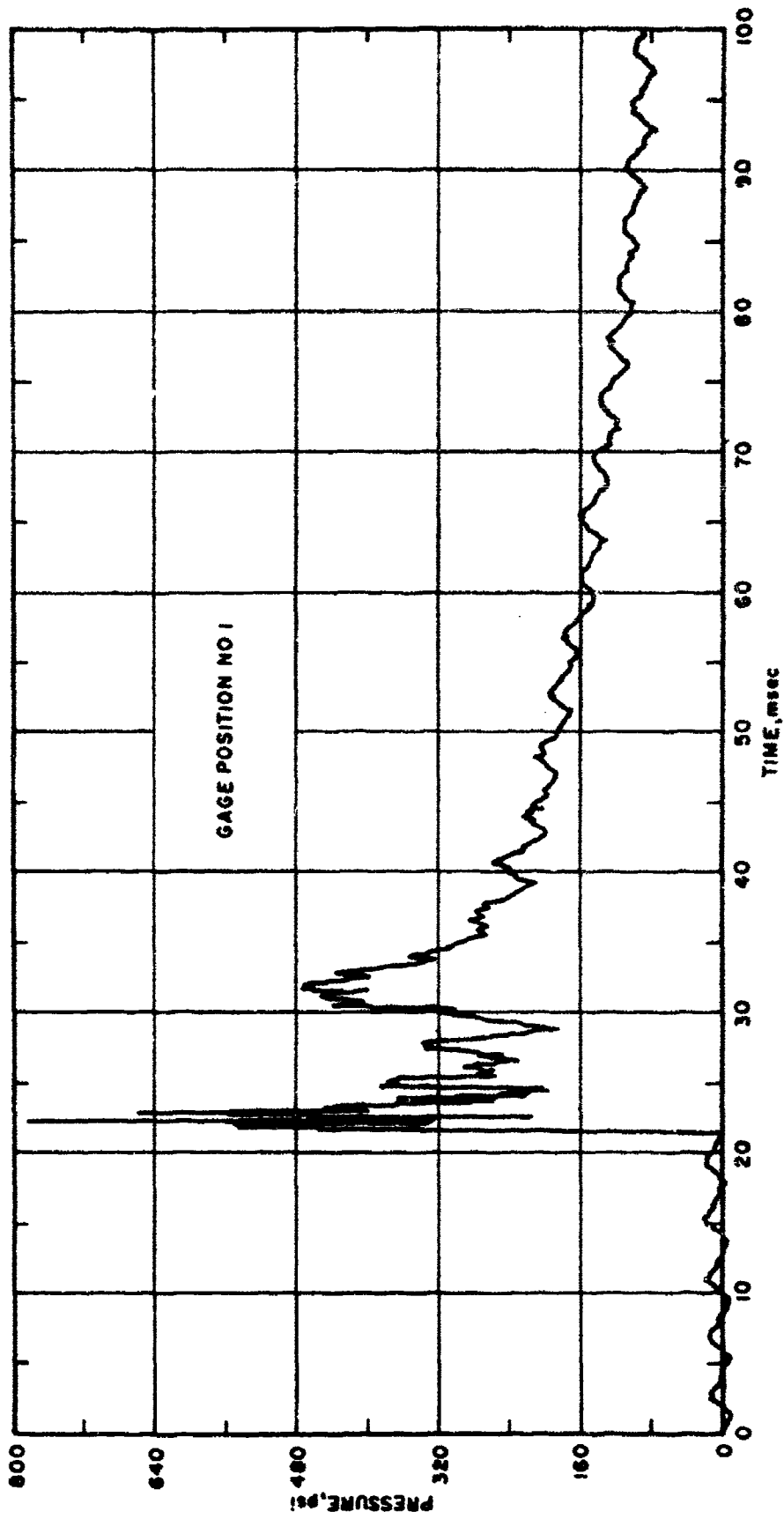


Figure B-1. Air Pressure versus Time

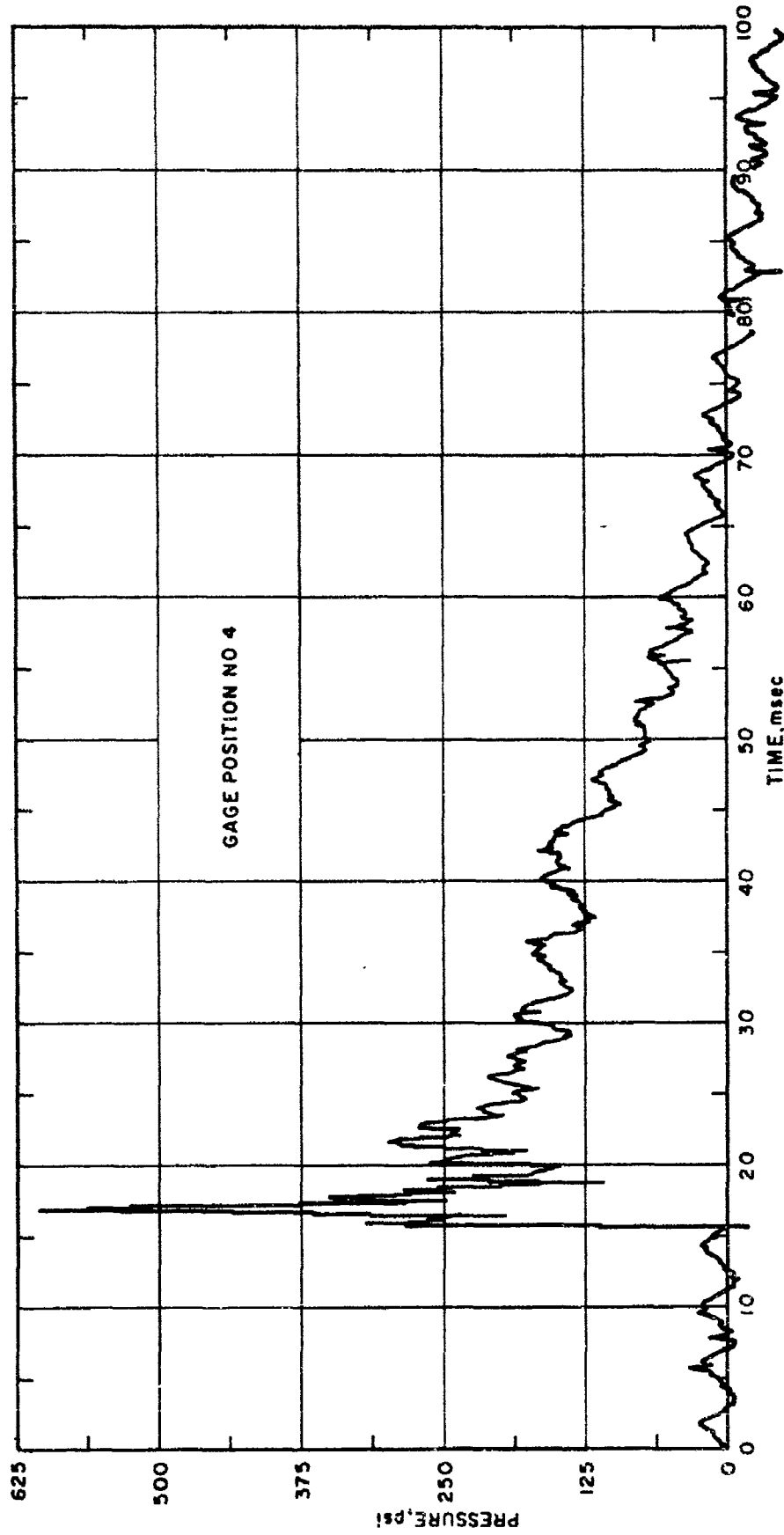


Figure B-2. Air Pressure versus Time

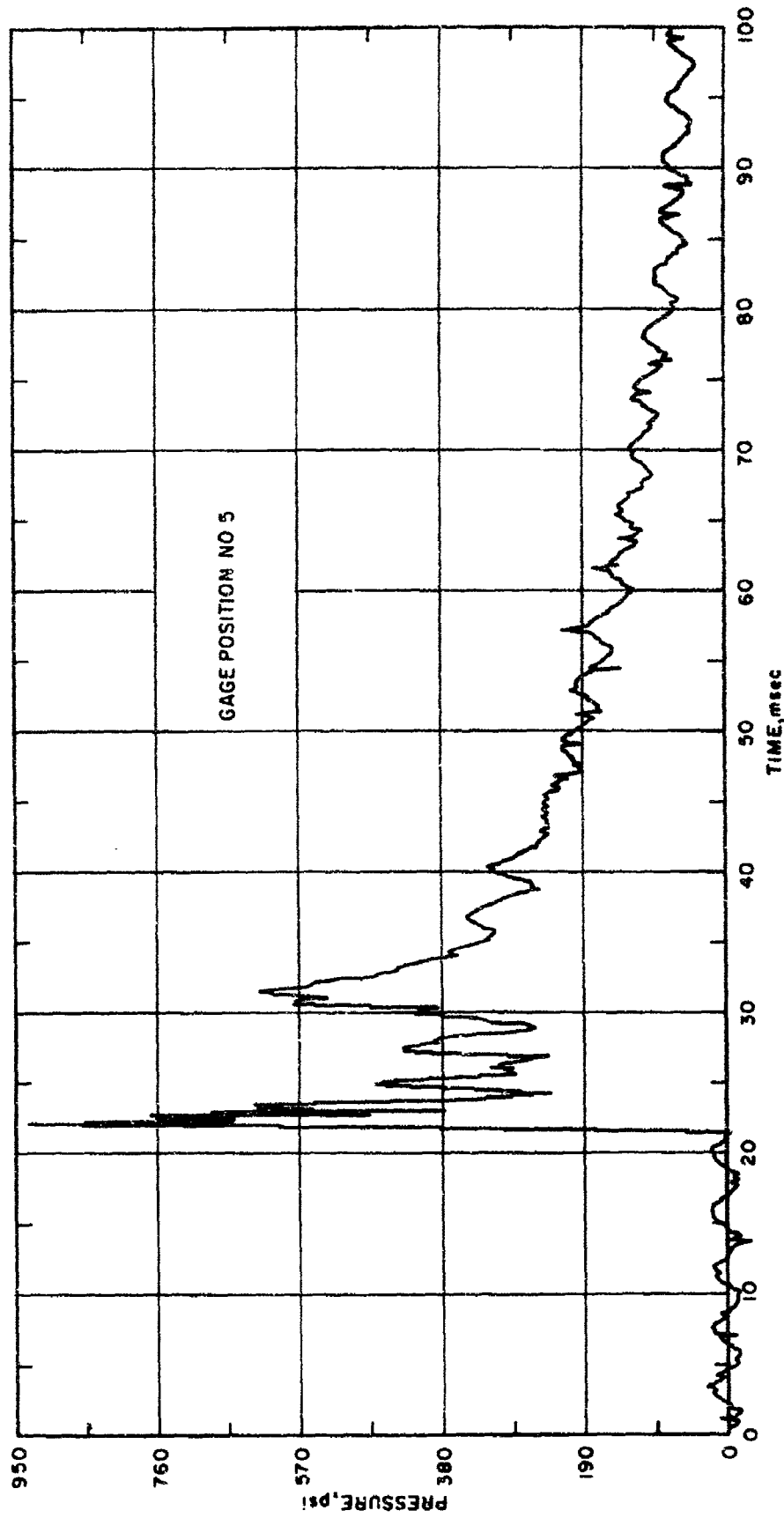


Figure B-3. Air Pressure versus Time

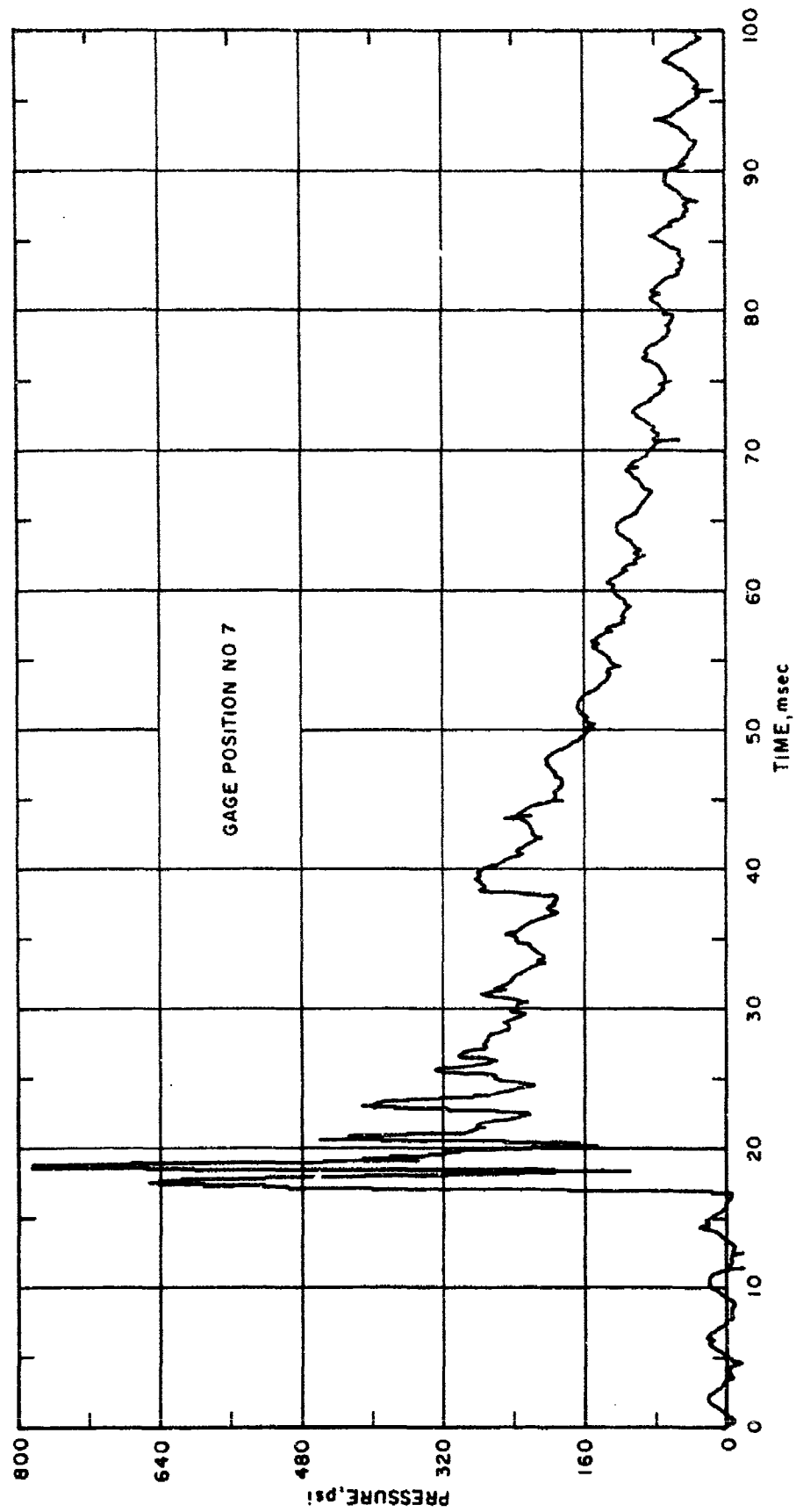


Figure B-4. Air Pressure versus Time

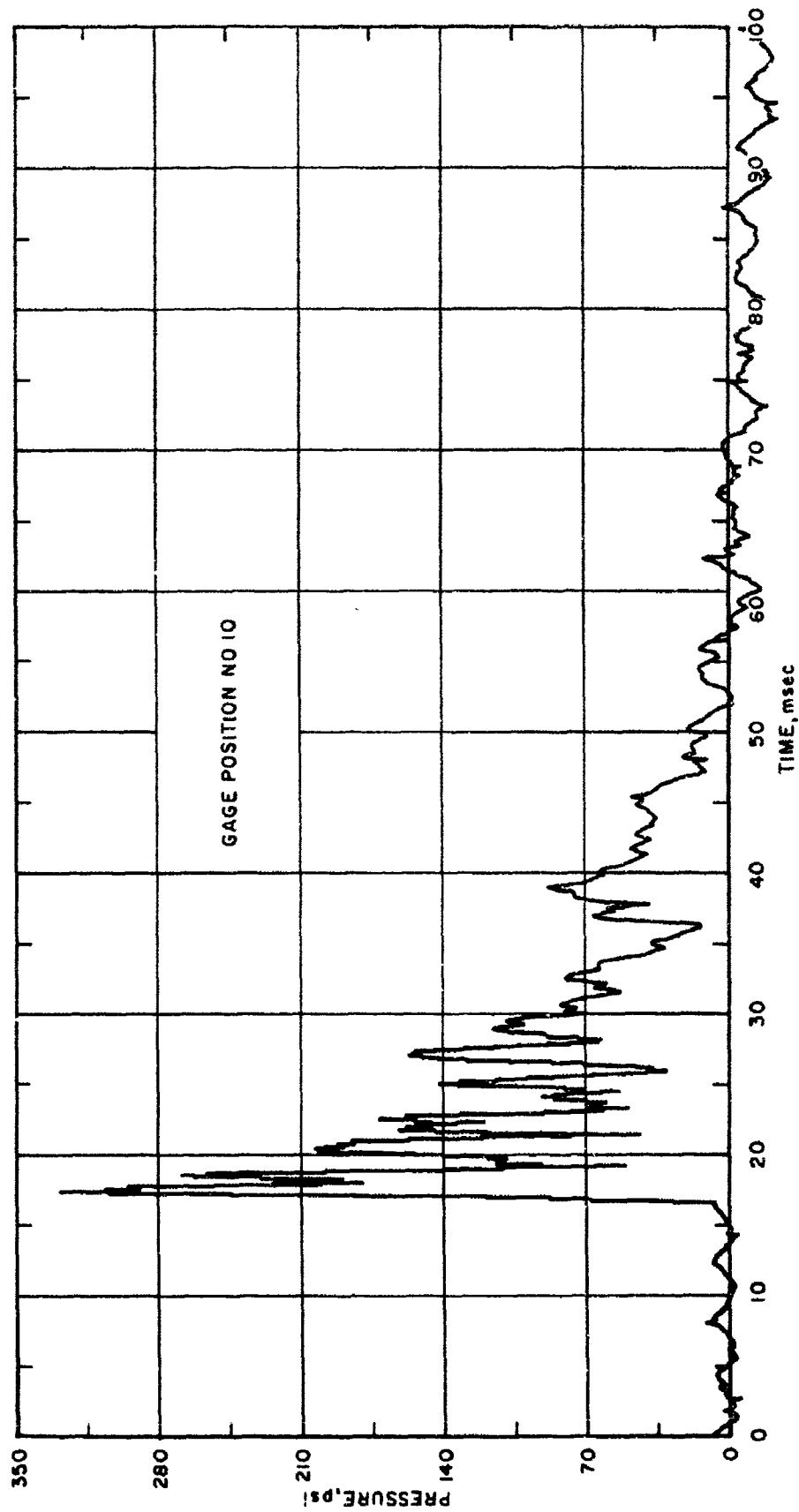


Figure B-5. Air Pressure versus Time

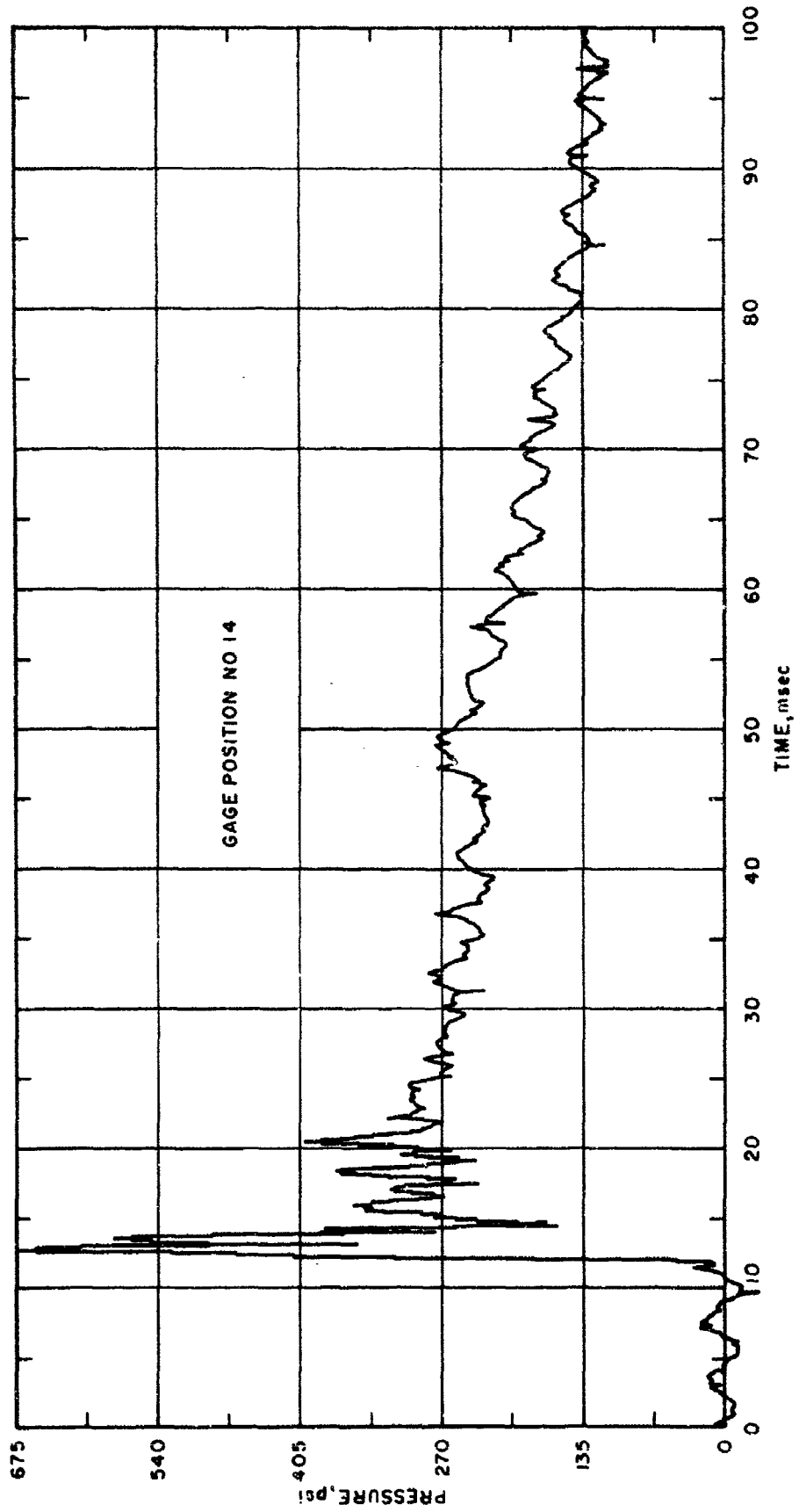


Figure B-6. Air Pressure versus Time

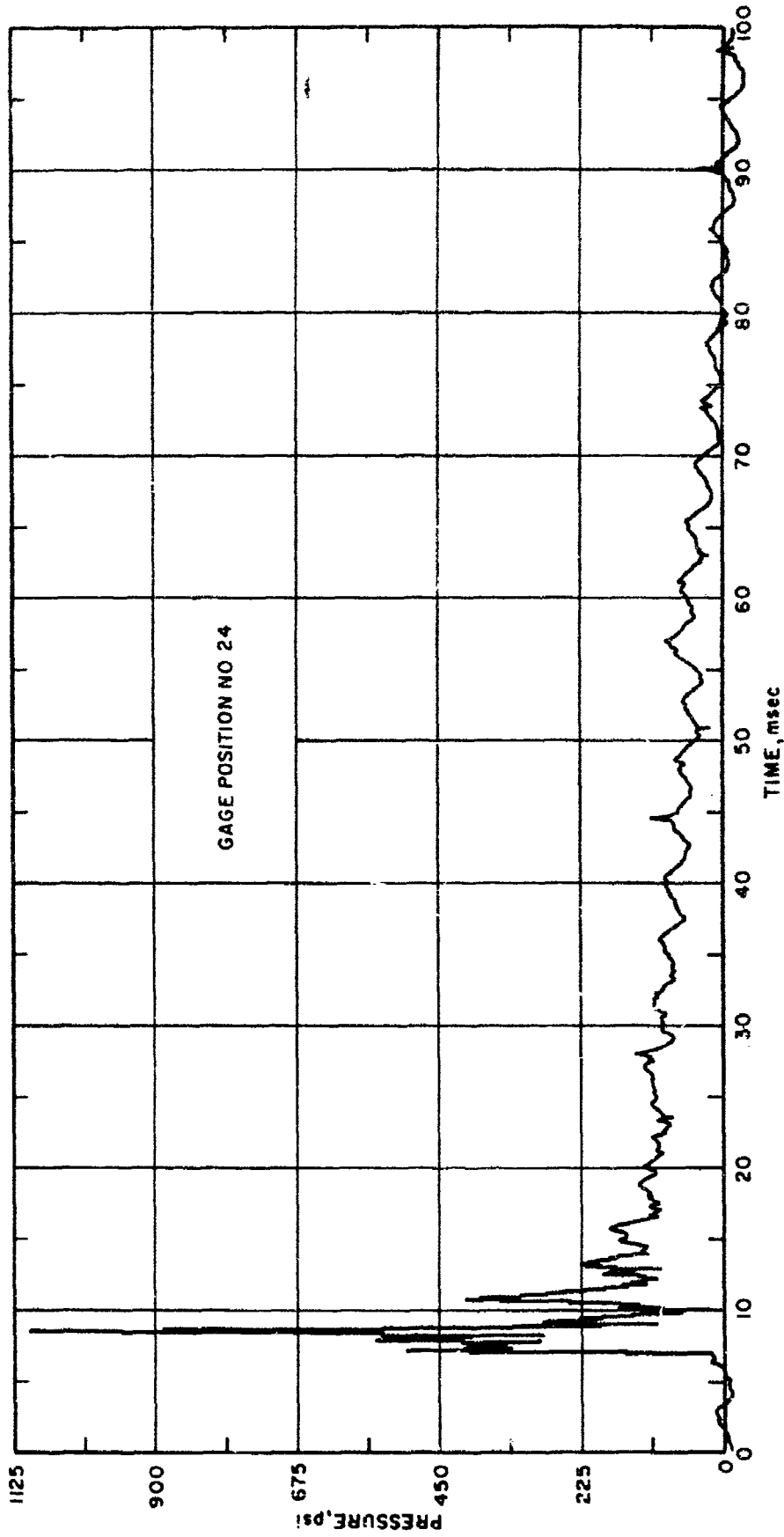


Figure B-7. Air Pressure versus Time

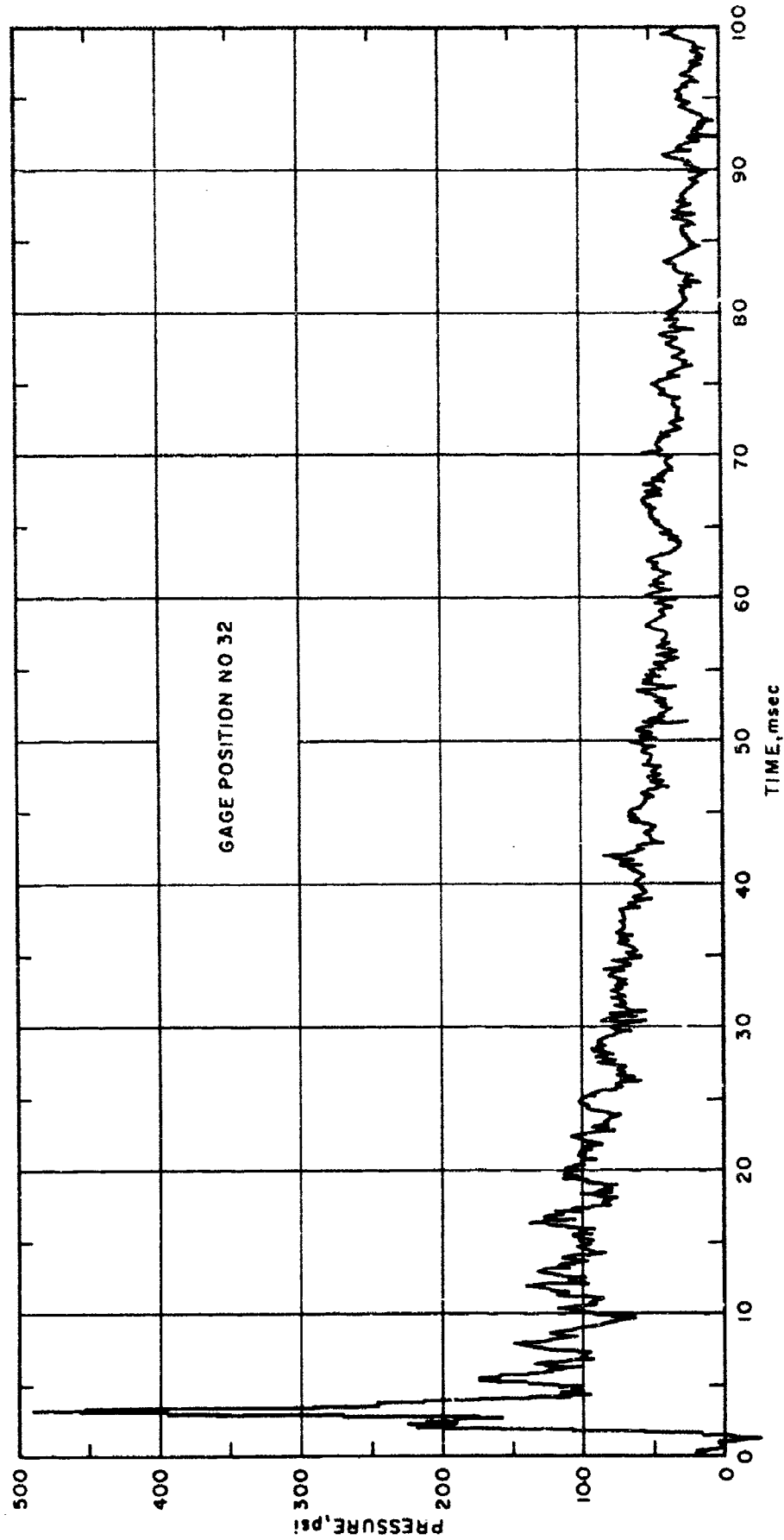


Figure B-8. Air Pressure versus Time

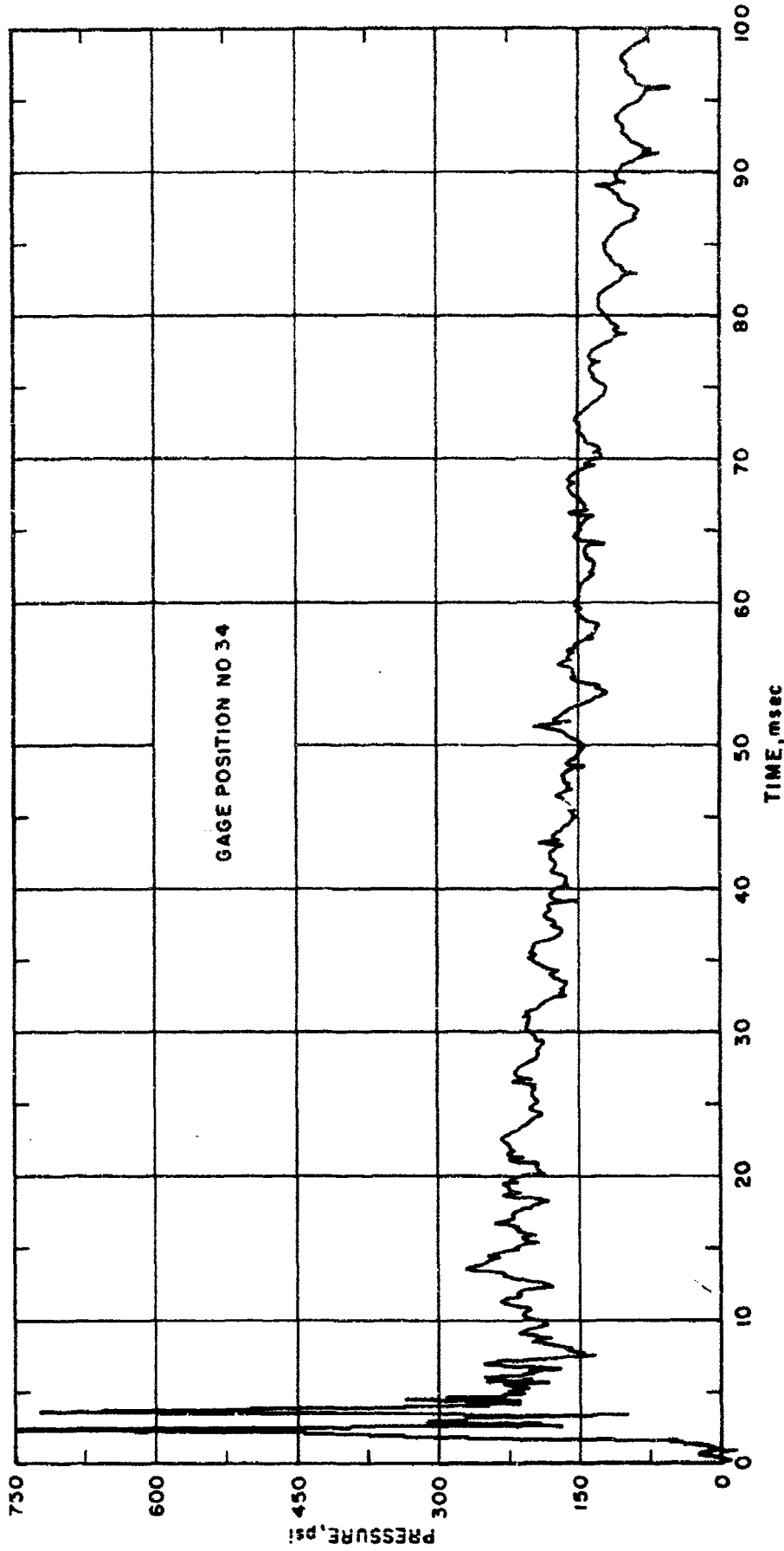


Figure B-9. Air Pressure versus Time

This page intentionally left blank.

APPENDIX C

FREE-FIELD GROUND MOTION RECORDS

This page intentionally left blank.

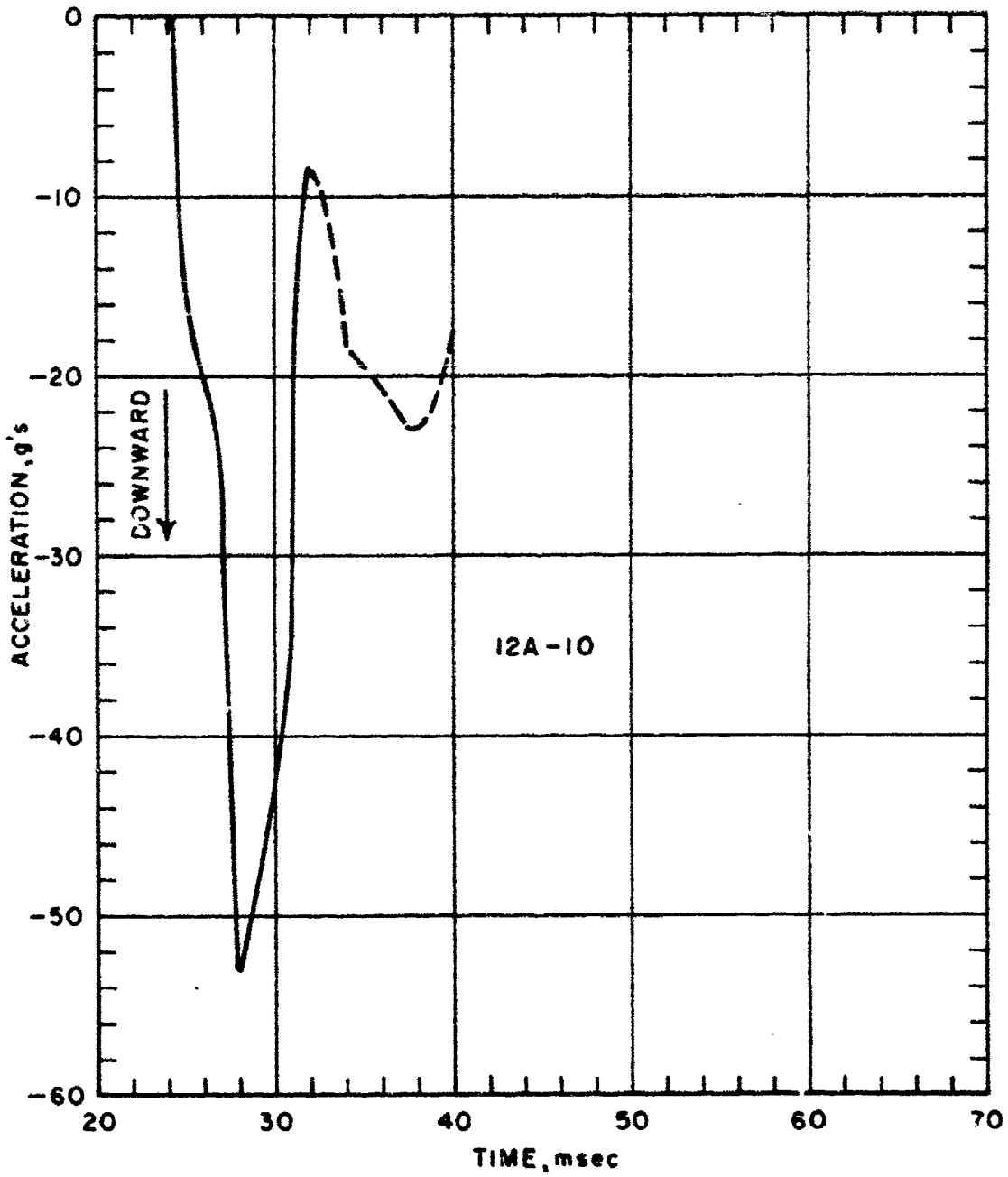


Figure C-1. Vertical Acceleration versus Time

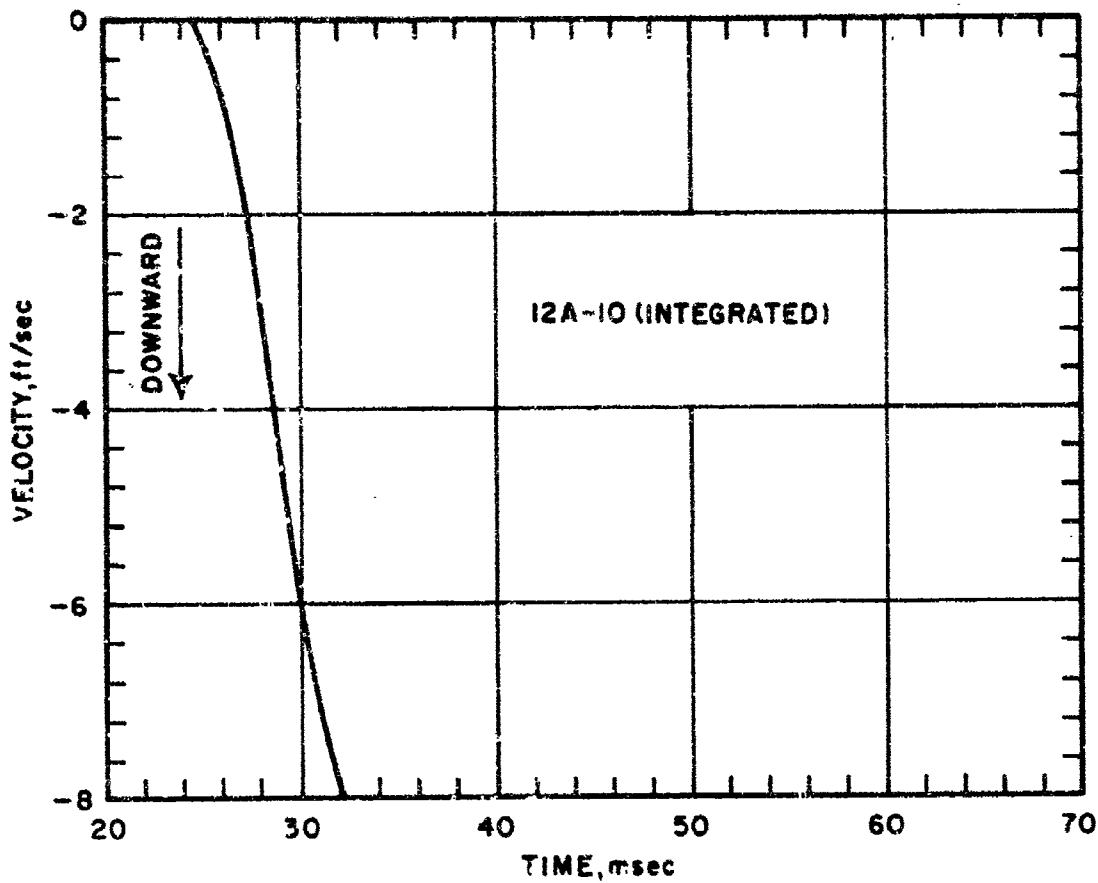


Figure C-2. Vertical Velocity versus Time

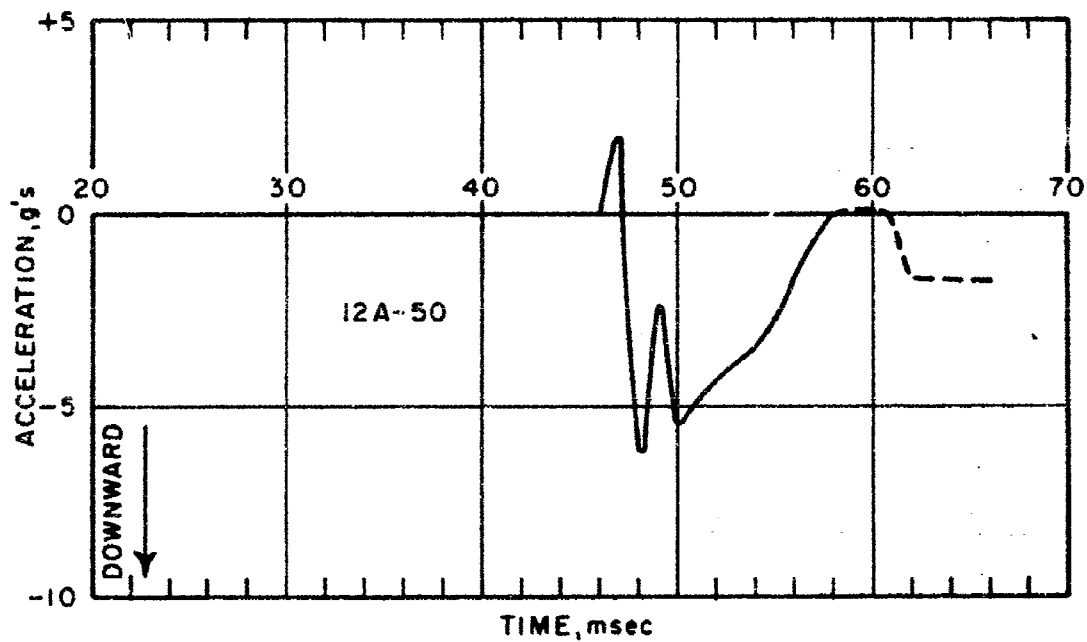


Figure C-3. Vertical Acceleration versus Time

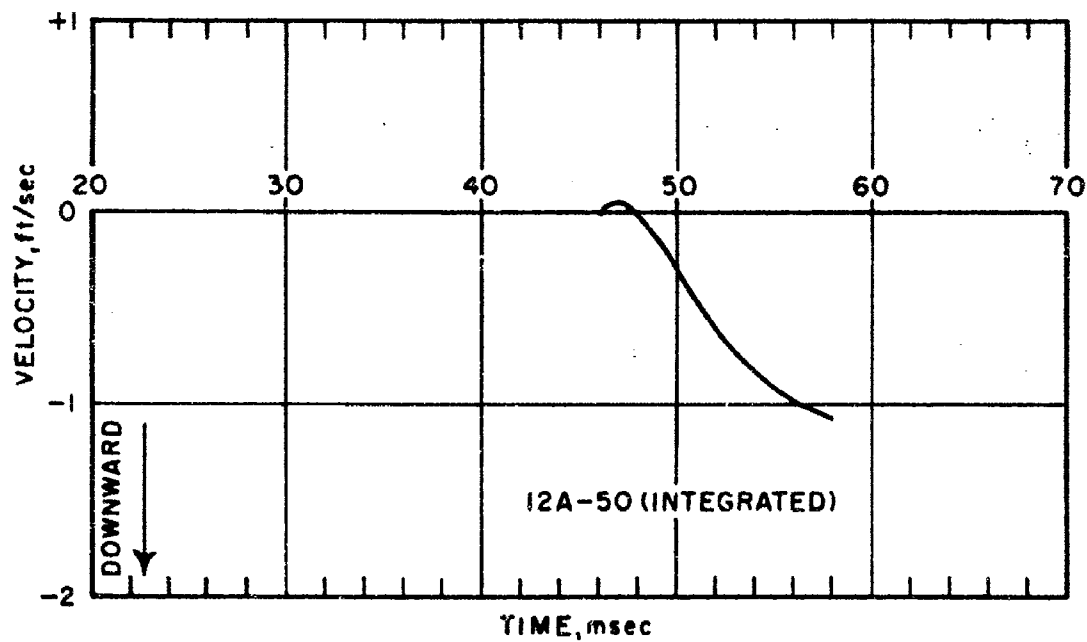


Figure C-4. Vertical Velocity versus Time

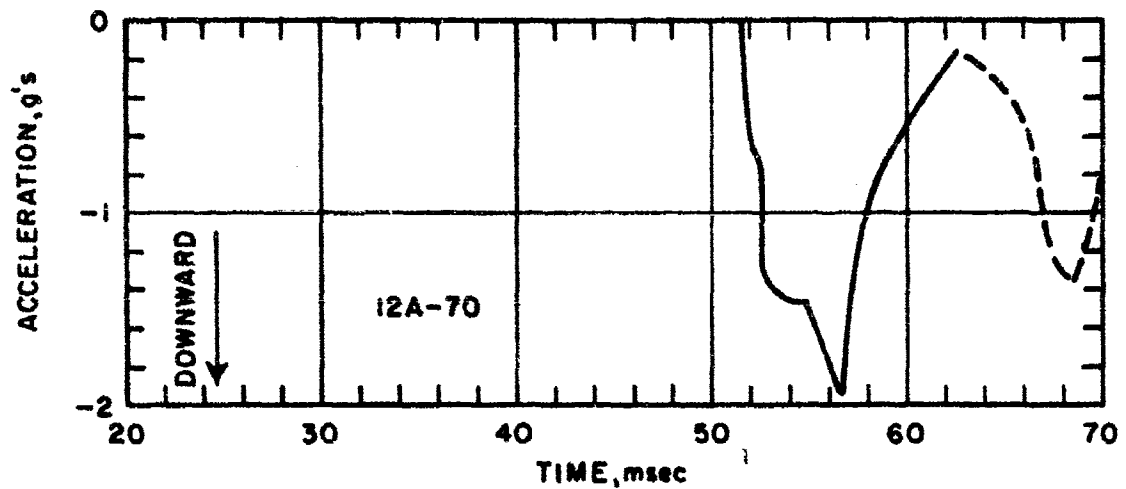


Figure C-5. Vertical Acceleration versus Time

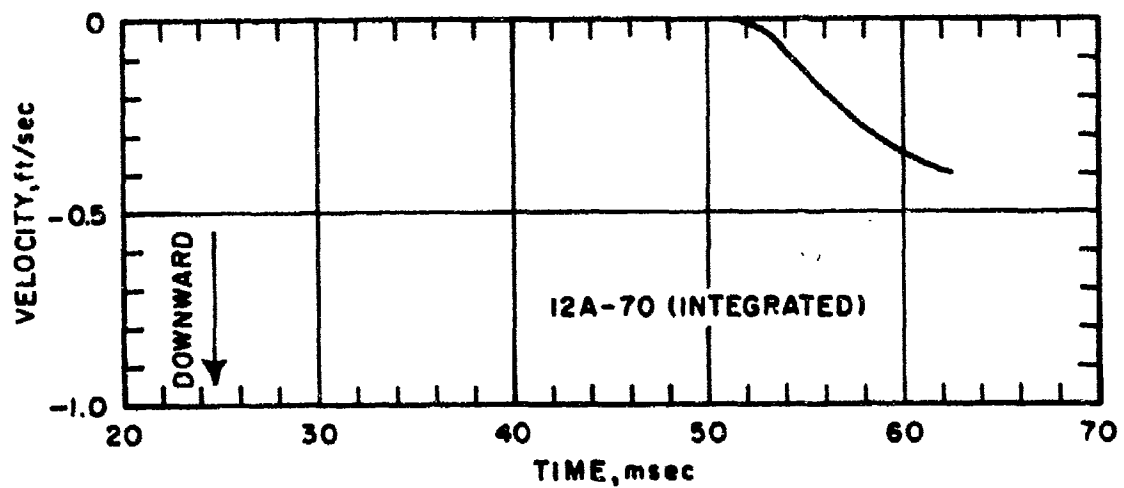


Figure C-6. Vertical Velocity versus Time

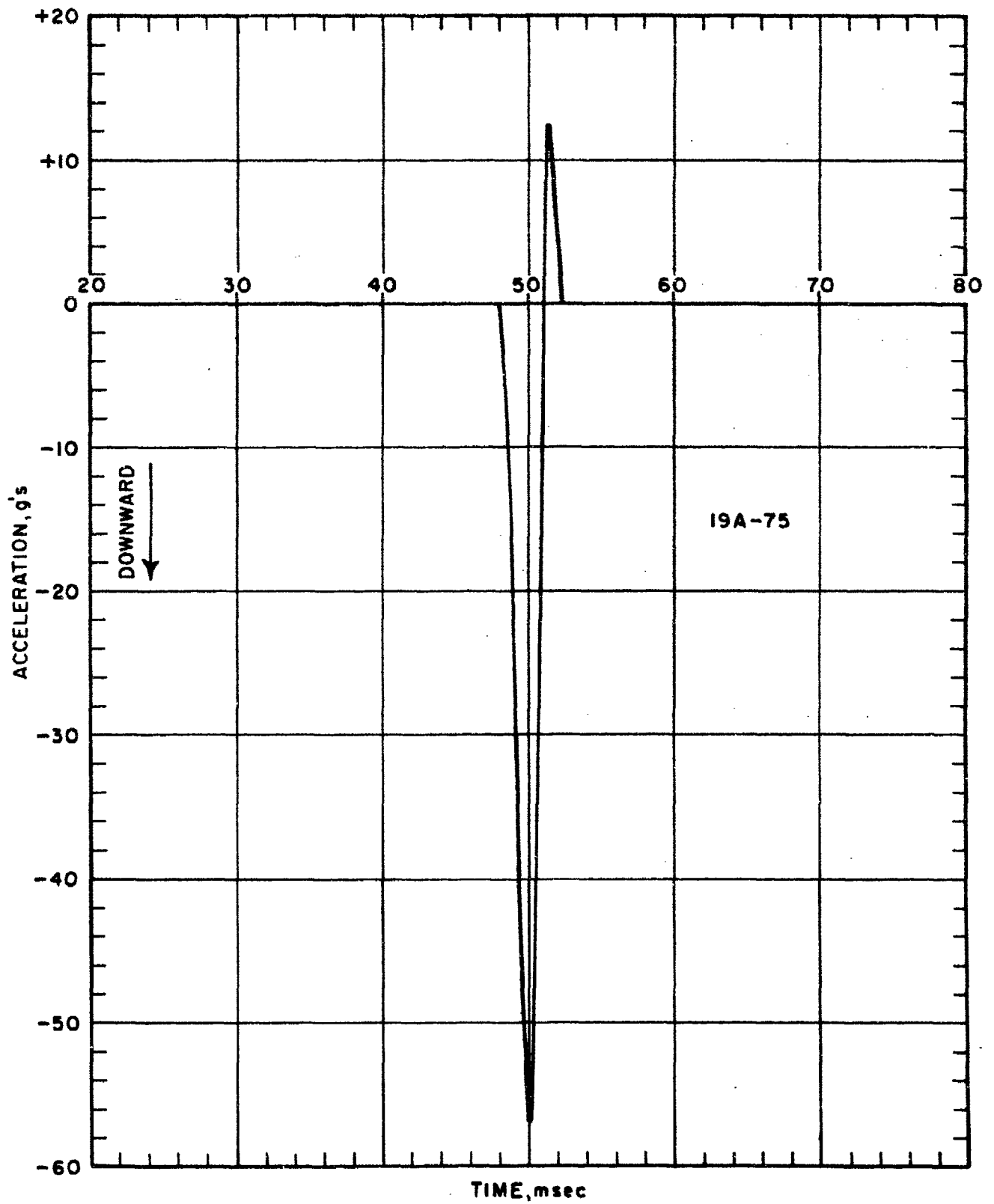


Figure C-7. Vertical Acceleration versus Time

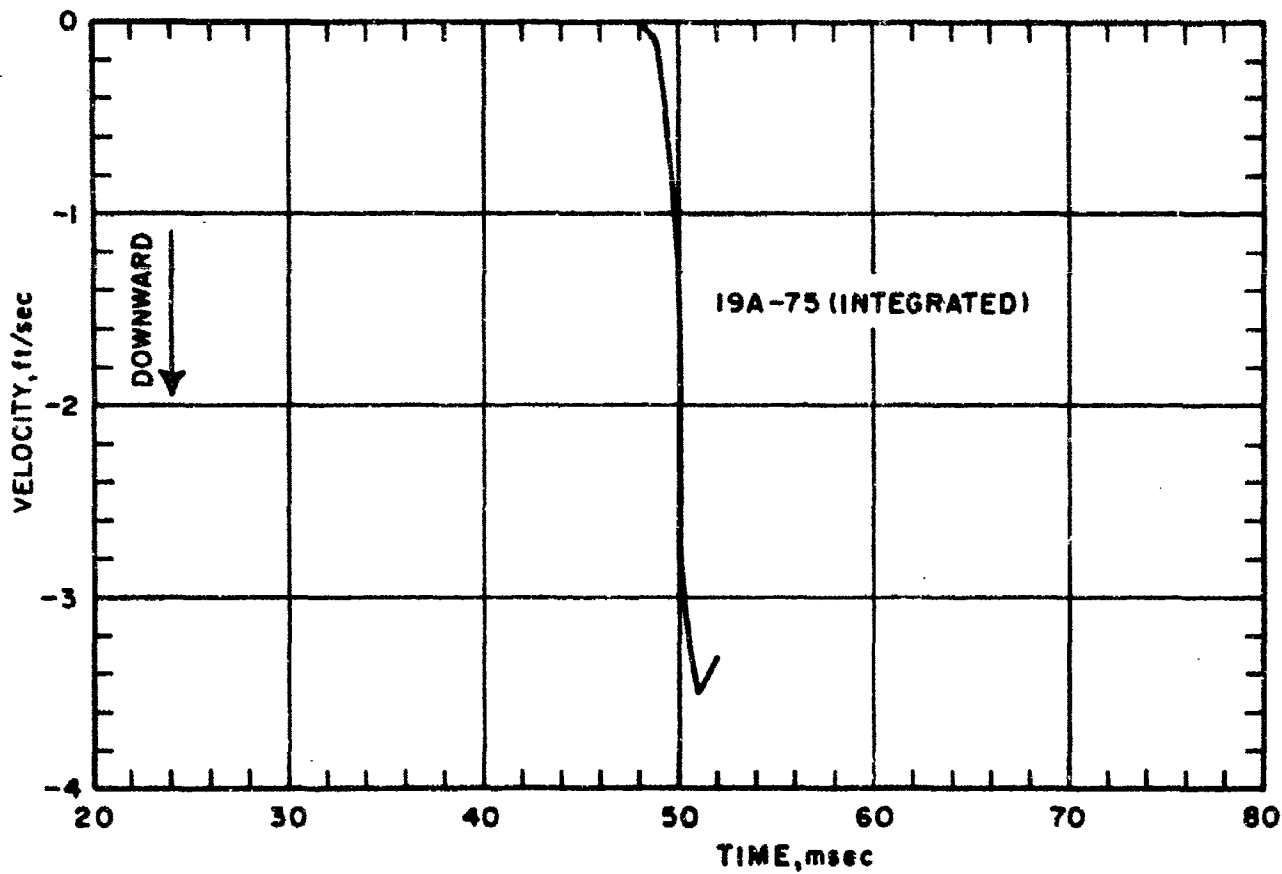


Figure C-8. Vertical Velocity versus Time

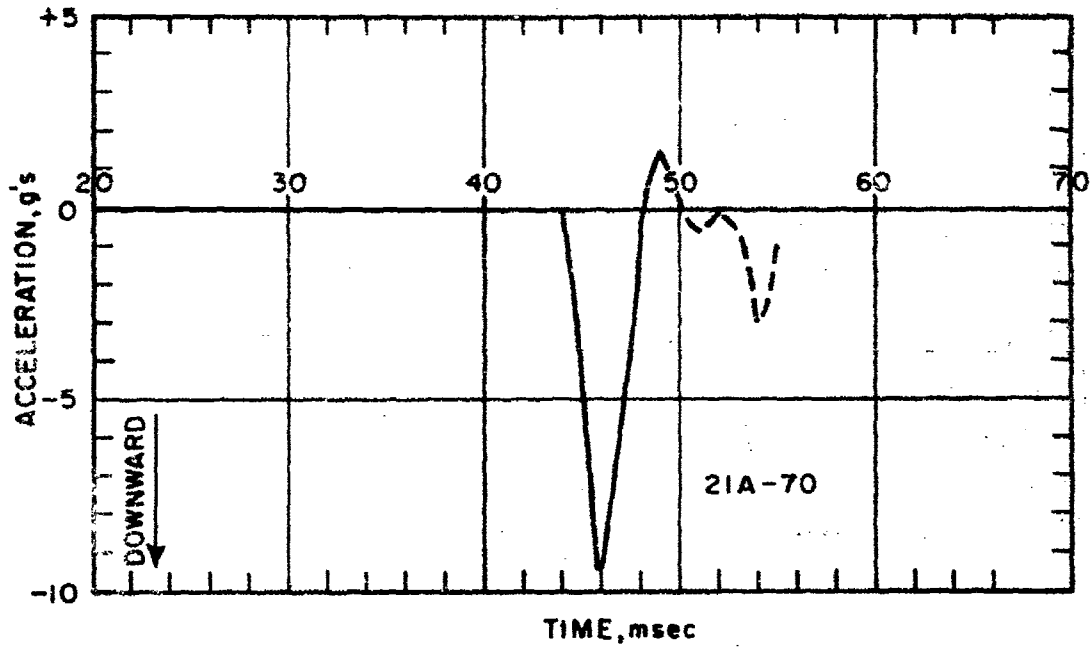


Figure C-9. Vertical Acceleration versus Time

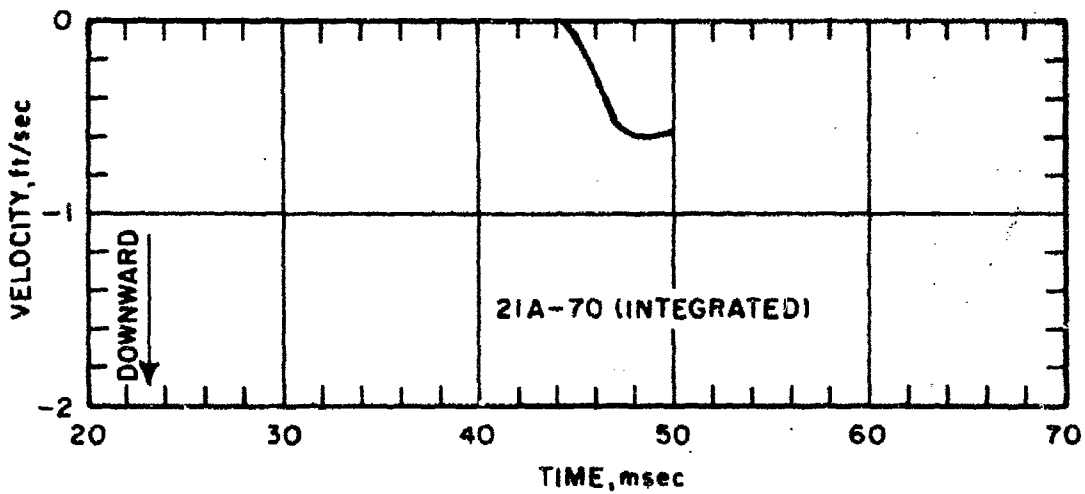


Figure C-10. Vertical Velocity versus Time

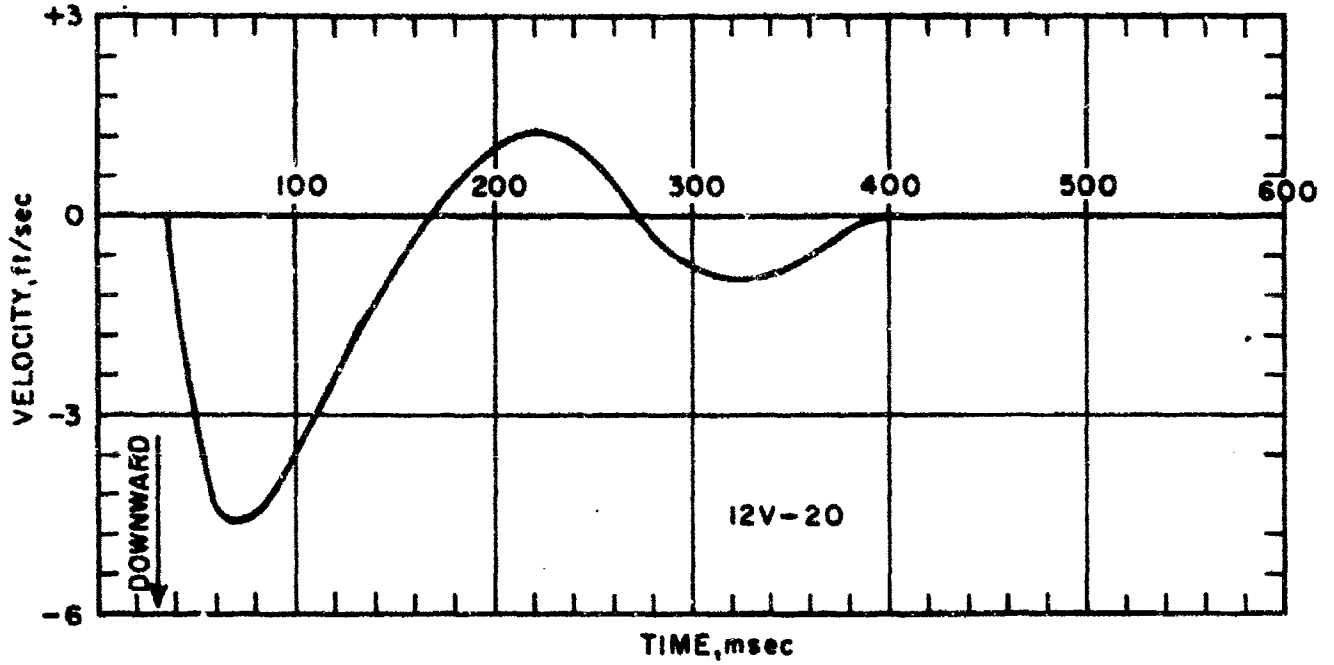


Figure C-11. Vertical Velocity versus Time

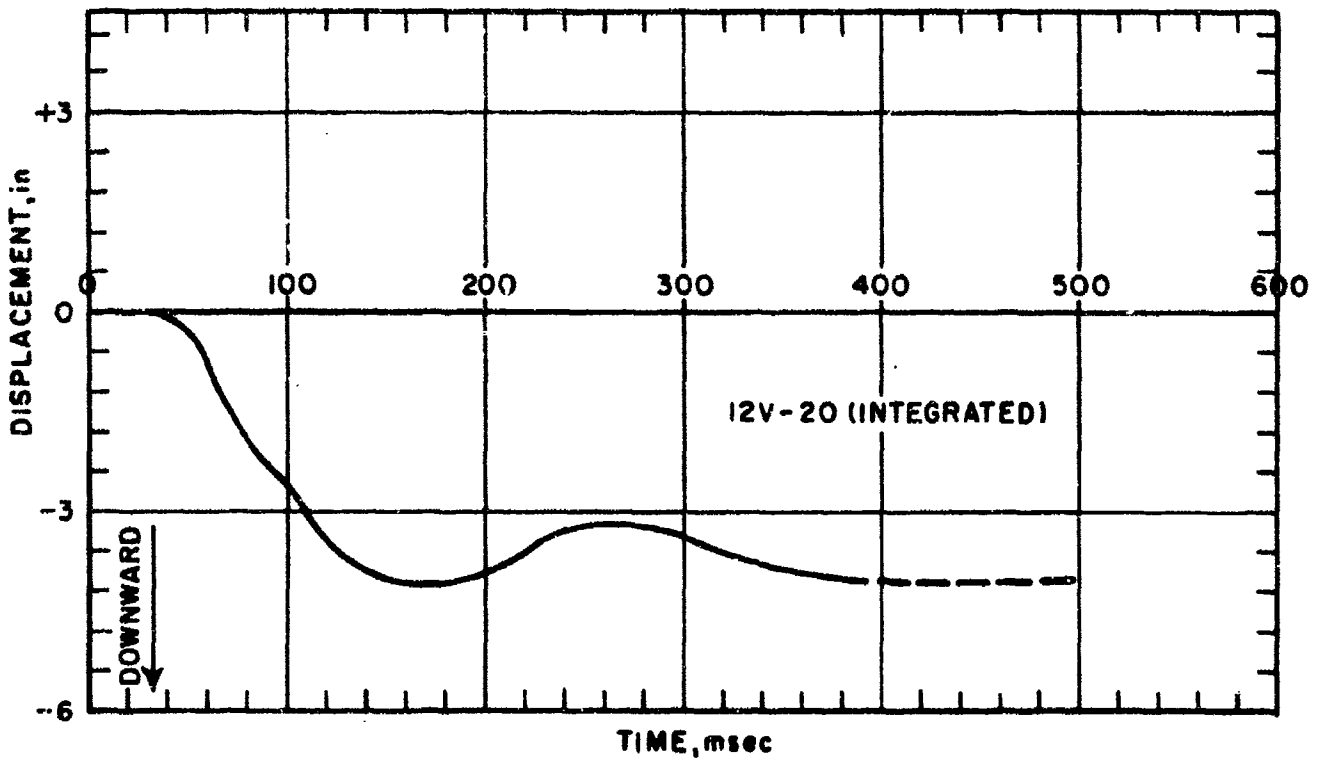


Figure C-12. Vertical Displacement versus Time

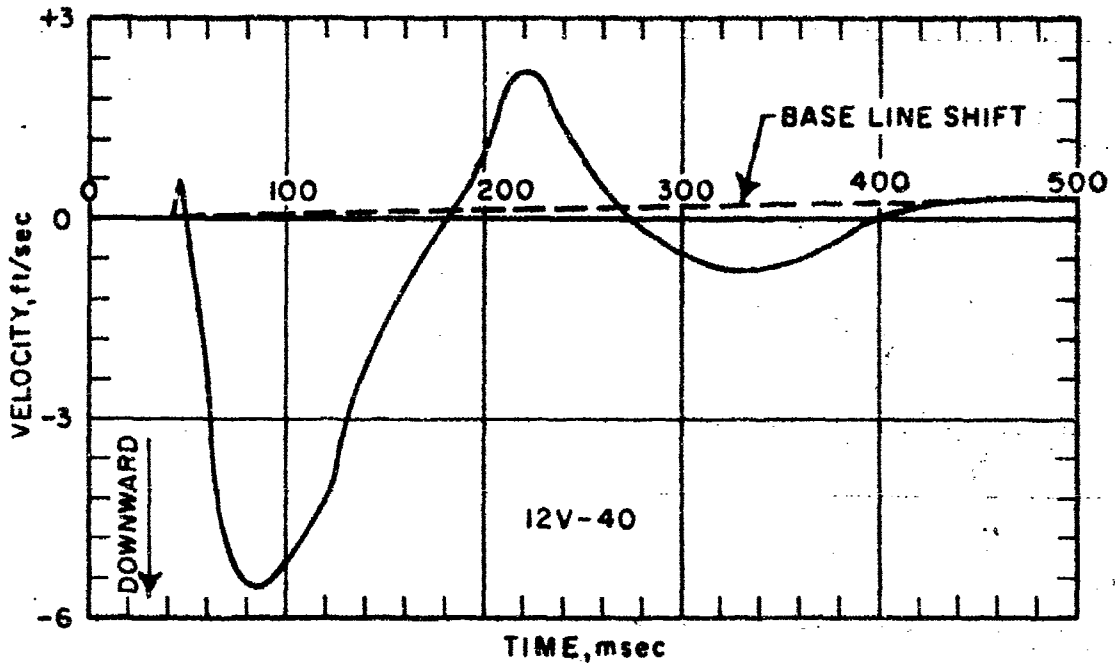


Figure C-13. Vertical Velocity versus Time

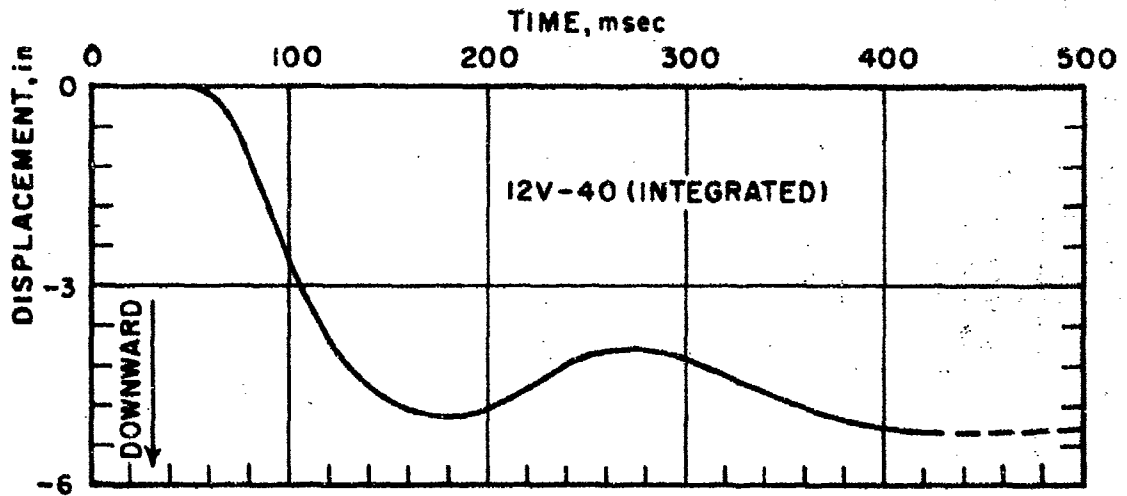


Figure C-14. Vertical Displacement versus Time

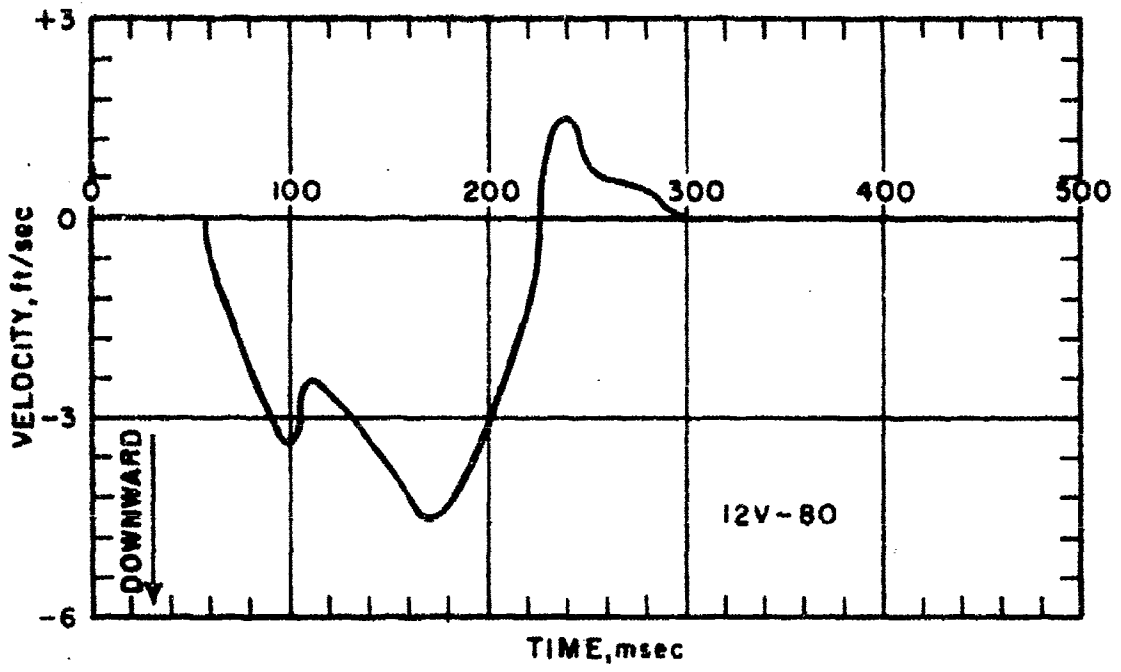


Figure C-15. Vertical Velocity versus Time

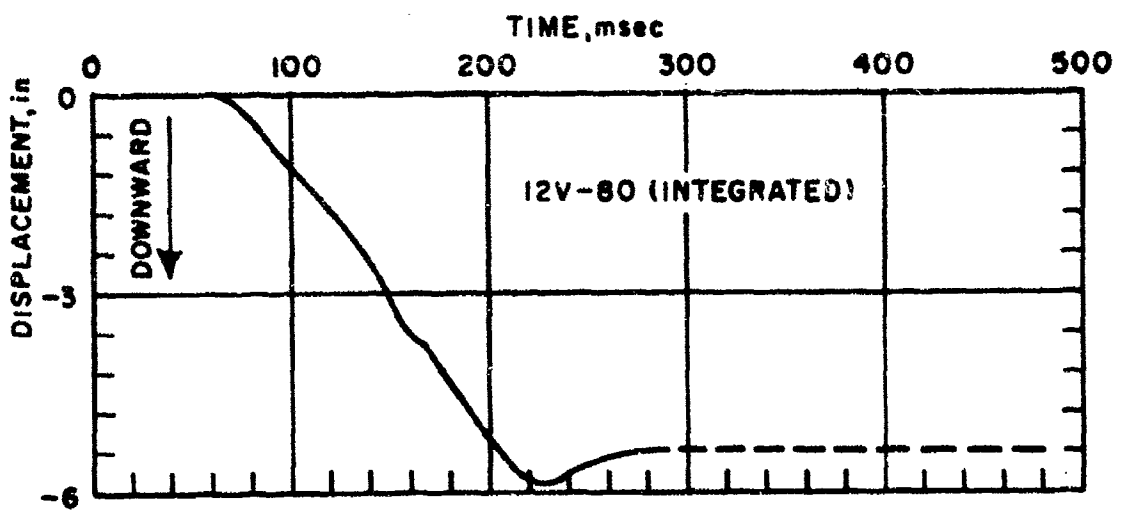


Figure C-16. Vertical Displacement versus Time

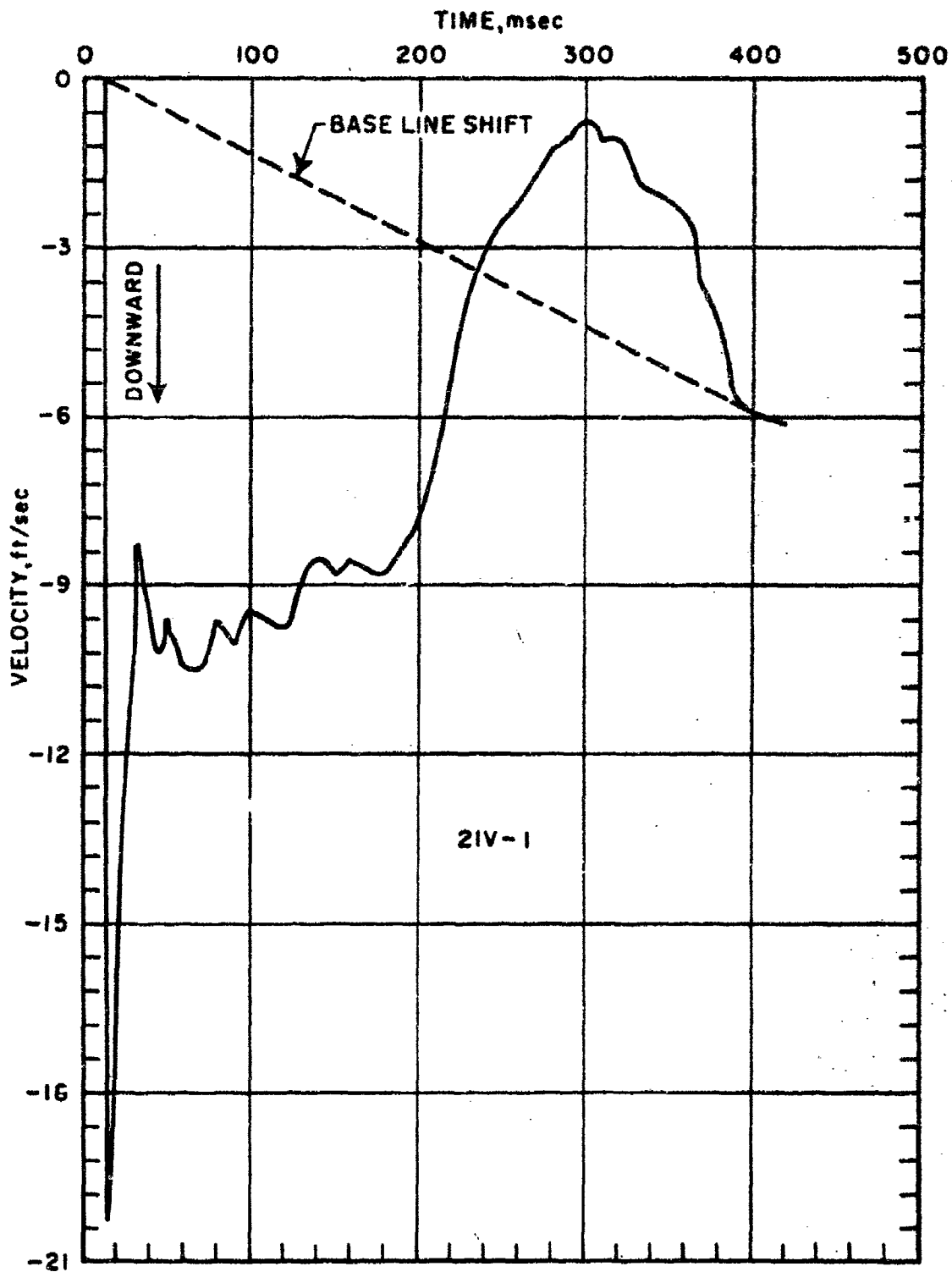


Figure C-17. Vertoca; Velocity versus Time

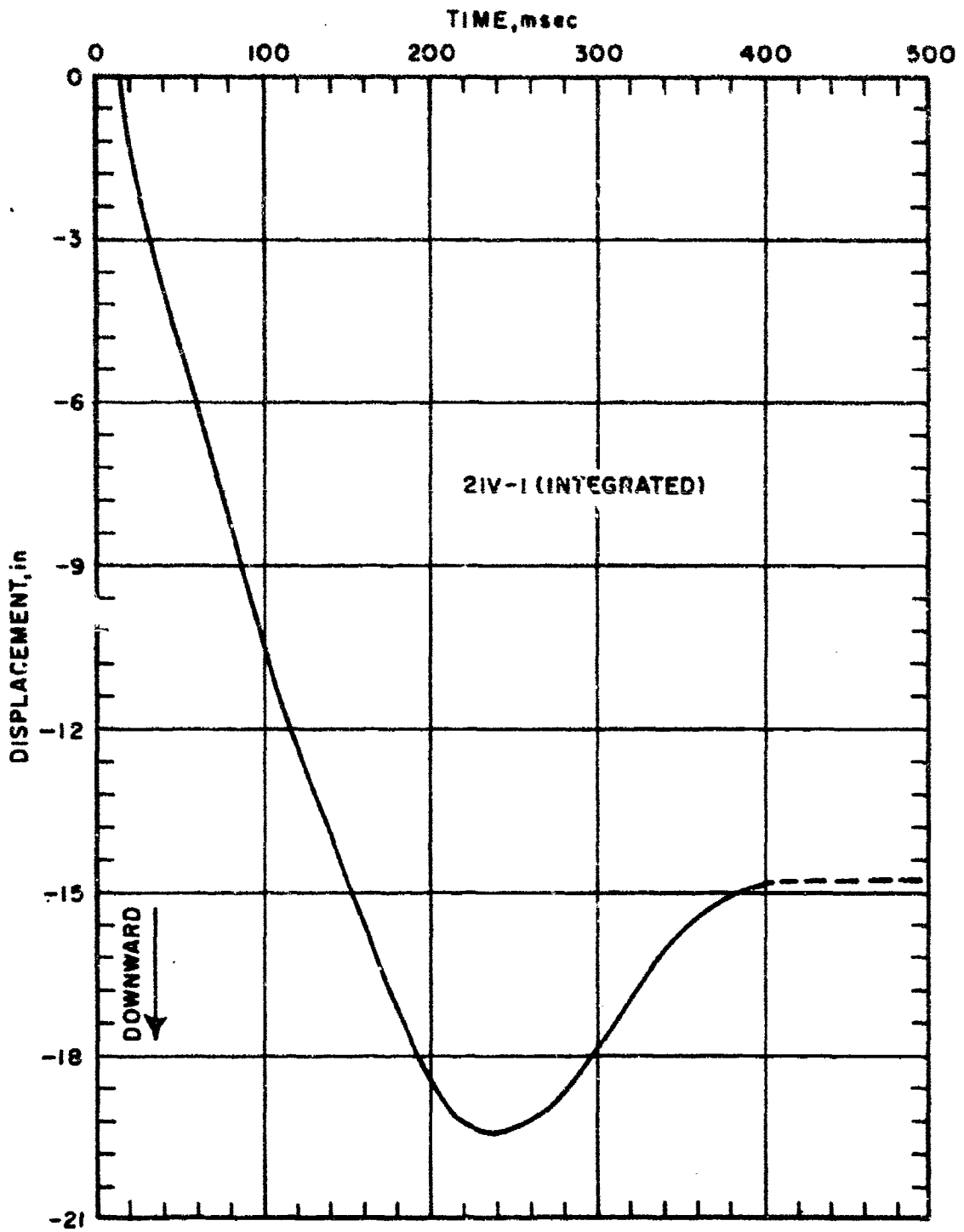


Figure C-18. Vertical Displacement versus Time

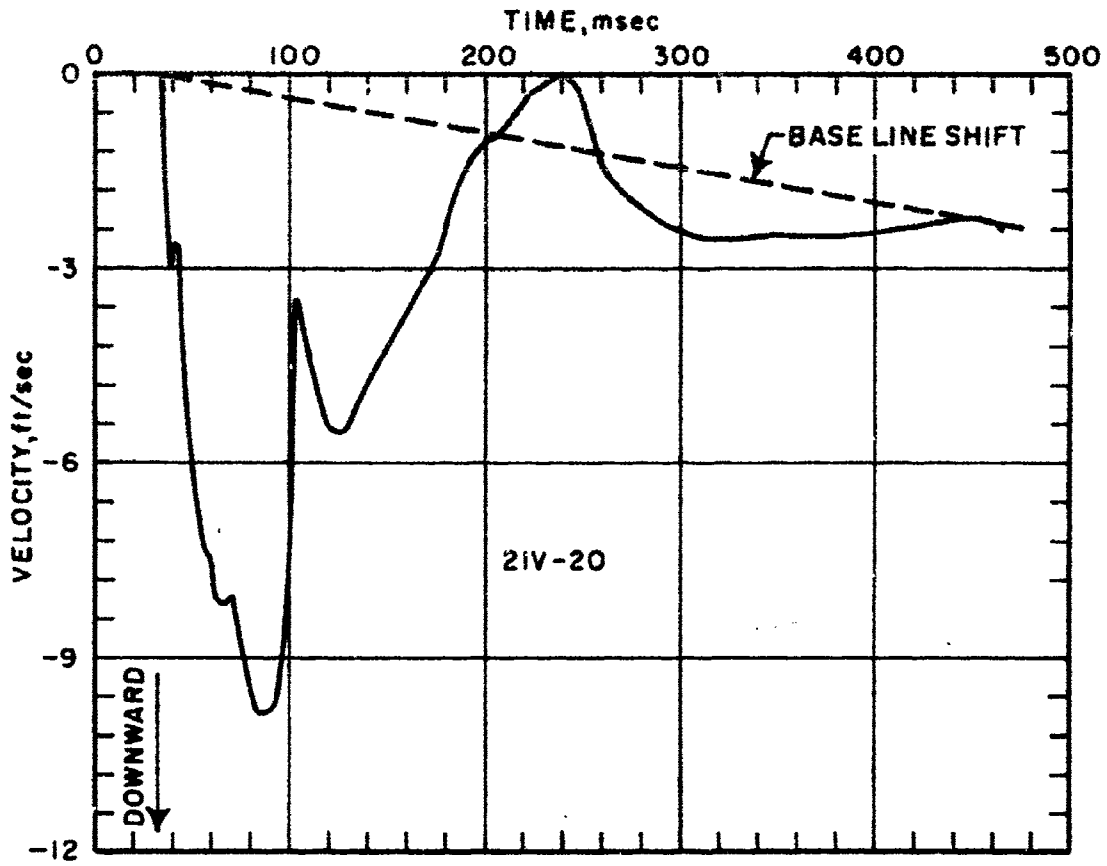


Figure 19. Vertical Velocity versus Time

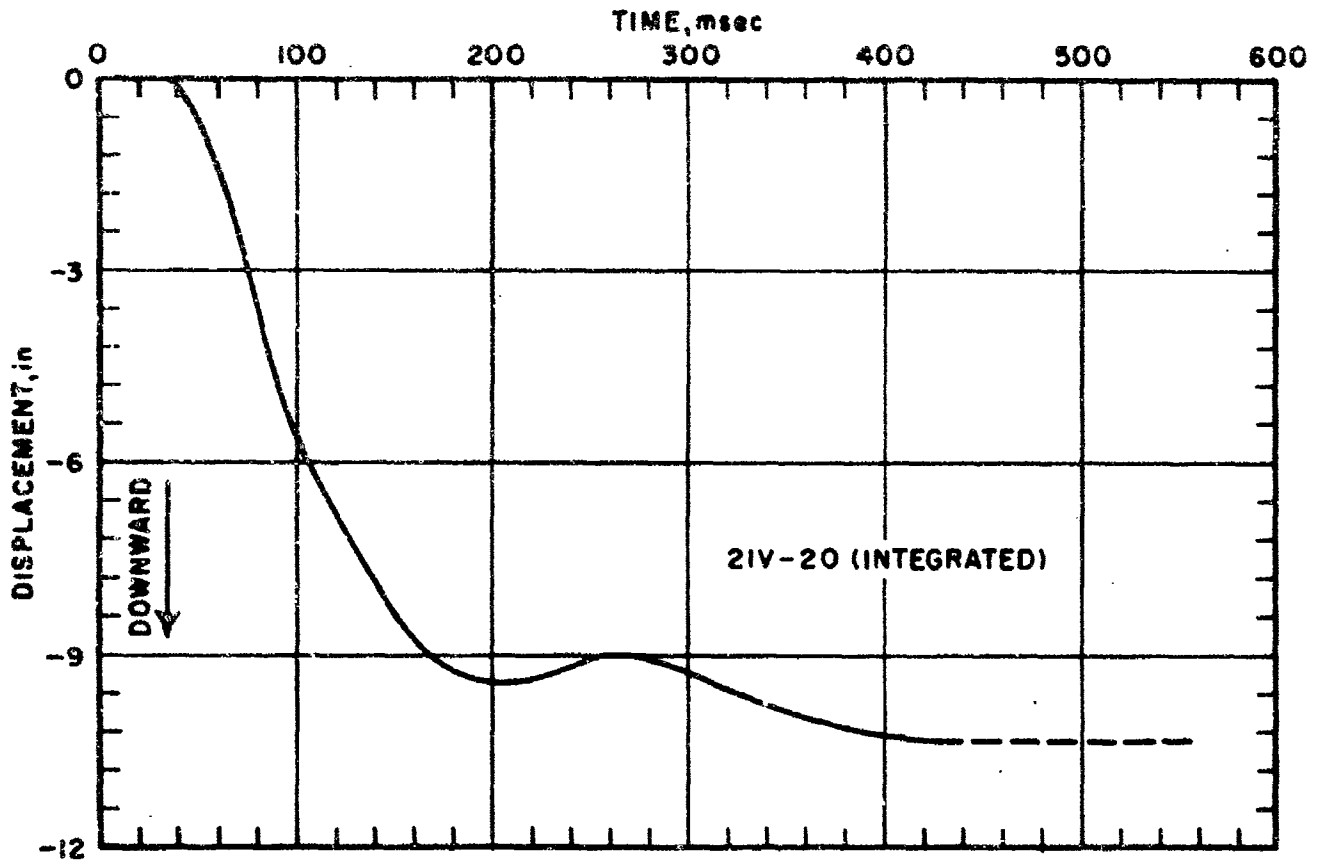


Figure C-20. Vertical Displacement versus Time

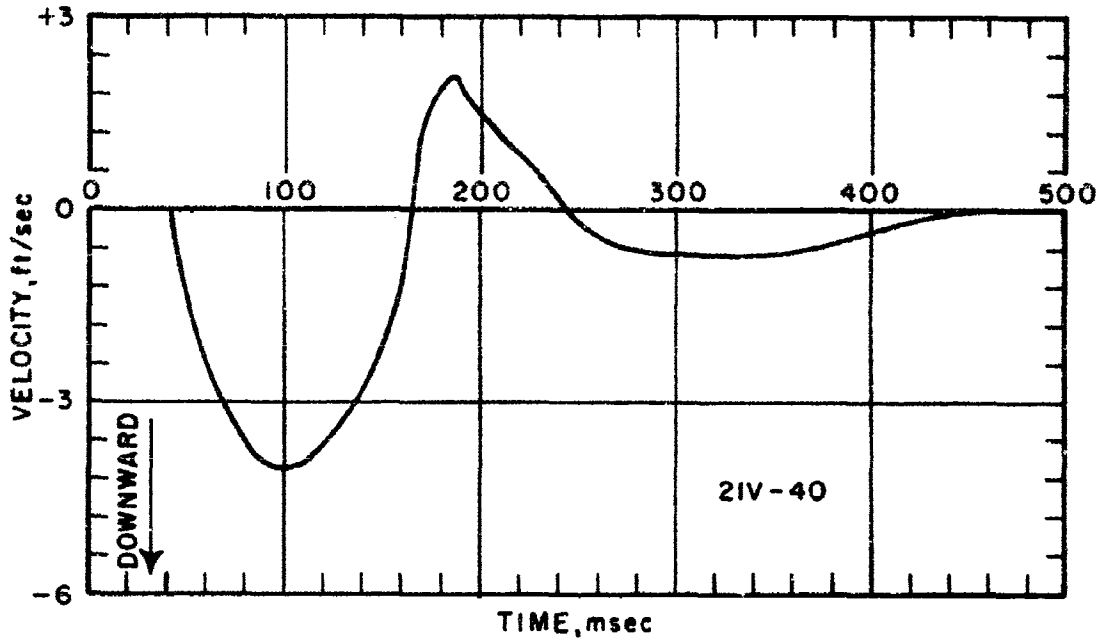


Figure C-21. Vertical Velocity versus Time

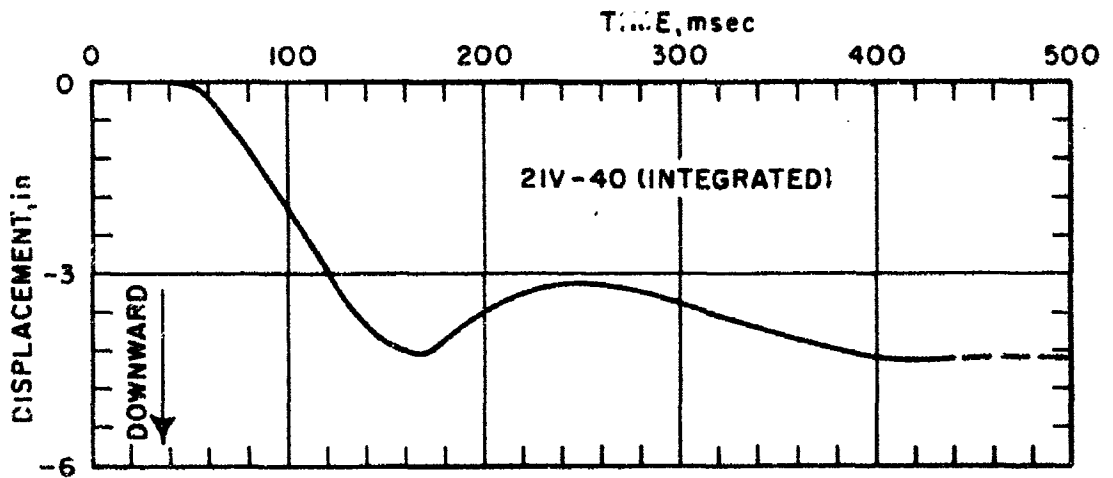


Figure C-22. Vertical Displacement versus Time

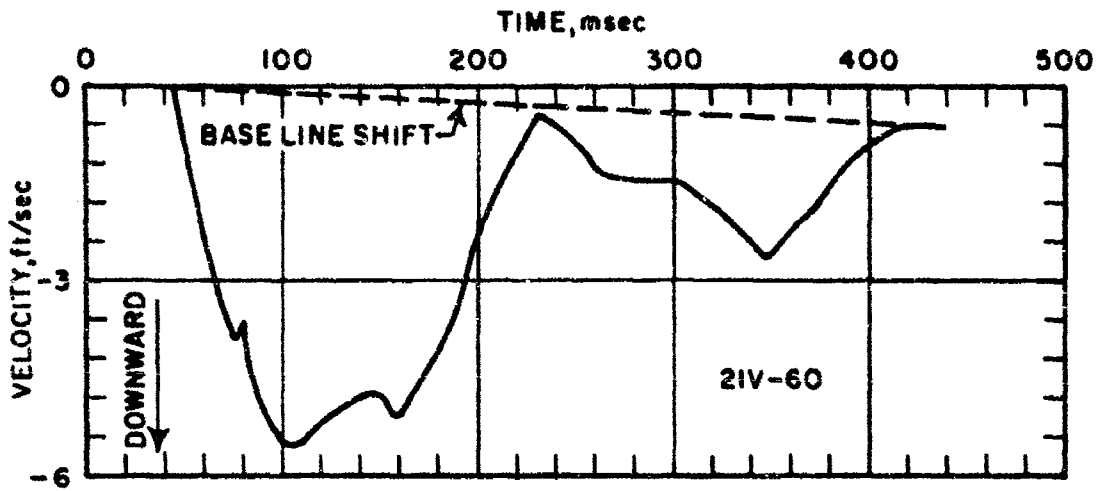


Figure C-23. Vertical Velocity versus Time

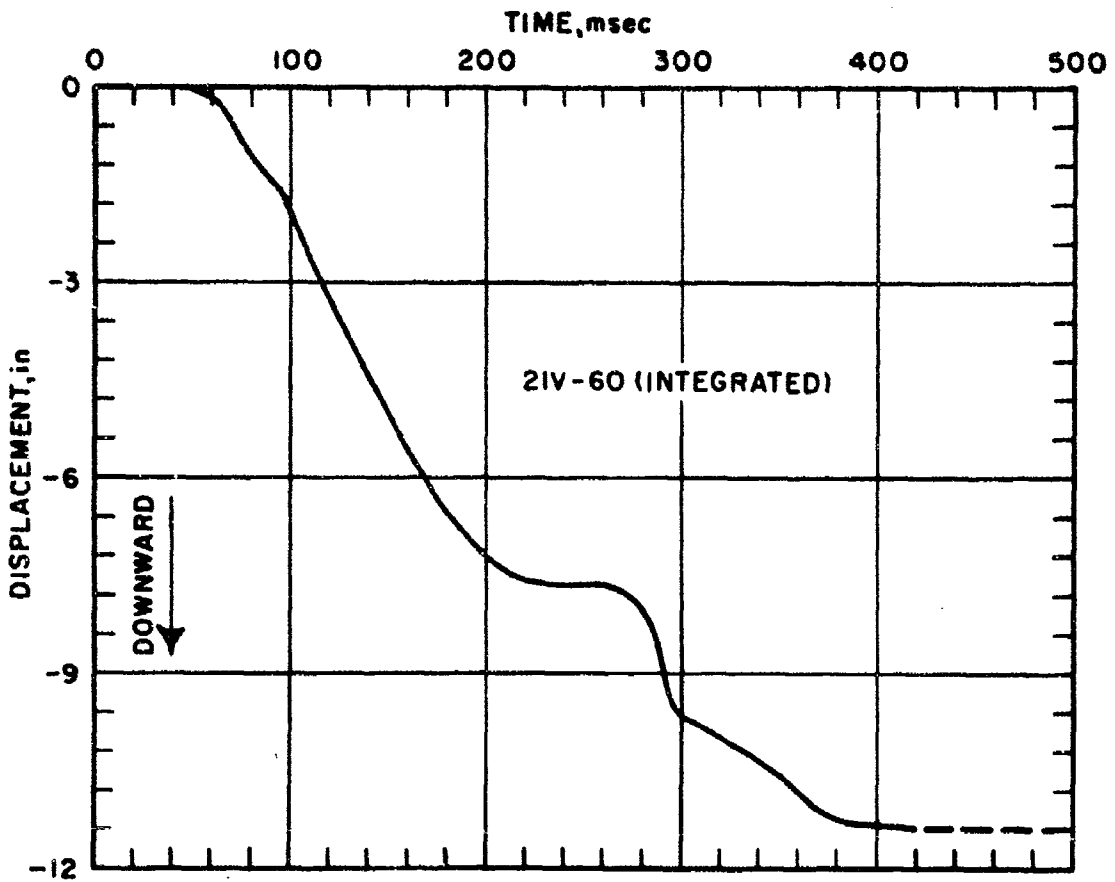


Figure C-24. Vertical Displacement versus Time

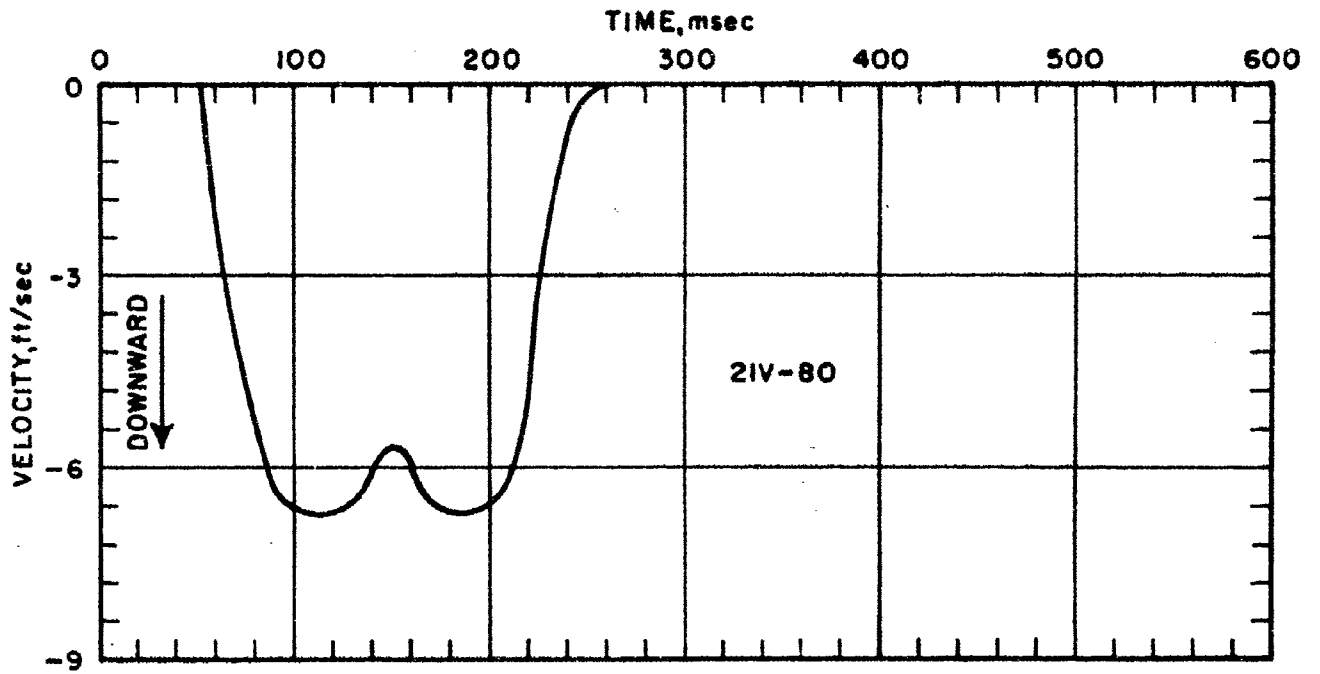


Figure C-25. Vertical Velocity versus Time

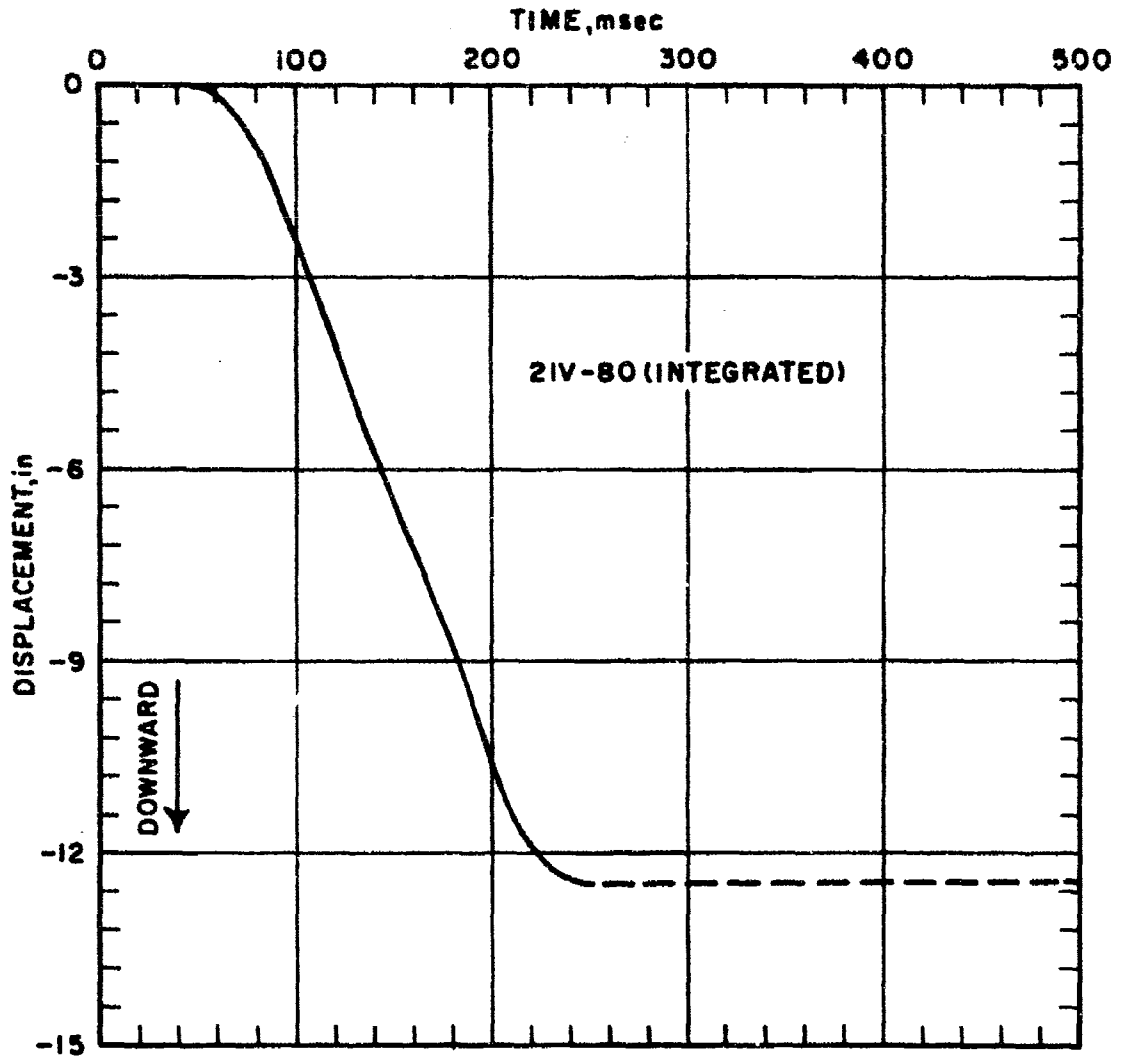


Figure 26. Vertical Displacement versus Time

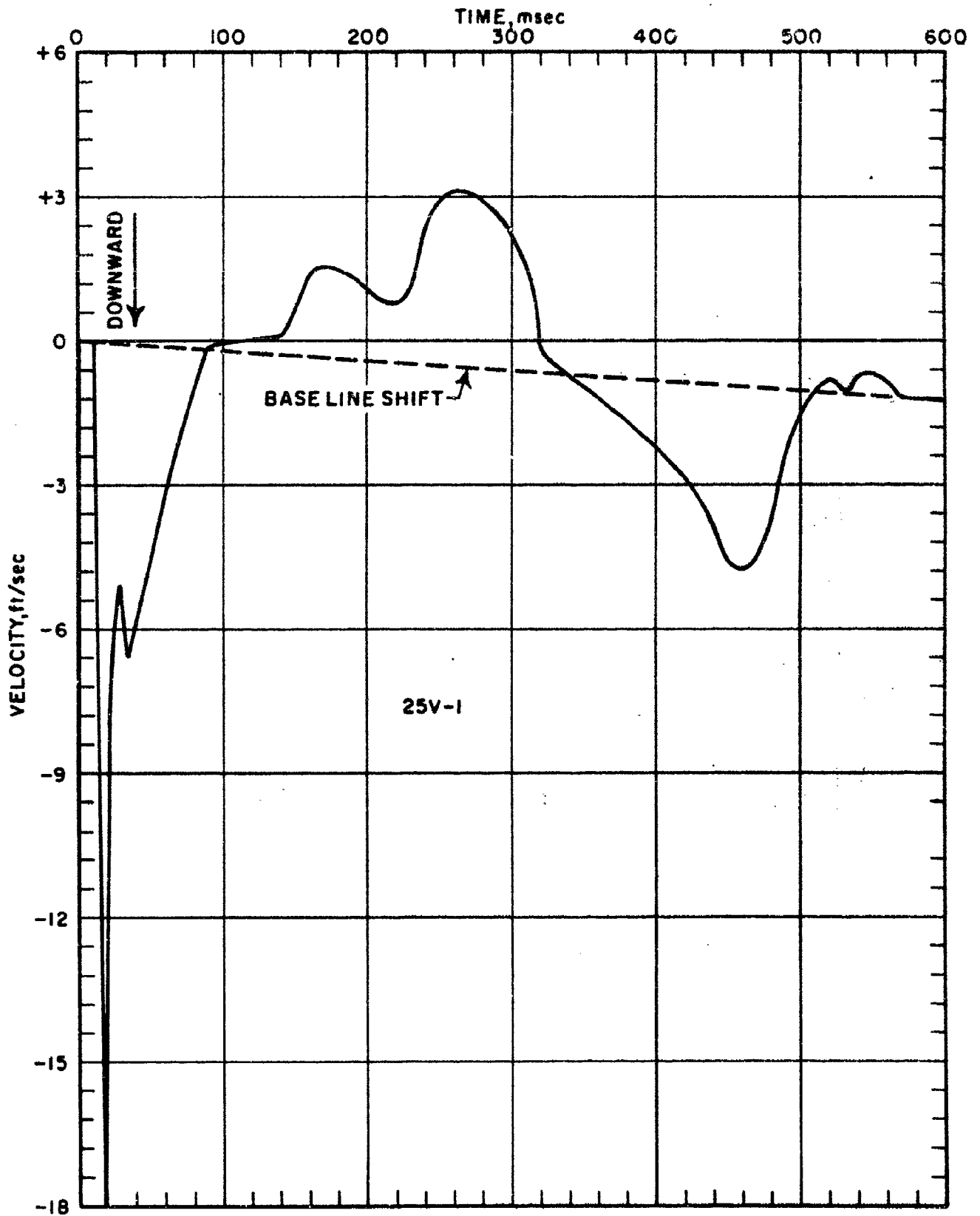


Figure C-27. Vertical Velocity versus Time.

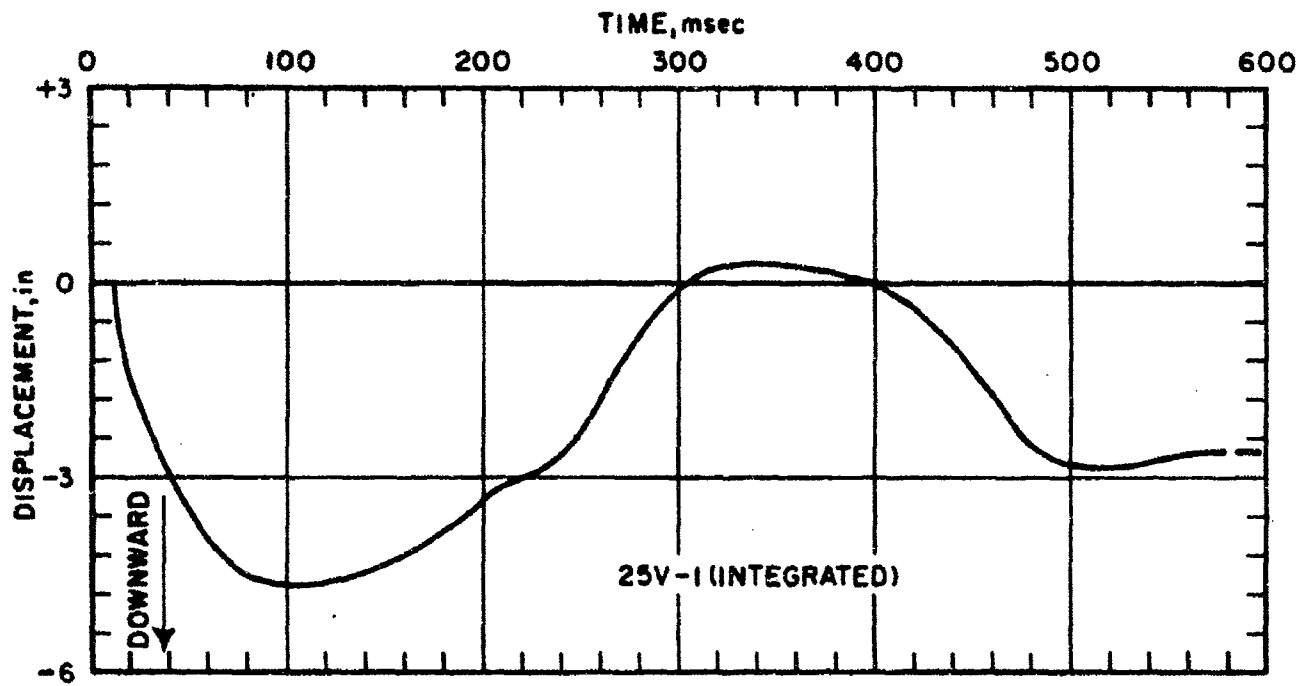


Figure C-28. Vertical Displacement versus Time

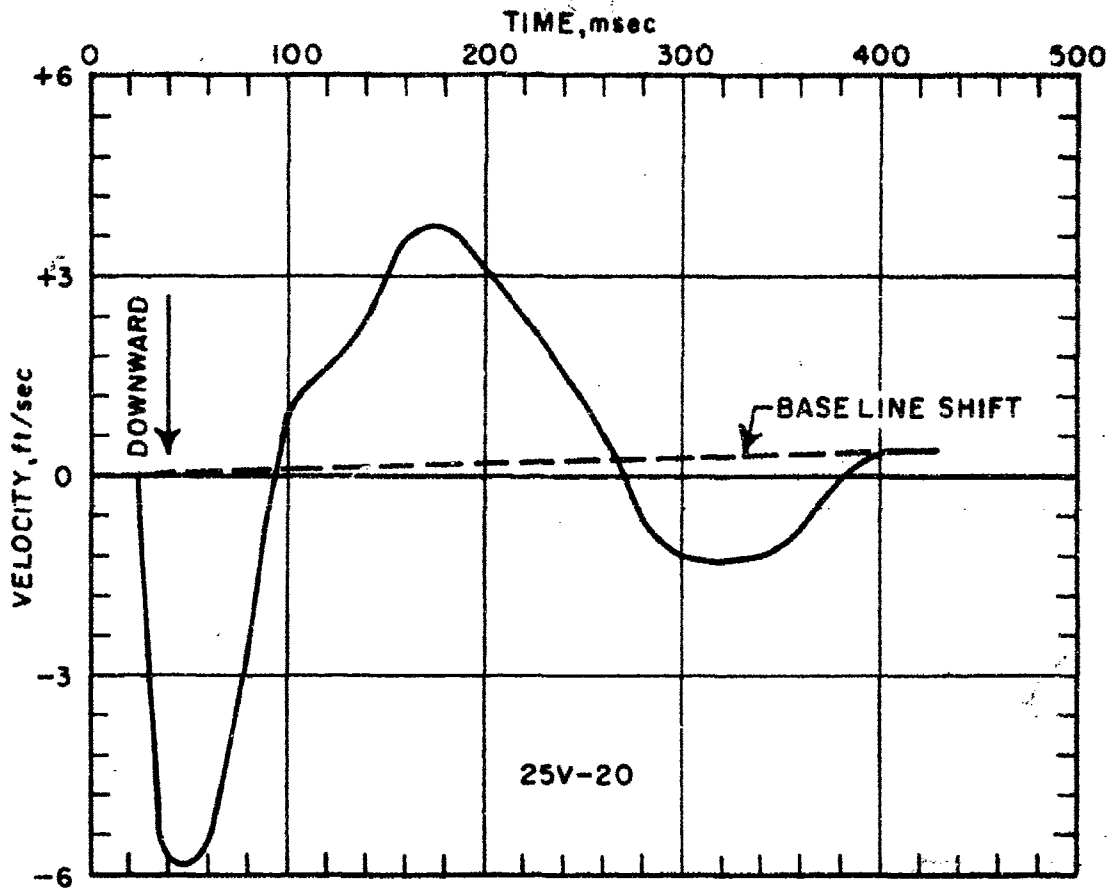


Figure C-29. Vertical Velocity versus Time

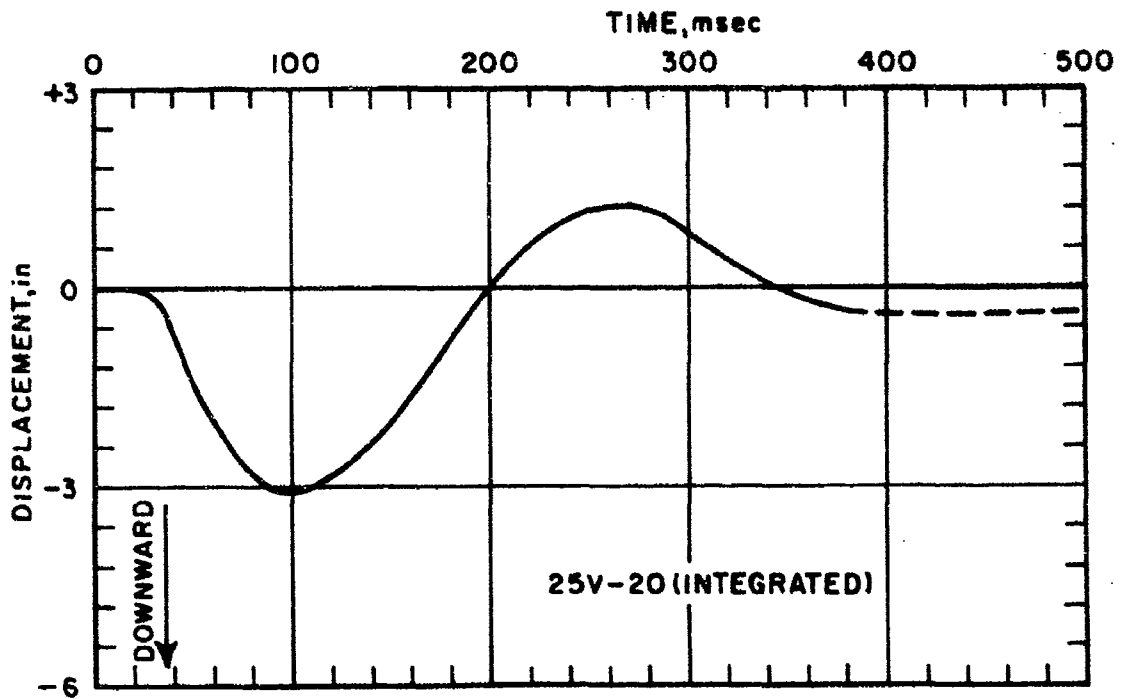


Figure C-30. Vertical Displacement versus Time

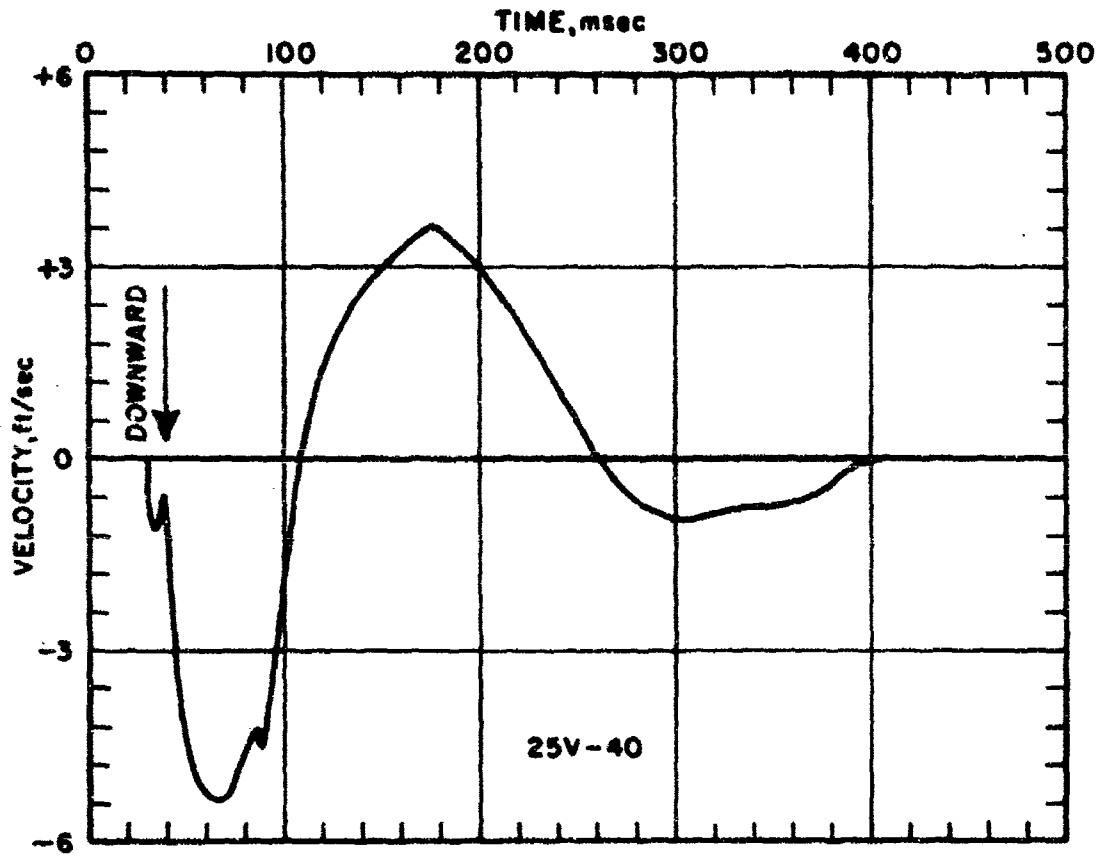


Figure C-31. Vertical Velocity versus Time

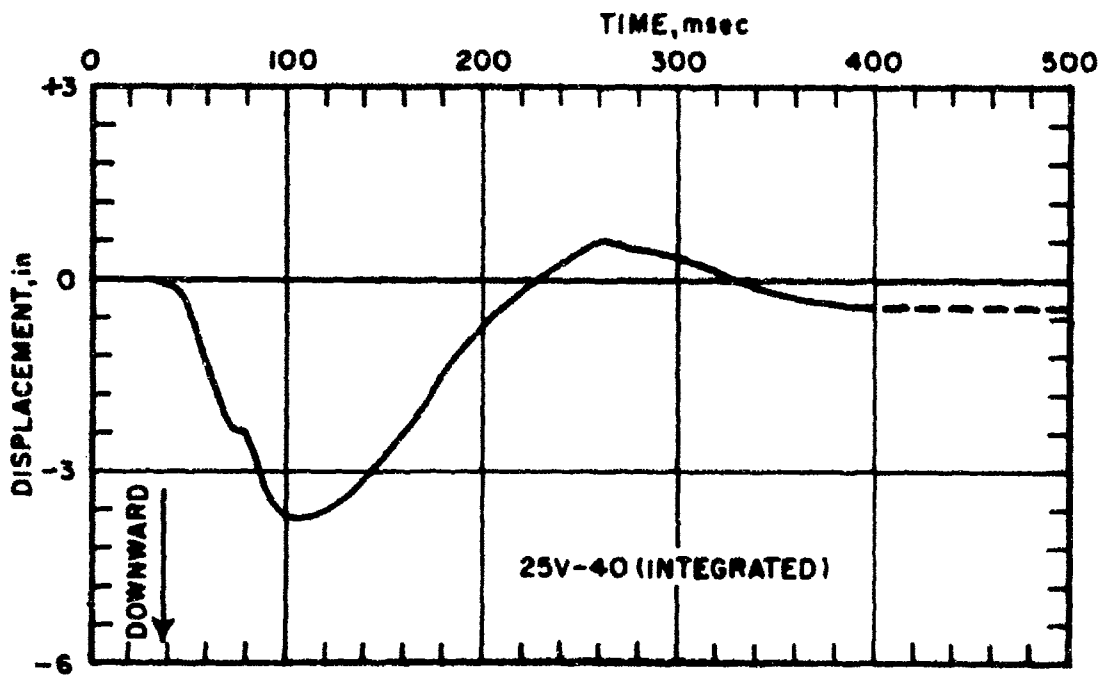


Figure C-32. Vertical Displacement versus Time

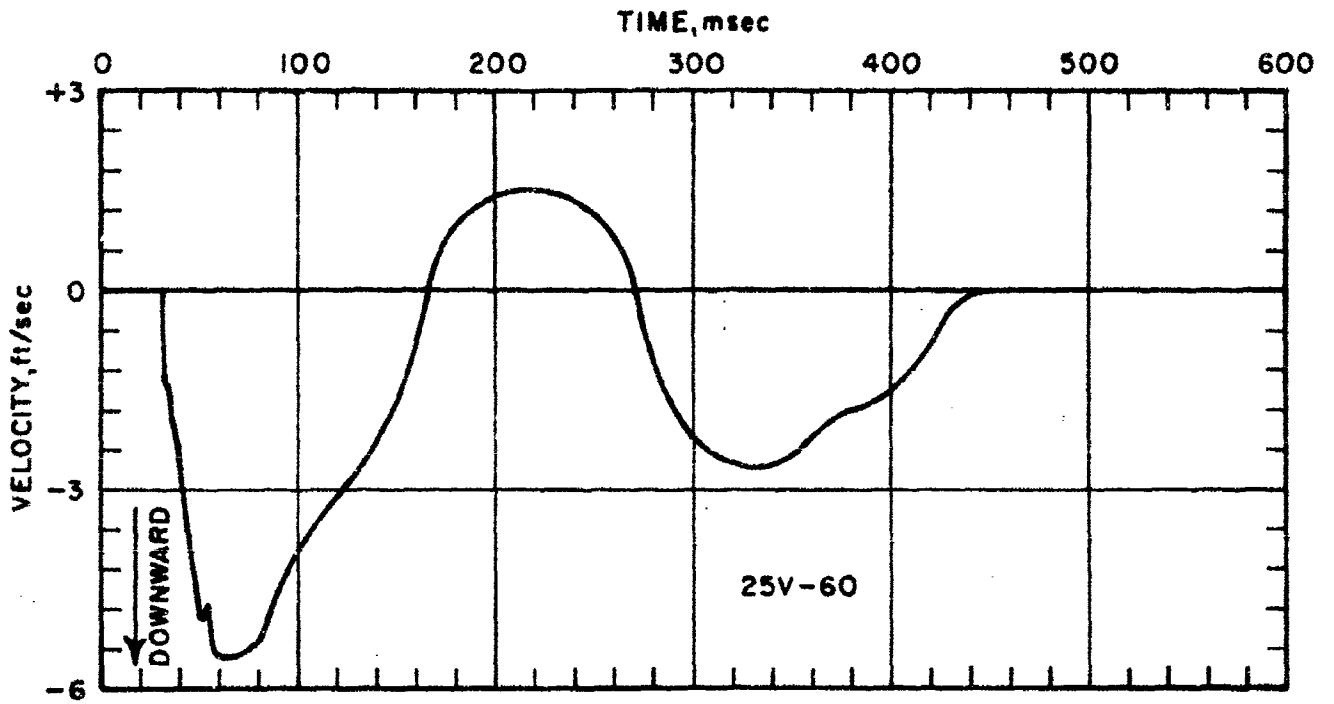


Figure C-33. Vertical Velocity versus Time

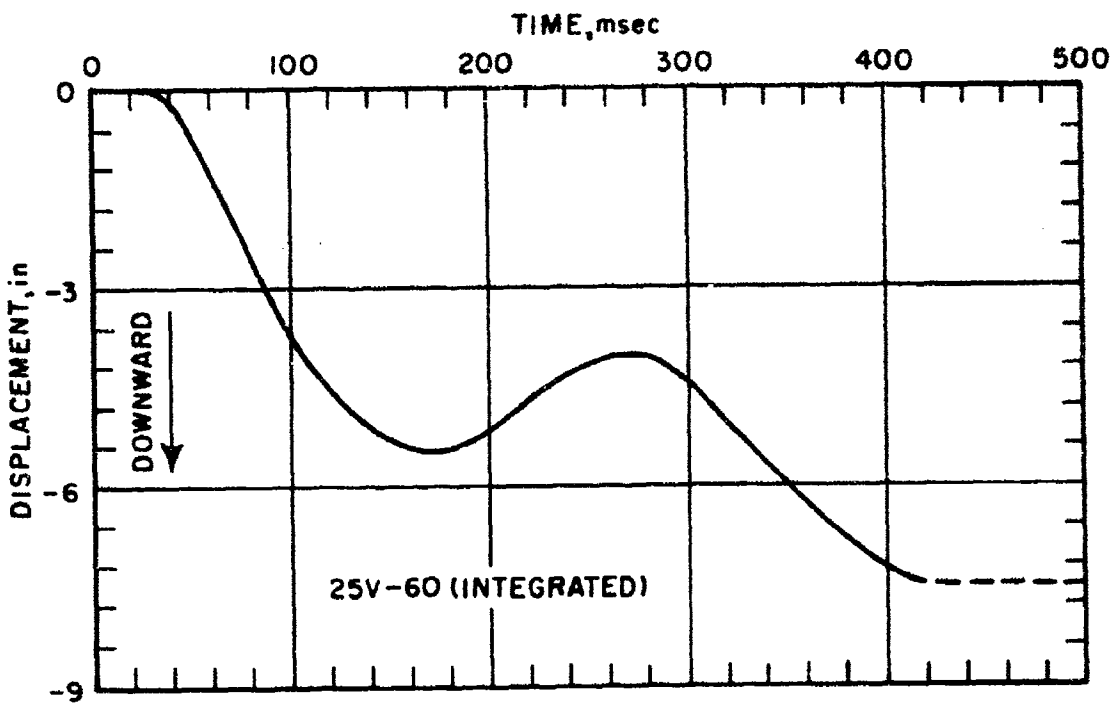


Figure C-34. Vertical Displacement versus Time

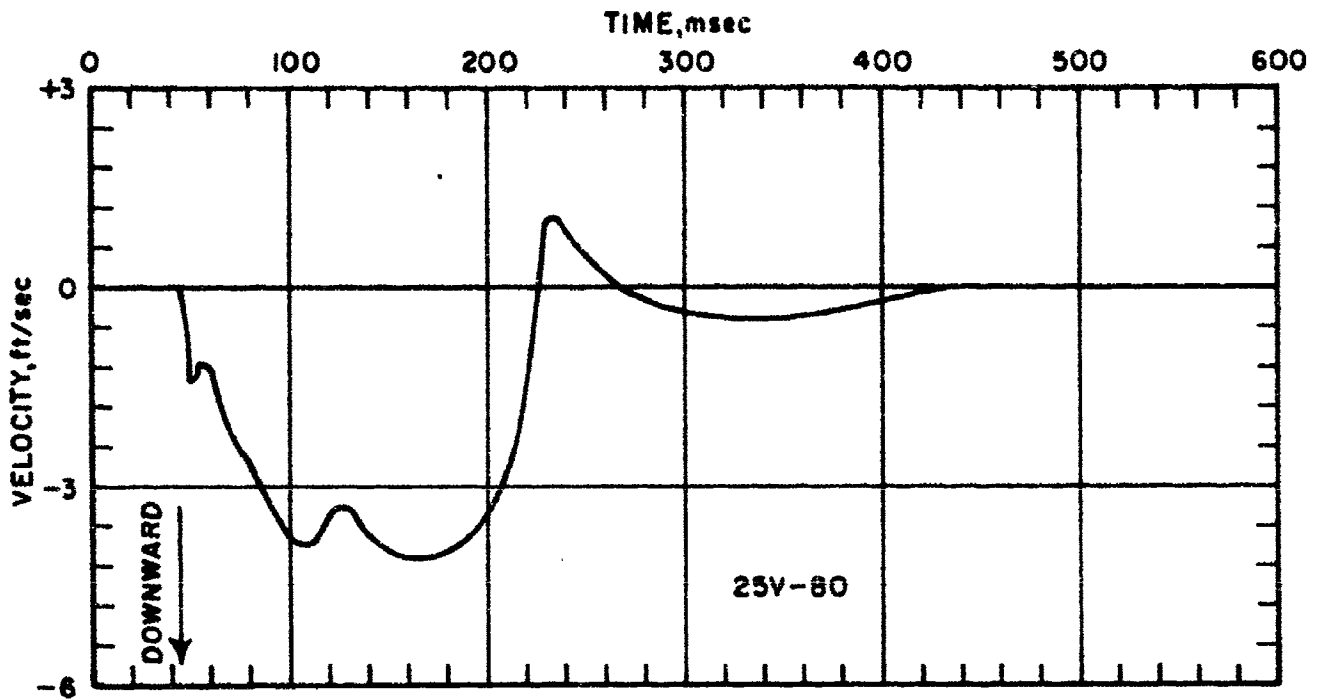


Figure C-35. Vertical Velocity versus Time

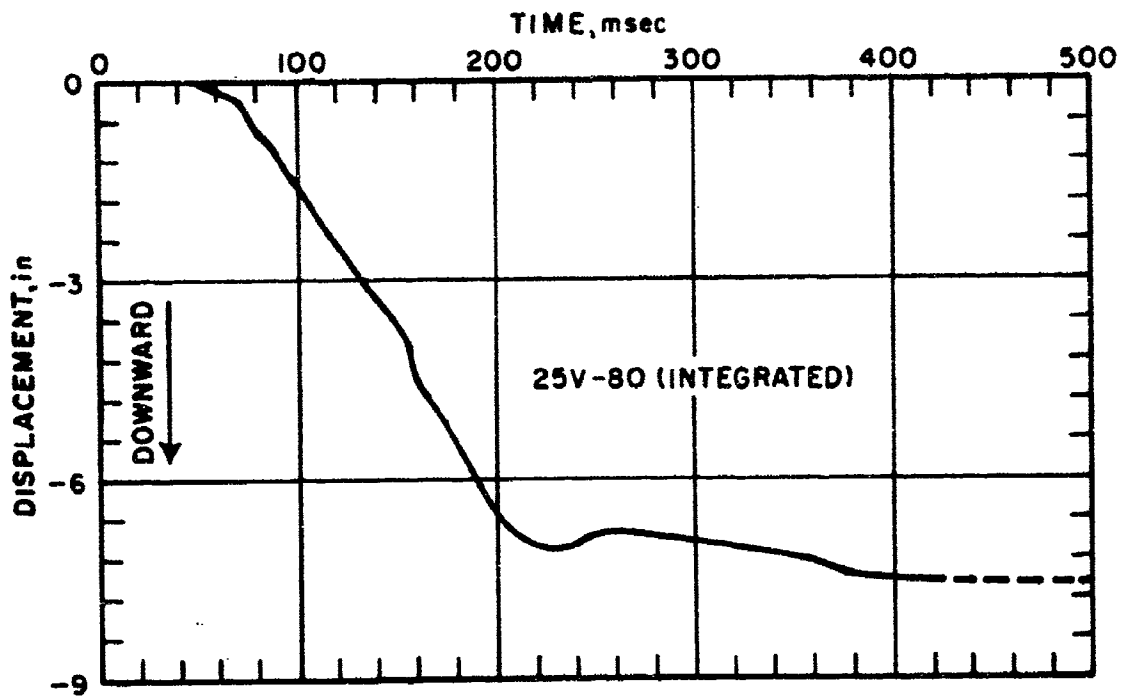


Figure C-36. Vertical Displacement versus Time

REFERENCES

1. D'Arcy, Gerald P., Capt; Auld, Harry E., Capt; Leigh, Gerald G., Capt; Simulation of Air-Blast-Induced Ground Motions (Phase I), AFWL TR-65-11 (Not yet published)
2. Croby, J. K., et al., Feasibility of Simulating the Mechanical Effects of a Nuclear Explosion Using Non-Nuclear Explosives, DASA-1264, December 1961.
3. Kurz, F. R., Investigation of Air-Blast-Induced Ground Motion Technique Using High Explosives, MRD Division, General American Transportation Corp., unpublished report to AFWL, November 1964.
4. Brode, H. L., A Review of Nuclear Explosion Phenomena Pertinent to Protective Construction, The RAND Corp., R-425-PR, May 1964.
5. Schwarz, S. D., Seismic Studies, Phase II Site, Geo-Recon, Inc., Letter Report to AFWL, September 1964.
6. Buchanan, S. J., Soil Investigation, Phase II Site, Spencer J. Buchanan and Assoc., Inc., Letter Report to AFWL, October 1964.
7. Newmark, N. M., and Haltiwanger, J. D., Air Force Design Manual, Principles and Practices for Design of Hardened Structures, AFSWC TDR-62-138, December 1962.
8. Sauer, F. M., (U) Ground Motion Produced by Aboveground Nuclear Explosions, AFSWC TR-59-71, April 1959. (SECRET-FRD)

DISTRIBUTION

No. cys

HEADQUARTERS USAF

Hq USAF, Wash, DC 20330

- 1 (AFCOA)
- 1 (AFOCE)
- 1 (AFNIN)
- 1 (AFRDPF, Maj Dunn)
- 1 USAF Dep, The Inspector General (AFIDI), Norton AFB, Calif 92409
- 1 USAF Directorate of Nuclear Safety (AFINS), Kirtland AFB, NM 87117

MAJOR AIR COMMANDS

AFSC, Andrews AFB, Wash, DC 20331

- 1 (SCT)
- 1 (SCLT)
- 1 (SCMC)
- 1 TAC (DE), Langley AFB, Va 23365
- 1 SAC, Offutt AFB, Nebr 68113
- 1 (DORQ)
- 1 (DE)
- 1 ADC (ADIDC), Ent AFB, Colo 80912
- 1 AUL, Maxwell AFB, Ala 36112
- 1 USAFIT Civ Eng Cen, Wright-Patterson AFB, Ohio 45433
- 1 USAFE, Dir Civ Eng, APO 633, New York, NY 09633
- 1 PACAF, Dir Civ Eng, APO 953, San Francisco, Calif 96553
- 1 USAFA, Colo 80840

AFSC ORGANIZATIONS

- 1 AFSC Scientific and Technical Liaison Office, Research and Technology Division, AFUPO, Los Angeles, Calif 90045
- 1 FTD, Wright-Patterson AFB, Ohio 45433
- 1 (TDBTL)
- 1 (TDEWG)
- 1 ASD (ASMC), Wright-Patterson AFB, Ohio 45433
- 1 ESD (ESF), Wright-Patterson AFB, Ohio 45433
- 1 RTD, Bolling AFB, Wash, DC 20332
- 1 (RTN-W)
- 1 (RTS)

DISTRIBUTION (cont'd)

No. cys

1 AF Msl Dev Cen (RRRT), Holloman AFB, NM 88330
 BSD, Norton AFB, Calif 92409
 1 (BSQ)
 1 (BSOT)
 1 (BSRA)
 5 (BSSRA)
 1 RADC (EMLAL-1), Griffiss AFB, NY 13442
 KIRTLAND AFB ORGANIZATIONS
 1 AFSWC (SWEH), Kirtland AFB, NM 87117
 AFWL, Kirtland AFB, NM 87117
 20 (WLIL)
 1 (WLA)
 1 (WLAS)
 1 (WLAV)
 30 (WLDC)
 1 (WLF)
 1 SAC Res Rep (SACLO), AFSWC, Kirtland AFB, NM 87117

OTHER AIR FORCE AGENCIES

Director, USAF Project RAND, via: Air Force Liaison Office, The
 RAND Corporation, 1700 Main Street, Santa Monica, Calif 90406
 1 (RAND Physics Div, H. Brode)
 1 (RAND Library)
 1 SACSO, Norton AFB, Calif 92409
 1 Hq OAR (RROS), Bldg T-D, Wash, DC 20333
 1 AFOSR (SRGL), Bldg T-D, Wash, DC 20333
 1 AFRL, L. G. Hanscom Fld, Bedford, Mass 01731

ARMY ACTIVITIES

1 Chief of Research and Development, Department of the Army (Special
 Weapons and Air Defense Division), Wash, DC 20310
 1 Director, Ballistic Research Laboratories (Library), Aberdeen
 Proving Ground, Md 21005
 1 Chief of Engineers (ENGMC-EM), Department of the Army, Wash, DC
 20315
 3 Director, US Army Waterways Experiment Sta (WESRL), P. O. Box 631,
 Vicksburg, Miss 39181

DISTRIBUTION (cont'd)

No. cys

2 Director, US Army Engineer Research and Development Laboratories,
ATTN: STINFO Branch, Ft Belvoir, Va

NAVY ACTIVITIES

1 Chief of Naval Research, Department of the Navy, Wash, DC 20390

1 Bureau of Yards and Docks, Department of the Navy, Code 22.102,
(Branch Manager, Code 42.330), Wash 25, DC

1 Commanding Officer, Naval Research Laboratory, Wash, DC 20390

1 Superintendent, US Naval Postgraduate School, ATTN: George R. Luckett,
Monterey, Calif

3 Commanding Officer and Director, Naval Civil Engineering Laboratory,
Port Hueneme, Calif

1 Commander, Naval Ordnance Laboratory, ATTN: Dr. Rudlin, White Oak,
Silver Spring, Md 20910

1 Commanding Officer, US Naval Weapons Evaluation Facility (NWEF,
Code 404), Kirtland AFB, NM 87117

OTHER DOD ACTIVITIES

2 Director, Defense Atomic Support Agency (Document Library Branch),
Wash, DC 20301

1 Commander, Field Command, Defense Atomic Support Agency (FCAG3,
Special Weapons Publication Distribution), Sandia Base, NM 87115

1 Director, Advanced REsearch Projects Agency, Department of Defense,
The Pentagon, Wash, DC 20301

1 Office of Director of Defense Research and Engineering, ATTN:
John E. Jackson, Office of Atomic Programs, Rm 3E1071, The Pentagon,
Wash, DC 20330

1 Chairman, Armed Services Explosives Safety Board, Wash 25, DC

1 US Documents Officer, Office of the US National Military Representa-
tive (SHAPE), APO 55, New York, NY

50 DDC (TIAAS), Cameron Station, Alexandria, Va 22314

AEC ACTIVITIES

Sandia Corporation, Box 5800, Sandia Base, NM 87115

1 (Information Distribution Division)

1 (M. Merrit)

1 (William Sigmon)

1 Sandia Corporation (Technical Library), P. O. Box 969, Livermore,
Calif 94551

1 University of California Lawrence Radiation Laboratory, ATTN:
Director's Office, Technical Information Division, P. O. Box 808,
Livermore, Calif 94551

DISTRIBUTION (cont'd)

No. cys

- 1 Director, Los Alamos Scientific Laboratory (Helen Redman, Report Library), P. O. Box 1663, Los Alamos, NM 87554
- OTHER
- 1 OTS (CFSTI, Chief, Input Section), Sills Bldg, 5285 Port Royal Road, Springfield, Va 22151
- 1 Office of Assistant Secretary of Defense (Civil Defense), Wash, DC 20301
- 1 Central Intelligence Agency (OCR), 2430 E Street NW, Wash, DC 20505
- 1 Institute for Defense Analysis, Rm 2B257, The Pentagon, Wash 20330
THRU: ARPA
- 2 Aerospace Corporation, ATTN: Mr. Italia, Ballistic Missile Div, San Bernardino, Calif
- 10 AF Shock Tube Facility, ATTN: Dr. Zwoyer, Box 188, University Station, Albuquerque, NM
- 2 University of Illinois, Civil Engineering Dept, ATTN: Dr. N. M. Newmark, Head, Talbot Laboratory, Urbana, Ill
- 5 Space Technology Laboratories, Inc., ATTN: Mr. Hoefs, San Bernardino Division, Norton AFB, Calif 92409
- 2 Ralph M. Parsons Co., ATTN: Mr. Melzian, 617 West 7th Street, Los Angeles 17, Calif
- 3 Boeing Co., ATTN: M. Head, Seattle 27, Wash
- 1 Arizona State University, ATTN: Prof P. Stein, Tempe, Ariz
- 1 Boeing Co., ATTN: Mr. R. Carlson, Suite 1005, First National Bank Bldg, 5301 Central NE, Albuquerque, NM
- 1 IIT Research Division, ATTN: Dr. E. Sevin, 10 West 35th Street, Chicago, Ill
- 1 Official Record Copy (Capt Auld, WLDC)

This page intentionally left blank.

DOCUMENT CONTROL DATA - R&D

(Security classification of title, body of abstract and indexing annotation must be entered when the overall report is classified)

| | | | |
|-------------------------------------------------------------------------------------------------------------------------------------------------------------------------------------------------------------------------------------------------------------------------------------------------------------------------------------------------------------------------------------------------------------------------------------------------------------------------------------------------------------------------------------------------------------------------------------------------------------------------------------------------------------------------------------------------------------------------------------------------------------------------------------------------------------------------------------------------------------------------------------------------------------------------------------------------------------------------------------------------------------------------------------------------------------------------------------------------------------|--|-----------------------------------------------------------------------------|----------------------|
| 1. ORIGINATING ACTIVITY (Corporate author) Air Force Weapons Laboratory (WLDC) Kirtland Air Force Base, New Mexico 87117 | | 2a. REPORT SECURITY CLASSIFICATION UNCLASSIFIED | |
| | | 2b. GROUP | |
| 3. REPORT TITLE SIMULATION OF AIR-BLAST-INDUCED GROUND MOTIONS (PHASE II) | | | |
| 4. DESCRIPTIVE NOTES (Type of report and inclusive dates) 1 July 1964 to 1 February 1965 | | | |
| 5. AUTHOR(S) (Last name, first name, initial) Auld, Harry E., Capt, USAF; D'Arcy, Gerald P., Capt, USAF; Leigh, Gerald G., Capt, USAF | | | |
| 6. REPORT DATE April 1965 | | 7a. TOTAL NO. OF PAGES 238 | 7b. NO. OF REFS 8 |
| 8a. CONTRACT OR GRANT NO. | | 9a. ORIGINATOR'S REPORT NUMBER(S) AFWL TR-65-26, Vol I | |
| b. PROJECT NO. 5710 | | 9b. OTHER REPORT NO(S) (Any other numbers that may be assigned this report) | |
| c. Subtask No. 12.166 | | | |
| d. | | | |
| 10. AVAILABILITY/LIMITATION NOTICES DDC release to OTS is authorized. | | | |
| 11. SUPPLEMENTARY NOTES | | 12. SPONSORING MILITARY ACTIVITY AFWL (WLDC) Kirtland AFB, NM 87117 | |
| 13. ABSTRACT Results from the Phase II, Long-Duration High-Explosive Simulation Technique (LDHEST) experiment are presented. This experiment simulates the air-blast-induced ground motions from a large-yield nuclear weapon over a plan area 96 feet by 150 feet. A specially designed matrix of primacord was utilized to produce the desired explosion in a confined volume of air. An overburden, or mass of material, was placed over the explosion to provide a reaction force to shape the resulting wave pulse and to provide the required long durations. The experiment produced an air pressure pulse which had a peak overpressure of 312 psi, a time to one-half peak pressure of 18.2 msec, and a total duration of 170 msec. The shock front traveled at an average velocity of 5,120 ft/sec. On the basis of these results, recommendations are made for future simulation experiments. The measured earth free-field motions and stresses are compared with theoretical calculations, and the validity of the technique for simulating the desired nuclear environment is established. | | | |

